A SYSTEMS ANALYSIS OF ELECTRODYNAMIC TETHERS INCORPORATING THEORETICAL MODELS OF ELECTRON COLLECTION PROCESSES

by

ROBIE I. SAMANTA ROY

S.B. Aeronautics and Astronautics
Massachusetts Institute of Technology, 1989

Submitted to the Department of
Aeronautics and Astronautics in Partial Fulfillment
of the Requirements for the
Degree of

MASTER OF SCIENCE
IN AERONAUTICS AND ASTRONAUTICS

at the

MASSACHUSETTS INSTITUTE OF TECHNOLOGY

February 1991

© Robie I. Samanta Roy, 1991

The author hereby grants to MIT permission to reproduce and to distribute copies of this thesis document in whole or in part.

Signature of Author_____
Department of Aeronautics and Astronautics
December, 1990

Certified by_____
Professor Daniel E. Hastings
Thesis Supervisor, Department of Aeronautics and Astronautics

Accepted by_____
Professor Harold Y. Wachman
Chairman, Department Graduate Committee

MASSACHUSETTS INSTITUTE
OF TECHNOLOGY

FEB 19 1991

LIBRARIES Aero

A SYSTEMS ANALYSIS OF ELECTRODYNAMIC TETHERS INCORPORATING THEORETICAL MODELS OF ELECTRON COLLECTION PROCESSES

by

Robie I. Samanta Roy

Submitted to the Department of Aeronautics and Astronautics
in December 1990 in partial fulfillments of the requirements
for the Degree of Master of Science in Aeronautics and Astronautics

ABSTRACT

A dynamic simulation program, incorporating detailed geomagnetic, ionospheric, and radiation impedance models, was developed to investigate the performance of electrodynamic tethers, both as power generators and thrusters. A theory of partially ionized gas emissions from a plasma contactor was worked out, and its impact on tether system performance examined. It was found that it is more effective to completely ionize the gas internally, than to partially ionize it externally, and that based on the specific power, the optimum gas to use is argon. The electron collection performance of a plasma contactor and bare wire tether, both separately, and in combination, were compared and contrasted. The power (and thrust) generated by a bare wire tether was found to have a higher dependence on the geomagnetic and ionospheric fluctuations. To control these large-scale fluctuations for both the bare wire and contactor tethers, a control strategy was developed incorporating a voltage regulator (and variable ion current emissions for the contactor). In addition, equatorial orbits greatly reduce power fluctuations. In this respect, it is found that tethers offer greater potential than previously envisioned.

As a pure thruster, the contactor tether was examined thrusting with constant current, voltage, thrust, and power. It was found that the best mode of operation was with constant power, with resulting power/thrust ratios better than those for ion or MPD engines. The concept of superconducting tethers was also explored and despite large increases in performance, was found to be impractical due to large cooling pump and mass flow rate requirements.

Thesis Supervisor: Professor Daniel E. Hastings
Title: Associate Professor of Aeronautics and Astronautics

Table of Contents

Abstract 1
Acknowledgments 2
Table of Contents 3
List of Figures 5
List of Tables 9

Chapter 1.0 Introduction 10

Chapter 2.0 Tether System Components and Issues 15
2.1 General Principles of Operation 15
2.2 Circuit Equation 17
2.3 Anodic Device 18
2.3.1 The Model of Gerver et al for Electron Collection 19
2.3.2 Extension of the Model of Gerver et al to Neutral Gas Emissions 26
2.3.3 Bare Tether Electron Collection 32
2.4 Cathodic Device 38
2.5 The Tether 40
2.5.1 Tether materials 40
2.5.2 Hollow Tethers 41
2.5.3 The Orbital Debris Environment and Multiple Tethers 42
2.5.4 Tether Deflection 43
2.5.5 Tether Temperature 46
2.5.6 Superconducting Tethers 49
2.6 The Radiation Impedance 54
2.7 Other Tether System Components 57
2.7.1 Batteries 57
2.7.2 Solar Arrays 58
2.7.3 Fuel Cells 61

ACKNOWLEDGEMENTS

Facts which at first seem
improbable will, even in
scant explanation, drop
the cloak which has
hidden them and stand
forth in naked and
simple beauty.

GALILEO GALILEI

I would like to thank my advisor, Professor Daniel Hastings, for all his advice and support on this project. His truly remarkable insight and constructive criticism are greatly appreciated. I would also like to express gratitude to Professor Manuel Martinez-Sanchez for his many enlightening discussions and suggestions. His depth of knowledge and intellect is truly admirable. Much gratitude is also expressed to Eduardo Ahedo, visiting professor, for all his help with the bare tether. I have learned a lot from his insistence on mathematical rigour.

I also would like to acknowledge my officemates for their invaluable assistance with the computers and their *camaraderie*. Lastly, a very special thanks to Dmitri Antonov, a visiting summer student from the Moscow Aviation Institute, for helping with some computational work on the radiation impedance.

2.7.4 The Power Regulator 62

Chapter 3.0 The Tether Electro-Magnetic Environment 63
3.1 The Geomagnetic Field 63
3.2 The Ionosphere 67

Chapter 4.0 The Simulation Model 70
4.1 General Overall Description 70
4.2 Orbital Mechanics 71
4.2.1 Coordinate Systems 71
4.2.2 Disturbing Accelerations 72
4.2.3 Perturbational Equations of Motion 73
4.2.4 Orbit Algorithm 74
4.3 Modes of Operation and Control Strategy 75

Chapter 5.0 Results and Discussion 79
5.1 Anodic Contactor Performance 79
5.2 Environmental Factors 83
5.3 Comparison of Anodic Devices (Contactor, Bare Tether, and Bare Tether+Contactor) for Power Generation 84
5.3.1 Uncontrolled Operation 84
5.3.2 Controlled Operation 87
5.4 Tether Deflection Results 90
5.5 Tether Temperature and Superconducting Tether Results 92
5.6 Orbital Mechanics Effects 94
5.7 Thrusting Mode of Operation 95
5.7.1 Contactor Thruster 95
5.7.2 The Bare Tether Thruster 99
5.8 Mixed Mode (Power Generation/Thrusting) 101
5.9 Radiation Impedance Effects 102
5.10 Hollow, Multiple Tethers and Variation of Length 103

Chapter 6.0 Conclusions 106

References 194

List of Figures

Figure		
1a,b	Schematics of Tether in LEO	109
2a,b	Diagram of Tether Circuits	110
3	Anisotropic Contactor Cloud	111
4	Bare Tether Circuit Schematics	111
5a	Thrust and Efficiency vs. Bare Anode Voltage	112
5b	Bare Tether Thruster Current Profile	112
6	Cathode Current-Voltage Characteristic	113
7	Tether Deflection Diagram	113
8	Evolution of Superconducting Temperatures	114
9	Superconducting Tether Diagram	114
10	Radiation Impedance for 20 m End Connector	115
11	Radiation Impedance for Various Size End Connectors	115
12	SAFE Weight Summary	116
13a	Induced Voltage, 28.5° Orbit	117
13b	Maximum Contactor Power, 28.5° Orbit	117
14	Map of Geomagnetic Field	118
15	Induced Voltage, 1° Orbit	118
16	Profile of Earth's Ionosphere	119
17a	Profile of Jupiter's Ionosphere	119
17b	Profile of Saturn's Ionosphere	120
17c	Profile of Uranus's Ionosphere	120
18a	Ionospheric Electron Density, Average Sunspot No.	121
18b	Ionospheric Electron Density, High Sunspot No.	121
18c	Ionospheric Electron Current, Average Sunspot No.	122
19	Orbital Mechanics Coordinate Systems	122
20a	Contactor Maximum Power vs. Efficiency	123
20b	Contactor Current vs. Efficiency	123
21a	Contactor Power vs. Iion and f (Good Conditions)	124
21b	Contactor Power vs. Iion and f (Poor Conditions)	124
21c	Contactor Cloud Radius vs. Iion and f (Good cond.)	125

21d Contactor Potential vs. Iion and f (Good cond.) 125
22a Max. Contactor Power vs. Iion and f (Simulation) 126
22b Specific Power of Cont. vs. Iion and f (Simulation) 126
23a Max. Contactor Power vs. Tether Diameter 127
23b Specific Power vs. Tether Diameter 127
24a Max. Contactor Power vs. Gas Molecular Weight 128
24b Specific Power vs. Gas Molecular Weight 128
25 Max. Contactor Power vs. Gas Emission Velocity 129
26a Max. Contactor Power vs. Operating Height 129
26b Specific Power vs. Operating Height 130
27a Variation of Max. Cont. Power with Seasons 130
27b Variation of Specific Power with Seasons 131
28a Comparison of Anodes (Average Maximum Power) . . . 131
28b Comparison of Anodes (Specific Power) 132
28c Comparison of Anodes (Efficiency) 132
28d Comparison of Anodes (Mass) 133
28e Comparison of Anodes (Drag Makeup Fuel) 133
28f Contactor Average Maximum Power 134
28g Bare Tether Average Maximum Power 134
28h Bare+Contactor Average Maximum Power 135
28i Contactor Current (Maximum Power) 135
28j Bare Tether Current (Maximum Power) 136
28k Bare+Contactor Current (Maximum Power) 136
28l Bare+Contactor Bare Current (Maximum Power) 137
28m Bare Tether Collecting Length (Maximum Power) 137
28n Bare+Contactor Collecting Length (Max. Power) 138
28o Contactor Efficiency (Maximum Power) 138
28p Bare Tether Efficiency (Maximum Power) 139
28q Bare+Contactor Efficiency (Maximum Power) 139
28r Anodic Contactor Voltage (Maximum Power) 140
28s Bare Anode Voltage (Maximum Power) 140
28t Bare+Contactor Anodic Voltage (Maximum Power) 141
28u Contactor Cloud Radius (Maximum Power) 141
29a Comparison of Controlled Anodes (Ave. Max. Power) . . 142
29b Comparison of Controlled Anodes (Specific Power) 142
29c Comparison of Controlled Anodes (Efficiency) 143
29d Comparison of Controlled Anodes (Mass) 143
29e Comparison of Controlled Anodes (Drag Makeup Fuel) . 144
29f Contactor Average Controlled Power 144
29g Bare Tether Average Controlled Power 145
29h Bare+Contactor Average Controlled Power 145
29i Contactor Current (Controlled) 146
29j Bare Tether Current (Controlled) 146

29k Bare+Contactor Current (Controlled) 147
29l Bare Tether Collecting Length (Controlled) 147
29m Bare+Contactor Collecting Length (Controlled) 148
29n Contactor Efficiency (Controlled) 148
29o Bare Tether Efficiency (Controlled) 149
29p Bare+Contactor Efficiency (Controlled) 149
29q Contactor Cloud Radius (Controlled) 150
30a Tether Deflection (To Scale) 150
30b Tether Endtip Deflection vs. Endmass 151
30c Base Deflection Angle vs. Endmass 151
30d Tether Endtip Deflection vs. Current 152
30e Base Deflection Angle vs. Current 152
30f Bare Tether Endtip Defl. and Base Defl. Angle 153
31a Tether Heat Flux (0° Declination angle) 153
31b Tether Heat Flux (23.5° Declination angle) 154
31c Tether Temperature, No Ohmic Heating 154
31d Tether Temperature, Maximum Power 155
31e Tether Temperature, Controlled 155
31f Tether Resistance Variations 156
31g Tether Length Variations 156
32a Heat Energy to Tether vs. Diameter 157
32b Pressure Drop Across Cooling Tube 157
32c Coolant Pump Power 158
32d Daily Coolant Mass Flow Rate 158
32e Final Temperature in Cooling Tube vs. Flow Velocity . . 159
32f Ave. Maximum Power, Superconducting Tether 159
32g Specific Power, Superconducting Tether 160
33a Electrodynamic Drag (Maximum Power, Cont.) 160
33b Semimajor Axis (Power Generation) 161
33c Semimajor Axis (Thrusting) 161
33d Longitude of Nodes 162
33e Argument of Perigee 162
33f Eccentricity (Power Generation) 163
33g Eccentricity (Mixed Mode) 163
33h Inclination 164
34a Ave. Thrust for Constant Current Thruster (CCT) 164
34b Mass/Thrust for CCT 165
34c Power/Thrust for CCT 165
34d Efficiency of CCT 166
34e Supply Voltage for CCT (I=4) 166
34f Supply Power for CCT (I=4) 167
34g Thrust for CCT (I=4) 167
35a Ave. Thrust for Constant Voltage Thruster (CVT) 168

35b Mass/Thrust for CVT 168
35c Power/Thrust for CVT 169
35d Efficiency of CVT 169
35e Supply Power for CVT (V=5000) 170
35f Current for CVT (V=5000) 170
35g Thrust for CVT (V=5000) 171
36a Ave. Thrust for Constant Power Thruster (CPT) 171
36b Mass/Thrust for CPT 172
36c Power/Thrust for CPT 172
36d Efficiency of CPT 173
36e Supply Voltage for CPT (P=20 kW) 173
36f Current for CPT (P=20 kW) 174
36g Thrust for CPT (P=20 kW) 174
37a Mass/Thrust for Constant Thrust Thruster (CTT) 175
37b Power/Thrust for CTT 175
37c Efficiency of CTT 176
37d Supply Voltage for CTT (F=2 N) 176
37e Supply Power for CTT (F=2 N) 177
37f Current for CTT (F=2 N) 177
38 Mass Comparison of Thrusters, <F> = 4 N 178
39a Thrust and Efficiency of Bare Thruster vs. Bare Length 178
39b Current and Power of Bare Thruster vs. Bare Length .. 179
39c Thrust for Partly Bare Tether, L=20 km 179
39d Thrust for Partly Bare Tether, L=15 km 180
39e Controlled Thrust for Partly Bare Tether, L=20 km ... 180
39f Controlled Thrust for Partly Bare Tether, L=15 km ... 181
39g Mass/Thrust for Bare Tether Thruster 181
39h Power/Thrust for Bare Tether Thruster 182
39i Efficiency of Bare Tether Thruster 182
39j Supply Power for Bare Thruster 183
39k Supply Voltage for Bare Thruster 183
39l Current for Bare Thruster 184
39m Thrust for Bare Thruster 184
39n Supply Power for Controlled Bare Thruster 185
39o Mass Comparison of Partly Bare Thrusters 185
39p Mass Comparison of Controlled Partly Bare Thrusters . 186
40a Radiation Impedance for D=6 m Contactor 186
40b Radiation Impedance for D=1 m Contactor 187
40c Radiation Impedance for D=0.5 m Contactor 187
40d Effect of Variable Ionospheric Impedance 188
40e Effect of High Constant Ionospheric Impedance 188
41a Hollow Bare Tether Maximum Power 189
41b Hollow Bare Tether Specific Power 189

42a Hollow Contactor Tether Maximum Power 190
42b Hollow Contactor Tether Specific Power 190
43a Maximum Power of Multiple Tethers 191
43b Specific Power of Multiple Tethers 191
44a Maximum Power vs. Tether Length 192
44b Specific Power vs. Tether Length 192

List of Tables

Table
1 Break-even points of Maximum Power and Controlled Tethers 193
2 Contactor Thruster Performance, <F> = 4 N 193
3 Uncontrolled and Controlled Bare Tether Thruster Performance 193

Chapter 1.0

Introduction

Tethers in space can be used for a wide variety of applications such as power generation, propulsion, remote atmospheric sensing, momentum transfer for orbital maneuvers, micro-gravity experimentation, and artificial gravity generation. These are only a few of the host of uses that have been envisioned and proposed for many years. In general, a tether is a long cable (even up to 100 km or more) that connects two or more spacecraft or scientific packages. Electrodynamic tethers are conducting wires that can be either insulated (in part or in whole) or bare, and that make use of an ambient magnetic field to induce a voltage drop across their length. The induced voltage is given by $|\mathbf{v}\times\mathbf{B}\bullet\mathbf{L}|$, where v is the relative velocity to the ambient plasma (the orbital velocity less the earth's rotational speed), B is the geomagnetic field strength ($2\text{-}6\times10^{-5}$ T), and L is the length of the tether. For a 20 km tether in low earth orbit (LEO), this voltage can fluctuate between 1500 to 5300 volts open circuit, depending on the orbital inclination. If a current is allowed to circulate through the tether and a load, substantial power on the order of 15-30 kW can be generated. However, this power is generated at the cost of orbital energy. Hence an electrodynamic force $|\mathbf{IL}\times\mathbf{B}|$, on the order of a few newtons, is exerted on the tether lowering the orbit. On the other hand, with a sufficiently large power supply onboard the spacecraft, the direction of the current can

be reversed and the tether becomes a thruster, raising its orbital height. Thus a spacecraft can use an electrodynamic tether system as a pure power generator (with a small rocket to periodically make-up for the drag), as a pure thruster, or in a combination of both roles.

The origin of the concept of space tethers dates back to the last century when the Russian astronautics pioneer Kostantin Tsiolkovsky conceived of an "Orbital Tower" in 1895[17]. His concept was a huge Eiffel Tower-like cable structure that would reach geosynchronous heights from the Earth's surface and could be used as a means for launching space flights. The next mention of tethers appeared in a Sunday edition of *Pravda* in 1960. Based on Tsiolkovsky's idea, Y. N. Artsutanov proposed a "Heavenly Funicular" which was a satellite in Geosynchronous Earth Orbit (GEO) with two long cables: one upwards, and one downwards towards the Earth's surface. These concepts captured the imagination of the famous science-fiction author Arthur Clarke, who wrote an article in 1963 entitled, "Space Elevator". He also published the first novel containing long orbiting tethers, The Fountain of Paradise in 1979. On the more "academic" side, R. D. Moore proposed a "Geomagnetic Thruster" in 1966. This device was a conducting wire terminated at both ends by plasma contactors, the first true electrodynamic tether. Another innovative idea appeared in 1969. To reduce the transmitter power requirements of geostationary communications satellites, A. Collar and J. Flower proposed "A (Relatively) Low Altitude 24 Hour Satellite". This concept used a tether that extended down from a satellite in GEO to a transmitting subsatellite in LEO. Many other variations of these concepts followed, but a notable one was H. Alfvén's "Solar Wind Engine" in 1972. Alfvén proposed a 500 km superconducting cable, terminated with ion and electron emitters, that would utilize the solar magnetic field for propulsion. Meanwhile, in the experimental arena, the first tether experiments were conducted during the Gemini Program in the 1960's and were aimed at exploring the dynamics of tethered space vehicles.

The years 1972-3 saw the dawn of the Shuttle-borne tether era. M. Grossi and his colleagues at the Smithsonian Astrophysical

Observatory (SAO), proposed using a tether as an orbiting ULF/ELF antenna to be carried on the Space Shuttle. Since then, much theoretical work has been done on tethers and the subject has grown substantially, culminating in the formation of a joint US-Italian space program with the goal of developing a Tethered Satellite System (TSS) to be operated from the Shuttle[27]. The TSS program plans to launch the first tethered satellite TSS-1, a 20 km upwardly deployed conducting tether. TSS-1 will explore some basic dynamic, control, and electrodynamic issues and is baselined to fly sometime during 1991. A second program, TSS-2, will follow a couple of years later and will consist of a 100 km non-conducting tether deployed downward. This mission's objective is to conduct experiments mainly related to upper atmospheric physics.

Over the last several years, there have been a number of system or engineering studies conducted, concentrating on the electrodynamic aspects of tethers. These studies have examined the uses of tethers in propulsion and/or power generation applications. We will review three of such studies. One of the very first of these studies was by Grossi and Arnold in 1984[16] who employed a computer simulation model that included a geomagnetic and ionospheric model. They found that the power generated varied by as much as ±20% due to magnetic field variations and hence batteries were required for power leveling purposes. In addition, they included tether dynamics in their simulation, and found that the interaction between dynamics and electrodynamics (i.e. tether oscillations driven by the electromagnetic force) was only significant for very high current levels (>15 A). The concept of orbital energy storage, or mixed mode operation was also introduced. The idea was that a tether would thrust in the day drawing power from solar arrays, and generate power during the night; the power/thrust levels being adjusted so that the semi-major axis (i.e. the energy) of the orbit would remain constant. However, the major drawback of their approach was that they did not include very realistic models of the current collection process. Nevertheless, this study contributed greatly to the early understanding of the engineering issues involved

with electrodynamic tethers.

In 1986, Martinez-Sanchez, Rivas, Prall, and Hastings[29,30] conducted a very thorough systems study employing state of the art theories and components. A tether was studied as a stand-alone power generator, as a thruster for an orbital tug, and as a combination generator/thruster for orbital energy storage. This study concluded that electrodynamic tethers were marginally better in some respects and worse in others compared to other alternative space power and propulsion technologies. One of the key factors was the variability of the geomagnetic field which drove the system mass, as was first noted by Grossi and Arnold. The variability of the ionosphere was also cited as a factor, but not rigorously included in the calculations. Concern was expressed that the ionospheric density would drop too low during the night, so that tether operation would momentarily cease. The outstanding technical difficulties that were cited were ionospheric impedance, contactor performance, insulator fault behavior, and tether dynamics. Moreover, this work was based on several simplifying assumptions about the current closure loop and the ability of the tether to extract and emit electrons into the ionosphere. The ionospheric impedance was neglected, and the contactor voltage drops were taken to be independent of the current levels.

Lastly, a recent study was conducted by Greene, Wheelock, and Baginski[14] on the proposed Getaway Tether Experiment (GATE), which consists of two small free-flying satellites launched from the Shuttle connected by a one km conducting tether. Their objective was only to show crudely, the feasibility of the GATE to bilaterally transfer energy between stored electrical energy and orbital momentum. The major drawbacks of their model were the elementary magnetic model they used, the absence of an ionospheric model, and oversimplified contactor models.

Since the publication of the first two studies, the understanding of the current closure loop and its associated impedance has been considerably improved. In addition, physically based models have been developed for the current collection to a tether via a plasma

cloud, although in many ways they are still far from being complete. The main purpose of this thesis is to incorporate these new models into an updated systems analysis and judge whether the previous conclusions are still valid or not. A detailed computer program has been developed to simulate the performance of a tether in low earth orbit. The program uses a highly accurate model of the geomagnetic field, supplied from the Smithsonian Astrophysical Observatory, courtesy of G. Gullahorn, and the latest International Reference Ionosphere model from the National Space Science Data Center, courtesy of Dr. D. Bilitza. Non-singular perturbational equations of motion are employed to take into account disturbances due to the oblateness of the earth, atmospheric drag, and electrodynamic forces in order to include their effect on the tether's orbital motion. Any low earth orbit can be accepted, and the program will provide time histories of various variables of interest such as, the orbital elements, current, induced voltage, power generated, the electrodynamic force, and the tether temperature. Temperature variations in the tether resistance and length are taken into account. In addition, based on the power output and current levels, the total system mass, and the mass of each system component are computed. The components include the tether, batteries (to level fluctuations), plasma contactors, and a power regulator.

In Chapter 2.0 of this thesis, we will discuss the various components and issues of the tether system. In addition, a theory for neutral gas emissions from an anodic plasma contactor is worked out, and the concept of superconducting tethers is explored. In Chapter 3.0, the tether environment in LEO will be presented. Chapter 4.0 discusses the overall simulation model, aspects of orbital mechanics, and a control strategy developed to reduce power fluctuations. The results and discussion follow in Chapter 5.0, and lastly, conclusions are offered in Chapter 6.0.

Chapter 2.0

Tether System Components and Issues

In this section, we will discuss the basic principles of tether operation, and the various components. These components include the anodic and cathodic devices, the tether itself, and other supporting items such as the power regulator and battery systems. A theory for neutral gas emissions is developed, and the concept of superconducting tethers is explored.

2.1 General Principles of Operation

Consider a tether in LEO as in Fig. (1). For prograde low inclination orbits, the velocity vector (**v**) of the vertically orientated tether points eastwardly, and is almost perpendicular to the magnetic field lines (**B**) which run south to north. Charged particles in the tether will experience a force given by the Lorentz relation,

$$\mathbf{F} = q(\mathbf{E} + \mathbf{v} \times \mathbf{B}) \qquad (1)$$

where **E** is the ambient electric field of the LEO plasma which is very small and will therefore be neglected. Hence the motional electric field **v** x **B** induces an EMF given by,

$$V_{ind} = \int \mathbf{v} \times \mathbf{B} \cdot d\mathbf{l} \qquad (2a)$$

where **dl** is an element of length along the tether. Strictly speaking, the velocity **v** is the relative velocity of the tether to the ambient plasma that is co-rotating with the earth. However, the rotational

speed of the earth is small compared to the orbital velocity of the tether, hence v will be taken to be the orbital velocity. In most cases, the tether is assumed to be straight so the induced voltage becomes,

$$V_{ind} = |\mathbf{v} \times \mathbf{BL}| \tag{2b}$$

where L is the length of the tether. If current is allowed to flow through the tether, an electromagnetic force on the tether will be,

$$\mathbf{F_{EM}} = \int \mathbf{I\, dl \times B} \tag{3a}$$

or when the tether is assumed rigid,

$$\mathbf{F_{EM}} = \mathbf{LI \times B} \tag{3b}$$

The direction of the current will determine the direction of the force, whether it will be a thrusting force, or a drag force. For an upwards (or downwards) deployed tether, if the current flows up (away from the earth), power is generated at the cost of orbital energy since the electromagnetic force is anti-parallel to the direction of motion. On the other hand, if a power supply large enough to reverse the induced EMF drives the current down, the electromagnetic force vector acts parallel to the direction of motion. Of course, these directions are reversed for retro-grade orbits.

In an electrodynamic tether, the current that flows is actually the electrons that are collected from the ambient ionospheric plasma. Electrons are drawn in on one end of the tether, and are ejected out the other, the particular end depending on whether the tether is thrusting or generating power. The end of the tether that must collect electrons and/or eject ions is called the anode. The other end that ejects electrons and/or collects ions is called the cathode. Paramount to this process of current flow are two important issues. One is the ionospheric resistance to a current flowing through it. The other is the actual ability for the collecting end of the tether to collect the electrons with little voltage loss. The electron emitting end does not pose a large problem since space tests have demonstrated that large currents can be ejected with little voltage drop.

The ionospheric impedance is actually due to a complicated electromagnetic phenomena. Analogous to a ship creating waves as

it moves through the water, a moving conductor through a plasma generates electromagnetic waves. These waves dissipate energy with some effective resistance, called the radiation impedance, which has been examined in some detail[3,38]. In Section 2.6, we discuss a model of radiation impedance that was incorporated in this simulation model.

Research is still actively going on to investigate means of electron collection and the underlying physical processes. Several different options exist for electron collection such as a passive large surface (like a balloon), a passive grid, a plasma contactor, or a light ion emitter. The most promising of these devices is the plasma contactor. The ambient electron density in low earth orbit (LEO) is rather low ($10^{10\text{-}12}$ m^{-3}), so to collect the required current requires a very large surface area (~100-1000 m^2 for 1 amp). Instead of using a large physical area, plasma contactors create a plasma cloud that expands out and collects ambient electrons while emitting ions. It is important to note that these contactors operate by ejecting fully or partially ionized gas. For a device using argon, the mass flow rate is about 13 kg/yr/amp. A recently proposed method for electron collection[35] discussed later, is to leave part of the tether bare, i.e. to have only part or the whole of the conducting wire uninsulated. As we will see later, for a 20 km tether, up to ten kilometers, which represents a rather large area, will be positive to the plasma and can collect electrons. The inherent advantage of this scheme is the absence of the mass and complexity of a collecting contactor.

2.2 The Circuit Equation

In the strict sense, the picture of electron emission and collection into the ionosphere as a DC phenomenon is not entirely correct. Electrons emitted and collected are constrained to travel along the magnetic field lines, or flux tubes which can be thought of as parallel transmission lines. These transmission lines are excited as the tether ends contact them, hence the phenomenon is fundamentally AC. However, since the magnetic field lines in reality form a continuous media, the current flow is DC.

A circuit equation can be written consisting of various voltage

drops for a tether system. For a tether generating power we can write,

$$V_{IND} = \Delta V_A + \Delta V_C + IZ_I + IR_T + IR_L \qquad (4a)$$

where ΔV_A and ΔV_C are the voltage drops across the anode and cathode respectively, Z_I is an effective ionospheric impedance, R_T is the tether ohmic resistance, and R_L is the load. If we define an efficiency, η, as,

$$\eta = \frac{Power_{LOAD}}{Power_{TOTAL}} = \frac{IV_{LOAD}}{IV_{IND}} = \frac{V_{LOAD}}{V_{IND}} \qquad (4b)$$

then, the circuit equation, Eqn. (4a), can be rewritten as,

$$\Delta V_A + \Delta V_C + I(Z_I + R_T) = V_{IND}(1 - \eta) \qquad (4c)$$

As we will see later, for any given operating conditions (i.e. V_{IND} and electron density), there exists a unique value of η where the power generated I^2R_L is maximized.

A similar equation can be written for a tether generating thrust, except now, an onboard power supply is required to reverse the current,

$$V_{IND} + \Delta V_A + \Delta V_C + I(Z_I + R_T) = V_{PS} \qquad (4d)$$

where V_{PS} is the voltage of the power supply. Figs. (2a,b) show schematics of these tether circuits. We shall examine each of these voltage drop terms in the following sections.

2.3 Anodic Device

Space experiments during the 1970's onboard the Space Electric Rocket Test (SERT) II[23,24] showed that electrons could be ejected into the ionosphere with relatively little voltage loss. However, space experiments where multi-ampere currents of electrons are collected have never been performed. Hence, this area of electron collection has been examined theoretically at some length for some time. However, even today, the models are still far from being complete. Due to the lack of any in-space tests, the validity of models can not be verified. The main complicating factor is the presence of the geomagnetic field which constrains electrons along the magnetic field lines thus making the problem anisotropic. For typical values of B ~ $2\text{-}6\text{x}10^{-5}$ T, the electron gyroradius ($m_e v/eB$) is about 2.5 cm. Due to the magnetized nature of the ambient plasma, spherical models

describing the electron collection process and ground based experiments where magnetized effects are weak, are inadequate. Theoretical work has fallen into two categories: collisionless double layer theory describing space charge limited clouds, and collisional quasi-neutral theory[13].

The various double layer models all have diverse hypotheses on the size of the inner core region of the plasma cloud where electrons are collected. Parks and Katz[32] used the requirement of matching the cloud density with the ambient density. Dobrowolny and Iess[9] presented another model where they required regularity of the self-consistent potential at the outer boundary of the core, $\partial\phi/\partial r(r_{core}) \approx 0$. Lastly, Wei and Wilbur[39] applied consistent space charge limited flow in the core: $m_i n_i u_i^2 \approx m_e n_e u_e^2$. More recently, Ahedo et al[1], developed a rigorous theory for the steady-state collisionless interaction between a spherical anode and an unmagnetized plasma. It was found that the maximum current collected was in the inertial motion limit. Due to their neglect or weak inclusion of magnetized effects, these models are more applicable to ground based experiments, but not to space. Ground based experiments have not been able to fully simulate space conditions due to different plasma densities and magnetic fields.

The other contactor model category is collisional quasi-neutral theory. Hastings[18] attempted to take magnetic effects into account by equating the electron collision frequency with the electron gyrofrequency, $\upsilon_e(r_{core}) \approx \omega_{ce}$, at the outer region of the cloud. Hastings, Gatsonis, and Rivas[19] examined a multi-region cloud that was anisotropic along the direction of orbital motion, not along the magnetic field. One drawback of this model was that it did not fully include anisotropic effects along the magnetic lines.

One of the latest models of contactor clouds, by Gerver, Hastings, and Oberhardt[13], is an anisotropic model orientated along the magnetic field. The next sections will describe this model and will extend it with the addition of neutral gas emissions and external ionization.

2.3.1 The Model of Gerver et al for Electron Collection

The Gerver model is an anisotropic contactor cloud orientated along the magnetic field, with $\upsilon_e < \omega_{ce}$. Along the magnetic field, the electrons are nearly collisionless, so that double layers form. Across the magnetic field, electrons diffuse collisionally, and the potential profile is quasi-linear. Fig. (3) schematically depicts the collection process.

The model is cast in cylindrical coordinates r and z, where r refers to the radial distance across the magnetic field lines, and z is the distance along the field lines. In general, the cloud will be much larger along the magnetic lines than across them. Therefore changes in the r-direction are more rapid than in the z-direction. The plasma density in the cloud is assumed to be great enough to short out the electric field due to the orbital velocity. Hence, the cloud will be cylindrically symmetric. Of course, at large distances away, this symmetry will break-down. The potential drop in the plasma cloud is assumed to be very much greater than the ion temperature T_i. Also, Gerver et al show that the electron temperature T_e is a few times less than the anode potential drop ϕ_o. Therefore it can be implied that within the cloud, $T_e/T_i \gg 1$. In the cloud region, the electron velocity is taken to be mostly azimuthal at the drift velocity,

$$v_d = \frac{e}{m_e \omega_{ce}} \frac{\partial \phi}{\partial r} \qquad (5)$$

where the electron temperature terms have been neglected. For contactor applications, this drift velocity is much greater than the radial flow velocity of ions emitted from the anode, which are unmagnetized since the scale lengths are all assumed to be much less than the ion gyroradius.

The mechanisms by which electrons are assumed to be transported across the magnetic field lines are various plasma instabilities such as the ion acoustic instability, the Buneman instability, the electron cyclotron drift instability, the modified two-stream instability, and the lower hybrid drift instability. Which of these processes is important depends on various parameters such as the ratios of the electron to ion temperatures, T_e/T_i, and the plasma frequency to the electron gyrofrequency, ω_{pe}/ω_{ce}. These instabilities will generate turbulent azimuthal electric fields which will create an

azimuthal drag force slowing the electrons down and causing them to drift radially inward towards the anode at a velocity,

$$v_{er} = \frac{\nu_e}{\omega_{ce}} v_d \tag{6}$$

Since $T_e/T_i \gg 1$, it was assumed that the most probable dominant instability would be the ion acoustic instability. For this type of instability, the electron collision frequency ν_e scales with the plasma frequency ω_{pe}. As a first approximation, and on the basis of some other theoretical and experimental evidence, Gerver et al assumed that,

$$\nu_e \approx 0.01\omega_{pe} \tag{7}$$

The governing equation is the electron continuity equation. The divergence of the radial flux of electrons due to n_e and the radial electric field and temperature and density gradients must be balanced by an inward flux of electrons along the magnetic field, neglecting ionization and recombination,

$$\frac{1}{r}\frac{\partial}{\partial r} r n_e v_r + \frac{\partial}{\partial z} n_e v_z = 0 \tag{8}$$

(In the next section, we will extend this theory by including ionization).

Since the flow of electrons along the magnetic field is highly collisionless, double layers will form at some distance z_o in both directions of the anode where,

$$J_i = \frac{I_i\, g(z_0)}{2\pi r_1^2} = \left(\frac{m_e}{m_i}\right)^{1/2} J_e^{\infty} \tag{9}$$

Here, g(z) is a correction factor to take into account focusing of the ions by the potential $\phi(r,z)$, and r_1 is the outer radius of the cloud. This is the well known result that relates ion and electron current densities across a double layer. A double layer is defined[7] as consisting of two equal but oppositely charged, essentially parallel but not necessarily plane space charge layers. The potential changes very rapidly inside, but does not have to do so in any monotonic fashion. Indeed, there can be instances where there are extremum inside. Generally, the following three conditions must be fulfilled: 1) The potential drop ϕ_o through the layer must obey the relation $|\phi_o| \geq$ kT/e where T is the temperature of the coldest plasma bordering the layer; 2) The electric field is much stronger inside the double layer

than outside, and the integrated positive and negative charges nearly cancel each other, and 3) Quasi-neutrality is locally violated in both space-charge layers. Even though the electrons are collisionless along the magnetic lines, it was assumed that a small drag force slowed down the electrons so that they do not escape through to the other end of the cloud "tube". This drag could be provided by small electron-electron streaming instabilities.

Because the electrons crossing the magnetic field are collisional, no double layer is formed in the radial direction. This means that the radius of the cloud is nearly independent of z. Hence Eqn. (8) can be solved by separating variables in r and z. The boundary conditions in r are:

$$\phi(r=a_o,z) = \phi_o + T_e \ln(n_e(z)/n_e(z=0)) \qquad (10a)$$

$$\frac{\partial \phi}{\partial r} = \frac{1}{e}\frac{\partial T_e}{\partial r} \text{ at } r=r_1 \qquad (10b)$$

$$\phi(r=r_1) = 0 \qquad (10c)$$

where a_o is the radius of the anode itself. The last statement enforces the condition that $v_r = 0$ outside the contactor cloud. Along the z-direction, at $z = \pm z_o$, the electron flux along the magnetic field lines satisfies,

$$-n_e v_z = \pm \frac{J_e^\infty}{e} \qquad (10d)$$

where J_e^∞ is the ambient electron saturation current given by,

$$J_e^\infty = e n_e \sqrt{\frac{kT}{2\pi m_e}} \qquad (10e)$$

We may now proceed to integrate Eqn. (8) and solve for the potential profile $\phi(r,z)$.

Integrating Eqn. (8) over z from $-z_o$ to $+z_o$ yields,

$$\int_{-z_0}^{+z_0} dz \frac{1}{r}\frac{\partial}{\partial r}(r n_e v_r) = 2\frac{J_e^\infty}{e} \qquad (11)$$

where Eqn. (10d) has been used for the z-direction term, the factor of two coming from the two ends of the cloud "tube". To continue the analysis, we need an expression for n_e. This can be obtained by imposing quasi-neutrality,

$$n_e = n_i = \frac{I_i\, g(r,z)}{4\pi(r^2 + z^2)e\sqrt{\frac{2e}{m_i}(\phi_o - \phi)}} \qquad (12)$$

where g(r,z) is again a focusing factor for the non-spherically symmetric expansion of the ions, and I_i is the emitted ion current. The expression for v_{er} can be found by substituting Eqns. (5,6,7),

$$v_{er} = \frac{\nu_e}{\omega_{ce}} v_d = \left(0.01 \frac{\omega_{pe}}{\omega_{ce}}\right) \frac{e}{m_e \omega_{ce}} \frac{\partial \phi}{\partial r} \tag{13}$$

The plasma frequency ω_{pe} is,

$$\sqrt{\frac{n_e e^2}{\varepsilon_o m_e}} \tag{14a}$$

and the electron gyrofrequency ω_{ce} is,

$$\frac{eB}{m_e} \tag{14b}$$

where B is the magnetic field strength. Instead of substituting a representative value for the magnetic field as Gerver et al did, we will leave it as a parameter since the B field does fluctuate in LEO as we will see later on. Thus we have,

$$v_{er} = \frac{0.01}{B^2} \sqrt{\frac{n_e m_e}{\varepsilon_o}} \frac{\partial \phi}{\partial r} \tag{15}$$

Substituting these expressions into Eqn. (11) gives,

$$\int_{-z_o}^{+z_o} dz \frac{1}{r} \frac{\partial}{\partial r} \left[r (r^2+z^2)^{-3/2} (\phi_o - \phi)^{-3/4} g(r,z)^{3/2} \frac{\partial \phi}{\partial r} \right] = \beta J_e^{\infty} B^2 I_i^{-3/2} \mu^{-3/4} \tag{16a}$$

where β is a constant given by,

$$\beta = \frac{2^{7/4}}{0.01} (4\pi)^{3/2} \varepsilon_o^{1/2} e^{5/4} m_p^{-3/4} m_e^{-1/2} \tag{16b}$$

and where μ is the molecular weight of the ions emitted, and m_p is the proton mass.

Since ϕ and $\partial\phi/\partial r$ are fairly independent of z, and the integrand of Eqn. (16a) is most strongly weighted near z=0, ϕ and $\partial\phi/\partial r$ can be taken out of the integral. In addition, Gerver et al considered any focusing effect near z=0 negligible, and set g(r,z) to 1. So we have,

$$\frac{\partial}{\partial r} \left[r (\phi_o - \phi)^{-3/4} \frac{\partial \phi}{\partial r} \int_{-z_o}^{+z_o} \frac{dz}{(r^2+z^2)^{3/2}} \right] = r \beta J_e^{\infty} B^2 I_i^{-3/2} \mu^{-3/4} \tag{17}$$

If we take z_o to be very large, the integral becomes, $2/r^2$. Therefore we are left with,

$$\frac{\partial}{\partial r} \left[\frac{1}{r} (\phi_o - \phi)^{-3/4} \frac{\partial \phi}{\partial r} \right] = r \frac{\beta}{2} J_e^{\infty} B^2 I_i^{-3/2} \mu^{-3/4} \tag{18}$$

This equation can be integrated again using Eqns. (10b,c) for the

integration constant:

$$(\phi_o-\phi)^{-3/4}\frac{\partial\phi}{\partial r} = -\frac{\beta}{4}J_e^{\infty}B^2I_i^{3/2}\mu^{-3/4}(r\xi - r^3) \tag{19a}$$

where ξ is a constant given by,

$$\xi = r_1^2 - \frac{1}{r_1}\phi_o^{-3/4}\left(\frac{\beta}{4}J_e^{\infty}B^2I_i^{3/2}\mu^{-3/4}\right)^{-1}\frac{1}{e}\frac{\partial T_e}{\partial r} \tag{19b}$$

Separating variables, and integrating one last time, we obtain:

$$(\phi_o-\phi)^{1/4} = \frac{\beta}{16}J_e^{\infty}B^2I_i^{3/2}\mu^{-3/4}\left(\xi\frac{r^2}{2} - \frac{r^4}{4}\right) + \Gamma \tag{20}$$

where the integration constant Γ can be obtained by using Eqn. (10a). However, since $a_o << r_1$ or z_o, the constant Γ can effectively be set to zero. Lastly, we can use Eqn. (10c,19b) to obtain,

$$(\phi_o)^{1/4} = \frac{\beta}{16}J_e^{\infty}B^2I_i^{3/2}\mu^{-3/4}\left(\frac{r_1^2}{2}\left(r_1^2 - f\left(\frac{\partial T_e}{\partial r}\right)\right) - \frac{r_1^2}{4}\right) \tag{21}$$

Based on the assumption $T_e << e\phi_o$, the function $f(\partial T_e/\partial r)$ can be neglected. Solving for the cloud radius r_1, we have,

$$r_1 = \left(\frac{64}{\beta}B^{-2}I_i^{3/2}\mu^{3/4}J_e^{\infty\,-1}\phi_o^{1/4}\right)^{1/4} \tag{22}$$

The ambient electron current and the cloud radius are related by,

$$2\pi r_1^2 J_e^{\infty} = I_e \tag{23}$$

where $I_e = I - I_i$. Thus by solving for the potential drop in the cloud ϕ_o from Eqn. (22), we have,

$$\phi_o = \left[\frac{I - I_i}{\frac{16\pi}{B\sqrt{\beta}}J_e^{\infty\,1/2}I_i^{3/4}\mu^{3/8}}\right]^8 \tag{24}$$

The two main equations of this theory are Eqns. (22) and (24), hence we examine some of their salient features. The main feature of the cloud radius is its dependency on the ambient electron current density J_e^{∞}. For a collecting surface of fixed area, the collected electron current I_e scales directly with J_e^{∞}. However, with a plasma contactor with B, I_i, and ϕ_o fixed, as the electron current density drops, the cloud expands as $(J_e^{\infty})^{-1/4}$, so that I_e scales as $(J_e^{\infty})^{1/2}$. Thus the dependency on the ionospheric electron current is reduced; if J_e^{∞} drops by an order of magnitude, (say going from day to night), the actual current will only drop by $(10)^{1/2}$ or about 3.2. Compared to passive electron collection, a plasma contactor works about three times better. Eqn. (22) also has the right scaling with the magnetic

field. As B increases, the electron gyroradius decreases making it harder for the cloud to increase its radius to capture more electrons.

The main feature of Eqn. (24) is that the potential drop of the cloud scales with $(I-I_i)^8$. The contactor acts almost like a diode. For small currents, the voltage drop can be very small, but as the current increases, the voltage drop increases very rapidly. Another interesting point is the dependence on the molecular weight of the emitted ions, μ. As the molecular weight increases, the voltage drop decreases. This is because as the ions become heavier, their velocity becomes slower, and they stay within the cloud longer. This increases the ion density which lowers the potential drop.

From the engineering point of view, we see that there are two parameters that can be controlled. One is the type of ion, and the other is the emitted ion current. These two parameters naturally lead to a number of questions. As the mass of the ion is increased, the potential drop of the anode decreases, and hence more power can be generated and the efficiency of the system increases. However, the mass flow rate increases also. Thus if too much mass is consumed, the specific power of the system defined as *Power/Mass* [W/kg] decreases. We can compute the mass consumption of an anodic plasma contactor as follows. The mass flow rate is $\rho v A$ through an orfice of some area A. The current density is $j_i = en_iv$, therefore, $\rho v = jm_i/e$ where m_i is the mass of the ion. However, the ion current $I_i = j_iA$. Therefore, the mass flow rate = $I_i(m_i/e)$ for complete ionization. Now if we let δ be the ratio of the total current to the ion current, I/I_i and f be the ionization fraction, we obtain the mass flow rate/total ampere,

$$\frac{\dot{m}}{I} = \frac{m_i}{e\delta f} \qquad (25)$$

which is the same equation as in [29]. For fully ionized argon, this gives a consumption rate of about 13.1 kg/amp-year, which is rather small indeed. The study of comparing power versus contactor mass consumption and the rationale for choosing a type of gas will be discussed later in Section 5.1. For mass calculation purposes, we will base the current level on the average ion current emitted for one year, and for hardware mass, we will follow [29], and use a value of 5

kg/maximum ampere of total current.

The second question that arises is the level of the emitted ion current. As can be seen in Figs. (21a,b), a saturation limit appears which will be discussed later. An increase in I_i from 1 to 2 amps, gives rise to a noticeable increase in the overall performance. However, further increases are much less effective. Increasing I_i increases mass consumption without increasing substantially the power generated. A related question to the ion current level is the ionization energy. The source of the ion current is an ionization chamber that requires power. Argon requires about 31.6 eV for an effective ionization. Thus 1 amp of ions would only require about 32 W which is quite low. Instead of having a chamber ionize the gas internally, an alternate idea is having neutral gas ionize outside the contactor by the electrons streaming in. This question of external ionization is explored in the next section as the Gerver et al model is extended with the inclusion of neutral gas emissions.

2.3.2 Extension of the Model of Gerver et al to Neutral Gas Emissions

The inclusion of neutral gas emissions in the Gerver et al model will require some modifications of the equations and the introduction of some new ones. Using spherical coordinates, $s = (r^2+z^2)^{1/2}$, the ion continuity equation, including ionization, is,

$$\frac{1}{s^2}\frac{\partial}{\partial s}(s^2 e n_i v_{is}) = e n_e n_n \langle \sigma_{en} v_e \rangle \qquad (26)$$

The term on the right hand side represents the production of ions from the neutral gas where n_n is the neutral gas density, and σ_{en} is an averaged electron-neutral ionization cross-section which is typically $\sim O(10^{-20}$ m). In the cloud close to the anode, the electron velocity v_e is much greater than the thermal velocity and is more or less directed radially with some speed v_{es}. If we assume that the neutral gas expands spherically,

$$n_n = n_{no}\left(\frac{a_o}{s}\right)^2 \qquad (27)$$

where n_{no} is the neutral gas density at a_o, the radius of the anode which is typically 5-10 cm. Eqn. (27) neglects the loss of neutral gas

to ionization. However, this will be reasonable for small ionization fractions. If the ions also expand isotropically, the ion current is,

$$I_i = 4\pi s^2 e n_i v_{is} \tag{28}$$

and since $en_e v_{es} = J_{es}$, we can rewrite Eqn. (26) as,

$$\frac{\partial}{\partial s}\left(\frac{I_i}{4\pi}\right) = n_{no} a_o^2 J_{es} \langle \sigma_{en} \rangle \tag{29}$$

We now introduce the neutral gas-electron collision mean free path at the exit of the anode, λ_{no}, which is $1/(n_{no}\langle\sigma_{en}\rangle)$ and multiply Eqn. (29) by $\sin\theta$ where θ is the inclination angle in spherical coordinates, and integrate over θ from 0 to π. Since the left hand side of Eqn. (29) is independent of θ, the integral of $\sin\theta$ over 0 to π is 2. For the right hand side, we note,

$$I_e = 2\pi s^2 \int_0^{\pi} J_{es} \sin\theta \, d\theta \tag{30}$$

and obtain the result,

$$\frac{\partial I_i}{\partial s} = \frac{I_e}{\lambda_{no}}\left(\frac{a_o}{s}\right)^2 \tag{31}$$

Now from conservation of current, $I = I_i + I_e$, therefore,

$$\frac{\partial I_i}{\partial s} = -\frac{\partial I_e}{\partial s} \tag{32}$$

thus we obtain an equation for I_e,

$$\frac{\partial I_e}{\partial s} = -\frac{I_e}{\lambda_{no}}\left(\frac{a_o}{s}\right)^2 \tag{33}$$

This equation can be easily integrated, and we use the boundary condition that the electron current is,

$$I_e(z_o) = I_{eo} = 2\pi r_i^2 J_e^{\infty} \tag{34}$$

at the ends of the cloud where $s=\pm z_o$. We thus obtain,

$$I_e = I_{eo} \exp\left(\frac{a_o^2}{\lambda_{no}}\left(\frac{1}{s} - \frac{1}{z_o}\right)\right) \tag{35}$$

At the anode, $s=a_o$ and,

$$I_{ea_o} = I - I_{ia_o} = I_{eo} \exp\left(\frac{a_o}{\lambda_{no}}\left(1 - \frac{a_o}{z_o}\right)\right) \tag{36}$$

where the subscript a_o denotes at the anode. Since $I_i = I - I_e = I_{iao} + I_{eao} - I_e$, we have finally,

$$I_i = I_{ia_o} + I_{ea_o}\left[1 - \exp\left(\frac{a_o}{\lambda_{no}}\left(\frac{a_o}{s} - 1\right)\right)\right] \tag{37}$$

We now have an expression for the ion current as a function of

distance from the anode. Thus we can obtain the ion density,

$$n_i = \frac{I_{ia_o} + I_{ea_o}\left[1 - \exp\left(\frac{a_o}{\lambda_{no}}\left(\frac{a_o}{s} - 1\right)\right)\right]}{4\pi(r^2+z^2)e\sqrt{\frac{2e}{m_i}(\phi_o - \phi)}} \tag{38}$$

which is also the electron density n_e because of quasi-neutrality. It is important to note that if there is no ionization, λ_{no} is infinite, and we recover the same result as in Eqn. (12).

The electron continuity equation, Eqn. (8), must also be modified with the inclusion of an ionization term.

$$\frac{1}{r}\frac{\partial}{\partial r}(rn_e v_{er}) + \frac{\partial}{\partial z}n_e v_{ez} = n_e n_n \langle \sigma_{en} v_e \rangle \tag{39}$$

Recombination can be neglected since it is usually so small. The ionization term on the right due to the production of electrons when the neutrals are ionized, can be rewritten using the same arguments before as,

$$\frac{1}{\lambda_{no}}\left(\frac{a_0}{r^2+z^2}\right)\left(\frac{J_e}{e}\right) \tag{40}$$

where J_e the electron current density is,

$$J_e = en_e\sqrt{\frac{2e\phi}{m_e}} \tag{41}$$

Making the above substitutions, Eqn. (39) becomes,

$$\frac{1}{r}\frac{\partial}{\partial r}\left(\frac{r(I_{ia_o} + I_{ea_o}\left[1 - \exp\left(\frac{a_o}{\lambda_{no}}\left(\frac{a_o}{s} - 1\right)\right)\right])v_{er}}{4\pi(r^2+z^2)e\sqrt{\frac{2e}{m_i}(\phi_o - \phi)}}\right) + \frac{\partial}{\partial z}(n_e v_{ez}) = \frac{1}{\lambda_{no}}\left(\frac{a_0}{r^2+z^2}\right)\left(\frac{J_e}{e}\right) \tag{42}$$

If the same assumptions are taken as in Gerver et al, we can use Eqn. (15) for v_{er}, and integrate over z from $-z_o$ to $+z_o$. We are then faced with a very formidable integral-differential equation,

$$\frac{1}{r}\frac{\partial}{\partial r}\left[r\left(\frac{I_{ia_o}}{4\pi e\sqrt{\frac{2e}{m_i}}}\right)^{3/2}\left(\frac{0.01\sqrt{\frac{m_e}{\varepsilon_o}}}{B^2}\right)\int_{-z_o}^{+z_o}\left(\frac{1 + \frac{I_{ea_o}}{I_{ia_o}}\left[1 - \exp\left(\frac{a_o}{\lambda_{no}}\left(\frac{a_o}{\sqrt{r^2+z^2}} - 1\right)\right)\right]}{(r^2+z^2)\sqrt{(\phi_o - \phi)}}\right)^{3/2}\frac{\partial\phi}{\partial r}dz\right]$$

$$-\frac{2J_e^{\infty}}{e} = \frac{a_o^2 I_{ia_o}}{\lambda_{no}}\sqrt{\frac{2e}{m_e}}\int_{-z_o}^{+z_o}\left(\frac{1 + \frac{I_{ea_o}}{I_{ia_o}}\left[1 - \exp\left(\frac{a_o}{\lambda_{no}}\left(\frac{a_o}{\sqrt{r^2+z^2}} - 1\right)\right)\right]}{4\pi(r^2+z^2)e\sqrt{\frac{2e}{m_i}(\phi_o - \phi)}}\right)\sqrt{\phi}\,dz \tag{43}$$

Now to make any analytical progress, we are forced to make some approximation, i.e. to expand in the limit of some parameter. A

suitable parameter is the ratio a_o/λ_{no} appearing in the exponentials. The question is whether this ratio can be physically large or small. This can be determined by manipulating Eqn. (37). At the edge of the cloud at $z=\pm z_o$, $a_o/s << 1$, therefore, Eqn. (37) reduces to,

$$I_{io} = I_{ia_o} + I_{ea_o}(1 - e^{-a_o/\lambda_{no}}) \tag{44}$$

From this we can see that,

$$I_{eo} = I_{ea_o} e^{-a_o/\lambda_{no}} \tag{45}$$

Combining with Eqn. (34),

$$r_1^2 = \left(\frac{I - I_{ia_o}}{2\pi J_e^{\infty}}\right) e^{-a_o/\lambda_{no}} \tag{46a}$$

If $a_o/\lambda_{no}>>1$, r_1 would be very small which is not physical since $r_1>a_o$. For very dense gas emissions, a_o/λ_{no} may be on the order of one, however, Eqn. (43) would not be able to be solved analytically. Thus it seems reasonable to let $a_o/\lambda_{no}<<1$. Physically this means the contactor length scale is smaller than the neutral-electron ionization mean free path at the exit. Eqn. (46a) can be used to provide an upper bound to the neutral gas density. If we take $r_1=a_o$, then we have,

$$(n_{no})_{max} = \frac{1}{a_o \langle \sigma_{en} \rangle} \ln\left(\frac{I - I_{iao}}{2\pi a_o^2 J_e^{\infty}}\right) \tag{46b}$$

For typical values, the maximum density is about 10^{19} m^{-3}.

We will first work with the numerator of the integral of the left hand side of Eqn. (43). If $a_o/\lambda_{no}<<1$, we can expand the exponential since $e^x \cong 1 + x$ for small x. Thus we have,

$$\left[1 + \frac{I_{ea_o}}{I_{ia_o}} - \frac{I_{ea_o}}{I_{ia_o}}\left(1 + \frac{a_o}{\lambda_{no}}\left(\frac{a_o}{\sqrt{r^2+z^2}} - 1\right) + \ldots\right)\right]^{3/2} \tag{47}$$

or,

$$\left[1 - \left(\frac{I_{ea_o}}{I_{ia_o}}\right)\left(\frac{a_o}{\lambda_{no}}\right)\left(\frac{a_o}{\sqrt{r^2+z^2}} - 1\right) + \ldots\right]^{3/2} \tag{48}$$

We now can apply the binomial expansion and obtain,

$$1 + \frac{3}{2}\left(\frac{a_o}{\lambda_{no}}\right)\left(\frac{I_{ea_o}}{I_{ia_o}}\right) - \frac{3}{2}\left(\frac{I_{ea_o}}{I_{ia_o}}\right)\left(\frac{a_o^2/\lambda_{no}}{\sqrt{r^2+z^2}}\right) \tag{49}$$

Thus we can break-up the z integral into two pieces. Letting $\bar{\alpha} = a_o/\lambda_{no}$, $\alpha = a_o^2/\lambda_{no}$, and $\Phi = Ie_{ao}/Ii_{ao}$, we have,

$$\left[1+\frac{3}{2}\bar{\alpha}\Phi\right]\int_{-z_o}^{+z_o}\frac{dz}{(r^2+z^2)^{3/2}}-\frac{3}{2}\alpha\Phi\int_{-z_o}^{+z_o}\frac{dz}{(r^2+z^2)^2} \tag{50}$$

For $z_o>>r$, the first integral reduces to $2/r^2$, and the second reduces to $\pi/2r^3$. We now expand the integral on the right-hand side of Eqn. (43). The result again is two integrals,

$$\left[1+\bar{\alpha}\Phi\right]\int_{-z_o}^{+z_o}\frac{dz}{(r^2+z^2)^2}-\alpha\Phi\int_{-z_o}^{+z_o}\frac{dz}{(r^2+z^2)^{5/2}} \tag{51}$$

In the limit for $z_o>>r$, the first integral becomes $\pi/2r^3$, and the second becomes $(4/3)/r^4$. Thus Eqn. (43) reduces to,

$$\frac{\partial}{\partial r}\left[\beta\left(\frac{(1+\frac{3}{2}\bar{\alpha}\Phi)\frac{2}{r}-\frac{3}{4}\alpha\Phi\frac{\pi}{r^2}}{(\phi_o-\phi)^{3/4}}\right)\frac{\partial\phi}{\partial r}\right]-\frac{2J_e^\infty}{e}r=\alpha\Gamma\left[(1+\bar{\alpha}\Phi)\frac{\pi}{2r^2}-\frac{4\alpha\Phi}{3\ r^3}\right]\sqrt{\frac{\phi}{\phi_o-\phi}} \tag{52a}$$

where,

$$\beta=\left(\frac{I_{ia_o}}{4\pi e\sqrt{\frac{2e}{m_i}}}\right)^{3/2}\left(\frac{0.01\sqrt{m_e/\varepsilon_o}}{B^2}\right) \tag{52b}$$

$$\Gamma=\frac{I_{ia_o}}{4\pi e}\sqrt{\frac{m_i}{m_e}} \tag{52c}$$

We make the following definitions to make the equations less cumbersome,

$$k_1=2\beta(1+\frac{3}{2}\bar{\alpha}\Phi) \tag{52d}$$

$$k_2=\frac{3}{4}\pi\beta\alpha\Phi \tag{52e}$$

$$k_3=\alpha\Gamma\frac{\pi}{2}(1+\bar{\alpha}\Phi) \tag{52f}$$

$$k_4=\frac{4}{3}\alpha^2\Gamma\Phi \tag{52g}$$

Thus we have,

$$\frac{\partial}{\partial r}\left[(\frac{k_1}{r}-\frac{k_2}{r^2})(\phi_o-\phi)^{-3/4}\frac{\partial\phi}{\partial r}\right]=\frac{2J_e^\infty}{e}r+\left[\frac{k_3}{r^2}-\frac{k_4}{r^3}\right]\sqrt{\frac{\phi}{\phi_o-\phi}} \tag{53}$$

Integrating with respect to r and applying the boundary conditions Eqn. (10b,c) which still hold, we obtain,

$$(\frac{k_1}{r}-\frac{k_2}{r^2})(\phi_o-\phi)^{-3/4}\frac{\partial\phi}{\partial r}=-\frac{J_e^\infty}{e}(r_2^2-r^2)+(-\frac{k_3}{r}+\frac{k_4}{2r^2})\sqrt{\frac{\phi}{\phi_o-\phi}} \tag{54a}$$

where,

$$r_2^2 = r_1^2 - \left(\frac{k_1}{r_1} - \frac{k_2}{r_1^2}\right)\phi_o^{-3/4}\frac{\partial T_e}{\partial r}J_e^{\infty\,-1} \tag{54b}$$

If we let,

$$f(r) = k_1/r - k_2/r^2 \tag{55a}$$

$$g(r) = -\frac{J_e^{\infty}}{e}(r_2^2 - r^2) \tag{55b}$$

$$h(r) = -k_3/r + k_4/2r^2 \tag{55c}$$

then Eqn. (54a) can be written as,

$$\frac{\partial \phi}{\partial r} - \frac{g(r)}{f(r)}(\phi_o - \phi)^{3/4} - \frac{h(r)}{f(r)}\phi^{1/2}(\phi_o - \phi)^{1/4} = 0 \tag{56}$$

which is a non-linear first order differential equation for the potential in the cloud. Comparing the order of magnitude of the variable coefficients in MKS units with, $\bar{\alpha}$~O(10^{-2}), α~O(10^{-3}), β~O($10^{19\text{-}20}$), Γ~O(10^{20}), and, k_1~O(10^{20}), k_2~O($10^{16\text{-}17}$), k_3~O(10^{17}), and k_4~O($10^{13\text{-}14}$). These give, f(r)~O($10^{19\text{-}20}$), g(r)~O($10^{19\text{-}20}$), and h(r)~O($10^{16\text{-}17}$). Thus as a first order solution to Eqn. (56), since g(r)/f(r) >> h(r)/f(r), we can neglect the last term and solve by separating variables. Doing so, we have

$$(\phi_o - \phi)^{1/4} = \frac{J_e^{\infty}}{4e}\int \frac{r_2^2 r^2 - r^4}{k_1 r - k_2}\,dr + C_1 \tag{57}$$

(Note that although α has units of length, the units of g(r) and h(r) are actually independent of length, and hence the fact that g(r) >> h(r) is indeed a general result.) Performing the integration, and using Eqns. (10a,c), we obtain,

$$\phi_o^{1/4} = \frac{J_e^{\infty}}{4e}\left[-\frac{r_1^4}{4k_1} - \frac{k_2 r_1^3}{3k_1^2} + \left(\frac{r_2^2}{k_1} - \frac{k_2^2}{k_1^3}\right)\frac{r_1^2}{2} + \left(\frac{k_2 r_2^2}{k_1^2} - \frac{k_2^3}{k_1^4}\right)r_1 + \left(\frac{k_2^2 r_2^2}{k_1^3} - \frac{k_2^4}{k_1^5}\right)\ln(k_1 r_1 - k_2)\right] \tag{58}$$

where r_1 can be eliminated by the use of Eqn. (46a). Thus we have the current-voltage relation for the contactor,

$$\phi_o = \left(\frac{J_e^{\infty}}{4ek_1}\right)^4\left[\frac{1}{4}\psi^2 + \frac{2}{3}k\psi^{3/2} - \frac{1}{2}k^2\psi - k^3\psi^{1/2} + (k^2\psi - k^4)\ln(k_1\psi^{1/2} - k_2)\right]^4 \tag{59a}$$

where $k = k_2/k_1$ and,

$$\psi = \frac{e^{-\bar{\alpha}}}{2\pi J_e^{\infty}}(I - I_{ia_o}) \tag{59b}$$

It is important to note that if there is no ionization, k=0, $\psi = (I - I_{iao})/2\pi J_e^{\infty}$, and we recover Eqn. (24), the result from Gerver et al.

We must find a relationship for the mean free path λ_{no} at the exit

of the anode. Even though the gas is neutral, we can still consider it having a fictitious "current". Using the ionization fraction, f, introduced in Eqn. (25), we can write the neutral "current" as,

$$I_{na_o} = I_{ia_o}(\frac{1}{f} - 1) \tag{60}$$

thus if f=1, there is no neutral gas emitted. Introducing the definition of current, $I_{nao} = en_{no}vA$, and the definition of λ_{no}, we have,

$$\lambda_{n_o} = \frac{evA}{I_{ia_o}(\frac{1}{f} - 1)<\sigma_{en}>} \tag{61}$$

where v is the velocity of the emitted gas, and A is the exit area. Even though the ionization cross-section is really energy dependent, we will assume it to be constant since its variation is not too large. Note that as f increases, λ_{no} increases; as f->1, λ_{no}->∞. (However for calculations, we will use f=0.99999 when full ionization is required.) Thus for a fixed neutral gas fraction, we have λ_{no} as a function of the emitted ion current. The expression for the mass flow rate, Eqn. (25), is the same. For fixed ion current, the mass flow rate will increase now as the ionization fraction decreases since more neutral gas will be emitted.

There are a number of issues that must be addressed regarding neutral gas releases. Along with the previously mentioned parameters, the type of ion and the emitted ion current, there is a new parameter, the ionization fraction. In addition, the effect of the velocity of the emitted gas must be explored. It is favorable to have a low exit velocity so that λ_{no} will be small, but not too small because we must be careful not to step outside the bounds of theory. Another factor is the exit area. However in most contactor devices, the orifice area is quite small, so that we will take the exit radius to be fixed at 5 cm. In Section 5.1, we will examine these issues, particularly the trade-off between ionizing all the gas internally as in the Gerver model, versus partial ionization. The impact on the performance and mass consumption will also be explored.

2.3.3 Bare Tether Electron Collection

Recently, an innovative method of electron collection was

proposed by Sanmartin, Martinez-Sanchez, and Ahedo[35]. Actually, the concept of leaving the tether bare was examined by Prall[33], but the idea was thought to be impractical due to such issues as tether surface material sputtering. As can be seen in Fig. (4a), during power generation, the upper part of the tether is positive with respect to the plasma and thus is able to collect electrons. This configuration is for a tether deployed upwards, (a downwards tether is for thrusting). The inherent advantages of this scheme are the absence of the added mass and complexity of an active emitting contactor. This model was included in the system study to compare and contrast its performance with that of an active plasma contactor and to see the effect of operating the two together to enhance current collection. The following is a brief explanation of the theory from [35].

As an upper bound on current collection, a bare tether positively biased to the LEO plasma, can be thought to act like an inertia-limited cylindrical probe. This means magnetic and motional effects can be assumed to be negligible. Due to the wire's potential, its cross-sectional area is increased in an analogous fashion as the capture cross-section of a planet due to gravity. In the following equations, as in Fig. (4a), point A refers to the upper extremity of the tether, point B is where the bare collecting part terminates (i.e. the potential $\phi=0$ for the generator), and point C is the very bottom where the cathode is. Note that the current increases in the bare part until point B where it is constant. The classical expression for the current collected per unit length is,

$$\frac{dI}{dy} = en_{e\infty}d\sqrt{\frac{2e\phi}{m_e}} \tag{62}$$

where d is the physical diameter of the tether. The potential profile along the tether is governed by Ohm's law,

$$\frac{d\phi}{dy} = \frac{I(y)}{\sigma A} \tag{63}$$

were σ is the conductivity of the tether, and A is the cross-sectional area. Combining Eqns. (62,63) gives,

$$\frac{d^2\phi}{dy^2} = \frac{2en_{e\infty}}{\sigma}\sqrt{\frac{2e\phi}{\pi A m_e}} \tag{64}$$

with the boundary conditions, $\phi(0)=\phi_A$, $d\phi/dy(0)=-vB$, where $vB = |\mathbf{v}\times\mathbf{B}\bullet\mathbf{L}|/L$, and $\phi=0$ at $y=L_B$. The equations can be non-dimensionalized by defining the following,

$$L^* = \frac{(\pi m_e vBA)^{1/3}}{2^{7/3}e}\left(\frac{3\sigma}{n_{e\infty}}\right)^{2/3} \tag{65a}$$

$$V^* = vBL^* \tag{65b}$$

$$I^* = vB\sigma A \tag{65c}$$

and letting $\xi=y/L^*$, $\varphi=\phi/V^*$, and $i=I/I^*$. Eqn. (64) then becomes,

$$\frac{d^2\varphi}{d\xi^2} = \frac{3}{4}\varphi^{1/2} \tag{66a}$$

with $\varphi(0)=\varphi_A$ and $d\varphi/d\xi(0)=-1$. The latter boundary condition originates from the voltage drop along the tether,

$$\Delta\phi = \phi_{tether} - vBy \tag{66b}$$

or, differentiating with respect to y, substituting Eqn. (63), non-dimensionalizing, and evaluating at the tip of the tether, y=0,

$$\frac{d\varphi}{d\xi} = i_A - 1 \tag{66c}$$

For a bare tether, $i_A=0$ at the tip. However, if a plasma contactor is placed at the tip, i_A is non-zero and will be a function of φ_A as governed by the contactor current-voltage relationship.

Integrating Eqn. (66a) twice,

$$\xi(\varphi) = \int_{\varphi}^{\varphi_A} \frac{d\varphi}{\sqrt{1 - \varphi_A^{3/2} + \varphi^{3/2}}} \tag{67}$$

Since the potential is zero at point B,

$$\xi_B = \int_{0}^{\varphi_A} \frac{d\varphi}{\sqrt{1 - \varphi_A^{3/2} + \varphi^{3/2}}} \tag{68}$$

From Eqn. (63), the current can be found,

$$i = 1 + \frac{d\varphi}{d\xi} = 1 - \sqrt{1 - \varphi_A^{3/2} + \varphi^{3/2}} \tag{69}$$

thus, the current flowing through the bottom of the tether and the load is,

$$i_L = 1 - \sqrt{1 - \varphi_A^{3/2}} \tag{70}$$

Recast in these non-dimensional variables, the circuit equation for power generation can be written as,

$$(\xi_C - \xi_B)(1 - i_L) = \rho_L i_L + \varphi_C(i_L) + \varphi_I \qquad (71)$$

where ρ_L is the non-dimensional load resistance $R_L I^*/V^*$, and φ_C and φ_I are the non-dimensional voltage drops for the cathode and ionospheric impedance respectively. Lastly, the generator efficiency defined just as in Eqn. (4b), can be expressed as,

$$\eta = \frac{i_L^2 \rho_L}{\xi_B - \varphi_A + i_L(\xi_C - \xi_B)} \qquad (72)$$

It is important to note that unlike the equations for the contactor, the equations for the bare tether are not explicit. Thus the equations need to be solved indirectly. Given φ_A, ξ_B and ξ_C are computed from Eqn. (68) and the definition of ξ respectively. Next, i_L is computed from Eqn. (70) and φ_C and φ_I are computed (or given). The load resistance ρ_L, can then be computed from Eqn. (71) and hence the power. Lastly, the efficiency can be calculated from Eqn. (72).

Due to the fluctuations of the induced voltage and ambient electron density, the zero potential point on the tether will fluctuate. Since the level of the fluctuations is large (up to km's), we can assume that the insulation terminates at the maximum fluctuation point. The tether can also be left completely bare. In this case, a portion of the tether will be negative with respect to the plasma and will collect ions. However, the ion current collected is very small (about 171 times less) and can be neglected. Thus to reduce mass, we will operate the pure bare tether without any insulation for power generation purposes.

It is interesting to examine the performance of a tether system where a contactor is placed at the top of a bare wire tether to enhance current collection. In this case, the current at the tip i_A, will be non-zero and Eqn. (66c) applies as a boundary condition. Eqn. (68) will therefore become,

$$\xi_B = \int_0^{\varphi_A} \frac{d\varphi}{\sqrt{(i_A - 1)^2 - \varphi_A^{3/2} + \varphi^{3/2}}} \qquad (73a)$$

and Eqn. (70) will read,

$$i_L = 1 - \sqrt{(i_A - 1)^2 - \varphi_A^{3/2}} \qquad (73b)$$

The solution process remains essentially the same, except now i_A and

φ_A must be related to each other via the contactor current-voltage characteristic. Section 5.3 gives a comparison of the power generating performance of a pure contactor system (wire fully insulated), pure bare tether, and a bare wire with a contactor.

A bare tether can also be operated as a thruster if it is deployed downwards. As shown in Fig. (4b), the entire length of the tether will be positive to the plasma and will collect electrons. Point B can be taken to be physically the same point as Point C, except the potential differs only by the drop across the cathode and ionosphere. The governing equations remain the same, except now, Eqn. (66c) becomes,

$$\frac{d\varphi}{d\xi} = i_A + 1 \tag{74}$$

This change of sign modifies Eqns. (73a,73b) so that,

$$\xi_B = \xi_C = \int_{\varphi_A}^{\varphi_B} \frac{d\varphi}{\sqrt{(i_A+1)^2 - \varphi_A^{3/2} + \varphi^{3/2}}} \tag{75a}$$

$$i_L = \sqrt{(i_A+1)^2 + \varphi_B^{3/2} - \varphi_A^{3/2}} - 1 \tag{75b}$$

where φ_B is the voltage drop at Point B,

$$\varphi_B = \frac{V_{BAT}}{V^*} - \varphi_C(i_L) - \varphi_I \tag{76}$$

The efficiency of the system is then,

$$\eta = \frac{vB\int_0^L I(y)dy}{I_L V_{BAT}} = \frac{I^* V^* (\varphi_B - \varphi_A - \xi_C)}{I_L V_{BAT}} \tag{77}$$

To solve these equations, requires a 2-step iteration scheme. First, i_L is chosen and φ_B is computed from Eqn. (76). Then, Eqn. (75b) is satisfied by iteration since i_A and φ_A are related. (Note if no contactor is used, i_A=0). Then the integral in Eqn. (75a) is computed and compared to ξ_C. The process is repeated until the integral converges to ξ_C.

In these equations, φ_A represents the voltage drop at the very end of the tether. If there is no contactor, it is clear that the minimum battery necessary for current to be collected along the entire tether, is the voltage supply V_{MIN} such that φ_A=0. (This gives the highest efficiency as seen in Eqn. (77).) If $V<V_{MIN}$ then φ_A will

actually become negative and the tether end will collect ions. Thus a plausible operating point for a bare tether would be for $\varphi_A=0$. This indeed gives the best efficiency as seen in Fig. (5a). Increasing φ_A increases the thrust, but the efficiency drops. This result shows that using a bare tether thruster with a contactor is not beneficial since efficiency is very important to thrusting applications due to the high premium on power in space. The minimum non-dimensional battery voltage $\varepsilon_{MIN} = V_{MIN}/V^*$, can be computed from Eqns. (75b,76) given a current i_L,

$$\varepsilon_{MIN} = \varphi_B + \varphi_C(i_L) + \varphi_I = [i_L(2 + i_L)]^{2/3} + \varphi_C(i_L) + \varphi_I \qquad (78)$$

The efficiency of a completely bare tether (even with $\varphi_A=0$), is quite low. This is because most of the current is collected near the bottom of the tether so that its contribution to the thrust is small. This problem can be alleviated by insulating the lower part of the tether. Thus the current will increase along the tether until the bare portion terminates, and then remains constant. Hence point B will lie somewhere in between A and C as shown in Fig. (4b). Writing a circuit equation for the system yields,

$$V_{BAT} = \Delta V_C(i_L) + (vB + \frac{I}{\sigma A})(L_C - L_B) + \Delta V_B + \Delta V_I \qquad (79a)$$

or in non-dimensional terms,

$$\varepsilon = \varphi_C(i_L) + \varphi_B + (1 + i_L)(\xi_C - \xi_B) + \varphi_I \qquad (79b)$$

where φ_B is given by Eqn. (76). If $\varphi_A=0$, Eqn. (79b) gives the minimum battery for greatest efficiency. The length of the insulated portion will be varied later in Section 5.7.2 to see the affect on performance. Intuitively, we can see that as the amount of bare tether decreases, the current collected will decrease and hence the thrust. However, the current will be collected near the end of the tether, thus the length along which the force acts is greater, and hence the efficiency should improve. We will see that indeed, this is the case.

Regardless of such improvements in efficiency, the bare thrusting tether is not able to reach the efficiency of a pure contactor tether although it can come quite close. The reason is the following: for a contactor tether, the thrust is F' = I'LB, and for a partially bare tether, the thrust is $F = IL_BB + aI(L-L_B)B$ where L_B is the length of

tether insulated, and a is a numerical factor <1 due to integrating the non-uniform current distribution over the bare portion. Thus to provide the same thrust as the contactor tether, the bare tether must have a current,

$$I = \frac{(1/a)I'}{2(\frac{L_B}{L}) + 1} \tag{80}$$

Due to the difficult nature of Eqns. (75-6), it is not possible to extract the exact functional dependence of the current distribution in the bare portion. Nonetheless, we can compute numerically the current profile as shown in Fig. (5b) for a 20 km bare tether. As can be seen, a quadratic fits rather well. Thus assuming a quadratic profile, we obtain a=1/3. For a completely bare tether (L_B=0) we have the result that the current in the bare tether must be *3 times* that of the contactor tether. However, as L_B increases, I approaches I'.

2.4 Cathodic Device

Since electron emission has been demonstrated in space with little expenditure of energy, less attention has been paid to the development of theoretical models of cathodic devices. There are several devices that can be used to emit electrons, and each has its advantages and disadvantages. Electron guns have no mass consumption, but due to space charge limitations, require kilovolts for multi-ampere currents. These high voltage drops are highly undesirable, since the total induced voltage at times in orbit will drop to a few kilovolts even for a 20 km tether. Another possible method is thermionic emission. Despite the simplicity of this concept and zero mass consumption, it also falls victim to undesirable space charge limitations as shown in [1]. Thus it seems a cathodic plasma contactor emitting an ionized neutral cloud is the best solution, despite its mass consumption (which is quite small). Since electron collection and emission are fundamentally two different processes, the models developed for the anode can not apply.

The following is a simple model that will be used for a plasma cloud emitted by a cathodic plasma contactor, which follows along the lines of [18]. The electron momentum equation is,

$$n_e m_e \frac{dv}{dt} = n_e e(E + v \times B) - \nabla p - m_e n_e \nu_{ei}(v_e - v_i) \tag{81}$$

We neglect inertia (which is quite customary), and assume that the contactor is emitting an ion cloud to neutralize the electrons, so that quasi-neutrality holds. In this case, very near the cathode, the dominant terms in the equation yield a balance between the electron density gradient and the potential. Since, p=nkT, and E=-$\nabla\phi$, we have for the total potential drop across the cloud,

$$\Delta\phi_C = -\frac{kT_e}{e} \ln\left(\frac{n_e}{n_{eo}}\right) \tag{82}$$

where n_{eo} is the electron density at the exit of the cathode, and n_e is the density at the edge of the cloud which would be taken to be the ambient electron density. The exit electron density can be related to the emitted electron current, which we will take to be the total current since the collected ion current is very small [1]. Thus using the definition of current, we have,

$$n_{eo} = \frac{I}{e v_e 4\pi a_o^2} \tag{83}$$

where again, a_o is the cathode exit radius. Fig. (6) shows the cathodic current-voltage characteristic for various ambient conditions. Here we have taken a_o to be 5 cm, and the electrons to have an energy of around 5eV. The mass flow rate from the cathode can be determined along similar lines of the anode mass flow rate. From the ion current density we have, $j_i = e n_i v_i$ where we take $n_i = n_e$ because of quasi-neutrality. The electron density n_e is simply I/ev_eA. Thus since the mass flow rate of the ions is ρvA, we have the ion mass flow rate per unit total ampere of current,

$$\frac{\dot{m}_i}{I} = \frac{m_i v_i}{e v_e} \tag{84}$$

Note since we do not have a detailed theory of ionization for the cathode, we will assume that it operates fully ionized. Various estimates for v_i and v_e can be used, but we will follow [29], and assume the v_i to be the ion acoustic speed, and v_e to be the electron acoustic speed. For typical values, Eqn. (84) can be expressed as $0.035(\mathcal{M})^{1/2}$ [kg/ampere/year] where $\mathcal{M}$ is the molecular weight of the gas emitted. Thus for argon, we obtain about 0.22 kg/amp/yr. For mass calculation purposes, we will follow [29], and use the average current for computing the gas mass for one year, and will

use a hardware mass value of 5 kg/maximum ampere.

2.5 The Tether

In this section, the choice of tether material, both for the conductor and the insulator, will be discussed. The equations for a tether deflected under a electrodynamic force will be presented, and the concept of superconducting tethers will be explored.

2.5.1 Tether materials

The obvious desirable qualities of an electrodynamic tether are low weight and low resistivity. As we will see later, the mass of the tether can be a substantial fraction of the whole system. Decreasing the tether mass however (for fixed length), has adverse effects. Making the tether thinner, increases the resistivity which scales inversely with the cross-sectional area, ($R=L/\sigma A$). Thus the selection of the type of conducting material is a very important concern. A figure of merit that can be used to compare various materials is the ratio of the conductivity to the density, σ/ρ. Prall[33], examined various materials and found that aluminum was better in this respect compared to copper, silver, nickel, and platinum. Thus for this study, aluminum will be used for the tether, with a density of 2700 kg/m^3. As will be seen later, due to large temperature fluctuations, the changes in the tether's resistance and length should be taken into account. The resistance was modelled as,

$$\rho = (-0.1497 + 3.8885e\text{-}3T + 2.3237e\text{-}5T^2)(10^{-8}\ \Omega\text{-m}) \qquad (85a)$$

which is a good fit for temperatures around 200°K, and the length change due to thermal expansions and contractions is taken to be,

$$L = L_o[1 + 12.9e\text{-}6(T - 273.15)] \qquad (85b)$$

Another important factor is the insulation surrounding the tether. Since the tether is surrounded by a conducting plasma, current can leak from the tether in regions where it is appropriately biased to the plasma. High voltage insulation in space presents many problems as is well known in the solar-cell community. Dielectrics in a plasma tend to break down and arcing occurs. Prall[33] also examined various insulators, comparing the dielectric strength and density. Prall came to the conclusion that anodized aluminum would

be a very suitable insulator having a dielectric strength of $5x10^6$ V/m which is almost an order of magnitude higher than polyethylene. For tether operating voltages, a sufficient thickness would be about 40 microns. Thus for this study, anodized aluminum will be used for insulation. Note that since so little insulation material is required, there will be little tether mass difference between a bare tether and a completely insulated tether. Of course arcing will still remain a problem, but perhaps, the aluminum will very likely form a protective oxide layer in space and enhance arcing protection. However, it remains for actual laboratory and space tests to verify this.

The length of the tether is an important design parameter. Rivas[34], examined tethers of varying length. For long tethers, the power generated obviously increases, but based on system masses and safety concerns (high voltage technology) it was found a 20 km to be more or less an optimum choice. We will vary the tether length in Section 5.10, but unless otherwise stated, a 20 km tether will be assumed.

2.5.2 Hollow Tethers

In order to reduce the weight of the tether, Nagle[31] suggested hollowing the tether. From our discussion in the last section, we know that reducing the cross-section will reduce the mass but increase the resistivity. In fact, the product of the resistance and the mass of the tether is a constant independent of the cross-sectional area. Thus it is not clear whether hollowing the tether is advantageous at all. However, for a bare tether that is collecting current, it might be advantageous to hollow the tether such that the overall diameter of the tether increases, but the cross-sectional area remains the same. This would allow for a greater area for electron collection. On the other hand, the heat flux to the tether would increase also, increasing the temperature and raising the resistance. The scheme was explored via simulation to see the effect on the power generated, and the specific power, and results are presented later in Section 5.10.

2.5.3 The Orbital Debris Environment and Multiple Tethers

Perhaps the first apparent reason for examining the use of multiple tethers is reliability against failure by orbital debris collisions. According to Kessler[25], within 2000 km of the Earth's surface, there is an estimated 3,000,000 kg of man-made orbiting objects. These objects are mainly in high inclination orbits and sweep past one another at an average speed of 10 km/s. Most of the mass consists of about 3000 used rocket stages, inactive payloads, and active payloads. About 700 of these objects have a radar cross section greater than 7 m^2. A smaller amount of mass, approximately 40,000 kg, consists of 4000 objects that are tracked by radars of the U.S. Space Command. Most of these objects are the result of more than 90 in-orbit satellite fragmentations. In addition to man-made objects, are meteoroids, although less hazardous. At any one instant, a total of 200 kg of meteoroid mass is within the same area above the Earth's surface. Most of these meteoroids are about 0.1 mm in size.

Based on various debris models and radar data, Carroll[8] estimated the number of tether cuts per year. For typical LEO orbits between 300 to 1000 km, the impact rate would range from 10^{-5} to 10^{-3} cuts/km-yr. Thus a 20 km tether in the worst case, would experience 0.02 cuts per year. Based on this information, Martinez-Sanchez[29] worked out the reliability and probability of survival for N tethers. It was shown that for a ten year mission, (which gave a single-tether probability of survival of 0.8), two tethers gave 96% reliability while ten gave 99%.

In addition to increasing reliability, multiple cables can decrease the effective resistance of the tether since they are joined in parallel. If N tethers, are operating on one contactor, the tether resistance is $(\Sigma\ 1/R_N)^{-1}$. For example, if there are four tethers, each with a resistance of 100 ohms, the effective resistance will be 25 ohms. Thus the number of the tethers and the individual resistance of each can be varied to see the effect on the specific power.

On the other hand, if there are several tethers attached to one large vehicle, say the Space Station, each with its own contactor, the

question arises as to the separation distance. This is a very difficult question because if the tethers are close to each other, their contactor clouds will interact. It is hard to say whether the effective area of two close contactor clouds will increase or decrease. Since the physics of a single isolated cloud are still far from being well understood, it is not appropriate to speculate on this issue here. However, this is something to keep in mind for future work.

2.5.4 Tether Deflection

A tether exploits gravity gradients for stability and orientation along the radial direction from the earth. Consider two satellites connected by a tether (that experiences no electromagnetic force). If the satellites have equal mass, the center of mass (and the center of gravity for tether lengths<100 km) will be located mid-way between. Both satellites are constrained by the tether with the same orbital angular velocity. Thus the tether speeds up the upper mass and slows down the lower mass. A satellite's orbital velocity is determined by a balance of gravitational and centrifugal forces. However, with the upper mass being pulled along at a velocity higher than that unique to its altitude, the centrifugal force is stronger than the gravitational force. Similarly with the lower mass, since it is traveling at a slower speed than that intrinsic to its height, the gravitational force is stronger than the centrifugal force. Thus the imbalanced forces on each endmass exert a torque on the system to orient it vertically. Above the center of mass (CM), the net force is upward; below, it is downward. This force is known as the gravity-gradient force and a very simple argument can derive its magnitude [2]. If we differentiate the gravitational and centrifugal forces on a mass m along the radial direction,

$$\frac{\partial F_G}{\partial r} = \frac{2GM_e m}{r^3} = 2m\Omega^2 \qquad \frac{\partial F_C}{\partial r} = m\Omega^2 \tag{86a}$$

where Ω is the orbital angular velocity. Placing the origin of our coordinate system at the center of mass and replacing r with z (z>0 above CM, z<0 below), we have,

$$F_Z = z\left(\frac{\partial F_G}{\partial z} + \frac{\partial F_C}{\partial z}\right) = 3m\Omega^2 z \tag{86b}$$

For tethered systems such as the TSS experiments, the origin of z will be more or less on the shuttle since it is much larger than the other endmass.

With electromagnetic and other small forces, the tether will deflect from the vertical. The main purpose of our calculating the deflection is to see whether the deflection angles are too severe. If the the angles are excessive, the endmass of the system will have to be increased and/or the thickness of the tether. As a first simple approximation, if we neglect the mass of the tether, assuming the endmass to be much heavier, and assuming the vehicle carrying the tether is much larger, a moment balance at the attach point for small angles gives,

$$f'_{em} I \frac{L^2}{2} = 3 m_E \Omega^2 L^2 \theta \tag{87}$$

where f'_{em} is the electromagnetic force per unit length per ampere, I is the current, L is the length, m_E is the end mass, and θ is the deflection angle. Typically, $f'_{em} \cong 3 \times 10^{-5}$ N/m-A, and taking an end mass of 500 kg, as for TSS-1, we have a deflection of I/50 radians. For a current of 5 amps, this is only 6°. However, in general, the mass of the tether can not be neglected, thus we must be a little more sophisticated. We will consider only a static condition, all dynamics will be neglected in light of the findings of Grossi[16]. In reality, unless some resonance phenomena occurs (i.e. due to forcing by electrodynamic forces), the deflection limits of a swinging tether will be somewhat larger than the static limits due to inertial over-swing, but not drastically different.

Consider a section of tether in equilibrium as in Fig. (7). We will consider small deflections so that our analysis is linear. Summing forces in the horizontal direction,

$$-T\frac{\partial w}{\partial y} + (T + \frac{\partial T}{\partial y}dy)(\frac{\partial w}{\partial y} + \frac{\partial}{\partial y}(\frac{\partial w}{\partial y})dy) + f_{em}dy \cos\frac{\partial w}{\partial y} = 0 \tag{88a}$$

Neglecting higher order terms, we obtain the deflection as a function of the tension and the electrodynamic force/unit length f_{em},

$$\frac{d^2w}{dy^2} = -\frac{f_{em}}{T} \tag{88b}$$

Summing forces in the vertical direction, we have,

$$(T + \frac{\partial T}{\partial y}dy)\cos(\frac{\partial w}{\partial y} + \frac{\partial}{\partial y}(\frac{\partial w}{\partial y})dy) - T\cos\frac{\partial w}{\partial y} + 3m\Omega^2 y dy = 0 \quad (89a)$$

Again neglecting higher order terms, we obtain the tension as a function of the vertical distance,

$$\frac{\partial T}{\partial y} + 3m\Omega^2 y = 0 \quad (89b)$$

where m is the tether mass/unit length. Integrating Eqn. (89b) with the boundary condition that the tension at the end y=L, is due to the endmass, m_E,

$$T(y) = -\frac{3}{2}m\Omega^2(y^2 - L^2) + 3m_E\Omega^2 L \quad (90)$$

We can now integrate Eqn. (88b) for the deflection using two boundary conditions for w: w=0 at y=0, and dw/dy(L)=0 since if the endmass is in equilibrium, the tension and gravity gradient forces are anti-parallel. Thus we obtain,

$$w(y) = \frac{f_{em}}{2\alpha\sqrt{\frac{\alpha}{\beta}}}\left[(\xi\ln\xi - \xi) - (\zeta\ln\zeta - \zeta) - \ln\left|\frac{L - \sqrt{\frac{\beta}{\alpha}}}{L + \sqrt{\frac{\beta}{\alpha}}}\right| y\right] + \frac{f_{em}}{\alpha}\left(\ln\sqrt{\frac{\beta}{\alpha}} - 1\right) \quad (91a)$$

where,

$$\alpha = \frac{3}{2}m\Omega^2, \quad \beta = 3m_E\Omega^2 L + \frac{3}{2}m\Omega^2 L^2 \quad (91b)$$

$$\xi = y - \sqrt{\frac{\beta}{\alpha}}, \quad \zeta = y + \sqrt{\frac{\beta}{\alpha}} \quad (91c)$$

This equation gives the deflection shape of the tether. For our purposes, we also need the deflection angle at the base,

$$w'(0) = \frac{f_{em}}{2\alpha\sqrt{\frac{\alpha}{\beta}}}\ln\left|\frac{L - \sqrt{\frac{\beta}{\alpha}}}{L + \sqrt{\frac{\beta}{\alpha}}}\right| \quad (92)$$

where w'(0) is measured in radians.

The above analysis is for a constant electrodynamic force on the tether. However, for a bare tether, the current and hence the force is not constant along the length as we have seen. Therefore to properly find the deflection, we must find how the force varies along the length of the tether. This was determined in Section 2.3.3, where we found the current profile to be approximately quadratic. To extend the deflection analysis to include both fully and partially bare tethers, we will divide the length of the tether into two sections as can be seen in Fig. (7). The insulated portion will be between y=0

and $y=L_B$, and the bare portion from $y=L_B$ to $y=L$. Thus the force per unit length along the tether is,

$$f_{em} = A = \frac{|I_L \mathbf{L} \times \mathbf{B}|}{L} \qquad 0 \le y \le L_B \tag{93a}$$

$$f_{em} = B\left(\frac{L-y}{L}\right)^2 \qquad L_B \le y \le L \tag{93b}$$

where B is $AL^2/(L-L_B)^2$ since the forces must be continuous at $y=L_B$. Note that if $L_B=L$, B must be zero and we will recover the previous case.

The governing equation still remains Eqn. (88b). The boundary conditions for the problem also are the same, except in addition, we must require continuity of the displacement and deflection angle at $y=L_B$. In other words, the two solutions for the two regions must match at the boundary. The solution in the first segment is Eqn. (91a) slightly modified (after using the B.C. at y=0),

$$w_1(y) = \frac{A}{2\alpha\gamma}\left[(\xi \ln|\xi| - \xi) - (\zeta \ln|\zeta| - \zeta)\right] + C_1 y + \frac{A}{\alpha}(\ln\gamma - 1)\,, \quad 0 \le y \le L_B \tag{94}$$

where $\gamma=(\beta/\alpha)^{1/2}$. The constant C_1 will have to determined from the solution in the second segment. Eqn. (88b) with Eqn. (93b) can be integrated twice, and yields (after using the B.C. at y=L),

$$w_2(y) = \frac{B}{\alpha L^2}\left[\frac{y^2}{2} - Ly + \lambda_1(\xi \ln|\xi| - \xi - \ln|L-\gamma|y) + \lambda_2(\zeta \ln\zeta - \zeta - \ln(L+\gamma)y)\right] + C_2 \,, \quad L_B \le y \le L \tag{95a}$$

where,

$$\lambda_1 = \left(\frac{L^2}{2\gamma} - L + \frac{\gamma}{2}\right), \quad \lambda_2 = \left(-\frac{L^2}{2\gamma} - L - \frac{\gamma}{2}\right) \tag{95b}$$

Thus C_1 and C_2 can be determined by matching Eqns. (94,95a) together at $y=L_B$. The results are,

$$C_1 = \frac{B}{\alpha L^2}\left[(L_B - L) + \lambda_1 \ln\left|\frac{L_B-\gamma}{L-\gamma}\right| + \lambda_2 \ln\left|\frac{L_B+\gamma}{L+\gamma}\right|\right] - \frac{A}{2\alpha\gamma}\ln\left|\frac{L_B-\gamma}{L-\gamma}\right| \tag{96a,b}$$

$$C_2 = w_1(L_B) - \frac{B}{\alpha L^2}\left[\frac{L_B^2}{2} - LL_B + \lambda_1(\xi \ln|\xi| - \xi - \ln|L-\gamma|L_B) + \lambda_2(\zeta \ln\zeta - \zeta - \ln(L+\gamma)L_B)\right]$$

where ζ and ξ are evaluated at $y=L_B$. The base deflection angle, w'(0), is just C_1, and we can see with $L=L_B$, C_1 reduces to Eqn. (92). Tether deflections will be discussed in Section 5.4.

2.5.5 Tether Temperature

It is important to determine the temperature of the tether

because primarily the resistance and secondarily the length are functions of the temperature. As the tether orbits, it undergoes drastic changes in temperature as it enters and departs the Earth's shadow and changes in the tether resistance alter the performance. Prall[33] computed the tether temperature and found the temperature to fluctuate typically around 200°K. Already at these lower temperatures, the resistivity of the tether drops noticeably. Thus to properly model the tether, the temperature must be computed.

To compute the temperature, one must first know all the heat fluxes to and from the tether. Heat is absorbed via the solar flux, the Earth's flux, both its own and the albedo, and very slightly, by aerodynamic heating. In addition, there is ohmic heating. Heat is emitted solely by radiation. Since the tether is quite thin, we will assume a lumped-parameter model, i.e. the tether temperature is uniform and no internal gradients exist. Thus we can write,

$$mC\frac{dT}{dt} = Q_{IN} - Q_{OUT} \tag{97a}$$

where m is the mass of the tether, C is the specific heat capacity, and Q_{IN} consists of,

$$Q_{IN} = Q_{SOLAR} + Q_{EARTH} + Q_{ALBEDO} + Q_{AERO} + I^2R_T \tag{97b}$$

and,

$$Q_{OUT} = \varepsilon\sigma T^4 A \tag{97c}$$

where A is the outer surface area of the tether and the other variables have their standard meaning. Ideally, the tether should have a very high emissivity and very low absorptivity. This can be achieved by suitable outer layers. If anodized aluminum is used as the insulating material, typical surface values are 0.9 for the emissivity and 0.2 for the absorptivity. We will now look at each of the terms contributing to tether heating.

The solar flux mainly depends on the latitude, the solar declination angle, and the hour angle. Other factors include such phenomena as the sunspot cycle, but these variations are not as important and we will neglect them. The declination angle is the angle the sun makes with the Earth's ecliptic and seasonally varies ±23.5°. An expression for the declination angle can be given by

$-23.5\cos(\pi M/6)$, where M is the month (1-12). The hour angle at a point on the earth's surface is the angle through which the Earth must turn to bring that point's meridian directly under the sun. Thus for instance, the hour angle at noon is 0° and at midnight, is 180°. From spherical geometry, the following relationship can be deduced[26],

$$\cos z = \sin(\text{LAT})\sin(\text{DECL}) + \cos(\text{LAT})\cos(\text{DECL})\cos(\text{HRANG}) \qquad (98)$$

where z is the sun zenith angle.

From NASA design criteria[10], the solar flux constant is taken to be $S=1353\pm21$ W/m^2. Thus the solar heat flux can be written as,

$$Q_{SOLAR} = S\alpha_s A_\perp \qquad (99)$$

where α_s is the surface absorptivity, and $A_\perp$ is the perpendicular area to the sun given by DLsin(z) where D is the tether diameter.

The heat flux from the Earth consists of two components. One component is the Earth's own emission $E=237\pm7$ W/m^2. The geometry of the surface area of the tether projected to the Earth's flux is quite complicated and depends on an Earth view factor which [8] gives as,

$$F = \frac{\theta - \sin\theta\cos\theta}{\pi}, \quad \theta = \sin^{-1}\left(\frac{r_E}{r}\right) \qquad (100a)$$

where r_E is the Earth's radius. Thus the Earth's own flux is,

$$Q_{EARTH} = \varepsilon EFA \qquad (100b)$$

Note that the total surface area, A, is involved in contrast to Eqn. (99) where the sun heats unidirectionally. The second component is the reflected solar radiation from the Earth, known as the albedo which is a small fraction of the solar flux. The albedo flux during the day is,

$$Q_{ALBEDO} = (0.3\pm0.02)S\alpha_S FA\cos z \qquad (101)$$

It should be noted that this equation is not exactly correct: at the Earth's terminator, (z=90°), the albedo is not exactly zero but is quite small.

The last external heat flux is the aerodynamic heating. Although this is a small contribution compared to the other fluxes, it becomes important at lower altitudes. As an upper bound, taking the Stanton number to be unity, the aerodynamic heating is,

$$Q_{AERO} = \frac{1}{2}\rho V_{rel}^3 A_\perp \qquad (102)$$

where ρ is the atmospheric density, and V_{rel} is the relative velocity

to the atmosphere. The atmospheric density as a function of altitude and the exospheric temperature, is given by [8] as,

$$70<z<118 \text{ km} \quad \rho \approx 11\exp(-z/6)$$

$$118<z<200 \text{ km} \quad \rho \approx (z - 95)^{-3}/2600$$

$$200<z \text{ km} \quad \rho \approx \frac{1.47\times10^{-16}T_{ex}(3000 - T_{ex})}{(1 + 2.9(z - 200)/T_{ex})^{10}} \qquad (103a)$$

T_{ex} is the temperature in °K of the exosphere which depends on its relationship to the sun. A rough approximation for this variation can be given by,

$$T_{ex} = 1100(1 + 0.12\cos \text{HRANG}) \qquad (103b)$$

This model is in relatively good agreement with the U.S. Standard Atmosphere. Section 5.5 gives the results and discussion of the heat fluxes and tether temperature.

2.5.6 Superconducting Tethers

As was already noted, the temperature of the tether fluctuates around 200°K (we will see later that the temperature is higher for higher currents, i.e. >7-10 A). Already at these lower temperatures, the resistance of the tether drops. Nevertheless, by setting the tether resistance to zero, as will be seen later, the peak power at times can increase by up to 40-50%. This suggests that it would be beneficial to look into the possibility of using a superconducting material for the tether, since the tether could be made thinner without changing the resistance which is effectively zero. Hence, the specific power can be increased. This idea was originally suggested by Nagle[31].

There are many interesting aspects of superconducting tethers that can be explored, of which only a few this thesis will examine. A material that exhibits superconducting properties around 200±20°K would be ideal. However, at this time, no such material exists. Fig. (8) shows the evolution of the superconductive transition temperature since the discovery of the phenomenon in 1911 by the Dutch physicist Heike K. Onnes.

The highest critical temperature today is around 125°K for a ceramic metal oxide compound Tl-Ba-Ca-Cu-O. Unfortunately, much research and development has yet to be done since these compounds

have very low critical current densities for practical applications and their mechanical properties are very poor. As can be seen in Fig. (8), all the latest superconductors have copper oxides in one form or another. It has been found that there is a direct correlation between the critical temperature and the number of copper-oxygen layers in a compound. Increasing the copper oxide layers raises the critical temperature. Maximum current flows along these layers, and not very well perpendicularly to them. Thus the conduction process is basically anisotropic. It is because of this anisotropy and the presence of grain boundary effects in the bulk ceramic, that limits current densities to the order of 10^{5-7} A/m^2. Above these levels, the material begins to lose its superconducting properties. For a tether 2 mm in diameter, this translates to a maximum current of 0.31-31 A. Thus a nominal current of about 10 A is in the range of the transition limit. Moreover, high-temperature superconductors have a granular or ceramic composition and are very brittle and inflexible. Some progress has been made in molding superconducting materials into fibers for use in cables, but much has yet to be achieved.

For the near term, it is more prudent to explore the feasibility of cooling the tether to liquid nitrogen temperatures (77°K), (or any other coolant temperature, since the analysis will be quite general). Of course, this will entail added mass and complexity. For example, what happens if a leak develops along a 20 km cooling jacket and the coolant is lost? Actively cooling the tether will also require a pump and power to run it. In addition, the heat removed would have to be radiated away in some fashion. Thus it seems reasonable to consider venting away the coolant once it reaches the top of the tether. In fact, the liquid nitrogen will most likely evaporate by the time it reaches the top, and the gaseous nitrogen can be fed into the plasma contactor. If the increase in power overcomes the added mass penalties, then superconducting tethers will indeed offer higher performance, increasing their attractiveness. We will now consider some of the heat transfer and cooling issues involved with actively cooling a superconducting tether.

A possible configuration for an active cooling scheme of a superconducting tether is shown in Fig. (9). A thin insulated cooling

jacket surrounds the superconductor and is connected via very low thermal conducting spacers. The coolant, liquid nitrogen, is pumped in through the bottom absorbing heat as it flows to the top. There are a number of questions and issues that must be addressed. Given a temperature range the superconductor must be maintained at, the coolant flow velocity, pump pressure, and diameter of cooling jacket must be determined. In addition, given a mass flow rate, we can determine the power required for the pump.

Consider a section of the cooled superconducting tether as shown in Fig. (9). We will sidestep the time varying nature of the problem by designing for the worst case heat flux. Thus although the heat flux is changing between night and day conditions, the system will be cooled quite adequately. We will also assume a semi-lumped parameter system due to the thinness of the tether. (After all the tether must be either reeled or coiled up in some fashion.) This means that radially, the temperature of the tether inside will be assumed to be more or less constant. Only axial temperature gradients will be considered. Balancing heat fluxes, we have,

$$q(x)A^* + q_{IN}\Pi_{po}dx = (q(x) + \frac{\partial q}{\partial x}dx)A^* + \varepsilon\sigma T^4\Pi_{po}dx + \dot{m}C_p dT \qquad (104a)$$

where A^* is the sum of A_c the coolant cross-sectional area and A_w the conductor cross-sectional area, Π_{po} is the outer perimeter, C_p is the specific heat capacity of the coolant, and q_{IN} is the total heat flux per unit area (W/m^2) into the tether. Note we are neglecting any heating due to ohmic heating since the superconductor has no resistivity. We will neglect any axial conduction through the cooling jacket since we assume that it is an insulator with very high thermal resistivity. Introducing a "weighted" thermal conductivity,

$$k^* = \frac{k_c A_c + k_w A_w}{A^*} = \frac{\bar{k}}{A^*} \qquad (104b)$$

Eqn. (104a) becomes,

$$\frac{d^2T}{dx^2} - \left(\frac{\rho U C_p A_c}{\bar{k}}\right)\frac{dT}{dx} - \left(\frac{\varepsilon\sigma\Pi_{po}}{\bar{k}}\right)T^4 = \frac{Q_{IN}}{\bar{k}L} \qquad (104c)$$

where Q_{IN} is the total heat (W) to the tether. We can relate the total heat flux as being radiated from some "back-ground" temperature. Thus,

$$T_{BK}^4 = \frac{Q_{IN}}{\varepsilon\sigma\Pi_{po}L} \tag{104d}$$

Rewritten, Eqn. (104c) becomes,

$$\frac{d^2T}{dx^2} - \left(\frac{\rho UC_pA_c}{\bar{k}}\right)\frac{dT}{dx} - \left(\frac{\varepsilon\sigma\Pi_{po}}{\bar{k}}\right)(T^4 - T_{BK}^4) = 0 \tag{104e}$$

We can non-dimensionalize this equation by defining, $\xi=x/L$ and $\theta=T/T_i$ where T_i is the initial temperature of the coolant flowing into the cooling jacket. The result is,

$$\frac{d^2\theta}{d\xi^2} - \left(\frac{\rho UC_pA_c}{\bar{k}/L}\right)\frac{d\theta}{d\xi} - \left(\frac{\varepsilon\sigma T_i^4\Pi_{po}L}{\bar{k}/L\,T_i}\right)(\theta^4 - \theta_{BK}^4) = 0 \tag{105}$$

As is conventional, we can ignore axial conduction in the coolant as long as the following condition is met, $1/Pe = 1/RePr << 1$. The question of axial conduction in the superconductor itself is a bit more difficult. However, in keeping with our assumptions of the semi-lumped parameter model, we will consider it negligible. This is valid as long as the temperature gradient along the tether is not too high. Furthermore, the axial heat conducted will be, $q_{cond}=k\Delta T/L$ and since L is very large, q_{cond} should be quite small. The second derivative term can be ignored to a very good first approximation since the coefficients of the other terms are much larger than this term. (Physically, we can really only specify one boundary condition, the inlet temperature.) Thus Eqn. (105) reduces to a first order equation,

$$\rho UC_pA_c\frac{d\theta}{d\xi} + \varepsilon\sigma T_i^3\Pi_{po}L(\theta^4 - \theta_{BK}^4) = 0 \tag{106a}$$

Denoting,

$$\alpha = \rho UC_pA_c \tag{106b}$$

$$\beta = \varepsilon\sigma T_i^3\Pi_{po}L \tag{106c}$$

we can separate variables and integrate. Since we want to know the temperature of the coolant by the time it reaches the end of the coolant tube, we use the boundary condition $\theta(\xi=0)=1$. The final result for the temperature at x=L, is an implicit function of $\theta(\xi=1)$,

$$\frac{1}{4\theta_{BK}^3}\left[2\tan^{-1}\left(\frac{\theta_L}{\theta_{BK}}\right) + \ln\left(\frac{\theta_L + \theta_{BK}}{\theta_L - \theta_{BK}}\right)\right] = \frac{\beta}{\alpha} + C_1 \tag{107a}$$

where,

$$C_1 = \frac{1}{4\theta_{BK}^3}\left[2\tan^{-1}\left(\frac{1}{\theta_{BK}}\right) + \ln\left(\frac{1 + \theta_{BK}}{1 - \theta_{BK}}\right)\right] \tag{107b}$$

We can now vary the various parameters such as the physical dimensions of the cooling tube, and the flow velocity to see the effect on the temperature rise along the tether. We must worry about the temperature not rising too high or else the nitrogen will boil before reaching the end, and the heat transfer characteristics will change substantially. (Due to the high pressures in the tube, the N_2 might reach its critical point, T_c=126.1°K, and then completely vaporize. However, by that time, the tether would be no longer superconducting, and the whole scheme would be useless.)

In addition to the the temperature profile along the tether, we must know the pressure needed by a pump to supply the coolant. The equation governing the pressure drop down the coolant tube is a well-known result. However, we must consider a new force on the fluid: the gravity gradient. For a Shuttle-borne tether, since the center of mass is more or less at the Shuttle, the fluid all along the tube will feel a force upwards. The pressure force and the gravity gradient force must be balanced by the frictional shear stress at the walls,

$$\frac{1}{2}\rho U^2 C_f \Pi_{pc} dx + dp A_c = 3m\Omega^2 x dx \qquad (108a)$$

where C_f is the skin friction coefficient, m is the coolant mass per unit length, and $\Pi_{pc}=2\pi(R_w + R_i)$ the wetted surface perimeter. In general for $Re_D = UD_h/\nu > 3000$, the flow will be turbulent in the tube. Thus we can use the following relation for C_f,

$$C_f = 0.046 Re_D^{-0.2} Pr^{-0.6} \qquad (108b)$$

Here, the Reynolds number is based on the hydraulic diameter $4A/\Pi_p=2(R_i-R_w)$. Thus we have the equation for the pressure,

$$\frac{dp}{dx} = \frac{3m\Omega^2}{A_c} x - \frac{1}{2}\rho U^2 C_f \frac{\Pi_{pc}}{A_c} \qquad (108c)$$

Integrating along the length, the total pressure drop is,

$$\Delta p = -\frac{3m\Omega^2 L^2}{2 A_c} + \frac{1}{2}\rho U^2 C_f \frac{\Pi_{pc}}{A_c} L \qquad (109)$$

Thus the gravity gradient force decreases the pump pressure needed. However, the decrease is very slight. For a 20 km tether, with R_w=1 mm, R_i=5 mm, and U=2 m/s, the hydrodynamic pressure drop is 46.52 MPa, while the gravity gradient decreases the pressure by 0.67 MPa. (Note that the presence of spacers in the tube will

increase the pressure drop, so this is a lower limit.)

Now that we know the pump pressure, we can compute the power required for some given mass flow rate. For an incompressible fluid, a pump with some efficiency η, requires the power,

$$P = \frac{1}{\eta}\dot{m}\frac{\Delta p}{\rho} \tag{110}$$

It is interesting to ask the question whether the capillary action of the fluid in the tube makes any contribution to decreasing the pressure drop. The phenomenon of capillary action is due to the effect of adhesion or surface tension between a wall and fluid. In the presence of gravity, the height the fluid will rise to in a thin tube is given by a balance between the gravity and surface tension forces. If we consider a thin tube of radius R with a fluid of density r, the balance of forces gives, $2\pi R\sigma = \pi R^2 h\rho g$, or, the height the fluid will rise to is,

$$h = \frac{2\sigma}{R\rho g} \tag{111}$$

where σ is the surface tension given in [N/m]. However in space, without the existence of any effective gravity, the fluid would continue to rise. However, surface tension is a force at an interface where the liquid terminates. Thus once the tube is completely filled, all the surfaces will be wetted, and the capillary action will cease to act.

2.6 The Radiation Impedance

The radiation impedance, the result of wave excitation by a moving conductor in a plasma, can be related to the energy propagated away. The power loss can be computed by integrating the Poynting vector around a closed surface surrounding the conductor,

$$P_{rad} = \int_S \mathbf{E} \times \mathbf{B} \cdot \hat{\mathbf{n}} dS \tag{112}$$

To evaluate the radiation impedance, we will use the theory and computational model in Wang[38] which is based on the work of Barnett and Olbert[3]. In [38], a computer code was developed to

compute the radiation impedance of a tether. Various geometries and ionospheric conditions could be entered. It was found that the radiated waves had frequencies in three distinct bands. The first band is the Alfvén band $0<\omega<\omega_{ci}$, where ω_{ci} is the ion gyrofrequency. The second is the lower hybrid band $\omega_{lh}<\omega<\omega_{ce}$, and the third is the upper hybrid band $\omega_{pe}<\omega<\omega_{uh}$, where ω_{lh} is the lower hybrid frequency, ω_{uh} is the upper hybrid frequency, ω_{ce} is the electron gyrofrequency, and ω_{pe} is the plasma frequency. For a tether, the second band is the most important, while the first contributes very little, and the third is not significant at all to the impedance. Due to the very complicated nature of the equations, variations in the impedance due to fluctuations in the ionospheric conditions and the dependence on tether geometry are prohibitively difficult to extract analytically. Barnett and Olbert were able to derive some simple relations, but only in the limit of certain parameters. Thus in order to understand these scaling relationships, we must resort to numerical experiments.

The main geometric factor is found to be the size of the end connectors (the plasma contactors) that emit to and collect current from the ionosphere. As the area decreases, the impedance increases. This is because, as the area decreases, the current density increases, increasing the strength of the wave perturbation. As we will see, the size of the plasma clouds produced by the contactors is quite large ranging up to 20-30 meters in radius. The question arises whether the size of the end connector should be taken to be the physical size of the contactor, which is rather small, or the size of the cloud. In the theory of Wang[38], the end connector is the boundary where the current is collected (or emitted), and $\nabla \cdot \mathbf{j} = 0$. This is not necessarily true on the surface of a contactor cloud. Thus it is not clear whether to use the size of a contactor cloud as the size of the end connector or not. For the bulk of this study, we will choose the size of the end contactor to be three meters in radius. Even though this size is small compared to the cloud radius, the impedance is rather small (1-10 ohms). In addition, we will examine the effect of using a one meter and half meter diameter contactor, where the impedance is noticeably higher (over 100 ohms for the

later).

Changes in the ionospheric conditions also affect the impedance. The two parameters of importance are the electron density n_e, and the geomagnetic field which affects the various plasma frequencies. As can be seen in Fig. (10), the main variation in impedance comes from variations in n_e, rather than B. As n_e increases, the impedance decreases. This is because the scalar conductivity of a plasma scales with the density. The impedance slightly increases with the magnetic field since increasing B, increases the ion and electron gyrofrequencies and hence the bandwidths of radiation. For this study, we will neglect variations of the impedance with the magnetic field, and include only effects due to density fluctuations. The magnetic field will be held at 0.4 G. For a three meter radius sphere, a curve fit to Fig. (11), yields a dependency of the impedance on n_e as,

$$Z_I = 0.055 - \frac{0.168}{x^{1.2}} + \frac{0.911}{x} \text{ [ohms]} \qquad (113a)$$

where $x = n_e[cm^{-3}]/10^6$. For a one meter contactor, we find,

$$Z_I = -0.224 - \frac{2.339}{x^{1.2}} + \frac{10.71}{x} \text{ [ohms]} \qquad (113b)$$

and for a 0.5 meter diameter contactor,

$$Z_I = 0.190 + \frac{1.917}{x^{1.2}} + \frac{16.558}{x} \text{ [ohms]} \qquad (113c)$$

For a bare tether, the surface area collecting electrons is rather large (equivalent to a sphere up to 8-16 meters in diameter). As a result, while the geometry of the end "contactor" is different, the radiation impedance is quite small (less than 1-2 ohms). However, the current collected over this surface is not uniform, as we saw in Fig. (5b) from Section 2.3.3. Unfortunately, the code used to compute the radiation impedance assumes that the current distribution over the collecting surface is uniform in the direction along the tether. In light of these uncertainties, we will simply use Eqn. (113a) for the bare tether.

Recent ground experiments by Urrutia and Stenzel[37] have shown that not only end contactors, but also the entire tether, will radiate waves and thus the radiation losses are considerably increased. We will examine the impact of high radiation losses by artificially setting the impedance to high values. This is clearly an

area for future study. The effect of ionospheric impedance will be discussed in Section 5.9.

2.7 Other Tether System Components

In addition to the tether and the anodic and cathodic devices, there are other components that comprise the overall tether system. These include the power regulator to regulate the current flowing to the load, batteries to make-up for power when the induced voltage and/or ionospheric density drops too low, and solar arrays or fuel cells to provide power for thrusting operations. Each of these components will be discussed briefly in the following sections.

2.7.1 Batteries

Batteries must provide for power leveling when the environmental conditions fluctuate as can be seen in Figs. (15,18a). The various factors that govern the choice of batteries are the depth of discharge (DOD), the charge/discharge efficiency, the lifetime, and the battery capacity, usually given in W-h/kg. Among the various candidates for space applications such as Silver-Zinc (Ag-Zn), Nickel-cadmium (Ni-Cd), Nickel-Hydrogen (Ni-H_2), and Silver-Iron (Ag-Fe), Ni-H_2 appears to have the most favorable characteristics currently. However, with further development in the very near future, Ag-Fe batteries will most likely dominate in performance.

Silver-zinc batteries are attractive because of their high energy density (110-132 W-h/kg) and good temperature-discharge performance. The major disadvantage is the low-cycle-life (20-200 cycles), thus these batteries are not desirable for longer-term missions. Nickel-cadmium batteries have enhanced cycling capabilities, but have a much lower energy density (22-26 W-h/kg). In addition, they have degraded high-temperature capability. Nevertheless, Ni-Cd batteries have been used on communications satellites during the 1960's and 70's for up to 7 year applications. With the development of the Nickel-hydrogen batteries in 1972, battery performance and life-time have been substantially improved. This battery differs from other cell-type standard batteries that consist of an anode and cathode in an electrolyte

solution. Ni-H_2 batteries use an H_2 anode, which means that gaseous hydrogen must be stored for consumption during discharge and regeneration during recharge. Thus Ni-H_2 batteries require a tank of H_2 gas which increases the volume by about a factor of two over Ni-Cd batteries. Typical life-times are in the range of 10 years with energy densities up to 30 W-h/kg.

Recently, a new type of battery, the Ag-Fe cell, has been developed at Westinghouse[6]. This battery has a maximum capacity of nearly 100 W-h/kg at close to 100% DOD and a charge/discharge efficiency of around 90-95%. The predominant electrochemical reaction during discharge is,

$$Ag_2O + H_2O + 2e^- \rightarrow 2Ag + 2OH^-$$

$$Fe + 2OH^- \rightarrow Fe(OH)_2 + 2e^-$$

$$Ag_2O + Fe + H_2O \rightarrow 2Ag + Fe(OH)_2$$

Currently, these types of batteries which are still in the development stage, are not able to be operated for more than 10-30 cycles before water is required. With periodic maintenance, even at high DOD rates, the cycle life exceeds 300 cycles (about 19 days in LEO). (Note: The cycle life was determined by a test that was terminated after 310 cycles-not by performance, but by decision; battery performance after 310 cycles did not decay appreciably at all.) However, Westinghouse is in the process of converting these batteries to a starved-electrolyte design which will be maintenance free. In the near future the performance of the battery is expected to increase substantially, and is being targeted for space and submersible applications. In light of these developments, while remaining realistic, for this study we will use Ag-Fe batteries with a energy density of 50 W-h/kg, and a charge/discharge efficiency of 90%.

2.7.2 Solar Arrays

A tether employed as a thrusting device, requires an on-board power supply. As a pure thruster, solar arrays may be used during the day, and batteries or fuel cells during the night. In the mixed mode of operation (orbital energy storage), where power is

generated at night, and thrusting is done during the day, solar arrays will also be needed. A solar array system consists of the solar cells, the panel on which they are mounted and a deployment mechanism.

There are basically two types of solar array systems: rigid panels and flexible panels. In rigid systems, the solar cells are fixed to a rigid substrate whereas in the flexible systems, the substrate is like a sheet that can be rolled or folded just like aluminum foil. The current trend in space systems is the use of flexible panels due to their lightness and remarkably low stowed volume. Flexible panels can be divided into two main deployment categories: foldout and rollout. The rollout type solar arrays are stored in a cylindrical drum and are deployed by "rolling out" the solar panels. The foldout systems operate by storing the panels "accordian-pleated" fashion and are deployed by unfolding them similar to a Japanese fan.

For typical thrusting applications, the power required is on the order of 20-30 kW. Thus very large solar arrays are required. To fill this need for large-area, lightweight solar arrays, Lockheed developed a series of new foldout flexible solar panels. These arrays are fabricated with a special technique where the solar cells are attached to a copper printed circuit laminated to a Kapton sheet, which is 1 mil thick. The result is a flexible solar array with one-tenth the stowed volume and one-third the weight of comparably sized rigid arrays. To demonstrate this technology, the Solar Array Flight Experiment (SAFE) was developed and flown on the Shuttle in 1984. When fully extended, the 84 panels were 13.5 feet wide and over 100 feet long. The design electrical power output of the array was over 12.5 kW and the total mass was about 427 kg, giving a specific power of 29.3 W/kg. Of the 427 kg total mass, 71% was made up of the solar array assembly, while 29% consisted of the special support structure for the Shuttle cargo bay. Fig. (12) gives a detailed mass breakdown taken from [28]. Since initial experiments tend to be over-designed, and the support structure is only vehicle specific, we will take the overall mass to be that of the wing assembly only, which gives a specific power of 41.0 W/kg.

We shall now examine some of the sizing issues in designing solar arrays for our tether systems. When sizing the solar arrays for pure

thruster applications, we will not consider any load power requirements. The solar arrays will only provide power for thrusting during the day and for charging the batteries or regenerative fuel cells that provide power for thrusting during the night. However for the mixed mode of operation, we will have to design the arrays to provide power for both thrusting and a load during the day.

The energy diverted from the solar array in the day to charge the batteries or fuel cells is,

$$E = \frac{P_{REQ}}{\eta_{CR}}\left(\frac{t_{SH}}{60}\right) \text{ [kW-hr]} \tag{114}$$

where t_{SH} is the shadow time in minutes typically 35 minutes, and η_{CR} is either the battery charge/discharge efficiency or the ratio of the fuel cell to electrolyzer voltage. Thus the power the solar array must produce is, the sum of the thrusting power and the charging power,

$$P_{SA}(EOL) = \frac{1}{\eta_P}\left[P_{THR} + E\left(\frac{60}{t_S}\right)\right] \tag{115}$$

where η_P is the power regulation and distribution efficiency, and t_S is the time in the sun in minutes, typically around 55 minutes. For sizing, we will use this equation for power requirements. Note that this is the power at end of life (EOL). The output of solar arrays degrades over time due to radiation damage. The degradation rate is actually a function of time. For a 7-year lifetime, total solar cell output typically degrades by about 18-25%. Approximately one-half of the total degradation usually occurs in the first two years. We will denote the total degradation for a given mission by ϕ_D. Since we will be comparing a tether/solar array system versus a battery/solar array system, the choice of ϕ_D is not critical. We will choose a degradation factor of 3%. Sunlight is transformed into electrical energy when the impinging photon energy is equal to the bandgap of the solar cell material. Since the solar spectrum contains many different wavelengths, only a small portion of solar energy is actually converted. Thus solar cell efficiencies are quite low, the upper bound usually in the neighborhood of 14-15%. Thus if the solar cell efficiency is η_S, the beginning of life (BOL) power is,

$$P_{SA}(BOL) = \frac{P_{SA}(EOL)/\eta_S}{1 - \phi_D} \quad (116)$$

This is the power that must be captured from the sun. Since the solar flux is about 1353 W/m^2, the solar array area required is,

$$A_{SA} = \frac{P_{SA}(BOL)}{1353} \quad (117)$$

in square meters.

2.7.3 Fuel Cells

For pure thrusting missions, during the night, power must be supplied and a fuel cell is an alternative to batteries. A fuel cell is an electrochemical cell where the reactants are supplied and the products are removed at a steady state, so that in principle, no changes need occur in the physical or chemical state of the cell with time. A fuel cell operates by consuming oxygen and hydrogen, and produces electricity and water. On the other hand, supplied with power, a fuel cell operates in reverse and produces hydrogen and oxygen. This arrangement is known as a fuel cell-electrolyzer system (FCE).

Compared to most of today's standard batteries (except the Ag-Fe), the FCE system has a higher useable energy density and hence lighter weight for a given required power, despite their lower charge/recharge efficiency. On the other hand, they are more complex and therefore less reliable. The mass flow rate of fuels (oxygen and hydrogen) consumed by a FCE system in kg/s is given by,

$$\dot{m} = \frac{P_{REQ}}{\Delta G}(0.018 \text{ moles/s})\left(\frac{V_{oc}}{V}\right) \quad (118)$$

where ΔG is the change in Gibbs free energy in the $H_2 + 1/2O_2 \rightarrow H_2O$ reaction which is about 228,000 J/mole. V_{oc}/V is the ratio of the open circuit to operating voltage which is similar to an efficiency, and is typically around 1/0.7. Thus the fuel consumption amounts to about 9.7 kg/kW/day. Using figures representative of the Shuttle fuel system, the dry fuel cell mass is around 10 kg/kW, and the electrolyzer 9 kg/kW. In addition, tanks are required to store the hydrogen, oxygen, and water, and we will take the tankage mass/stored mass to be 0.15.

2.7.4 The Power Regulator

To handle induced voltage fluctuations, and charge/discharge operations, a power regulator will be needed for the tether system. Rivas[34], examined various regulators such as switching-type regulators, series and shunt dissipative regulators, and pulse-width-modulated regulators. The design choices made for the tether as a power generator was the switching non-dissipative regulator, and for the thrusting mode, a pulse-width-modulated boost regulator. We will use the same choices. The total specific mass of these devices is taken to be 6 kg/kW (peak) and the efficiency to be 97%.

Chapter 3.0

The Tether Electro-Magnetic Environment

An electrodynamic tether would not be able to operate without two crucial elements, a magnetic field, and a conducting plasma medium. In this section, we discuss primarily the particulars of the Earth's magnetic field and the ionosphere. A few comments are also made on the magnetic and ionospheric conditions on other planets of our solar system where tethers might be able to operate.

3.1 The Geomagnetic Field

The magnetic field around the Earth extends out into space tens of thousands of kilometers. The generation of the geomagnetic field comes from a number of different sources, both terrestrial and extraterrestrial. The primary source is the convection motion of the conducting molten metals in the core of the Earth that constitute a self-exciting dynamo. Residual permanent magnetism in the Earth's crust also contributes. The sun's radiation also has a pronounced effect and contributes to the dynamic and ever-changing nature of the geomagnetic field. Atmospheric winds produced by solar heating move charged particles, produced by solar ionizing radiation, which constitutes an ionospheric current that generates its own field. The gravitational fields of the sun and moon also induce tidal motions on the air that produce a weak field. Lastly, a number of field contributions arise directly or indirectly from the interaction of the

solar wind and its magnetic field with the main field of the Earth. Most notable, is the compression of the geomagnetic field behind the bow shock and the intrusion of solar plasma into the main field. Even today, many aspects of the geomagnetic field are not well understood. For instance, it has been observed that the polarity of the field reverses with a period of several hundred thousands of years. (This reversal would have effects on tethers, reversing the directions of the induced voltages.)

In LEO, the Earth's magnetic field varies between $2\text{-}6 \times 10^{-5}$ Tesla (or 0.2-0.6 Gauss). In contrast to some of the other planets, Mercury's magnetic field is about 100 times smaller. Venus has virtually no intrinsic magnetic field (0.00001 G), and Mars' field is about 0.004 of the Earth's. On the other hand, due to its liquid metallic hydrogen core and rapid rotation rate (about 10 hours), Jupiter's field is about 15-20 times larger than the Earth's. It is interesting to note in regards to electrodynamic tether applications, that if the tether is beyond the synchronous altitude of 2.2 Jupiter radii, both power and thrust can be generated, the energy coming from the co-rotating plasma. Saturn's magnetic field is slightly less than Jupiter's, but still much greater than the Earth's. The magnitude of Uranus' field is slightly larger than the Earth's. However, the field is tilted 58° to the planet's rotation axis, producing a highly non-uniform "cork screw" structure which is quite undesirable for tether operation.

The gross characteristics of the geomagnetic field can be modelled to a first approximation as a dipole field with spherical components r, θ, ϕ, where r is the radius from the center of the Earth, and θ is measured from the dipole axis (i.e. the geomagnetic co-latitude). Thus we have from [20],

$$B_r = -\frac{M}{r^3} 2\cos\theta$$
$$B_\theta = -\frac{M}{r^3} \sin\theta$$
$$B_\phi = 0 \qquad (119)$$

where M is the dipole moment of the Earth, about 7.9×10^{15} T/m^3. The geomagnetic North Pole is located at 78.56°N, 290.24°E, so thus it is offset by about 11.5° from the geographic North Pole. Granted that

this model is a first approximation, it is however a rather poor one. It gives an equatorial field intensity of 0.308 G while in reality, the actual intensity varies by more than 25%. Thus to accurately simulate the induced voltage a tether will generate, we must turn to a much more accurate spherical-harmonic potential model.

Any field derivable from a potential function can be expressed as a harmonic expansion (we will use the same technique for the gravitational model in Section 4.2.2). The coefficients of the various terms only need to be adjusted by a least-squares method to best fit measured data. The magnetic scalar potential can be written as a spherical-harmonic expansion[20],

$$\Phi = R_E \sum_{n=1}^{\infty} \sum_{m=0}^{n} P_n^m(\cos\theta)\left[\left(\frac{R_E}{r}\right)^{n+1}(g_n^m \cos m\phi + h_n^m \sin m\phi) + \left(\frac{R_E}{r}\right)^{-n}(A_n^m \cos m\phi + B_n^m \sin m\phi)\right] \tag{120}$$

where r, θ, and ϕ are the geographical coordinates of radial distance, colatitude, and east longitude, and R_E is the radius of the Earth. The functions $P_n^m(\cos\theta)$ are the partially normalized Schmidt functions,

$$P_n^m(\cos\theta) = \left[\frac{\varepsilon_m(n-m)!}{(n+m)!}\right]^{1/2} P_{n,m}(\cos\theta) \tag{121}$$

where $\varepsilon_m = 2$ if $m>0$, or $\varepsilon_m = 1$ if $m=0$ and $P_{n,m}$ is the associated Legendre function. The field can now be computed by,

$$\mathbf{B} = -\nabla\Phi \tag{122}$$

so thus the northward, eastward, and downward components respectively are,

$$B_\theta = \frac{1}{r}\frac{\partial\Phi}{\partial\theta}$$
$$B_\phi = -\frac{1}{r\sin\theta}\frac{\partial\Phi}{\partial\phi}$$
$$B_r = \frac{\partial\Phi}{\partial r} \tag{123}$$

In the potential function, those terms containing the coefficients g and h arise from sources within the Earth, while the coefficients A and B arise from external currents. It should be noted that most spherical-harmonic models, including the one used in this thesis, become unreliable with increasing distance from the Earth. Beyond about two to three Earth radii, these models breakdown because the geometry of the external field is not well suited for spherical-

harmonic analysis. However, these altitudes are well above tether operating regimes thus these models are more than adequate. In addition, these models can not take into account various fluctuations due to unpredictable events such as geomagnetic storms due to solar flare activity. However, these fluctuations are quite small indeed, usually measured in nano-Teslas (nT).

The magnetic model used in this thesis was a detailed spherical-harmonic model obtained from the Smithsonian Astrophysical Observatory (SAO). This model used the International Geomagnetic Reference Field (IGRF) Epoch 1975.0 coefficients and extrapolated them to 1980.0. The input to the program called, NEWMAG, is the geocentric latitude, east longitude, distance from the center of the Earth, and the point's cartesian coordinates in an arbitrary inertial space. The program will then return the three components of the magnetic field in that inertial space. The model is sufficiently accurate to model many of the irregularities and anomalies of the geomagnetic field.

As can be seen in Fig. (13a), the induced voltage for a Shuttle-type inclination orbit of 28.5° varies greatly. These fluctuations are highly undesirable for power generation since the power will fluctuate by factors up to 7 or 8, as in Fig. (13b). On the other hand, these fluctuations are not as important for thrusting applications. The fluctuations are not only due to the angle variation with the magnetic North Pole, but the dominant variability is due to the groundtrack of the vehicle sweeping over large "pothole" anomalies over the South Atlantic and Southeast Asia as can be seen in Fig. (14). In order to avoid these anomalies, a spacecraft will be forced to fly a more equatorial orbit which is nonetheless more advantageous since the velocity vector becomes more or less perpendicular to the magnetic field lines, increasing the induced voltage. However, to reach a low-inclination orbit from a higher latitude implies large fuel costs. Fig. (15) shows the induced voltage for a 1° orbit, and the dramatic reduction in voltage fluctuations which lead to power fluctuations of only a factor of 2 to 3, as can be seen in Fig. (28f). Note how the fluctuations for each orbit are more or less uniform. The average induced voltage is also higher. Thus a tether system can

be designed for an average typical orbit, rather than a particular "worst" orbit as was done in [34]. The voltage still fluctuates due to angle variations with the magnetic North Pole, but the groundtrack avoids to a large extent, the anomalies. In addition, using a control technique, (to be discussed in Section 4.3), employing a power regulator to vary the effective load impedance and using variable ionized gas emissions from the contactor, fluctuations in the output power can be further suppressed, as we will see later on. The cancellations of these fluctuations in part, negates the somewhat pessimistic conclusions of an earlier system study[29]. Unless otherwise stated, all our results will be for a 1° inclined orbit.

3.2 The Ionosphere

The regions at the altitudes in which tethers will operate in are known as the F2 and topside layers of the ionosphere. The upper regions of the Earth's atmosphere are ionized due to high energy particles and radiations, and a dilute plasma consisting of electrons, ions, and neutrals exists. This is a region where complex electromagnetic interactions occur, and rich phenomena such as the aurora take place.

The ionosphere is divided into six major regions. Fig. (16) shows a characteristic density profile at midlatitudes. In the equatorial region, this profile is distorted somewhat by the geomagnetic field, and in the polar region, the profile is distorted by ionization by energetic particles, magnetospheric coupling, and other effects. Starting from 70 to 90 km, is the D layer which consists mainly of NO^+ and O_2^+ ions, and is only present during daylight hours. Between 95 and 140 km is the E layer which is also made up of NO^+ and O_2^+ ions. The peak density usually occurs at a peak altitude of 110 km. In the E region, at sunset, the electron density drops by a factor of 10 or more in tens of minutes before reaching a nighttime equilibrium. From 140 to 400 km, is the F region which is divided into F1 and F2 regions at about 200 km. In the F1 region, the major components are monoatomic oxygen and NO^+ ions, while in the F2 layer, monoatomic oxygen and nitrogen ions are dominant. In the F1 layer, the electron density has a peak near 200 km, and in the F2 layer, near 300 km

during the day and at higher altitudes during the night. Above 400 km, is the topside ionosphere where the sole major component is monoatomic oxygen ions. Lastly, above 1200 km, exists the plasmasphere where the leading component is H^+.

Ionospheres also exist on most of the other planets in our solar system. Mercury's ionosphere is rather weak, due to having little or no atmosphere. Due to virtually no magnetic field, there is no magnetosphere to protect Venus. Thus the solar wind directly impinges on the upper atmosphere. The electron density typically peaks during the daytime at $1\text{-}3 \times 10^5$ cm^{-3} at an altitude of 160 km. During the nighttime, the density falls below 1×10^4 cm^{-3}. The same situation prevails also on Mars due its weak magnetic field. Peak electron densities of around 1×10^5 cm^{-3} are found at an altitude of around 130 km during the day. In contrast, due to its large magnetic field, Jupiter has a large ionosphere and magnetosphere extending out some 3-7 million kilometers. Voyager measurements indicate that the plasma temperature in some regions surrounding Jupiter is between 300 to 400 million °K. However, the plasma is very dilute in these hottest regions, (about $0.01/cm^3$); elsewhere, the density can be greater than $10^5 cm^{-3}$. Another interesting phenomena, is a huge current sheet that lies about 11° to the rotational axis. Due to the large rotation rate of Jupiter, centrifugal forces spew out charged particles in a huge plane. The Pioneer probes sent back data that Saturn has large radiation belts very similar to the Earth's. The structure of the magnetosphere is also very similar to Jupiter's. However the charged particle densities are quite low (10^4 cm^{-3} or less). One of the main reasons is that Saturn's rings absorb many of these particles. Figs. (17a-c) show electron densities for Jupiter, Saturn, and Uranus. It appears that Jupiter and Saturn are the most promising for potential future electrodynamic tether applications for either power generation, or more importantly, orbital maneuvering. Gabriel et al[12], examined tether performance in the Jovian ionosphere, but this is a possible area for future work.

A model of the Earth's ionosphere, the International Reference Ionosphere (IRI)-86 was used for the simulation program in this thesis, courtesy of the National Space Science Data Center. The IRI-

86 was the result of a joint project of the International Union of Radio Science (URSI), and the Committee on Space Research (COSPAR), and is based primarily upon experimental data taken by rocket sounding tests, incoherent scattering tests, and ionosondes. The experimental data is then fitted to analytical expressions. The IRI-86 can produce profiles of the electron density, the neutral, electron, and ion temperatures, and relative percentage densities of ions such as O^+, H^+, He^+, O_2^+, and NO^+. The inputs to the program are the latitude and longitude, (in either geocentric or geomagnetic coordinates), the altitude, the solar sunspot number, the month, and the time. (The solar sunspot number is given by k(n+10g) where n is the number of individual spots visible on the solar disk, g is the number of sunspot groups, and k is a station constant for a particular observatory.) The model is limited in altitude for the electron density, from 60 km(day) to 1000 km, for the temperatures, from 120 to 3000 km, and for the ion densities, from 100 to 1000 km. Accuracy is greatest at mid-latitudes, and starts to decay in the polar and equatorial regions. The program is run interactively, but was modified to serve as a subroutine and compute only the electron temperature and density.

As can be seen in Fig. (18a), the electron density varies by more than an order of magnitude between day and night. The density is also dependent upon the solar sunspot number as can be seen by comparing Figs. (18a,b) where in Fig. (18b), the sunspot number was doubled to 120. (Unless otherwise mentioned, we will generally use an average sunspot number of 60.) These seasonal variations will affect tether performance, as we will see later on, but not in significant ways. Using Eqn. (10e), the ambient electron saturation current can be computed and is shown in Fig. (18c).

Chapter 4.0

The Simulation Model

In this section, we will discuss the details of the simulation model such as the overall algorithm structure, the orbital mechanics, and the modes of operation. We will also discuss a control strategy used to limit the fluctuations in the power as was seen in the last section.

4.1 General Overall Description

The overall goal of the program is to simulate the performance of a tether system in LEO. The user can enter various initial conditions such as the initial orbital elements and height, the number of orbits to simulate, a total system mass (for acceleration purposes), and the mode of operation, i.e. pure thruster, pure power generator, or mixed mode. If thrusting is chosen, the method of thrusting must be selected, i.e. constant voltage, current, force, or power. If power generation is selected, the particulars of the power level must be chosen. The type of anodic device can than be selected: either the bare wire, plasma contactor or both. If the plasma contactor is selected, the ion current level, ionization fraction, and gas emission velocity must be entered. The choice of a superconducting tether can be made, and other details such as the month, time, and solar sunspot number must be entered. Lastly, physical dimensions such as the tether length and diameter are given. The program will then output time profiles of power generated, current, electrodynamic

forces, pertinent orbit data, efficiency, and contactor data. In addition, the masses of the various components of the system are computed.

4.2 Orbital Mechanics

There are several reasons for including orbital mechanics in the simulation model. The first and most obvious reason is that the trajectory of the vehicle must be computed in some fashion as it orbits the Earth to provide position and velocity information to compute the various environmental conditions. The second is that since the tether will exert an electrodynamic force, whether it be drag or thrust, the orbit will be influenced, and it is important to see what that influence will be. The first reason is the most important for this thesis because the second has been done already. Prall[33] analyzed partly analytically and through simulation, the orbital dynamics of tethers. One of his findings was that the mixed mode of tether operation was undesirable due to a constant increase of the orbit's eccentricity. Since the electrodynamic force is on the order of several newtons, it can be treated as a disturbing acceleration, along with the oblateness of the Earth, and atmospheric drag. The appropriate equations of motion will then be perturbational ones.

4.2.1 Coordinate Systems

In celestial mechanics, many different coordinate systems are used. In this model, we have used four coordinate systems as shown in Fig. (19). All are right-handed cartesian coordinate systems. The first is an inertial coordinate system [X,Y,Z]. We do not worry about the rotation of the Earth about the Sun, and hence the axis X is always pointing towards the Sun. The second axis system is fixed to the Earth, [x,y,z]. Thus this is a rotating coordinate system and the $\Theta(t)$ denotes the angle between x and X which changes 2π radians every day. This reference frame is necessary for computing latitude and longitude. The third coordinate system is denoted by [n,m,h] and lies in the plane of the orbit where n points along the line of nodes, and h is perpendicular to the plane of the orbit. The last reference frame also lies in the plane of the orbit denoted by [e,p,h], where e

points along the line of apsides (or perigee). The standard Euler angles that form in part the orbital elements are: Ω the longitude of the ascending node which is the angle between X and n, ω the argument of perigee which is the angle between n and e, and i the orbit inclination which is the angle between h and z or Z.

4.2.2 Disturbing Accelerations

The disturbing accelerations we will consider are the electrodynamic force, the oblateness of the Earth, and aerodynamic drag. Assuming the tether is rigid, the electrodynamic force is given by Eqn. (3b). Thus the disturbing electrodynamic acceleration is,

$$\mathbf{a}_{dEM} = \frac{L\mathbf{I} \times \mathbf{B}}{M} \tag{124}$$

The oblateness of the Earth causes phenomena known as regression of the nodes, and precession of the argument of perigee. These effects are important to include, because for higher inclination and elliptic orbits, they will increase the sweep area of the groundtrack. Although the most desirable orbit is a circular equatorial one, we want our model to be most general. Analogous to the formulation for the magnetic field, the Earth's gravitational field can be written as a spherical-harmonic expansion. To a very good approximation, the Earth is axially symmetric. Thus in coordinates where r is the radial direction, and z is the axial direction, the gravitational acceleration can be written as[5],

$$\mathbf{a}_g = -\frac{\mu}{r^2}\left\{\mathbf{i}_r - \sum_{k=2}^{\infty} J_k\left(\frac{R_E}{r}\right)^k\left[P'_{k+1}(\cos\phi)\mathbf{i}_r - P'_k(\cos\phi)\mathbf{i}_z\right]\right\} \tag{125}$$

where μ is the Earth's gravitational constant, the P' terms are derivatives of Legendre polynomials, ϕ is the geocentric co-latitude, and the J_k's are the coefficients for the Earth to the fourth term,

$$\begin{aligned} J_2 &= 0.00108263 \\ J_3 &= -0.00000254 \\ J_4 &= -0.00000161 \end{aligned} \tag{126}$$

In Eqn. (125), the first term is the acceleration due to a point mass, and the other corrective terms will be called the disturbing gravitational acceleration $\mathbf{a}_{dGRAV}$. For the sake of completeness, the Legendre polynomials used are,

$$P_2(x) = \frac{1}{2}(3x^2 - 1)$$
$$P_3(x) = \frac{1}{2}(5x^3 - 3x)$$
$$P_4(x) = \frac{1}{8}(35x^4 - 30x^2 + 3)$$
$$P_5(x) = \frac{1}{8}(63x^5 - 70x^3 + 15x) \qquad (127)$$

For long-term, low-altitude missions, the atmospheric drag is important. The disturbing drag acceleration can be written as,

$$a_{dDRAG} = -\frac{1}{2}C\rho v_{rel}^2 i_{rel} \qquad (128)$$

where C is the ballistic coefficient, $A_\perp C_d/M$. C_d will be taken to be 2.2[8]. The density ρ, and relative velocity are the same as discussed in Section 2.5.5. Thus these three disturbing accelerations will perturb the orbit of the tether vehicle. Of the three, the electrodynamic force is the most important, and for typical currents, ranges from 3-7 N. In the next section, we will examine the equations of motion.

4.2.3 Perturbational Equations of Motion

For equatorial orbits, the line of nodes does not exist. For circular orbits, the apsidal line has no meaning. Thus standard variational equations become singular for these types of orbits. The standard orbital elements are a, e, i, Ω, ω, and f, where a is the semi-major axis, e is the eccentricity, f is the true anomaly, and the others are the Euler angles. It is possible to find combinations of these elements that are not singular and recast them into a new set of elements known as *equinoctial variables*. These new variables are[5],

$$P_1 = e \sin \varpi \qquad P_2 = e \cos \varpi$$
$$Q_1 = \tan \frac{1}{2} i \sin \Omega \qquad Q_2 = \tan \frac{1}{2} i \cos \Omega \qquad (129)$$

where $\varpi = \omega + \Omega$ is known as the longitude of perigee. It is easy to see that the standard elements are recoverable,

$$e^2 = P_1^2 + P_2^2 \qquad \tan^2 \frac{1}{2} i = Q_1^2 + Q_2^2$$
$$\tan \varpi = \frac{P_1}{P_2} \qquad \tan \Omega = \frac{Q_1}{Q_2} \qquad (130)$$

provided that P_2 and Q_2 are non-zero.

Recasting the disturbing acceleration into polar coordinates in the orbital plane, the following are the differential equations governing

how the orbital elements change. The equation for the semi-major axis is,

$$\frac{da}{dt} = \frac{2a^2}{h}\left[(P_2 \sin L - P_1 \cos L)a_{dr} + \frac{p}{r}a_{d\theta}\right] \qquad (131a)$$

where h is the angular momentum of the orbit, related to p, the parameter, by $p=h^2/\mu$. Here we introduce the true longitude $L=\varpi + f$. The equations for P_1, P_2, Q_1, and Q_2 are,

$$\frac{dP_1}{dt} = \frac{r}{h}\left\{-\frac{p}{r}\cos L a_{dr} + \left[P_1 + (1+\frac{p}{r})\sin L\right]a_{d\theta} - P_2(Q_1 \cos L - Q_2 \sin L)a_{dh}\right\} \qquad (131b)$$

$$\frac{dP_2}{dt} = \frac{r}{h}\left\{\frac{p}{r}\sin L a_{dr} + \left[P_2 + (1+\frac{p}{r})\cos L\right]a_{d\theta} + P_1(Q_1 \cos L - Q_2 \sin L)a_{dh}\right\} \qquad (131c)$$

$$\frac{dQ_1}{dt} = \frac{r}{2h}(1 + Q_1^2 + Q_2^2)\sin L a_{dh} \qquad (131d)$$

$$\frac{dQ_2}{dt} = \frac{r}{2h}(1 + Q_1^2 + Q_2^2)\cos L a_{dh} \qquad (131e)$$

where a_{dr} is the radial acceleration in the orbital plane, $a_{d\theta}$ the tangential, and a_{dh} the vertical. As in any celestial mechanics problem, Kepler's equation must also be solved. Instead of using the mean anomaly M, we can use the mean longitude, $l = \varpi + M$. Thus the equation for the mean longitude is,

$$\frac{dl}{dt} = n - \frac{r}{h}\left\{\left[\alpha\left(\frac{p}{r}\right)(P_1 \sin L + P_2 \cos L) + \frac{2b}{a}\right]a_{dr} + \alpha\left(1+\frac{p}{r}\right)(P_1 \cos L - P_2 \sin L)a_{d\theta} + (Q_1 \cos L - Q_2 \sin L)a_{dh}\right\} \qquad (131f)$$

where n is known as the mean motion from Kepler's third law, $\mu=n^2a^3$, b is the semi-minor axis, and $\alpha=a/a+b$. These equations were integrated with the 4th-order Runge-Kutta Method.

4.2.4 Orbit Algorithm

Initial conditions must first be given. These include the initial orbital elements e, i, Ω, ω, f, and the distance from the center of the Earth r. The parameter of the orbit p, can than be computed from the equation of orbit,

$$p = r(1 + e \cos f) \qquad (132)$$

Next, the angular momentum of the orbit is computed, $h = (\mu p)^{1/2}$. With the above information, we can already compute the state vector in inertial coordinates,

$$\begin{aligned}\mathbf{r} = {} & r(\cos\Omega\cos\theta - \sin\Omega\sin\theta\cos i)\mathbf{i}_x \\ & + r(\sin\Omega\cos\theta + \cos\Omega\sin\theta\cos i)\mathbf{i}_y \\ & + r\sin\theta\sin i\,\mathbf{i}_z\end{aligned} \qquad (133a)$$

$$\mathbf{v} = -\frac{\mu}{h}[\cos\Omega(\sin\theta + e\sin\omega) + \sin\Omega(\cos\theta + e\cos\omega)\cos i]\mathbf{i}_x$$
$$-\frac{\mu}{h}[\sin\Omega(\sin\theta + e\sin\omega) - \cos\Omega(\cos\theta + e\cos\omega)\cos i]\mathbf{i}_y$$
$$+\frac{\mu}{h}(\cos\theta + e\cos\omega)\sin i\,\mathbf{i}_z \qquad (133b)$$

where $\theta=\omega + f$. After computing the disturbing accelerations, we must then compute new orbital elements and update the state vector. This is done as follows: We first compute P_1, P_2, Q_1, Q_2, ϖ and L using the old elements. The semi-major and minor axes can be determined from their definitions,

$$a = \frac{p}{1 - e^2} \qquad b = a\sqrt{1 - e^2} \qquad (134)$$

With a known, n can be found. Knowing the true anomaly, the eccentric anomaly E, is computed from the relation,

$$\tan\frac{E}{2} = \sqrt{\frac{1-e}{1+e}}\tan\frac{f}{2} \qquad (135)$$

which enables us to find the mean longitude l through Kepler's equation,

$$M = E - e\sin E \qquad (136)$$

We can then compute new values of a, P_1, P_2, Q_1, Q_2, and l from Eqns. (131a-f). The updated classical orbital elements e, i, Ω, ϖ can be found from Eqns. (130). Knowing ϖ and l, we know M and solving Eqn. (136) for E, we can use Eqn. (135) to find the new true anomaly f and then repeat the cycle.

Results and the effects of the electrodynamic force on the orbit will be discussed in Section 5.6.

4.3 Modes of Operation and Control Strategy

The tether can operate as a pure power generator, pure thruster, or both. As a pure power generator, despite the control strategy that will be discussed shortly, batteries are required to level fluctuations in the power output due to variations in the geomagnetic field, and the ionosphere. The actual power level delivered, P_D, is then that value where,

$$E_{EXCESS} = \int \left(P - \frac{P_D}{\eta_{reg}}\right) dt \qquad (137a)$$

which is the excess energy that is used for charging the batteries, is equal to,

$$E_{DEFICIT} = \int \left(\frac{P_D}{\eta_{reg}} - P \right) dt \qquad (137b)$$

where $E_{DEFICIT}$ is the energy that the battery must provide. Thus the battery is sized so that it is capable of delivering $E_{DEFICIT}$. The integration is performed over all the orbits, which for low inclinations, provides roughly the average over any one orbit. The specific power (W/kg), and the specific mass (kg/kW) are based on this delivered power.

For the pure power generator, the electrodynamic drag will lower the orbit, thus a rocket, or other propulsive device must be used to maintain a given orbital height, to prevent the tether system from falling too low. The average fuel consumption of the rocket can be determined by knowing the average force the rocket must produce which is the average drag force,

$$\bar{\dot{m}} = \frac{\bar{F}_{Drag}}{g I_{sp}} \qquad (138)$$

For our purposes, we will use an efficient liquid hydrogen, oxygen rocket with a specific impulse (Isp) of 450 seconds.

As a thruster, the tether can operate in several modes: constant voltage, current, force, or power. For constant voltage, a supply voltage is entered and the circuit equation, Eqn. (4d), is solved for the current. If the supply voltage is too low, i.e. at times when the induced voltage is high, the current is set to zero and the thruster is turned off. For constant current, Eqn. (4d) determines the supply voltage which will fluctuate because of the induced voltage. If the tether is thrusting with constant force, the current must be determined from the relationship, $F = ILB\sin\theta$, where θ is the angle between the magnetic field and the direction of the tether. Once the current is known, then the supply voltage follows as in the previous case. Lastly, for constant power, the product of the current and supply voltage must always be a given constant. The process of determining the current and supply voltage is an iterative one. First a current is guessed and from Eqn. (4d) the voltage is computed. The product IV is checked with the given power and the current is modified accordingly. These modes of thrusting are only for a

contactor tether. As was mentioned in Section 2.3.3, the bare tether thruster will be operated at a maximum efficiency condition.

For mixed mode operation, (or orbital energy storage), the tether thrusts during the day where power is drawn from solar arrays, and generates power during the night. The amount of power generated and thrust produced is such that they balance, and the energy of the orbit is fixed. Thus loss in orbital height during the power generation phase is made up during the thrusting phase. In other words,

$$\int_{night} F_{Drag}\, v dt = \int_{day} F_{Thrust}\, v dt \tag{139}$$

To control the large power fluctuations as seen in Figs. (13b,28f), we must return to a statement made in Section 2.2. It was noted that for any given operating conditions, there exists a unique value of the efficiency ($\eta = V_{load}/V_{ind.}$) such that the power generated is maximized. We will now proceed to prove this. For power generation, the circuit equation, Eqn. (4a), is,

$$\left(\frac{I - I_{iao}}{\beta}\right)^8 + A \ln\left(\frac{\alpha}{I}\right) + I(R_T + Z_I + R_L) = V_{ind} \tag{140}$$

where we have used the Gerver et al model (f=1), Eqn. (24), for the anode characteristic, and Eqn. (82) for the cathode characteristic. (Here we have included the case of full ionization only for simplicity for the following analysis; if the general anode characteristic, Eqn. (59), is used, it is more prudent to find an optimum numerically-which is what is done.) The problem is to maximize the load power I^2R_L with the constraint being Eqn. (140). This is a standard Lagrange optimization problem, where we can define a function,

$$L = I^2R_L + \lambda\left[\left(\frac{I - I_{iao}}{\beta}\right)^8 + A \ln\left(\frac{\alpha}{I}\right) + I(R_T + Z_I + R_L) - V_{ind}\right] \tag{141a}$$

where λ is a Lagrange multiplier. Differentiating L with respect to R_L and I, we obtain,

$$R_L = 8\frac{(I - I_{iao})^7}{\beta^8} - \frac{A}{I} + R_T + Z_I \tag{141b}$$

which gives us the value of the load resistance (and hence the efficiency) that maximizes the load power. Thus Eqn. (141b) can be inserted into Eqn. (140) to give an equation solely in terms of the

current, I. Fig. (20a), shows graphically the existence of an optimum efficiency. (A similar optimum also occurs for the bare tether.) When we say the tether is producing maximum power, this means that it is operating at the maximum efficiency point.

In addition, to the optimum efficiency, we introduce two other notions used in controlling the power generated. They are the upper and lower limits for the desired power level. Large scale fluctuations are undesirable due to large battery mass requirements, thus it is desirable to limit the peaks of the fluctuations by imposing an upper limit. If the power exceeds this upper limit, then the power regulator will increase the efficiency of the system, (i.e. increasing the voltage across the load) thus lowering the power to the load since the current will decrease. With respect to Fig. (20a), this means we are operating the system to the right of the maximum. Of course, one could always decrease the efficiency of the system to lower the power delivered, but this is highly undesirable since the current (and drag) increase as seen in Fig. (20b).

On the other hand, the contactor can be controlled to vary the current that is collected. If the power generated falls below a certain level set by a lower bound, then either the ion current can be increased, or the ionization fraction can be decreased in order to increase the current and hence the power generated. As we will see in Section 5.1, it appears to be more effective to increase the ion current than to decrease the ionization fraction. Thus if the power falls below the lower limit, the strategy is to increase the ion current to boost the power. For a tether with a contactor both these strategies are applicable, however, for a pure bare tether, there is no means for increasing the power below the lower limit. This is one of the major disadvantages of the pure bare tether - since it is a passive collecting device, it is dependent solely on the ambient conditions.

Chapter 5.0

Results and Discussion

We will now examine and discuss the results of the simulation program developed and the analysis of the various issues addressed in the preceding sections.

5.1 Anodic Contactor Performance

The performance of the contactor will be examined by two methods. One will be by fixing the environmental conditions (i.e. V_{ind} and n_e) and solving the circuit equation for the power generated. The other will be by dynamic simulation where all effects are taken into account. The first method will give the basic behavior of the system so that we can understand how the contactor works, while the latter method is more realistic, but more complicated, due to many factors such as temperature variations.

Figs. (21a,b) show the maximum power generated (at optimum efficiency) versus the ion current emitted (I_{iao}) and the ionization fraction (f) for fixed environmental conditions. Fig. (21a) is for desirable conditions, (i.e. high V_{ind} and n_e), and Fig. (21b) for poor conditions. As the ion current emitted increases, so does the power generated because the total current, which is the sum of the electron (I_e) and ion (I_i) currents, increases. However, the power reaches a saturation value because the total current is *limited by the system.* (This is not a space-charge limited effect, since the contactor is

always assumed to operate space-charge limited.) The reason for the limitation can be explained as follows. The circuit equation can be written as $f(I) = V_{ind}$,(the induced voltage), where the left hand side is made up of all the voltage drops. For the anode with full ionization, the voltage drop scales as $((I-I_{iao})/I_{iao}^{3/4})^8$ (the same argument applies to the case with partial ionization, but the scaling relationship is much more complicated). Thus as I_{iao} increases, the total current I also increases, but not as fast as I_{iao}, and hence $I-I_{iao}$ decreases. However, the total current can not continue to increase with increasing I_{iao} since the voltage drops of the other components are increasing (and the sum of all the voltage drops must always be V_{ind}). Hence an upper bound is set on the current where the anode drop is zero and thus the electron current collected decreases so that $I=I_e+I_i$=const. The drop in electron current is apparent in Fig. (21c) where we can see the cloud radius reaching a maximum, and then starting to decrease, and in Fig. (21d) where the voltage drop across the cloud decreases to zero as the power saturates. The same limiting behavior is observed when the ionization fraction is decreased (i.e. more neutral gas is released). For low ionization values and higher ion currents, the saturation phenomena is stronger because the cloud radius, and hence the electron current collected, decreases more sharply with increasing external ionization and higher ion currents (recall from Eqn. (46a), $r^2 \sim \exp(-a_o/\lambda_{no})$, where $\lambda_{no} \sim (I_{iao}(1/f-1))^{-1}$).

For constant ion current, decreasing the ionization fraction (i.e. increasing external ionization) increases the power because the current is increased (see Eqn. (60)). However, the most important observation of these results is a direct comparison between internal and external ionization. A contactor operating with I_{iao}=2 Amps and f=1 emits the same amount of mass as a contactor operating with I_{iao}=1 Amp and f=0.5. A glance at Figs. (21a,b) shows that the power generated is substantially higher for full internal ionization versus partial external ionization. Furthermore, increasing the amount of neutral gas released to f=0.25, and keeping I_{iao}=1 A, still does not quite reach the power level of f=1, I_{iao}=2 A. (Note that for f=0.25 and I_{iao}=1 A, the mass consumption is twice that of f=1, I_{iao}=2 A.)

This is because external ionization is not very efficient; neutral gas is wasted because not all of it is ionized. In fact, for the case I_{iao}=1 A and f=0.5, only about a quarter of the neutral gas emitted is ionized. For a contactor with conditions as in Fig. (21a), an ionization fraction of about 0.23 with I_{iao}=1 A is needed to provide the same amount of power as a contactor with I_{iao}=2 A, f=1. This means an additional 3.34 "amps" of neutral gas are required to produce one amp of ion current. Based on this model, a very important conclusion is reached: it is better to fully ionize the gas internally than to allow some to ionize externally. (It is important to note that we have neglected any considerations of the plasma "igniting". Larger amounts of neutral gas perhaps may cause a discharge and a rapid increase in ionization.) Thus for the control strategy to keep the power generated above a certain lower limit, we will just control the ion current emitted, and leave the gas fully ionized which is more efficient. In most cases, increasing the ion current from one to two amps is sufficient.

Figs. (22a,b) show the averages of the maximum power generated and the specific power from a full dynamic simulation (averaged over 16 orbits or one day). Now all variations in the geomagnetic field, the ionosphere, and temperature are taken into account. The same trends as above are present, but are damped. This is because as the current increases, the ohmic dissipation increases, heating the wire and causing further increases in ohmic losses. This is why for the case I_{iao}=2 A, with a 2 mm diameter tether, the power actually *decreases* with decreasing ionization. However, increasing the tether size to 2.5 mm decreases tether losses, and the power then can increase with f decreasing. In Fig. (22b), the specific power decreases in general with decreasing ionization fraction and increasing ion current. This is simply because, more gas is being emitted, and the system mass increases faster than increases in the power generated. The exception here, is the special case where the diameter is increased to 2.5 mm. The resulting increase in power outweighs the increase in mass consumption when the ion current is doubled.

However, the diameter of the tether can not be increased too

large, or the mass of the tether will dominate. In Figs. (23a,b), we see the existence of an optimum tether diameter (for I_{iao}=1 A). If the tether is too thin, the resistance will be too high and the power generated will be low. On the other hand, if the tether is too thick, it becomes too heavy. Thus an optimum exists, and for a tether operating at maximum power with I_{iao}=1 A, the optimum is 2 mm. Note that the power generated reaches a limit with increasing tether diameter. This limit is the power a superconducting tether would generate. Unless specifically mentioned, most of the results will be for a 2 mm tether.

The size of the contactor clouds required, as seen in Fig. (21c), can range up to 40-45 m in diameter. Recalling the discussions in Section 2.3.1, the length of the cloud along the magnetic field lines, z_o, is assumed to be much larger than the cloud radius. Thus the cloud is very large indeed. However, comparing this cloud to the clouds created by artificial releases from the shuttle which can have dimensions on the order of kilometers, these contactor clouds are not unrealistic. In the end, it remains for experiments to determine the actual behavior of plasma contactors, and whether such large clouds will be able to be created.

The results so far have been based on a particular type of gas used by the contactor - argon. However, in principle, any type of gas can be used. The main factor involved in choosing a gas is its molecular weight. The ionization energy can be considered as another factor, but for most gases, the ionization energies are comparable, (i.e. Xe=12.1 V, Ar=15.8 V). Thus a tradeoff with the molecular weight exists. As the molecular weight increases, the power increases as discussed in Section 2.3.1, but the mass expended also increases. Figs. (24a,b) show the dependency of the power generated and specific power on the molecular weight of the gas. Clearly argon yields the highest specific power, and will be used throughout all calculations. Due to the simplicity of the model for the cathode, no dependence on gas arises in the voltage-current characteristic. Thus for simplicity and commonality, we will assume use of argon for the cathode.

The last issue regarding contactor operation, was the gas emission

velocity which appeared as a parameter in the expression for the mean free path for ionization λ_{no} (Eqn. (61)). One could always assume the gas to be choked at the thermal velocity, however, λ_{no} decreases with the gas velocity and therefore for fixed ion current, the current should increase. Fig. (25) shows maximum power generated for various ionization fractions and emission velocities for fixed conditions. For fully ionized gas, the gas velocity has no effect on power since λ_{no} is theoretically close to infinite. However, for ionization fractions less than one, decreasing the gas velocity increases the power slightly as would be expected. Allowing the velocity to decrease too much, however, violates one of the assumptions of the theory: $a_o/\lambda_{no}<<1$. For example, from Fig. (25), with f=0.1, v=1 m/s yields $a_o/\lambda_{no}=2.7$ which clearly is a violation. Thus with this important constraint, the velocity was chosen to be 10 m/s. This value is rather arbitrary, but it gives maximum power while keeping within the bounds of the validity of the theory. Since we have found that it is more advantageous to operate the contactor fully ionized, the choice of the gas velocity really has no impact.

5.2 Environmental Factors

The geomagnetic field and the ionosphere are fixed by nature. The only environmental "parameters" we can vary are the solar sunspot number, (which is fixed by the sun's solar cycle), the month, (which sets the solar declination angle and affects the ionosphere and the tether temperature), and the operational altitude of the tether. The effect of orbital inclination with respect to the geomagnetic field has been already addressed. The above "parameters" can be varied to see the relative importance of their impact on tether performance.

Many different factors determine a space vehicle's orbital altitude, among them being atmospheric drag, and mission objectives. For an electrodynamic tether, we would expect the best performance where the electron density and the geomagnetic field are the greatest. Figs. (26a,b) show average maximum power and specific power versus operating altitude. As would be expected, peak power is generated at an altitude between 250-300 km where peak electron density occurs. The geomagnetic field roughly drops as $1/r^3$

thus the closer to earth, the greater the induced voltage (also the orbital velocity increases). However, the magnitude of all the magnetic field fluctuations also increases, increasing the battery mass needed to level power output. Thus the specific power optimizes at a slightly higher altitude than the maximum power due to less battery mass. It should be noted that fuel for drag makeup was not included here; the effect of adding it would be to lower the curve in general, but the left hand side would be lowered more sharply due to the low altitude. The overall effect would be to raise the optimum altitude slightly, but not appreciably. This is because the atmospheric drag increases as the altitude decreases, but the electrodynamic drag decreases also. For increasing altitude, the atmospheric drag decreases, but the electrodynamic drag increases and then starts to decrease.

The effect of variations in the time of the year and sunspot number on tether performance is less pronounced as seen in Figs. (27a,b). In general, as the solar activity increases, the electron density increases, and hence the power output of the tether increases and then begins to saturate as we have seen before. (Since we have not included the dependency of solar heating with sunspot number, this trend might be damped somewhat.) The effect of the time of year is more subtle. During March and September, the vernal and autumnal equinoxes, the solar declination angle is zero, which means tether heating (in an equatorial orbit) is a minimum. Thus the tether resistance is low and power is high. Conversely, during June and December, the summer and winter solstices, tether heating is increased, as is the resistance, and hence the power is lowered. In addition, the ionosphere is affected by the time of year, and these effects are also present. Overall, these effects are quite moderate and do not pose any form of restriction whatsoever. If not otherwise stated, the month chosen for all calculations was April, with an average sunspot number of sixty.

5.3 Comparison of Anodic Devices (Contactor, Bare Tether, and Bare Tether+Contactor) for Power Generation

5.3.1 Uncontrolled Operation

The purpose of this section is to compare and contrast the performance of tether systems generating power using either a contactor, a bare tether, or both for electron collection. Maximum power generated, specific powers, efficiencies, and mass breakdowns will be shown and discussed. We will sometimes refer to a combined bare and contactor tether as a combination tether.

Fig. (28a) shows a comparison of the average maximum power generated for the various anodic systems. The contactor is shown with two different ion emission rates: 1 A and 0.1 A. Due to the lack of space experiments with actual plasma contactors, there is a large level of uncertainty as to how well a plasma contactor will actually operate. For instance, what the level of electron current collected for a given potential drop will be, is to a large extent uncertain. To take this uncertainty into account, we will simulate a contactor collecting large electron currents with relatively little voltage drop (good performance), by operating the contactor with a large ion current emission rate. Conversely, to simulate a contactor collecting small electron currents with relatively large voltage drop (poor performance), we operate the contactor with a small ion current emission rate. The poor performance mode also shows the effect of a contactor malfunction, i.e. the scenario of a valve improperly opening and only a fraction of the intended gas emission level being achieved. In contrast, the simplicity of the bare tether, and the lack of any active components, lends a definite advantage to the reliability of a bare tether. In addition, inertia limited theory describing the electron collection process is much better understood.

We can see the effect of a malfunctioning contactor is very serious. However, it is interesting to note that a reduction in the emitted ion current by a factor of ten, diminishes the power generated only by about a factor of four. From Fig. (28a), it also can be seen that the bare tether is comparable to a good contactor. However, as can be seen from the power profiles in Figs. (28f,g), a bare tether is not able to cushion the effects of fluctuations as well as a contactor cloud (the line on the graphs denotes the actual power delivered after leveling with batteries). The contactor power varies by about a factor of three, while the bare tether by about a factor of

five. A plasma cloud is more capable of contracting and expanding to adjust to electron density variations. Nevertheless, the performance of a bare collecting wire is impressive and its specific power, seen in Fig. (28b), is very comparable to a good contactor, and far better than a poor contactor. The specific powers for the various systems in Fig. (28b), follow more or less the trend of the power produced, except for the pure bare tether. Even though its power output is less than that of a combination poor contactor and bare tether, its specific power is higher. This is because the system mass is less due to the absence of an anodic contactor.

The effect of placing a contactor at the end of a bare tether can also be seen in Figs. (28a,b). The combination of a good contactor and bare tether increases the performance by an insignificant amount. However, with a poor contactor, the performance increases dramatically. With a good contactor, the current collected is large, and hence the anodic voltage drop is large also. Thus little potential is allowed to the bare tether to collect electrons. A comparison of Figs. (28m,n) shows the length of the bare tether collecting current for a pure bare tether and with the addition of a contactor (I_{iao}=1 A) (the line on the graphs denotes the average values). A pure bare tether at times, will use up to half its length for current collection, whereas with a contactor at the tip, the length fluctuates around an eighth of the total length, and at times will peak up to a third. Another important point about the bare and contactor combination, is that the system appears to handle ambient fluctuations slightly better than a pure contactor. This is because not only can the contactor's cloud adjust, but also the length of bare tether collecting can vary, so in effect, the system has two degrees of freedom. This can be seen by comparing Figs. (28f,g,h) which are the power output profiles for each system. However, the effect is very weak. Figs. (28i,j,k) also show the current profiles for the contactor, bare, and contactor and bare tethers operating at maximum power, and in comparing Figs. (28k,l), one can see the division of current collection between the contactor and the bare tether and how the contactor dominates in current collection. The current in the pure bare tether is the highest because it is the least efficient, as can be seen in Fig.

(28c). A plasma contactor gives the highest efficiency because the potential drop across the cloud is not as large as the drop across the bare tether. This can be seen in Figs. (28r,s,t) where the anodic voltage drops are shown for each system. Fig. (28u) shows the contactor cloud radius for the pure contactor. The expansion and contraction of the cloud follows the ambient electron density. For the combination system, the cloud radius of the contactor is slightly larger since more current must be collected. This is because combining a contactor and bare tether results in a reduction of efficiency (due to the bare part), and hence more electrodynamic drag. Figs. (28o,p,q) show efficiency profiles for the different systems over a one day period.

Fig. (28d) shows a comparison of mass breakdowns for the various systems. Included is the mass of the tether, power regulator, batteries, contactor(s), and an additional miscellaneous mass of 100 kg. Note that in this comparison, the mass of fuel needed for drag makeup is not included. The system mass of the poor contactor is the least simply because the mass scales with the power and the current. Beside the poor contactor, the pure bare tether has a lower system mass than the others because an anodic contactor is not needed. The other three systems are very comparable in overall system mass, with the combination of good contactor and bare tether having the highest mass. This is because this combination has the highest peak currents and power. Note that the tether mass of the systems is almost the same, due to the insignificant mass of the anodized aluminum insulation. Fig. (28e) shows the drag makeup fuel consumption per day. Since the pure contactor systems are the most efficient, they have the least fuel consumption. The combination tether with a good contactor has the highest consumption since it has the highest current. Nevertheless, the conclusions from these results show that for power generation, it will be prudent to leave the tether bare in light of uncertainties in contactor operation.

5.3.2 Controlled Operation

As we have seen, the power generated operating at maximum

power is subjected to large-scale fluctuations. Hence the battery mass required to level these fluctuations is undesirable. We will now see the effect of imposing the control strategies described in Section 4.3. The choice of the upper and lower limits is really the choice of the systems designer. One can increase the power output by imposing a lower limit and having no upper limit. Or by imposing an upper and lower limit, the power generated will be reduced to a narrower bandwidth, but the specific power will increase, since the system mass will decrease due to the decrease in fluctuations. (The system mass is always high with large fluctuations, due to large battery mass for power leveling and the regulator mass that must handle the peak power loads.) The effect of these limits will, of course, depend on the actual tether system, for example, the size of the tether and the type of anodic device. Thus there are many possibilities to designing a system. We will not consider all these possibilities, but will focus on the trends and the general behaviors of the control strategies.

In Figs. (29f,g,h), we see the power profiles of the anodic systems, this time with an upper limit of 20 kW, and a lower limit of 19.5 kW. Thus we attempt to keep the power within a 500 W band. Note that we have not included the poor contactor alone since it is not able to generate these high power levels. On the poor contactor and bare combination, we do no impose a lower limit since we assume the contactor is fixed to operate at 0.1 A. Fig. (29f) shows the power generated over one day for a pure contactor tether. The upper limit strategy works very well, limiting the power to 20 kW maximum. Except for for a number of places where the geomagnetic field and/or the electron densities are too low, the lower limit is also quite effective. It is useful to compare Figs. (28f) and (29f) to see the dramatic effect of the control strategy. Figs. (29a) and (29b) show the power delivered and the specific power for the various anodes operating under the control strategy. Note for the pure contactor, the power delivered has dropped from 22.7 to 19.3 kW, but the specific power has increased from 33.7 to 36.7 W/kg. In Fig. (29g), the power profile for a bare tether is shown. The upper limit constrains the power below 20 kW, but for a bare tether, there is no way of

imposing a lower limit as mentioned in Section 4.3. Thus the power delivered is much lower compared to the contactor tether. However, the specific power is almost the same since no anodic contactor is required. This clearly shows one of the major disadvantages of the bare tether. In contrast, the bare tether and good contactor combination has the capability of both control limits. Fig. (29h) shows their effect on the power profile of the combination tether system. A somewhat anomalous result can be seen. It appears that the lower limit strategy is slightly less effective on the combination. At some points where the ion current needs to be increased, the power from the combination tether drops about 400W below that of the contactor tether. Apparently, with the poor efficiency of the bare portion, the performance is lowered slightly. Lastly, we note that the poor contactor and bare combination performs slightly better than the bare tether, but not by a significant amount since we have fixed the ion current and did not set a lower limit. Due to the contactor, the efficiency is slightly higher (Fig. (29c)) than the pure bare tether, but the specific power is lower due to the additional contactor.

The current collected by the systems is shown in Figs. (29i,j,k). In general, the current is driven down by the control strategy which results in much higher efficiencies, as seen in Figs. (29c,n,o,p). However, we see again that the pure contactor is the most efficient. The contactor cloud radius must now fluctuate even more due to the control strategy. Fig. (29q) shows these variations. Compared to the maximum power case, the cloud must be smaller at times due to the upper limit, and at other times larger due to the lower limit. Figs. (29l,m) show the length of tether collecting for both the bare and combination tethers. Again, the bare portion of the combination tether collects less due to the contactor.

The mass breakdowns of the various systems is presented in Fig. (29d). Here we see the total mass of the systems reduced by over 100 kg. Except for the bare tether and the poor contactor combination, the need for batteries is almost eliminated due to the control strategy. Regardless of more battery mass, the bare tether still has the least mass because of one less contactor. However, with the additional battery mass, the poor contactor combination has the

largest mass. Fig. (29e) shows the fuel needed for drag makeup per day. Fuel requirements are reduced by over 20 kg, with the pure contactor still requiring the least amount due to its high efficiency. Overall, this control strategy is very effective in reducing the effect of the fluctuations of the geomagnetic field and ionosphere, and thus reduces the over-dimensioning of tether systems that would otherwise be required.

Lastly, following [29], it is useful to determine when the mass of a tether system, including drag makeup fuel, breaks even with the fuel consumption of a fuel cell producing the same amount of power. Below this break-even point, the tether system is heavier, beyond, the fuel cells are heavier. Thus the smaller the break-even point, the more efficient the tether system. Table (1) summarizes the results for both maximum power and controlled cases. Here we see that the pure contactor tether is the best in this respect with uncontrolled and controlled break-even points of 5.3 and 4.3 days respectively. The next best system is the combination with good contactor due to high power generated despite large fuel requirements. Pure bare tethers come next in performance, with the systems with a poor contactor having the longest break-even points (up to 10 days) due to their poor performance.

5.4 Tether Deflection Results

In this section we will discuss some results from the analysis of the static bending of the tether. The current level, the endmass, and not so importantly, the tether mass itself (or mass/unit length), all influence the magnitude of the tether deflection. Two important parameters will be looked at: the tip deflection, and the connection point deflection angle. For a given vehicle design, the later is perhaps more important due to the location of the tether, etc. For example, if a tether is located in the aft of the shuttle cargo bay, excessive deflection angles might lead to the tether coming into contact with the vertical stabilizer. The other undesirable effect of large deflection angles is a decrease in the induced voltage since this is the dot product of $\mathbf{v}\times\mathbf{B}$ and $d\mathbf{l}$ along the tether.

We have neglected any deflection of the tether in all the

calculations so far. However, the validity of this assumption was checked to see how the performance of the tether would be affected by deflection as long as the currents were not excessively high (i.e. >15 A). For typical power generation operation, the induced voltage decreased by 1-2% maximum. Thus this effect is negligible. In addition, since the tether is in an equatorial orbit, out of plane forces are quite small, $O(10^{-6} m/s^2)$, thus out of plane deflections are not considered.

The most important parameter of tether deflection, is the endmass. In Fig. (30a), the actual deflection profile is shown for two different endmasses, 100 and 500 kg. The current is taken to be 10 amps, and the tether is 2 mm in diameter. With a 100 kg endmass, the tip deflection is slightly less than 4 km. Fig. (30b) shows the variation of the tip deflection versus the endmass for the same case, and Fig. (30c) depicts the dependence of the base deflection angle again with the endmass. As we would expect increasing the endmass decreases the tether deflection. For a fixed endmass, Figs. (30d,e) show tether tip deflection and base deflection angle for various currents. The dependences on current are linear since the electrodynamic force is linear with current. However, for very large currents, large deflections occur and nonlinear effects would have to be included.

For a bare tether generating power, even though the current is non-uniform at the tip, the current levels are on the same level as the contactor tethers (although slightly higher due to higher inefficiencies). However, for a completely bare tether thruster, as we will see, the currents can be considerably higher. Nevertheless, the deflections are not excessive. This is because most of the electrodynamic force acts at the base of the tether. As discussed earlier, these currents can be reduced by partly insulating the tether. Fig. (30f) shows endtip deflection and base deflection angle for a bare tether with varying insulation. Note that maximum deflections are reached when the tether is completely insulated, and hence a constant force acts along the entire length of the tether. As a further example, despite the very large current of 150 A shown in Fig. (5b), for an endmass of 300 kg, the tip deflection is 3.4 km, and the base

angle is about 38°, neither of which are excessively large.

The endmass required will depend greatly on the application, i.e. deflection limitations and current levels. For our purposes in this study, we conclude that a 100 kg endmass is sufficient. A tether with a contactor is immediately at an advantage since part of the endmass is the mass of the contactor with its gas supply. Hence only part of the 100 kg miscellaneous mass for the system need be used for this purpose. However, with the pure bare tether, the endmass will be effectively useless mass.

5.5 Tether Temperature and Superconducting Tether Results

Incorporating all the external heat flux components discussed in Section 2.5.5 yields Fig. (31a) which is a typical heat flux time history for a 2 mm diameter tether over four orbits, or a quarter of a day (for a declination angle of 0°). The heat flux of course will change seasonally, as can be seen in Fig. (31b) (for a declination angle of 23.5°) - the implications of which we have already seen. Knowing the heat flux, the tether temperature can be calculated as shown in Fig. (31c). Here, heating due to tether ohmic losses is not included. Thus, this is the temperature a superconducting tether would have (if it were 2mm in diameter). Fig. (31d), shows tether temperature including the ohmic heating for a 2 mm diameter tether. Due to the large currents during maximum power operation, ohmic losses appreciably heat the tether. When the current is controlled by the control strategy, the temperature is noticeably lower as seen in Fig. (31e) for a contactor tether with an upper/lower limit of 20/19.5 kW. The need for computing the tether temperature to find its impact on mainly the tether resistance and less importantly, the length variations, is shown in Figs. (31f,g). Here we see the tether resistance variations over one day for a controlled contactor tether, and the tether length variations for an uncontrolled contactor tether. The resistance can range up to over 200 ohms when the power is not controlled for a 2 mm tether.

For a superconducting tether that is actively cooled, a cooling jacket surrounding the tether increases the area exposed to the

external heat fluxes thus increasing the total heat energy absorbed (but also the heat radiated away). Fig. (32a) shows the total heat absorbed versus the diameter of the tether. (Recall, solar heating is proportional to the area projected to the sun, while albedo heating is proportional to the total surface area.) This heat that is absorbed, must be transported away by the cryogenic cooling fluid. Figs. (32b,c,d) show the results of the analysis of Section 2.5.6, namely the pressure drop across the length of the tether, the coolant pump power, and the daily coolant mass flow rate as functions of the mean flow velocity. The tether wire itself is taken to be 2 mm in diameter, and dR is the distance between the tether and the interior of the cooling jacket. The cooling jacket is taken to be 1 mm thick. Due to the extremely small area the coolant must pass through, (after all, the tether must be wound on a reel in some fashion), the pressure drop is prohibitively high. (Compare these pressures to the Shuttle's main engine liquid hydrogen turbopump which has a discharge pressure of 48.5 MPa!) At such high pressures, the structural integrity of the cooling jacket can be severely called into question. The hoop stress on a tube of radius r and thickness t is pR/t where p is the internal pressure. For a 5 mm radius tube of thickness 1 mm, the stress at a flow velocity of 2 m/s is 325 MPa. The yield point of a very high-tensile strength aluminum alloy is around 248 MPa, thus this material would fail. Increases in thickness would be accompanied with unwanted increases in mass. In addition, the power of the coolant pump required (even for a very good efficiency of 0.5) is too costly. Lastly, the daily coolant mass flow rates are unrealistically high (5,000-10,000 kg/day).

The above values have been for low coolant flow velocities. At such low velocities, the convective heat transfer is very small, and the temperature drop across the tether is very high, such that the results are not physical (i.e. the analysis is not valid since the N_2 would have evaporated in the first few hundred meters of the coolant tube.) Neglecting the unachievable high flow rates, we can see what velocities would be necessary to keep the temperature drop reasonable. For design purposes, the system must be capable of cooling during the highest heat flux. Fig. (32e) shows the results of

applying Eqn. (107) to a tether in a cooling jacket of radius 5 mm. The high flow velocities are completely unattainable. In the likely event that the coolant vaporizes before reaching the end, the heat transfer rate would increase at first due to the phase transformation, but then would decrease. Since the coolant is now a gas, the pressure drop would decrease (and the pumping power also), but only by roughly an order of magnitude[15]. For all practical purposes, we can conclude that convective cooling a 20 km long superconducting tether is an impossibility. Needless to say, the performance of a superconducting tether is highly desirable, as can be seen in Figs. (32f,g). The high powers generated are impressive. In addition, the absence of tether losses reduces the saturation effect discussed in Section 5.1. One can consider other avenues of approach to cooling that are beyond the scope of this thesis. Future work could perhaps investigate electro-thermal means of heat transfer, such as use of the Peltier effect.

5.6 Orbital Mechanics Effects

In this section, we will present some of the particulars of the orbital motions of tethers. The dominant force on the tether system is of course the electrodynamic force which will raise or lower the orbit, hence changing the semimajor axis. In addition, alternately thrusting and generating power will cause the eccentricity of the orbit to change. The effect of the earth's oblateness is well known: it causes the regression of the nodes, and the precession of the argument of perigee. These have little influence on the tether for equatorial orbits. However for higher inclinations, these effects cause the groundtrack of the orbit to sweep over a larger area, hence subjecting the tether to more variations in the geomagnetic field.

Fig. (33a) shows the variations in the electrodynamic drag of a 2 mm tether generating maximum power with I_{iao}=1 amp. Typical thrust profiles will be shown in the next section. The electrodynamic drag force causes a reduction in the semimajor axis as shown in Fig. (33b). For this case, the decrease amounts to about 7.5 km/day. For a thruster (at constant 20 kW power), Fig. (33c) shows an increase in the semimajor axis of about 3 km/day. Variations in the other

orbital elements are shown in Figs. (33d-h) over one day periods. In Fig. (33d), we see the regression of the nodes, about 8.5°/day, and in Fig. (33e), precession of the argument of perigee, about 16°/day. These effects still occur for a 1° orbit, but are unimportant. For pure power generation, there is no mean change in the eccentricity as seen in Fig. (33f); the same is true for thrusting. However, for mixed mode operation, the eccentricity increases as seen in Fig. (33g). In this mode, the tether produces power and thrust in such a way that the energy of the orbit (or the semimajor axis) is more or less constant. Despite the fact that the semimajor axis remains constant, increases in the eccentricity will cause the perigee (r_p) of the orbit to decrease, since $dr_p/dt = -ade/dt$. Thus for a 300 km orbit, if the eccentricity grows at 0.0004/day, the perigee will be lowered at the rate of 2.7 km/day. It was for this reason, Prall[33] found this mode of operation not desirable for long duration missions. Lastly, Fig. (33h) shows variations in the inclination for a generating tether, whose mean change is zero. The same result is found for the other modes of operation.

5.7 Thrusting Mode of Operation

5.7.1 Contactor Thruster

In this section, we will show and discuss results of a tether in the thrusting mode of operation. Rivas[34], compared thrusting strategies, although in a slightly different context, and examined thrusting with constant current, constant supply voltage, constant power, and constant thrust. We will do the same, but in more detail. In addition, results for a bare tether thruster are shown, and another strategy is developed to control large undesirable fluctuations in the thrust.

One way to thrust with a tether is to operate at constant current. In this way, the thrust will only vary due to variations in the magnetic field since F=ILB. Fig. (34a) shows the average thrust produced over 16 orbits versus the total tether current, I. The relationship is linear as it should be. Two important figures of merit for a thruster are its mass per unit thrust (M/F), and the power required per unit thrust (P/F). (In all these results we will use the

average values of the thrust and power required). Fig. (34b) shows the M/F versus the total current for various emitted ion currents, I_{iao}. Initially, the M/F drops with increasing I since the thrust increases more than the system mass. However, for fixed I_{iao}, as I continues to increase, M/F starts to rise sharply. This is because when the electron density drops substantially during the orbit, the contactor cloud must expand to very large dimensions to collect the required current. Hence very large contactor potential drops are necessary, which implies a large power supply. Since the power supply required becomes large, the mass of the regulator increases, and M/F rises substantially. The steep increase in the power required is seen in Fig. (34c) which shows P/F versus current. In addition, the efficiency of the system drops as depicted in Fig. (34d). This problem can be easily rectified by increasing the ion current. This decreases the contactor potential drop (recall $\phi_c \sim ((I-I_{iao})/I_{iao}^{3/4})^8$), and thus reduces the M/F and P/F, and increases the efficiency as can be seen. A given ion current has its range of applicability. For example in Fig. (34b), for I=4 A or below, it is best to operate with I_{iao}=1 A. For 4<I<7 it is best to operate with I_{iao}=2 A, and so on. For small I, operating with high I_{iao} is not beneficial since the M/F actually increases due to excessive unnecessary contactor gas consumption. In general, P/F will always increase with I and the efficiency will decrease. This is simply because as the current increases the voltage drops (losses) of the various components increase and hence the efficiency will drop and the power required will increase. (Recall the anodic contactor acts like a diode; the potential is small for small currents, and rapidly increases for larger currents.) Figs. (34e-g) show time profiles of the supply voltage required, the supply power, and the thrust produced for a const I=4 A system. The large fluctuations follow the induced voltage, since the power supply must reverse the induced voltage by a certain amount to always keep the same current. The resulting thrust varies by almost 1 N.

Another method of thrusting is to fix the voltage supply (V_{sup}). With constant voltage thrusting, the current will fluctuate substantially since I is driven by V_{sup}-V_{ind} where V_{ind}, the induced

voltage, undergoes large variations. When V_{ind} is low, the current is high, and vice versa. In fact, if V_{sup} is not sufficiently large, there will occur periods where $V_{ind}>V_{sup}$ and the thruster will effectively be turned off. This is why in Fig. (35a) we show the average thrust while thrusting, and the overall average thrust. For low V_{sup}, these two values are quite different since the thruster must be shut off often and the overall average thrust is low. In an equatorial 300 km orbit, the maximum induced voltage is about 5300 V, thus for V_{sup} around 5400-5500 V and above, the thruster will work continuously. Fig. (35b) shows the M/F, based on both the overall average thrust and the average thrust while thrusting, versus the supply voltage. As V_{sup} increases, M/F decreases since the thrust increases more than the mass. However M/F levels off and will eventually increase due to large losses and the accompanying large power supply (and mass) requirements. Note the excessively high M/F=1118.5 kg/N for V_{sup}=4000 V due to the low overall average thrust. The P/F and efficiency are shown in Figs. (35c,d). Again increases in current (or V_{sup}) drive the efficiency down and P/F up. In the constant voltage figures, we have only shown one point with I_{iao}=2 A, the rest are for 1 A. The reason can easily be seen in Fig. (35c). Since the current is not being held constant, increasing the ion current increases the total current which increases the power supply. In fact, the increase in power results in P/F almost doubling. Thus a thruster with V_{sup}=6000 V, and I_{iao}=2 A would require on the average, at least a 109 kW power supply. Additionally, there are problems operating at higher ion currents for lower V_{sup} since at times $I=I_e+I_{iao}$ is very low and I_e can not be negative. Figs. (35e-g) show time profiles for the supply power, the current, and the thrust for a constant V_{sup}=5000 V system. As can be seen, this mode of thrusting is quite undesirable due to large variations. In addition, dynamic tether forcing problems might exist with such large scale current fluctuations. Note how the thrust ranges from 0 to 5 N.

Another possibility for thrusting is with constant supply power. The current and supply voltage are regulated such that their product is always constant. Intuitively, this appears to be a good method since the large scale fluctuations in the power are eliminated. Fig.

(36a) shows the average thrust produced versus the supply power. For high powers, increasing the ion current increases the thrust simply because for a fixed contactor potential, the current can be greater with a higher ion current. In other words, as I_{iao} increases, $\Delta\phi_{cont.}$ decreases, hence V_{sup} decreases and therefore I and F increase. The M/F versus the supply power is shown in Fig. (36b). Again, increasing power decreases M/F which levels off due to increasing system losses. Increasing I_{iao} decreases M/F for higher powers, but the effect is less pronounced. Figs. (36c,d) show the P/F and the efficiency. Again P/F increases and the efficiency decreases with P, and increasing I_{iao} decreases P/F and increases the efficiency somewhat. Time profiles of the supply voltage, current, and thrust are shown in Figs. (36e-g). Note how the thrust varies by only a little more than 0.25 N.

The last method of thrusting we will discuss is with constant thrust. With this method, the current must vary with the magnetic field since F=ILB. Shown in Fig. (37a) is the M/F versus the thrust level. This figure qualitatively looks very similar to the one for the constant current case (after all, if B were constant, the two methods are equivalent). We see again that increasing I_{iao} decreases M/F (for a given range of applicability). In Figs. (37b,c), we see the P/F and the efficiency; again both of which look very similar to the constant current case. Lastly, Figs. (37d-f) show time profiles for the supply voltage, supply power, and current for a F=2 N system. For this constant thrust level, the power supply varies between 16.3 and 17.6 kW.

From the results so far, it appears that the constant power method is best overall in terms of system mass and power requirements. For a better comparison, we will now examine a point design where we require each system to produce an average thrust of 4 N. Fig. (38) compares the system masses, and Table (2) shows the variations in the thrust produced and the power required. Clearly, the constant power system is better. With constant power, the mass is the lowest since the system does not encounter such large variations as can be seen in the power requirements of the others. The constant voltage method is the worse, with a mass over

200 kg higher. If indeed constant thrust is required, this system is only 33 kg heavier. We conclude that the best method of thrusting is with constant power.

5.7.2 The Bare Tether Thruster

As mentioned in Section 2.3.3, increasing the insulated length on a bare tether thruster is beneficial. Figs. (39a,b) show the variation in thrust, efficiency, current, and supply power with the length of bare tether for fixed ambient conditions. Leaving the entire tether bare gives the highest current (>150 A) and thrust (>25 N) , but also the highest power required (1.61 MW) and lowest efficiency (<15%). Clearly, leaving the entire tether bare is highly undesirable. It should be noted that for such large non-uniform currents (which could easily melt the tether), the ohmic dissipation will be non-uniform and hence the tether temperature. Since we will not consider operating a tether like this, these non-uniformities will not be included in the analysis. However, in principle, for longer bare lengths, the tether cross-section could be shaped to vary with the current.

Decreasing the bare length greatly increases the efficiency, but decreases the thrust. Leaving only 1 km bare, results in a thrust of about 1 N, an efficiency of 95%, and a power requirement of only 7.8 kW. However, as in the power generating role, the bare tether thruster is a victim of the large variations in the operating conditions. From dynamic simulation over one day, Figs. (39c,d) show the thrust versus the bare length for tethers 15 and 20 km in length. Here we show the average, maximum, and minimum thrust values. The thrust envelope diverges greatly with increasing bare length, ranging from 0.2 to 6.9 N for a bare length of 2.5 km. Lengthening the bare portion is not effective in increasing the thrust during low ionospheric conditions. However, during very good conditions, the thrust greatly increases. Thus, while the maximum thrust curve rapidly increases, the minimum thrust curve increases very little, and the average thrust does not increase as rapidly. Since the tether must be sized to handle peak powers and currents, the situation is not desirable, and we must attempt to control the thrust.

Our strategy will be as follows. If the thrust is above a specified limit, then ϕ_A (the voltage at the tip) will be allowed to become negative by decreasing the battery supply, thus decreasing the amount of tether collecting electrons. This decreases the current and hence the thrust. Since the equations (see Section 2.3.3) can not support $\phi_A<0$, we decrease the length of the tether in the equations. Physically, the tether is acting as if some of the bare portion has been cut off. Thus both the induced voltage and the bare portion decrease. The tether is shortened a little (by 100 m) until the thrust is below the specified level. This strategy alleviates large fluctuations by reducing peak currents which substantially increase the power (and mass) required.

Figs. (39e,f) show the effect of this strategy on the average, maximum, and minimum thrust profiles. The 20 km tether is limited at 4 N, and the 15 km tether at 3 N. The average thrust curve will approach closer to the maximum curve as the bare length increases since more of the thrust will be weighted towards the upper limit. Fig. (39g) displays the M/F (based on the average thrust) for controlled and uncontrolled tethers. The control strategy very effectively lowers M/F. In general, as the bare length increases, initially M/F decreases since the thrust increases more than the mass, but then starts to increase due to increasing system losses. However, for the controlled tethers, this increase is very small. In Fig. (39h), we see the P/F (again based on the average thrust). For the uncontrolled tether, P/F rises steeply due to the large fluctuations. With the control strategy, the increase is less severe. Lastly, in Fig. (39i), the efficiency is shown. The sharp decrease in efficiency with increasing bare length is noticeably lessened. The last observation is that in all these results, the 20 km tether is better than the 15 km tether. This is because due to the shorter length, the thrust is always less. Figs. (39j-m) present the supply power and voltage, the current, and the thrust for an uncontrolled 20 km tether with 2 km bare. Note how the power supply required fluctuates from below 5 kW to nearly 75 kW. The effect of controlling this system below 4 N is shown in Fig. (39n) where the power required is noticeably moderated.

The last aspect of bare tether thrusting systems we present here, is their overall system mass. A comparison of the system masses for the uncontrolled tethers is shown in Fig. (39o). Increasing the bare length drives the peak power and hence the regulator mass very high. In stark contrast, the system mass for the controlled tether seen in Fig. (39p), increases very little in comparison. For a 20 km tether with a bare length of 2.5 km, the uncontrolled tether is almost twice as heavy as its controlled counterpart. Table (3) shows the associated maximum and minimum power levels required for both controlled and uncontrolled cases.

To compare with the contactor tethers in Fig. (38), where the average thrust is 4 N, we operate a bare tether with 3 km bare, and impose an upper limit on the thrust of 6.25 N. The mass of this system is 911 kg, and the power supply ranges from 93.49 kW to 3.38 kW with an average of 45.28 kW. The average efficiency is 71.9 with P/F = 11.32 kW/N and M/F = 227.75 kg/N. Clearly, the power levels and mass are much higher than any of the contactor systems. While a controlled bare tether thruster offers impressive performance, a contactor tether thruster operating with constant power is the preferred choice.

To conclude this thrusting section, it is interesting to compare these results for tethers with other electric propulsion systems as was done in [30]. The P/F ratio for ion engines typically is between 20-25 kW/N, and for an MPD engine, 27-30 kW/N. Arcjets with H_2 have ratios as low as 10 kW/N. Thus on the basis of P/F, tethers offer greater performance than other electric propulsion devices with the exception of arcjets. However, arcjets consume mass (up to 5-6 g/s), while tethers do not.

5.8 Mixed Mode (Power Generation/Thrusting)

In this section, we will briefly look at the results for a tether system operating in mixed mode. The tether will generate power during the night, and during the day, it will generate sufficient thrust to maintain the semimajor axis of the orbit. We will use a system with the best performance. Hence, we choose a pure contactor tether due to its controllability, and during thrusting operations, it will

thrust with constant power. This tether system will then be compared to a solar array and batteries or FCE system.

The first system examined is a contactor tether generating power with an upper limit of 20 kW, and a lower limit of 19.5 kW. A constant power supply of 20 kW is used for thrusting, which is sufficient to maintain the orbital energy. This system produces 19.32 kW of power during the night, and the tether system mass is 512.7 kg. Adding the mass of the solar array needed for the load and thrusting during the day, 989.2 kg, brings the total system mass to 1501.9 kg for a specific power of 12.87 W/kg. In contrast, a solar cell/battery system providing 19.32 kW, has a mass of 1259.2 kg with a specific power of 15.35 W/kg. Substituting the batteries with a fuel cell/electrolyzer system increases the mass to 1523 kg with a specific power of 12.69 W/kg. Thus the solar cell/battery system has a mass advantage over the tether system, and the FCE system is comparable.

We have also examined a contactor system with an upper limit of 25 kW, and a lower limit of 24.5 kW. A constant power supply of 28 kW is needed for thrusting to maintain the orbital semimajor axis. The power delivered is 22.68 kW for a tether system mass of 603.6 kg. Adding the solar array mass of 1274.9 kg, yields a total system mass of 1878.5 kg for a specific power of 12.07 W/kg. The solar array/battery system sized for the same power level, has a mass of 1478 kg with a specific power of 15.35 W/kg, and the FCE system has a mass of 1787.7 kg with a specific power of 12.69 W/kg. Again we see that the tether system has the highest mass.

Thus we reach the same conclusion that was reached in [29], namely, tether systems for orbital storage offer no mass advantage over competing conventional power systems. However, due to the control strategy developed, the difference between the systems is not as great as observed in [29]. Due to the inability of controlling the large scale power fluctuations, the difference between a tether system and a solar array/battery system was over 2600 kg for a 50 kW power level.

5.9 Radiation Impedance Effects

Using the various models discussed in Section 2.6, we show the radiation impedance encountered by a tether over one day. Figs. (40a-c) show the radiation impedance versus time for end connector sizes of 6, 1, and 0.5 m in diameter respectively. The large peaks in the impedance occur when the electron density drops to low values during the night. For the 6 m diameter case, the impedance fluctuates between 0.5 and 7.4 ohms, while for the 1 m case, variations are between 5 and 60 ohms. Variations between 15 and 160 ohms are seen for the 0.5 m end contactor case. The effect on system performance is seen in Fig. (40d). Degradation of system performance is only important for very small end connectors. In light of the findings of [37], we can see the effect of large radiation impedances by artificially fixing the impedance at large values. Fig. (40e) shows the power delivered and the specific power for fixed impedance values of 100, 200, and 300 ohms. At these high values the performance of the tether is significantly reduced. These results indicate that indeed, if the radiation impedance is large, it is a critical factor in tether performance.

5.10 Hollow, Multiple Tethers, and Variation of Length

In this section we will discuss some of the results of physical variations of the tether, including hollowing both bare and contactor tethers, using multiple tethers, and length variations.

For a bare tether generator, the effect of hollowing the tether is shown in Figs. (41a,b). As we would expect, increasing the tether diameter, increases the current collected. In principle, doubling the diameter would double the current, since the collecting surface area scales with the diameter. We see that the increase in power is more or less linear, however, due to system saturation effects, the increase is very small, and the power begins to reach a limit. Since the cross-sectional area is kept constant, the tether resistance and mass are constant also. Thus the specific power increases directly with the power. From these results, it is beneficial to increase the diameter of the tether. Of course, constraints such as tether handling and volume will impose limitations on the tether diameter.

These same trends apply to a bare tether thruster, although they

are quite weak. Increasing the tether diameter from 2 mm to 3 mm results in a decrease in the mass/thrust by about 1 kg/N. In principle for both power generation and thrusting, only the upper portion of the tether needs to be hollowed, but then, the equations for the bare tether become much more complicated for a non-uniform cross-section, thus we have left the whole tether hollow. We can conclude that hollowing a bare tether in such a way that its cross-sectional area is constant, is beneficial in both power generating and thrusting modes.

For a hollow contactor tether, Figs. (42a,b) show the results of power generated, and specific power for a tether of constant 2 mm diameter. As would be expected, hollowing a tether increases the resistance, but decreases the mass. Thus the maximum power generated will always decrease, but the specific power will remain more or less constant, except for a large hollow, because the mass of the tether and the resistance change by the same proportion. For a large hollow, the resistance is very high, therefore heating effects cause the power generated to drop more steeply, and thus the specific power curve drops. We conclude from these results that hollowing a tether for use with a contactor is not beneficial.

As mentioned earlier, the use of multiple tethers not only increases reliability, but also will decrease effective tether resistance since they are in parallel. Figs. (43a,b) show the results of power generated and the specific power for multiple tether systems operated with one contactor. In addition, the tether size is varied. Indeed, the power generated increases with the number of tethers as we would expect. For a given tether size, the specific power displays an optimum. This is because, for a small number of tethers, the resistance is high, whereas for a large number of tethers, the mass is excessive. Analogous to our finding an optimum tether diameter, there exists an optimum number of tethers for a given tether diameter.

Since the induced voltage across a tether is linear with the length, one would expect the power delivered to be more or less linear with length. Fig. (44a) shows this relationship, and Fig. (44b) shows the variation of the specific power. The tether mass also increases

linearly with length, but the other system components, which scale with the current and power, do not. Therefore the variation of specific power with tether length is not linear. When designing a system, the length of the tether will of course be determined by other factors as well. Concerns were voiced in [29,34] regarding the high operating voltages associated with very long tethers. This is an area that requires more examination.

Chapter 6.0

Conclusions

In this thesis, a detailed simulation program has been developed to investigate the performance of electrodynamic tethers both as power generators and thrusters. Based upon the Gerver et al model, a theory of partially ionized gas emissions from a plasma contactor has been worked out, and its impact on system performance examined. It is found that it is more effective to completely ionize the gas internally, than it is to partially ionize it externally and that based on the specific power, the optimum gas to use is argon. The electron collection performance of a recently developed scheme, the bare wire tether, has been compared and contrasted with a plasma contactor. The power (and thrust) generated by a bare wire tether is found to have a higher dependence on the geomagnetic and ionospheric fluctuations than the contactor tether. To control large-scale fluctuations in the power generated, a control strategy has been developed and found to be quite effective for both kinds of tethers. However, since the bare wire tether is a passive collecting device, the control strategy is not as effective as it is for the contactor tether. In addition, a control strategy was used on the bare tether thruster to successfully moderate large fluctuations in the thrust. The main merit of the bare tether is the absence of the mass and complexity of an active collecting contactor. The combination of a contactor and bare tether has also been examined for power generation. If the

contactor is not functioning well (or emission rates are low), the bare tether substantially increases current collection, otherwise, little gains are achieved. Overall, current collection by a bare tether is less efficient than by a contactor since the contactor's cloud can expand to large distances with little voltage drop. However, in light of uncertainties in contactor performance, it perhaps would be prudent to leave the tether bare, at least for initial experiments.

As a pure thruster, the contactor tether was examined thrusting with constant current, voltage, thrust, and power. It was found that the best mode of operation was with constant power, with resulting power/mass ratios better than those for ion or MPD engines. In addition, a contactor tether operating in mixed mode was examined and compared to conventional solar array/battery and fuel cell systems. As found in an earlier system study[29], the tether system has no mass advantage over the conventional systems. However, the margin is much smaller than previously found due to the control strategy used, and the over-dimensioning of the system required to handle large-scale fluctuations is greatly reduced. Equatorial orbits also reduce fluctuations substantially compared to higher inclinations. In this respect, tethers offer greater potential than previously envisioned.

With the radiation impedance theory used, it was found that only for small end connectors (<0.5 m) is the tether system performance appreciably degraded. However, in light of the findings of Urrutia and Stenzel, if the radiation impedance is indeed large, the impact on tether performance is substantial. This is an area for more future research. Future research could also explore other alternative methods of cooling a superconducting tether, since it was shown that forced convective cooling was impractical due to large pump and mass flow rate requirements. In addition, to make the simulation program developed more complete, tether dynamics could possibly be included.

Lastly, it must be emphasized that the results pertaining to contactors are based on a particular model. More work has yet to be done to provide a fuller understanding of all the detailed phenomena in contactor operation, but in the end, actual in-space experiments

are imperative to determine the performance of not only contactors, but tether systems in general.

Fig. 1a Schematic of Tether in LEO.

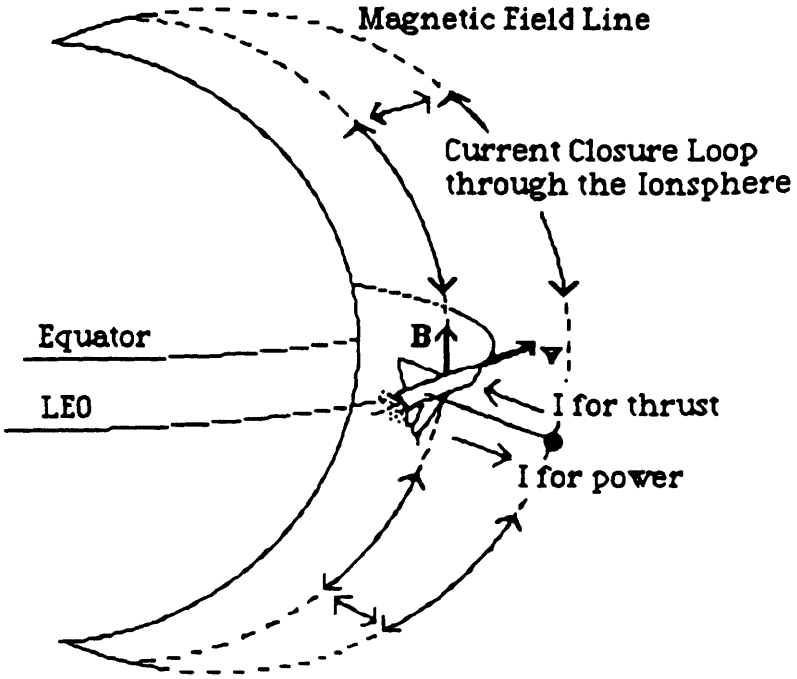

Fig. 1b Modes of Electrodynamic Tethers

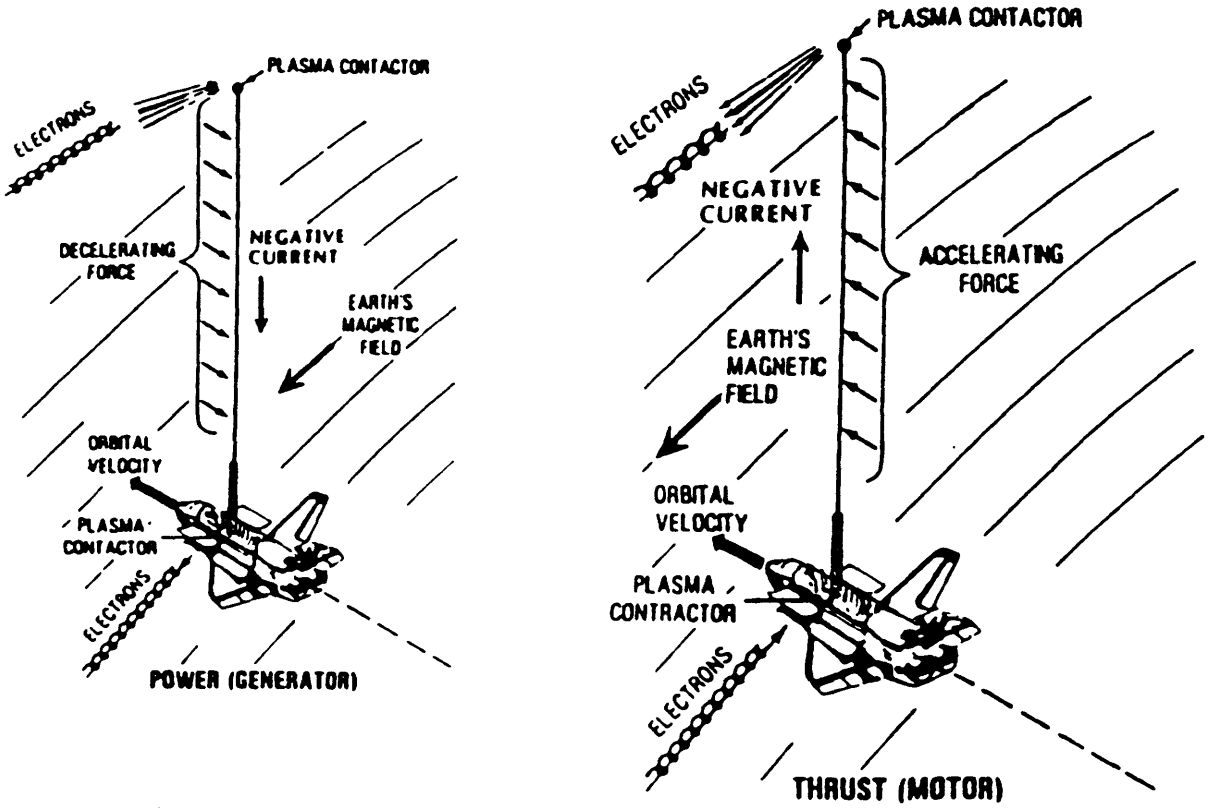

Fig. 2a Diagram of Tether as Generator, Deployed Upwards. (From [29])

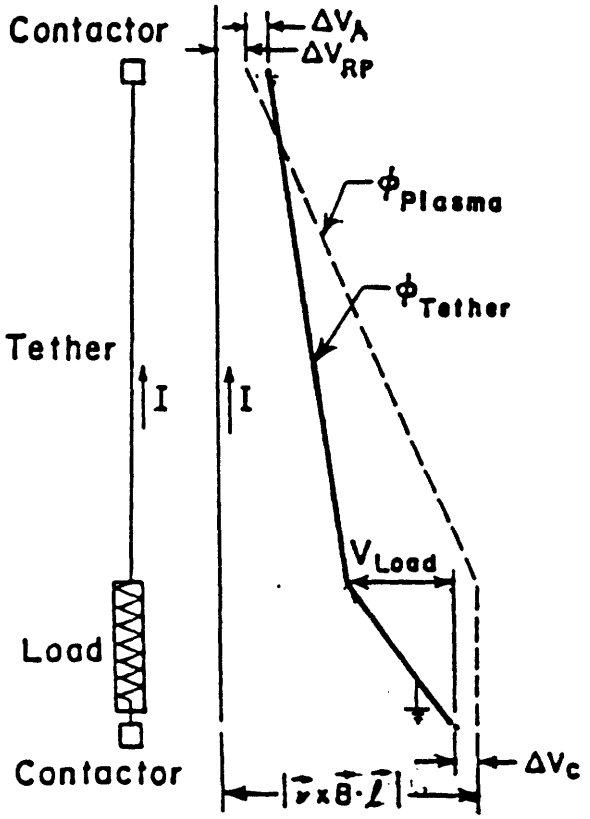

Fig. 2b Diagram of Tether as Thruster, Deployed Upwards. (From [29])

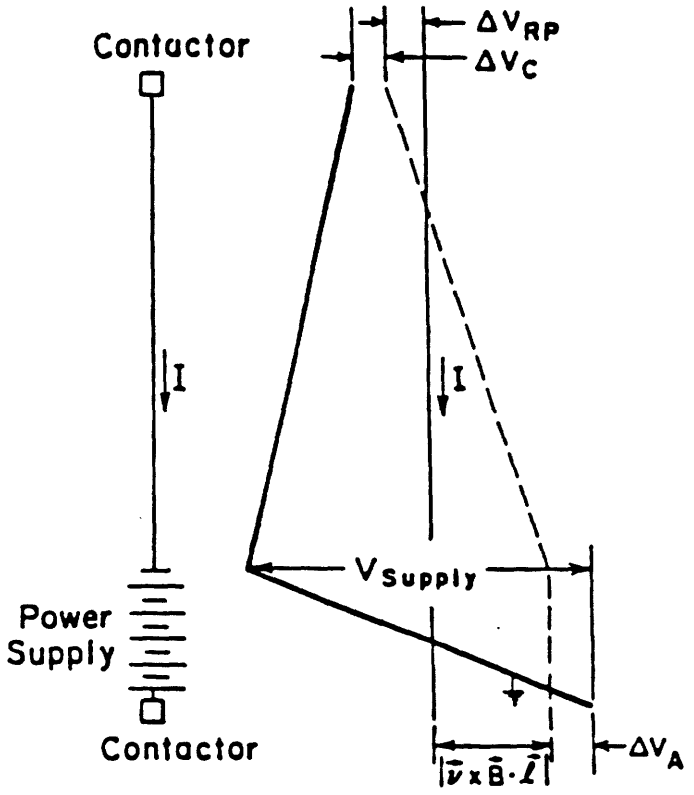

Fig. 3 Gerver et al Anisotropic Contactor Cloud

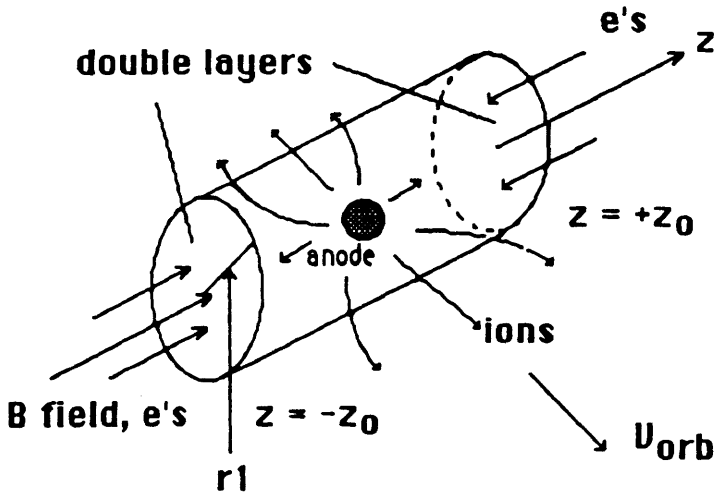

Fig. 4 Bare Tether Circuit Schematics

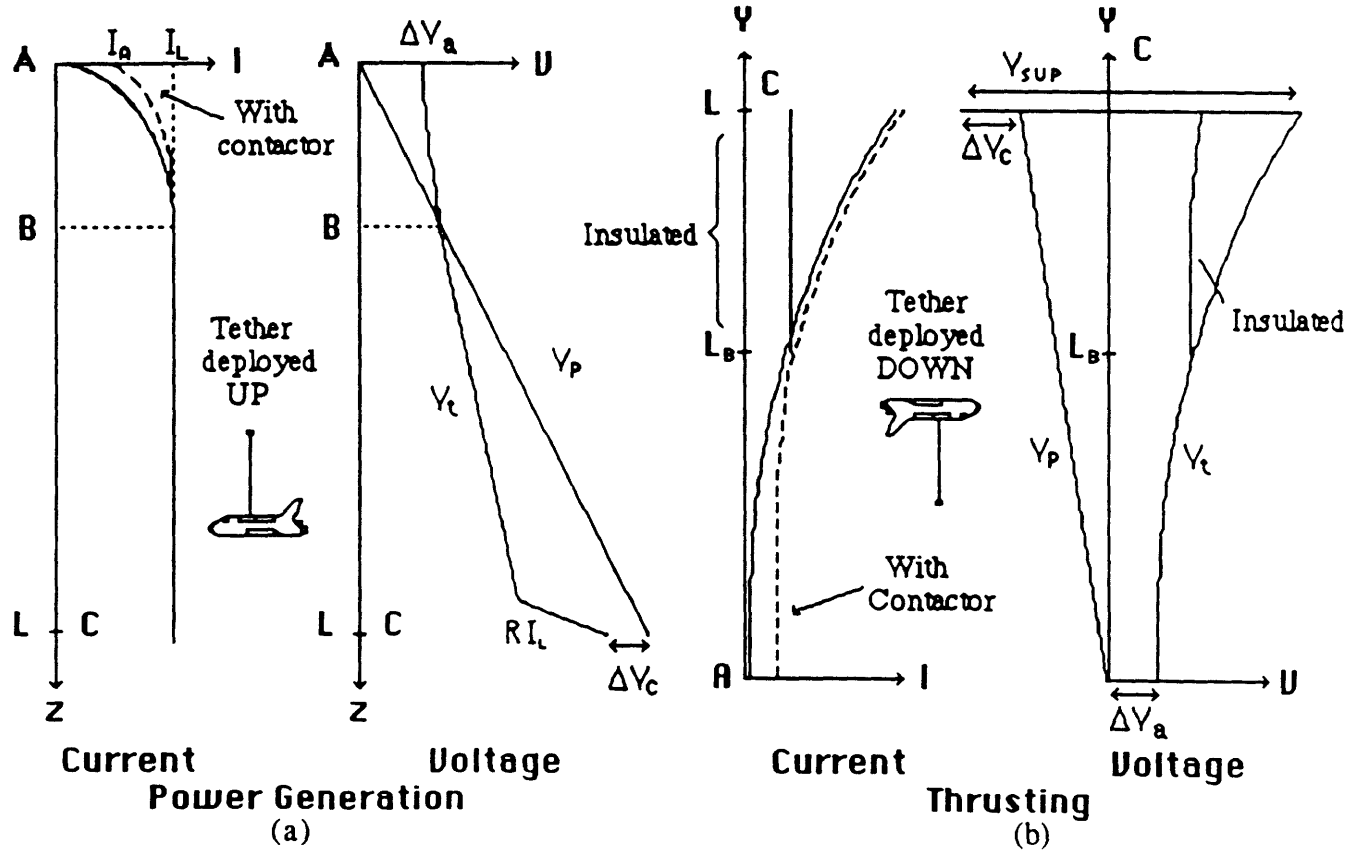

Fig. 5a Thrust and Efficiency vs. Bare Anode Voltage (ne=5e11, Vind=4000, L=20km, Lb=2km)

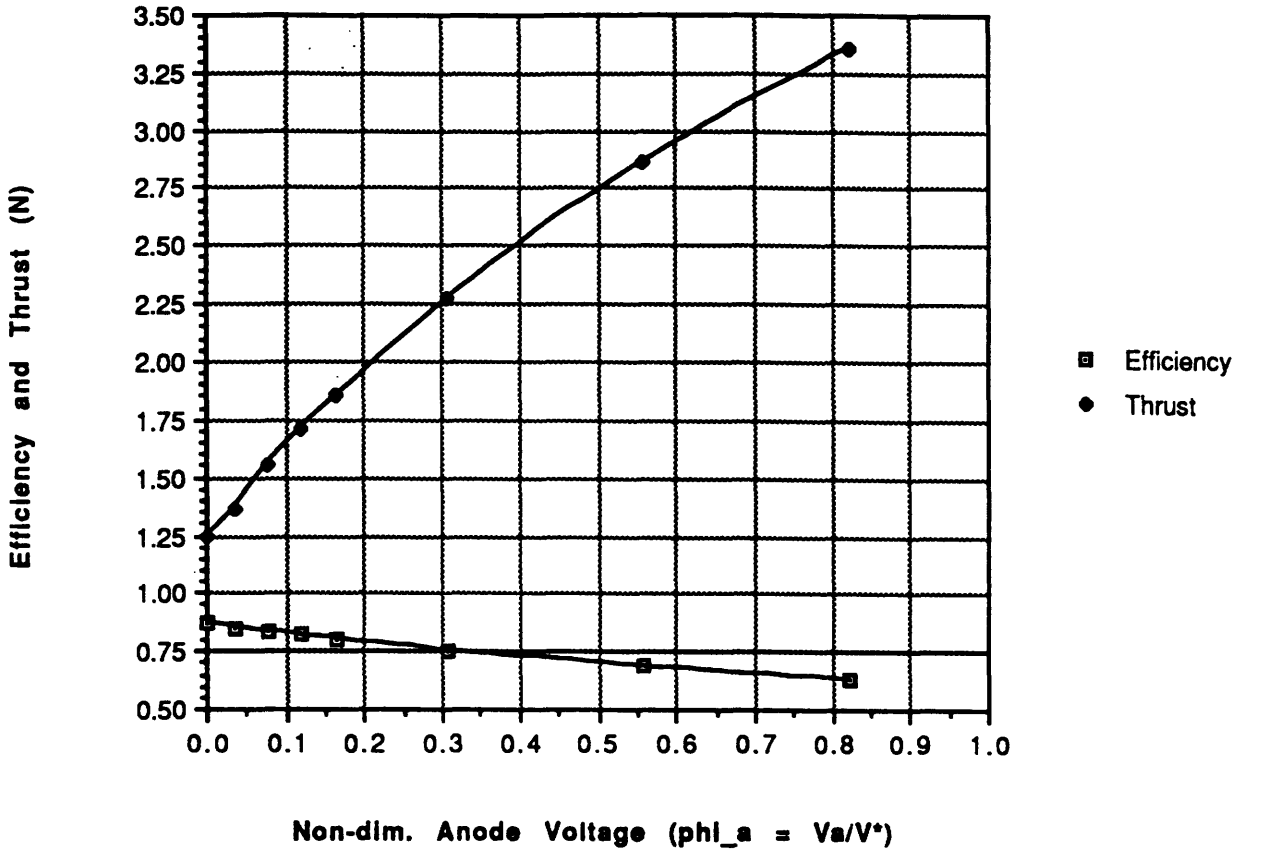

Fig. 5b Current Profile in Bare Tether Thruster

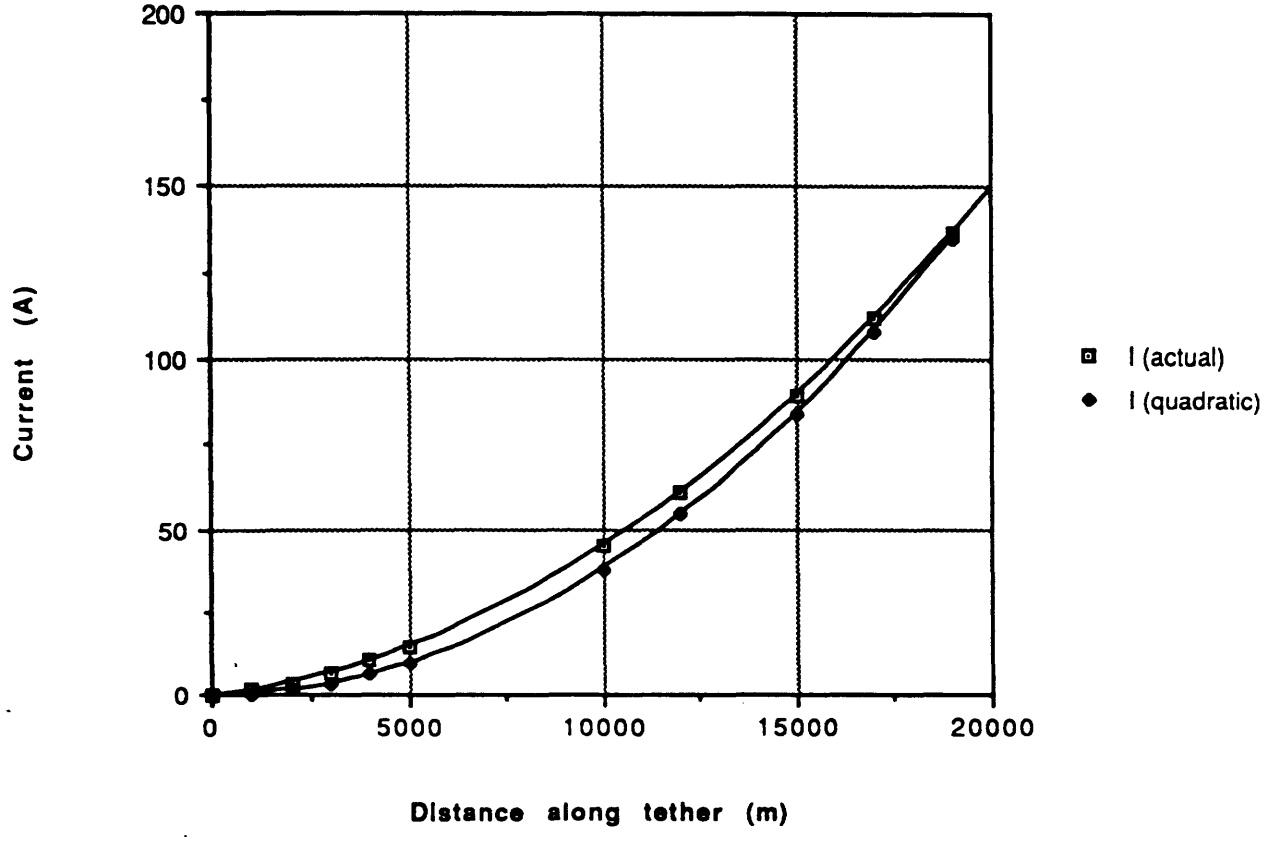

Fig. 6 Cathode Current-Voltage Diagram

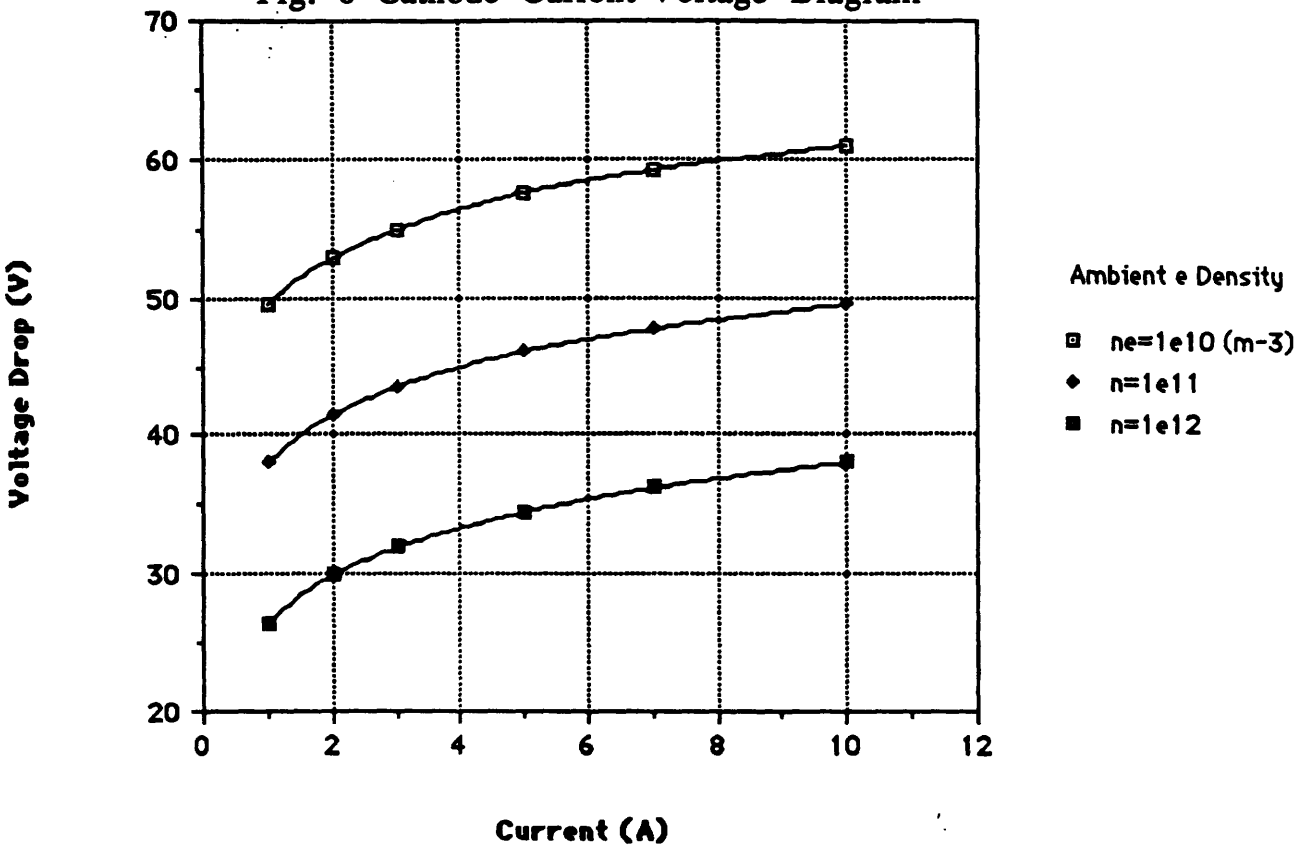

Fig. 7 Tether Deflection Diagram

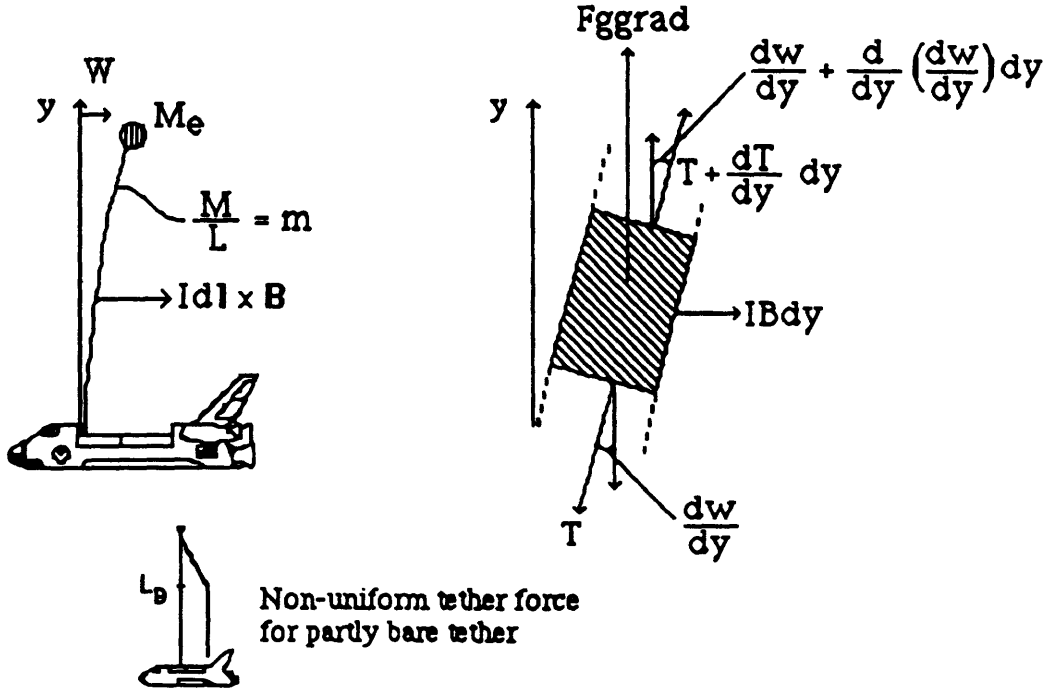

Fig. 8 Evolution of Superconducting Temperatures (From [36])

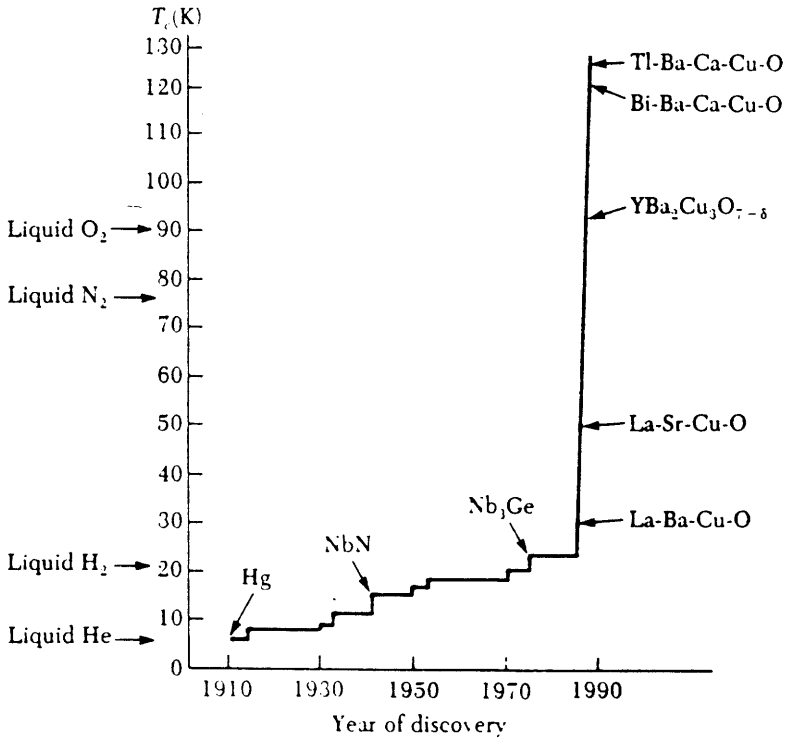

Fig. 9 Superconducting Tether Heat Balance

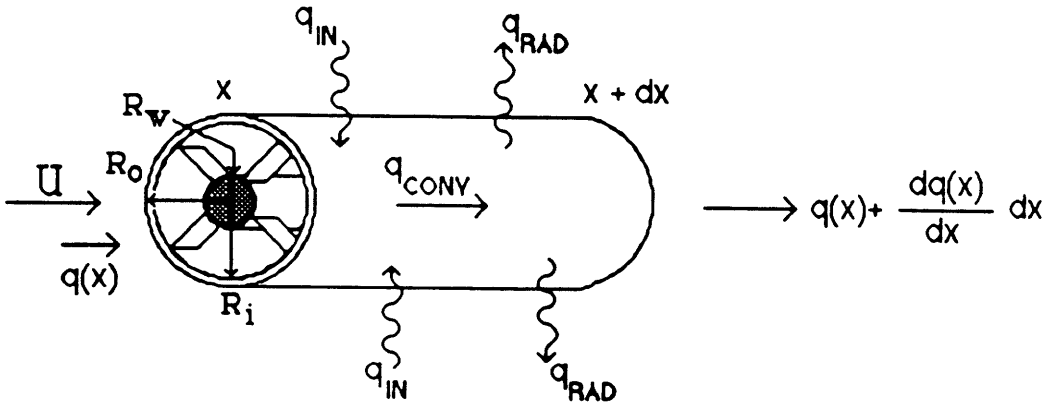

Fig. 10
Radiation Impedance for D=20 m End Connector

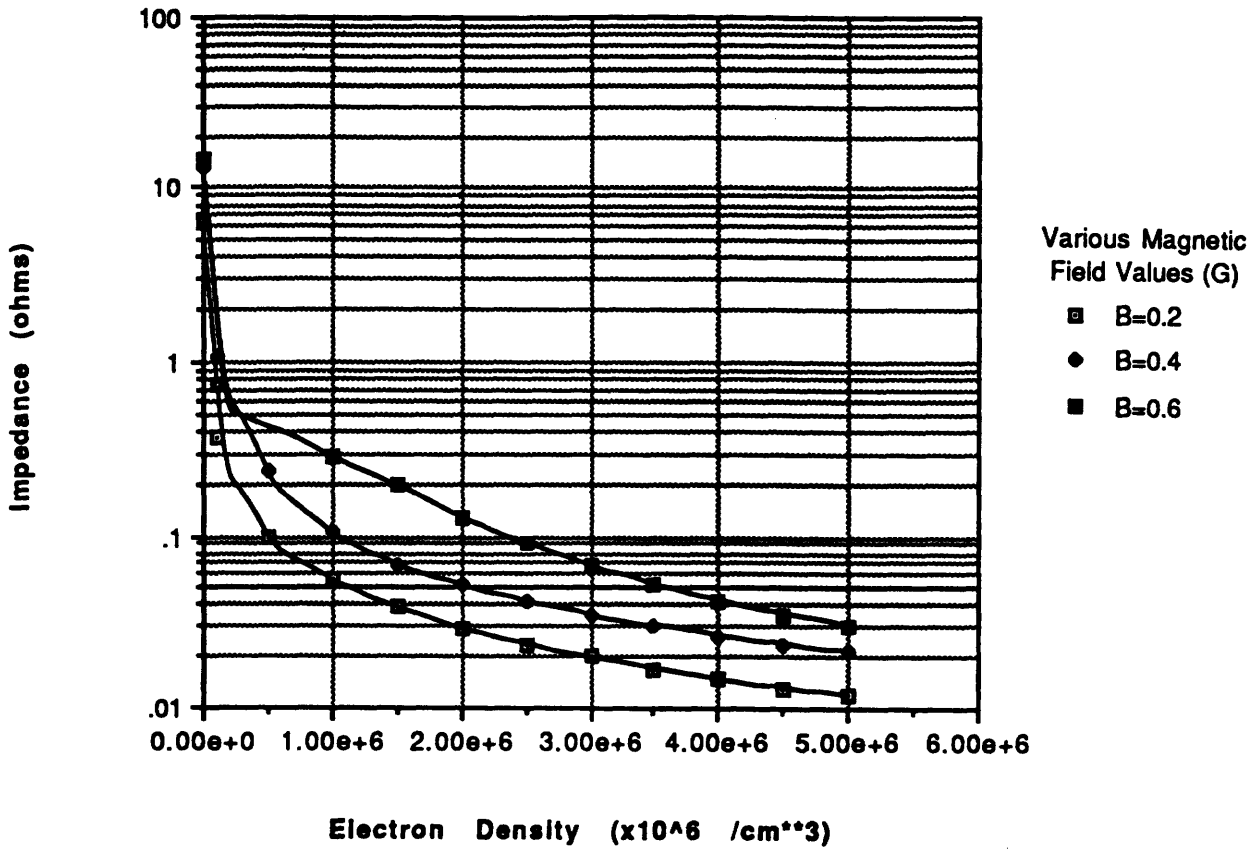

Fig. 11
Radiation Impedance for Various End Connectors (B=0.4G)

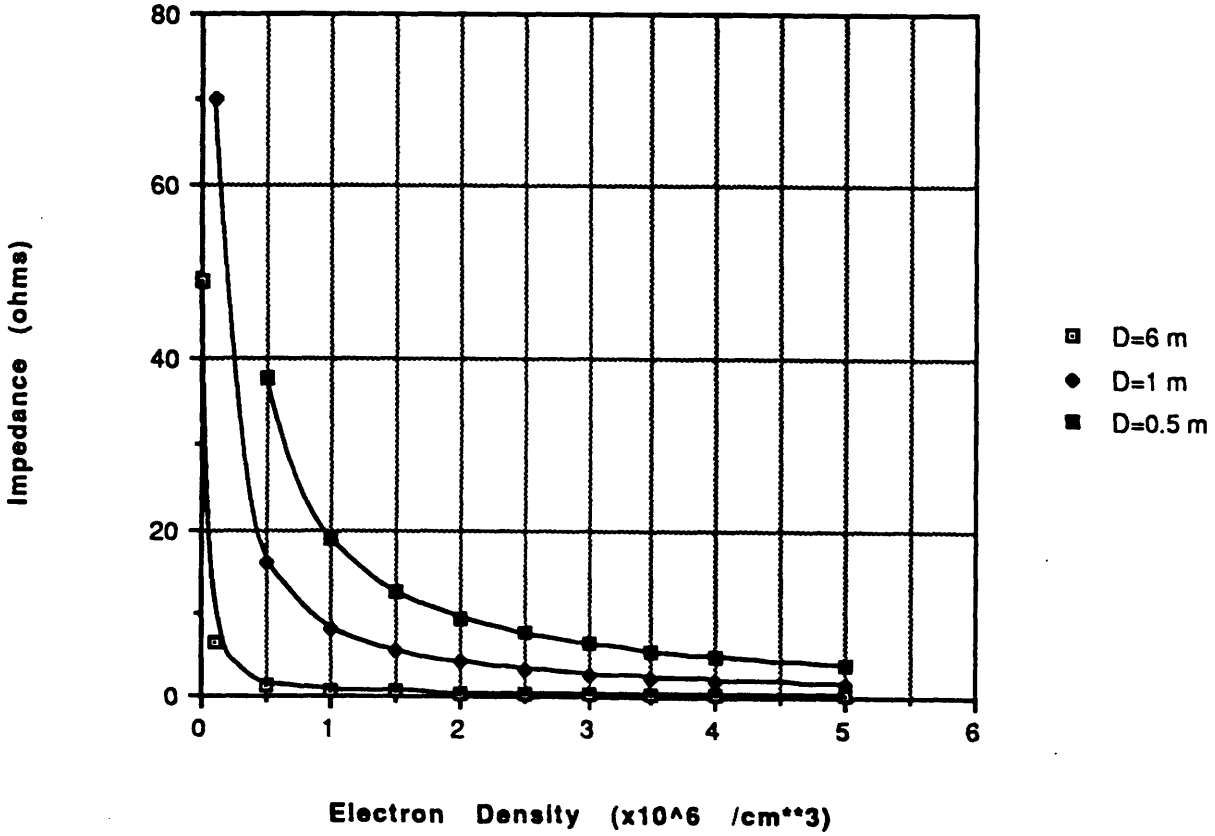

Fig. 12 SAFE Weight Summary (From [28])

Components	Weight (lb)
Experiment Total	940.0
Support Structure & Separation System	270.0
Separable Wing Assembly	670.0
Blanket	303.0
Panels	280.5
Harness	18.5
Tension Bars	4.0
Container	90.5
Base Hardware	43.5
Tension System	18.5
Latch System	16.0
Support Struts	9.0
Cover	27.0
Tip Hardware	32.0
Latch System	22.0
Tip Fitting	10.0
Mast	122.0
Boom	45.0
Canister	49.0
Drive	25.0
Lock	3.0
Jettison Capability	34.0
Grapple	21.0
Grapple Fitting	7.0
Rear Support	6.0
Wires & Connectors	7.0
Misc. Fasteners & Adhesives	11.0

Fig. 13a Induced Voltage, 28.5° Orbit

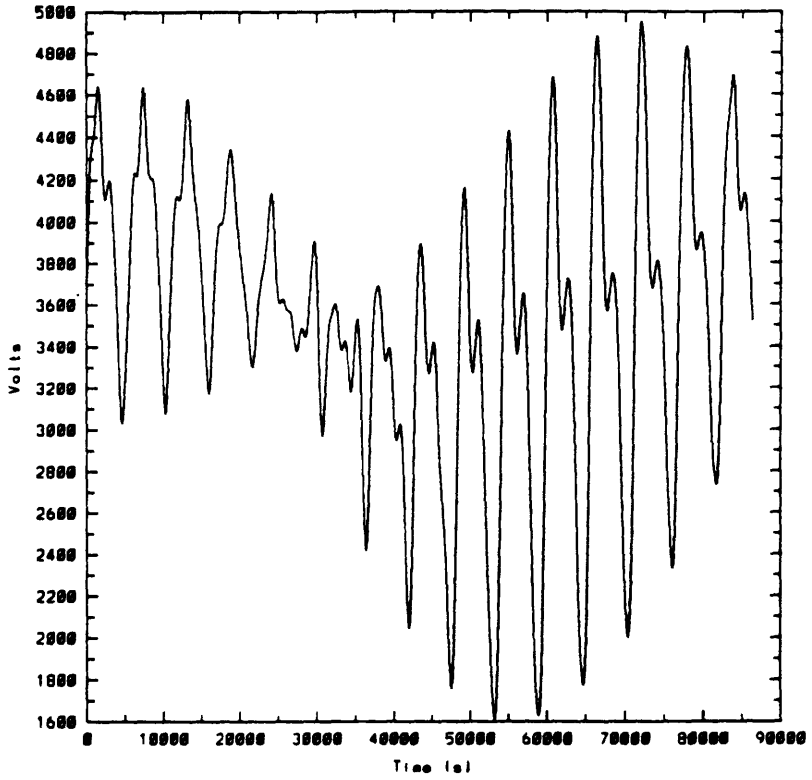

Fig. 13b Maximum Contactor Power, 28.5° Orbit

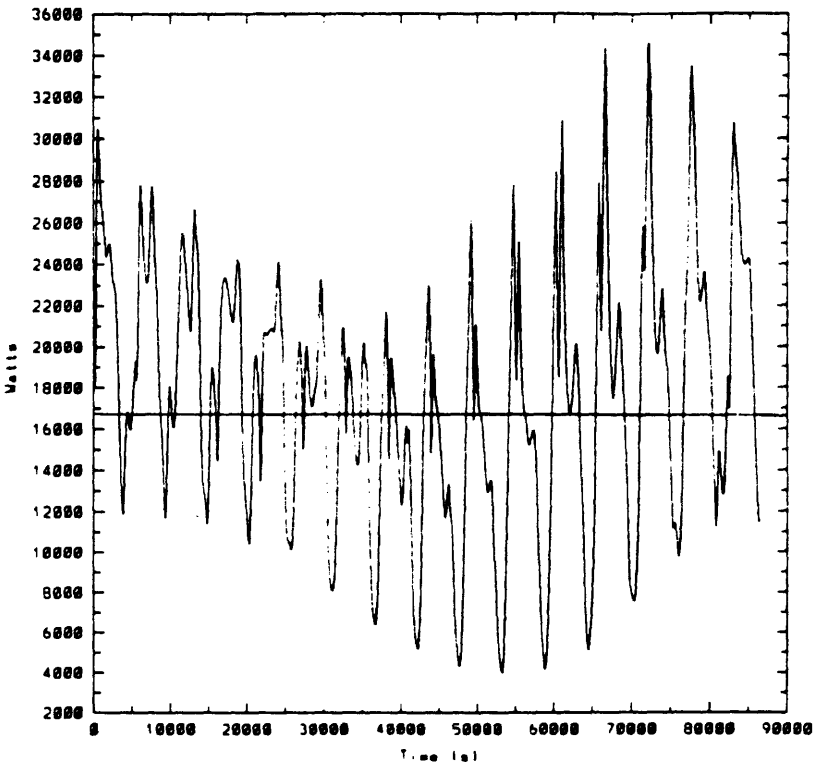

Fig. 14 Map of Magnitude of Geomagnetic Field

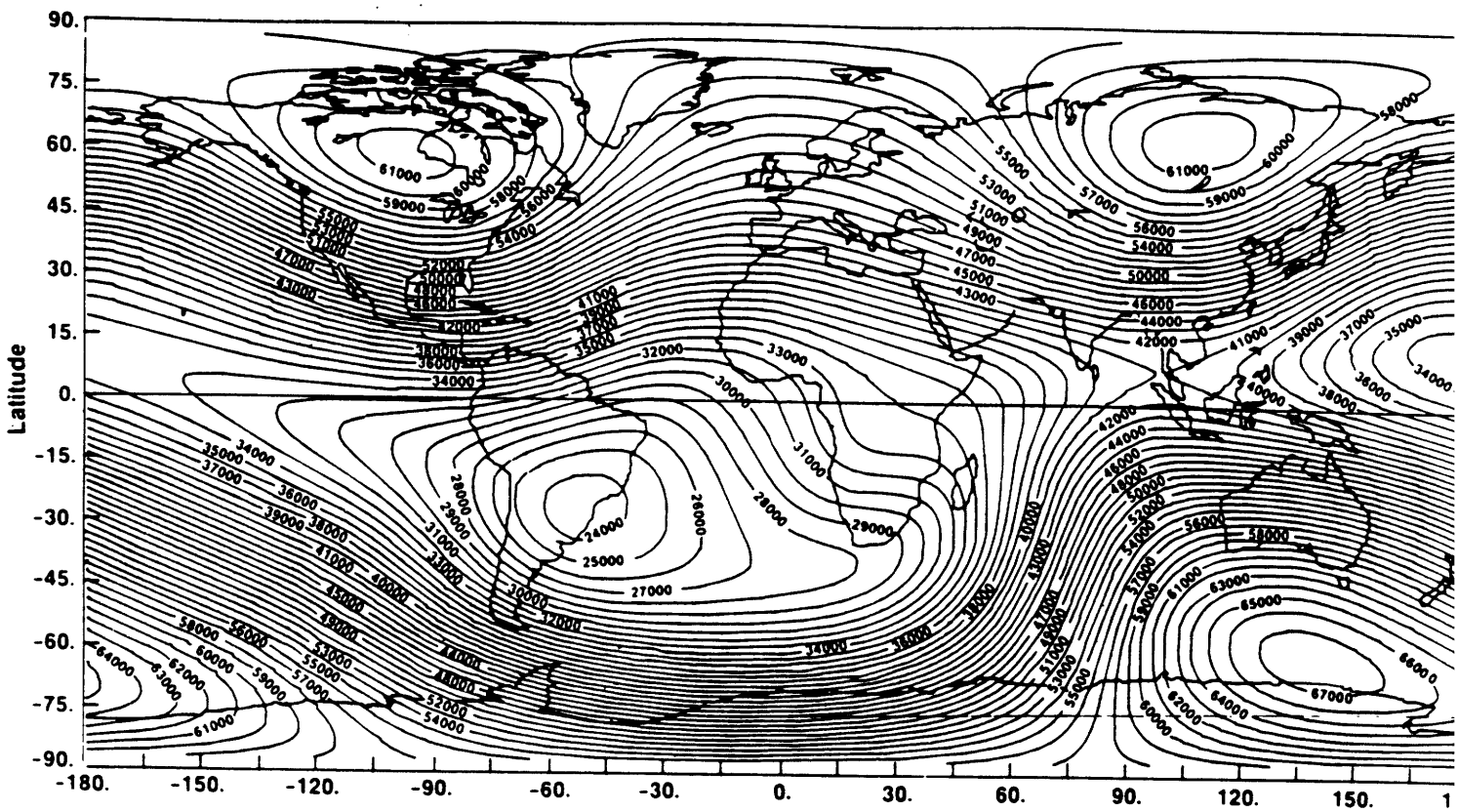

Fig. 15 Induced Voltage, 1° Orbit

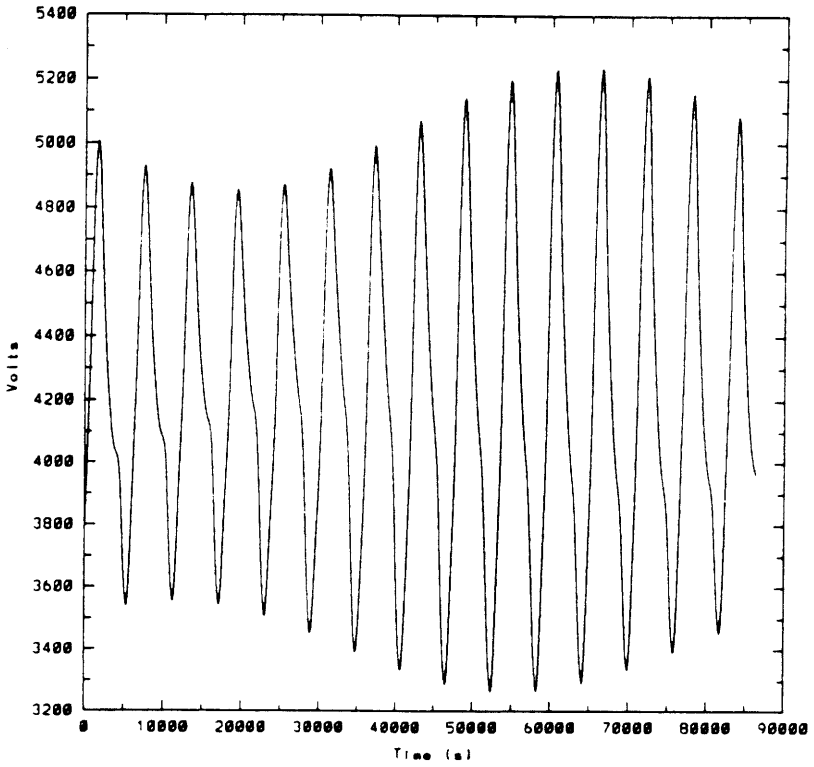

Fig. 16 Profile of Earth's Ionosphere (From [20])

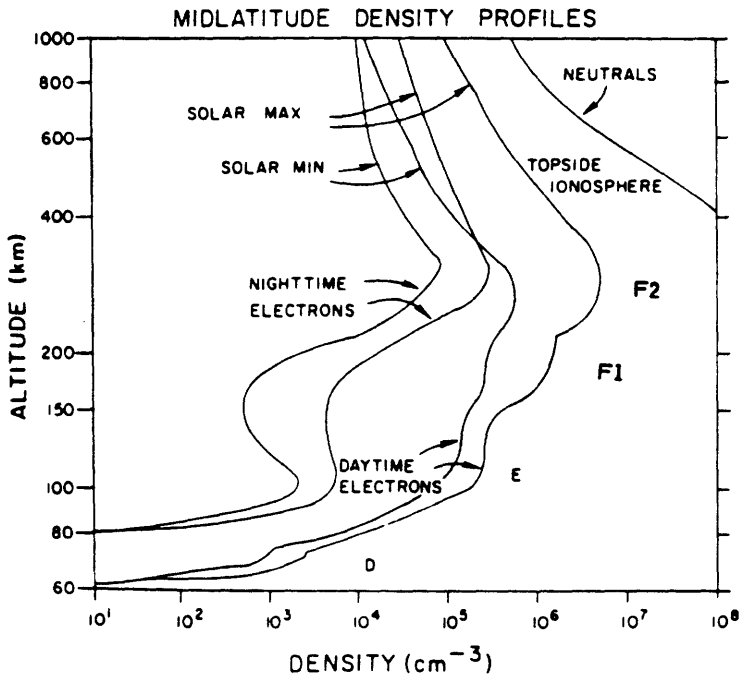

Fig. 17a Profile of Jupiter's Ionosphere (From [22])

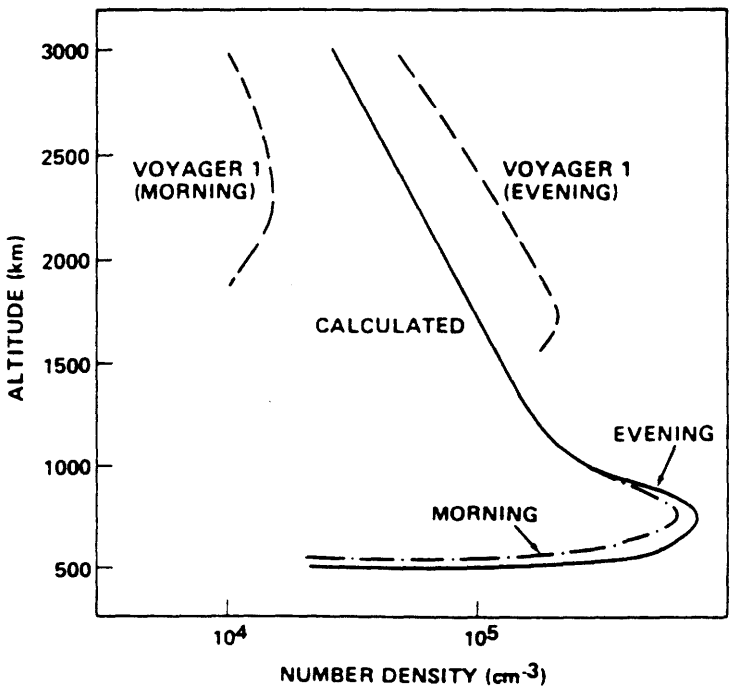

Fig. 17b Profile of Saturn's Ionosphere (From [22])

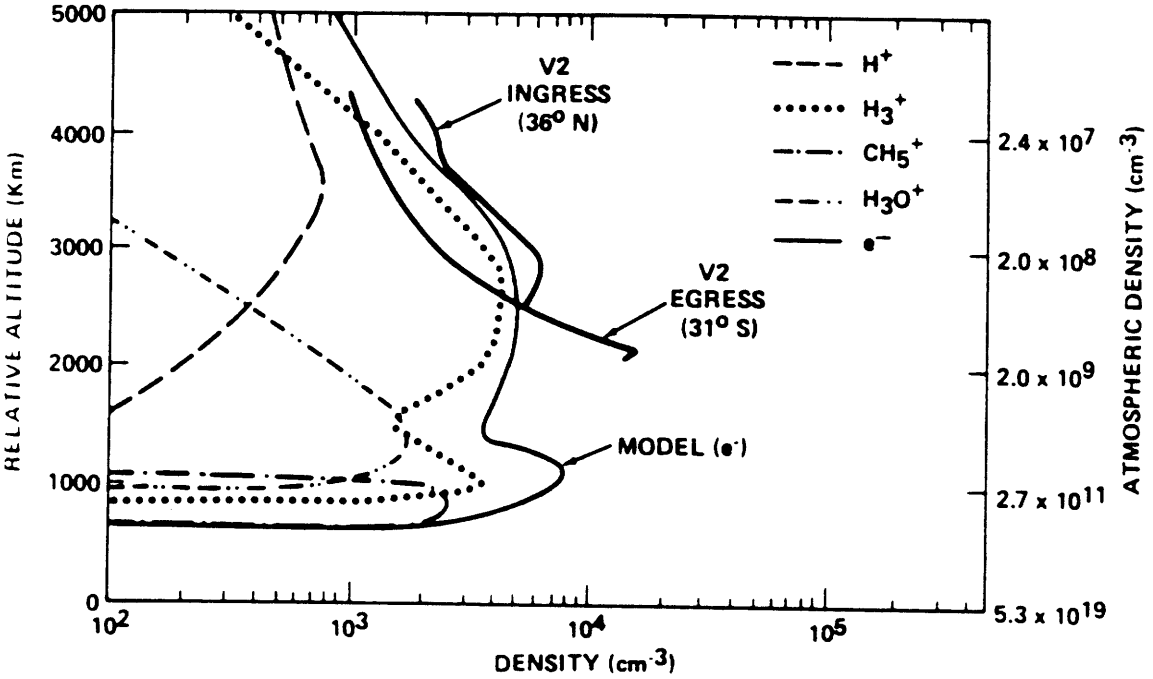

Fig. 17c Profile of Uranus' Ionosphere (From [22])

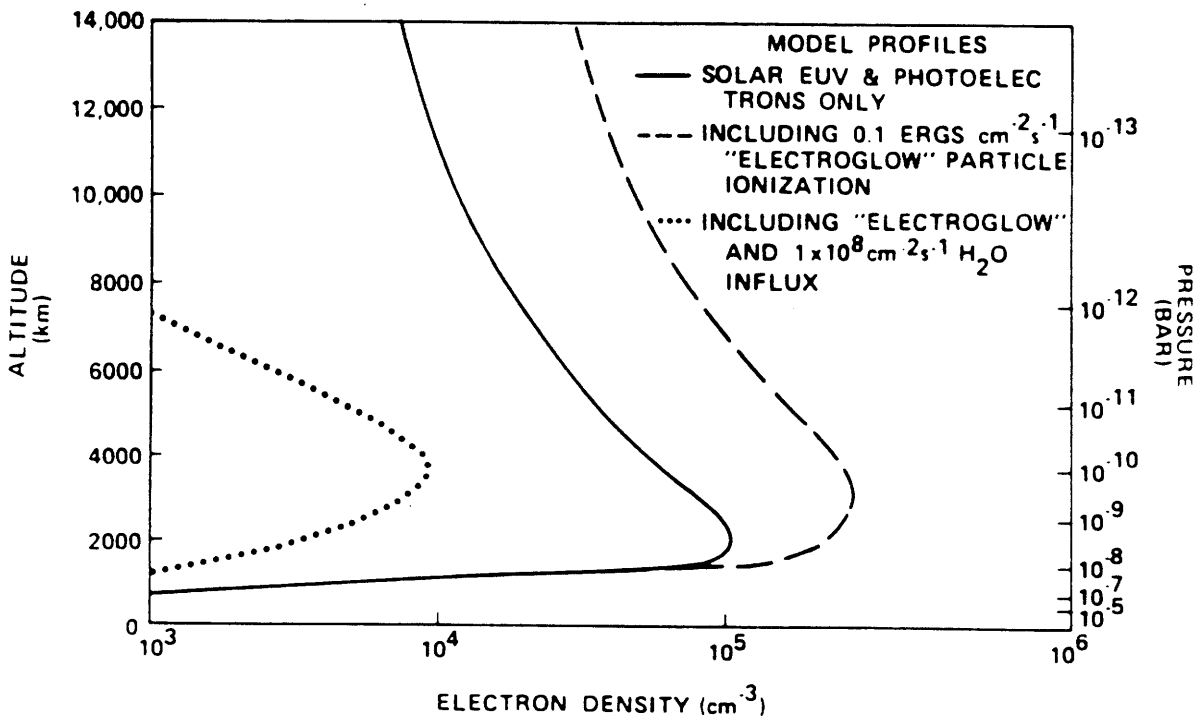

Fig. 18a Ionospheric Electron Density, Average Sunspot No. of 60

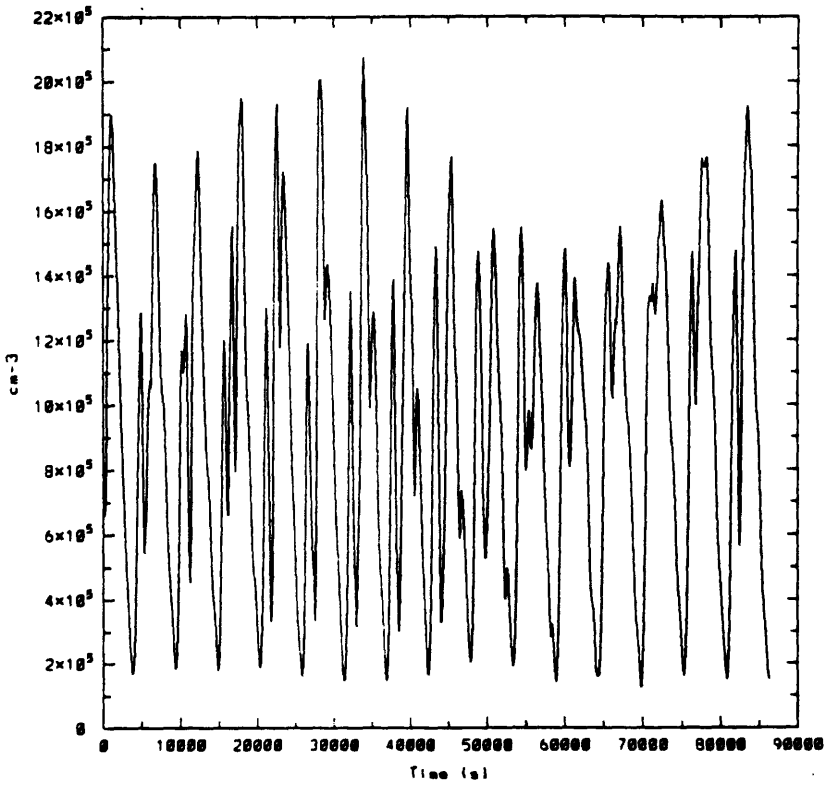

Fig. 18b Ionospheric Electron Density, High Sunspot No. of 120

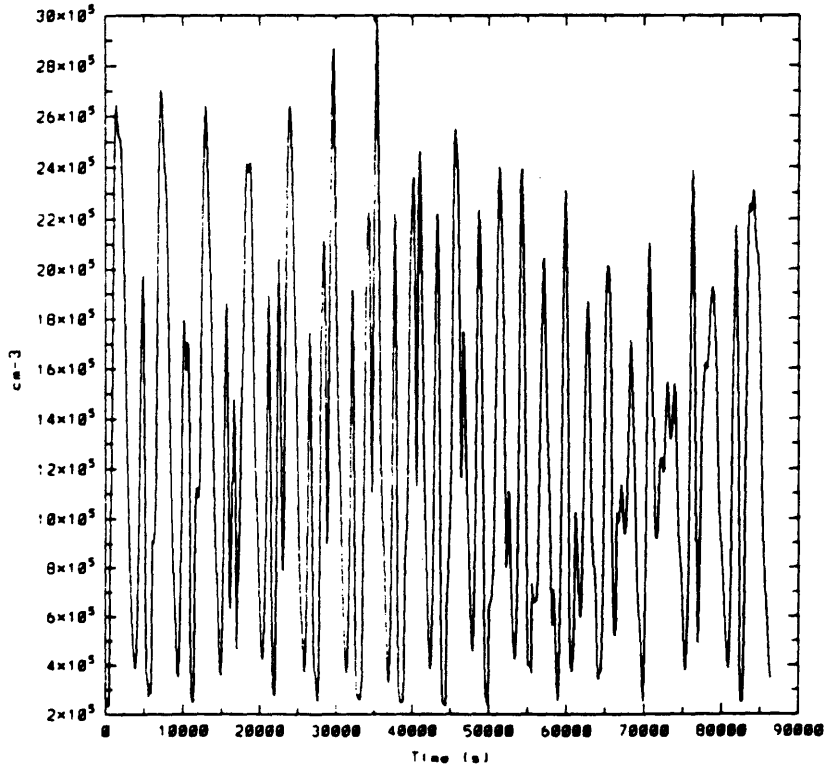

Fig. 18c Ionospheric Electron Current (Je), Average Sunspot No.

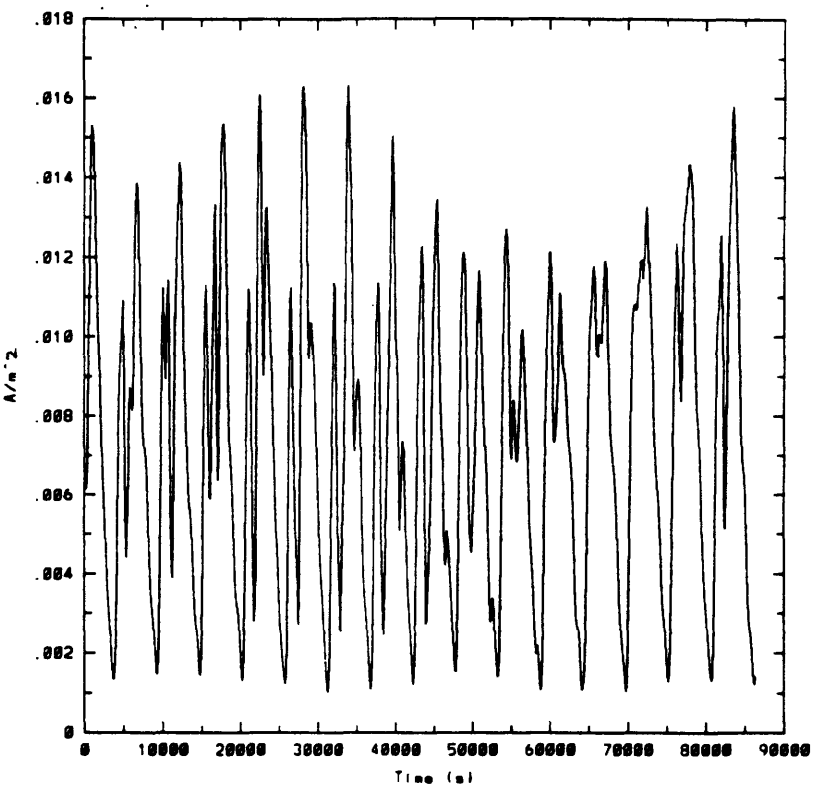

Fig. 19 Orbital Mechanics Coordinate Systems

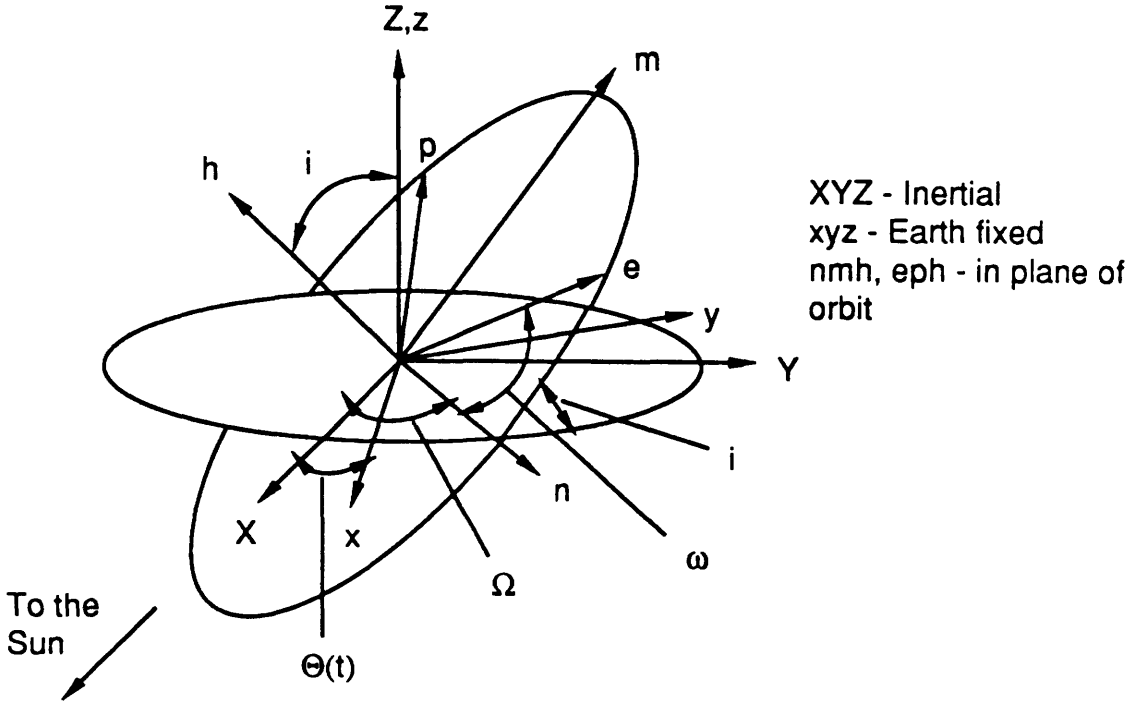

Fig. 20a Maximum Power vs. Efficiency

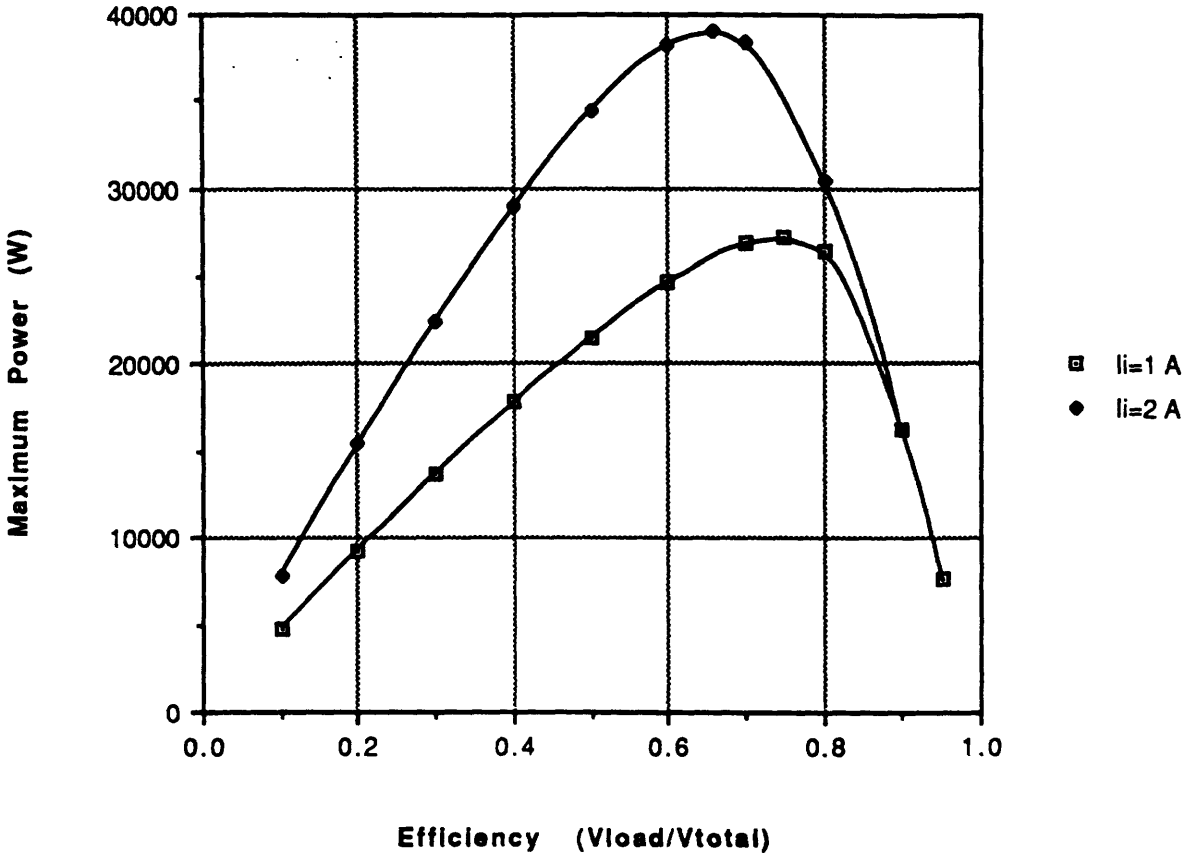

Fig. 20b Current vs. Efficiency

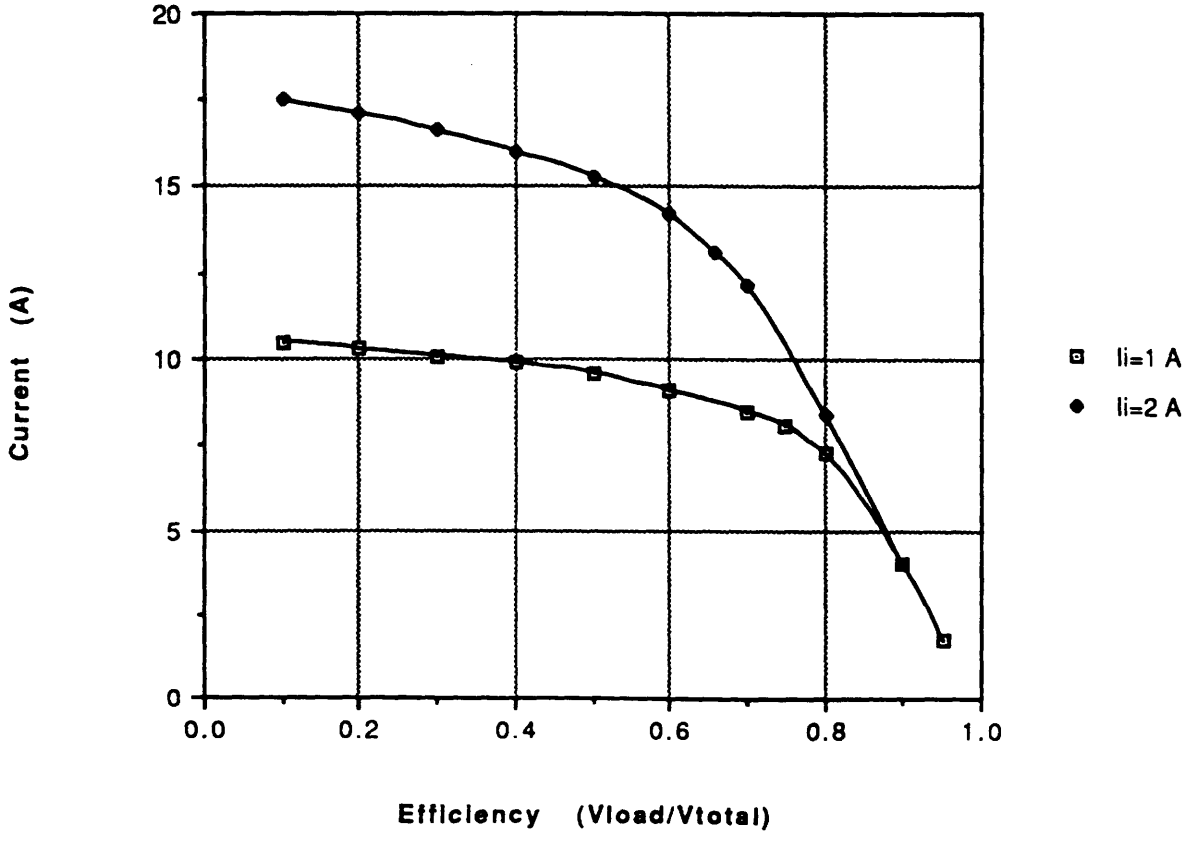

Fig. 21a Contactor Power vs. Iion and f

V=4500, Je=0.005

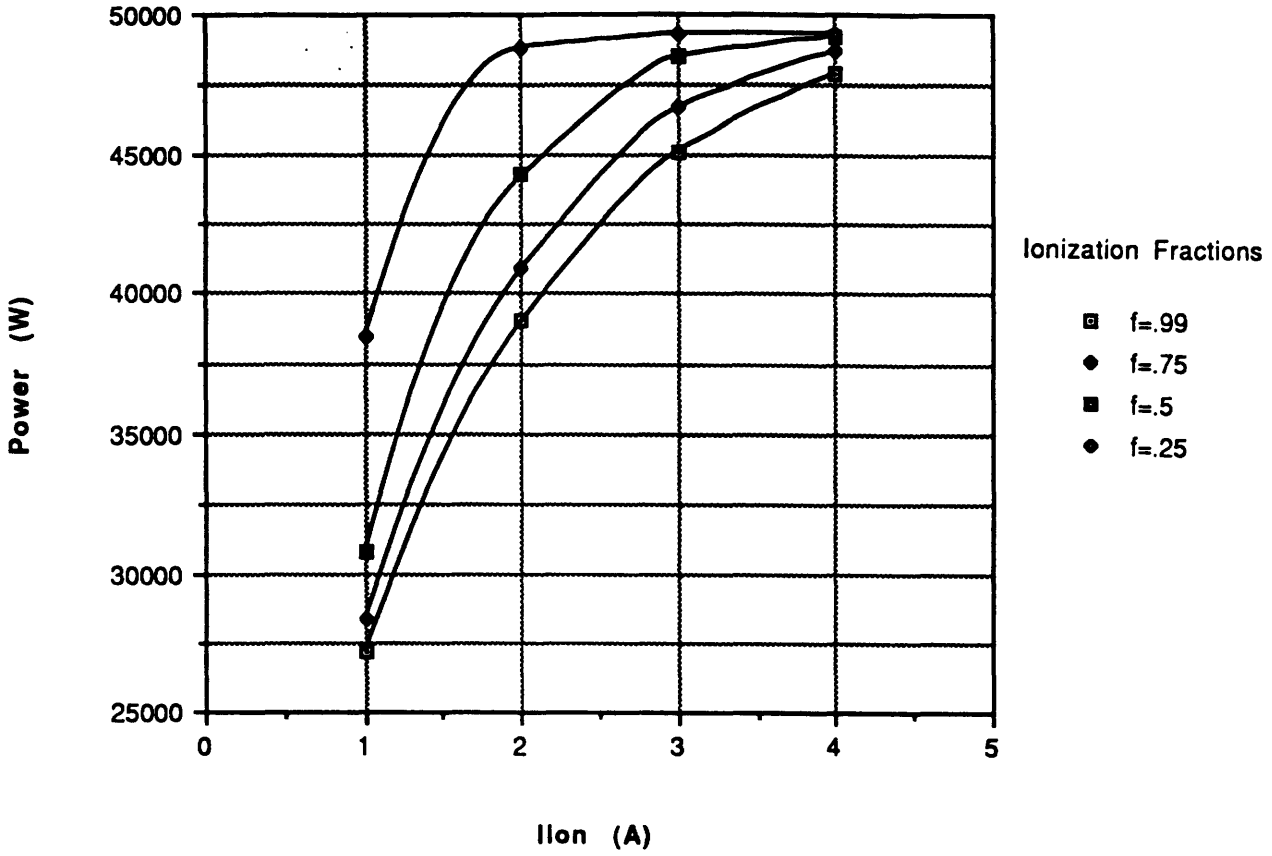

Fig. 21b Contactor Power vs. Iion and f

V=3000, Je=0.001

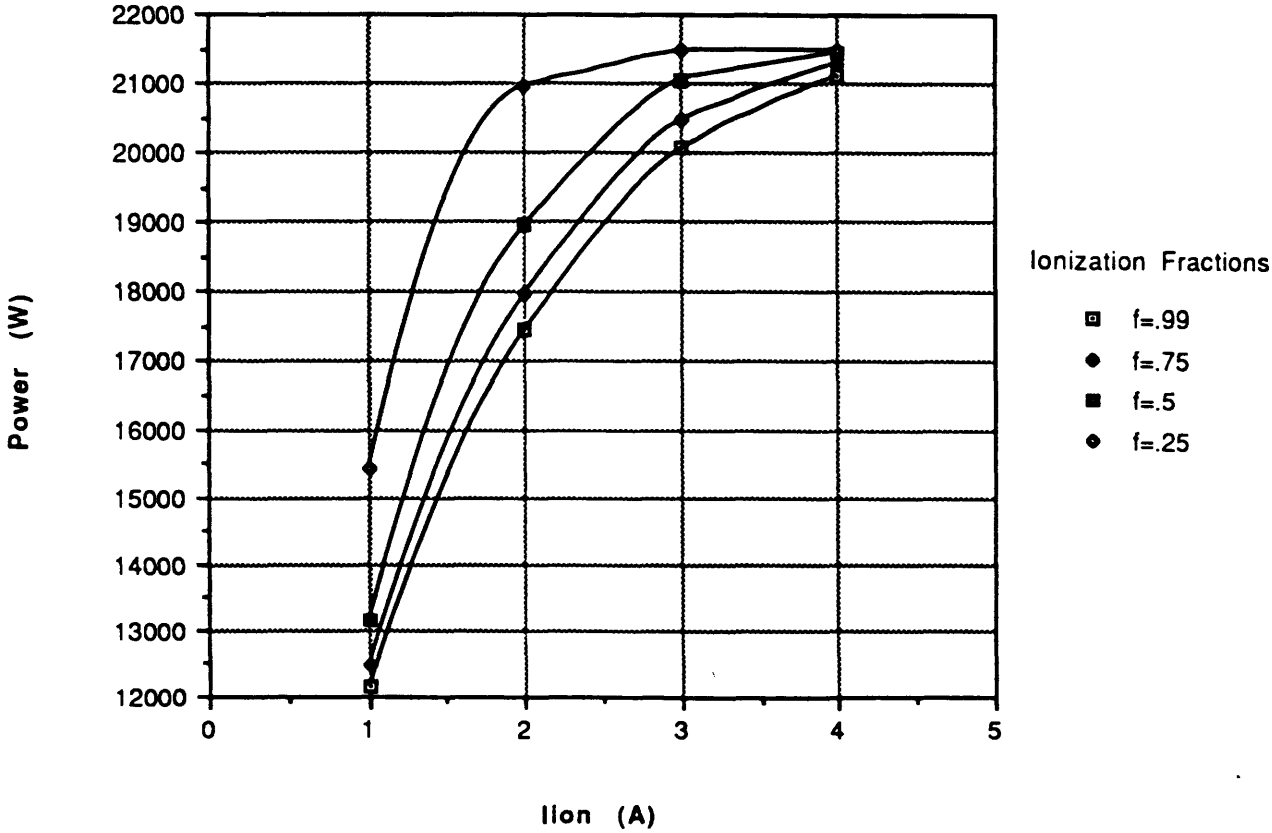

Fig. 21c Contactor Cloud Radius vs. Iion,f

(Corresponding to Fig. 21a)

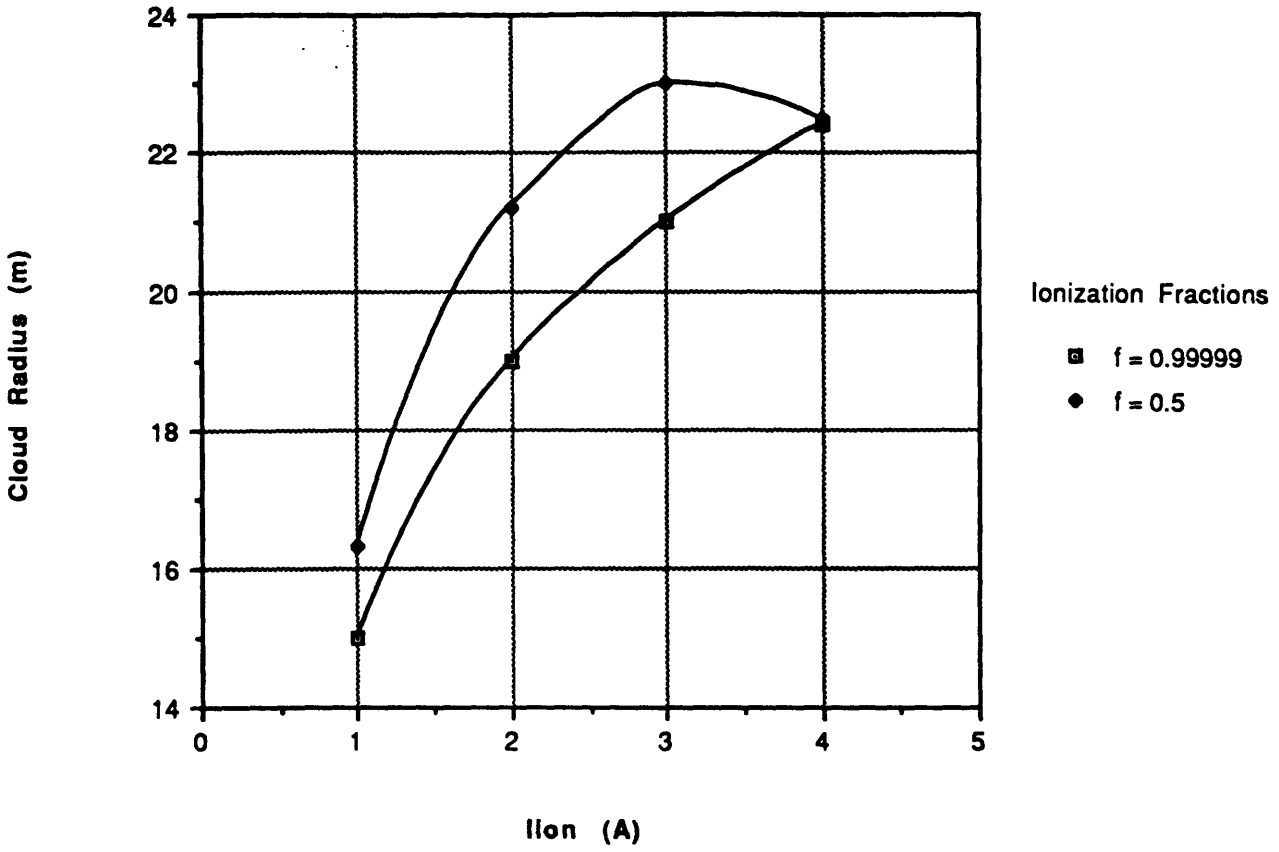

Fig. 21d Contactor Potential vs. Iion,f

(Corresponding to Fig. 21a)

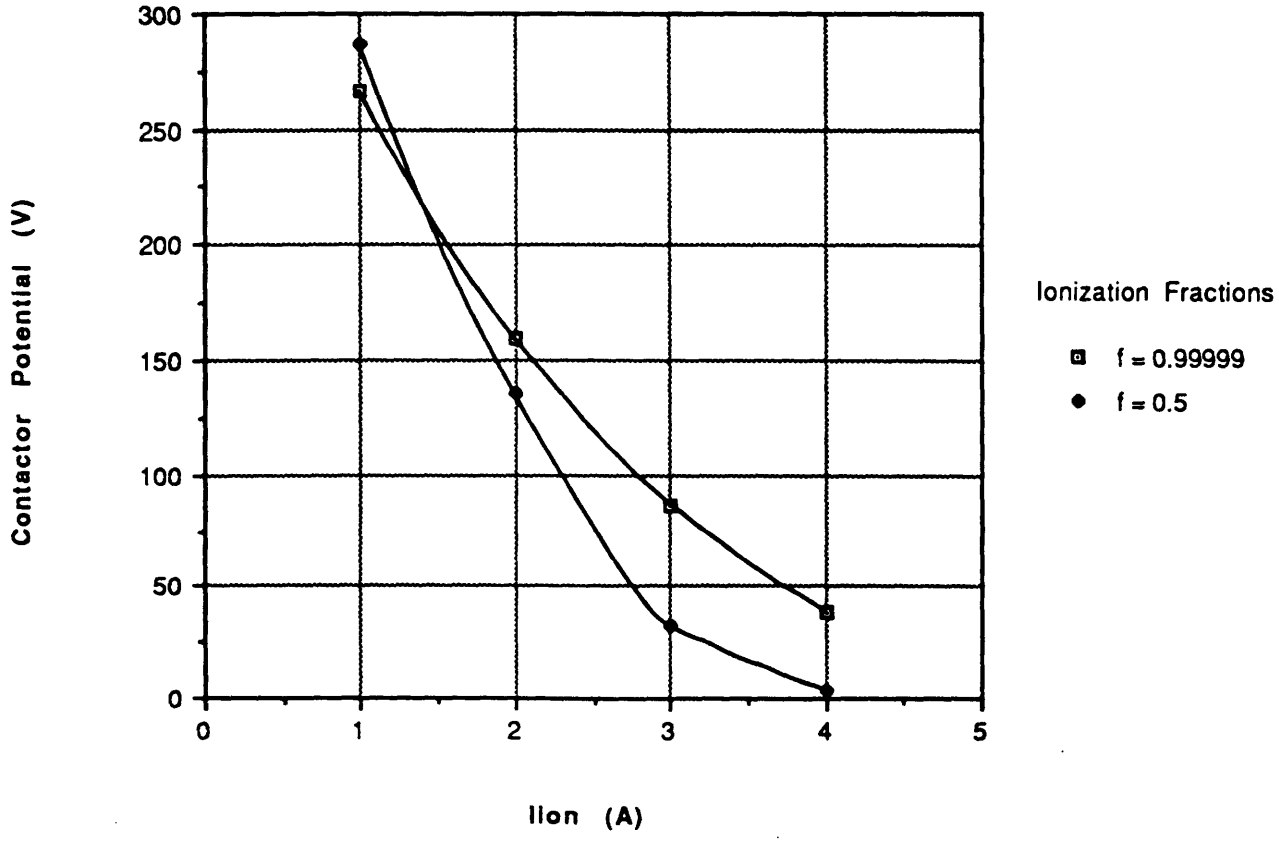

Fig. 22a Contactor <Maximum> Power vs. Iion/f (Simulation)

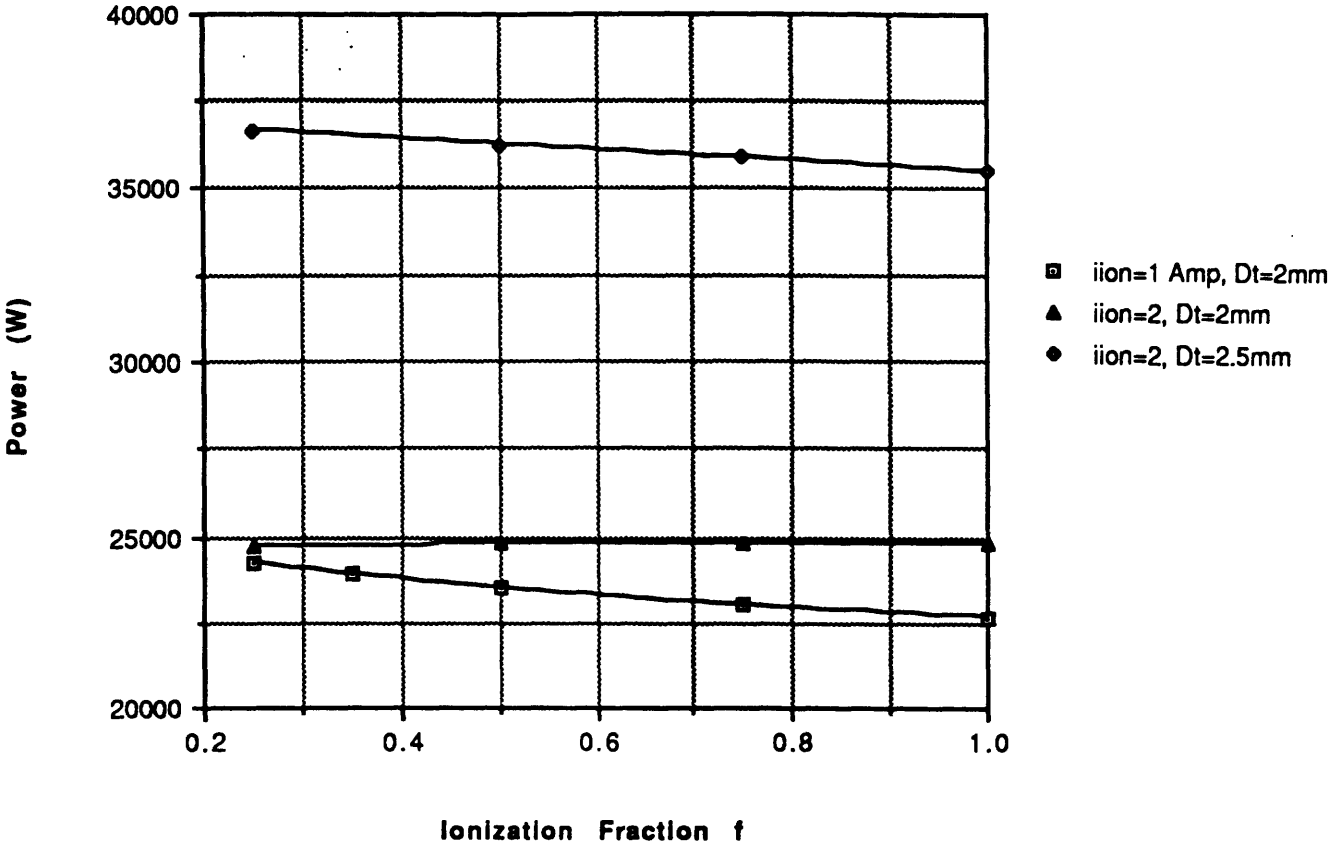

Fig. 22b Specific Power vs. Iion/f (Maximum Power, Simulation)

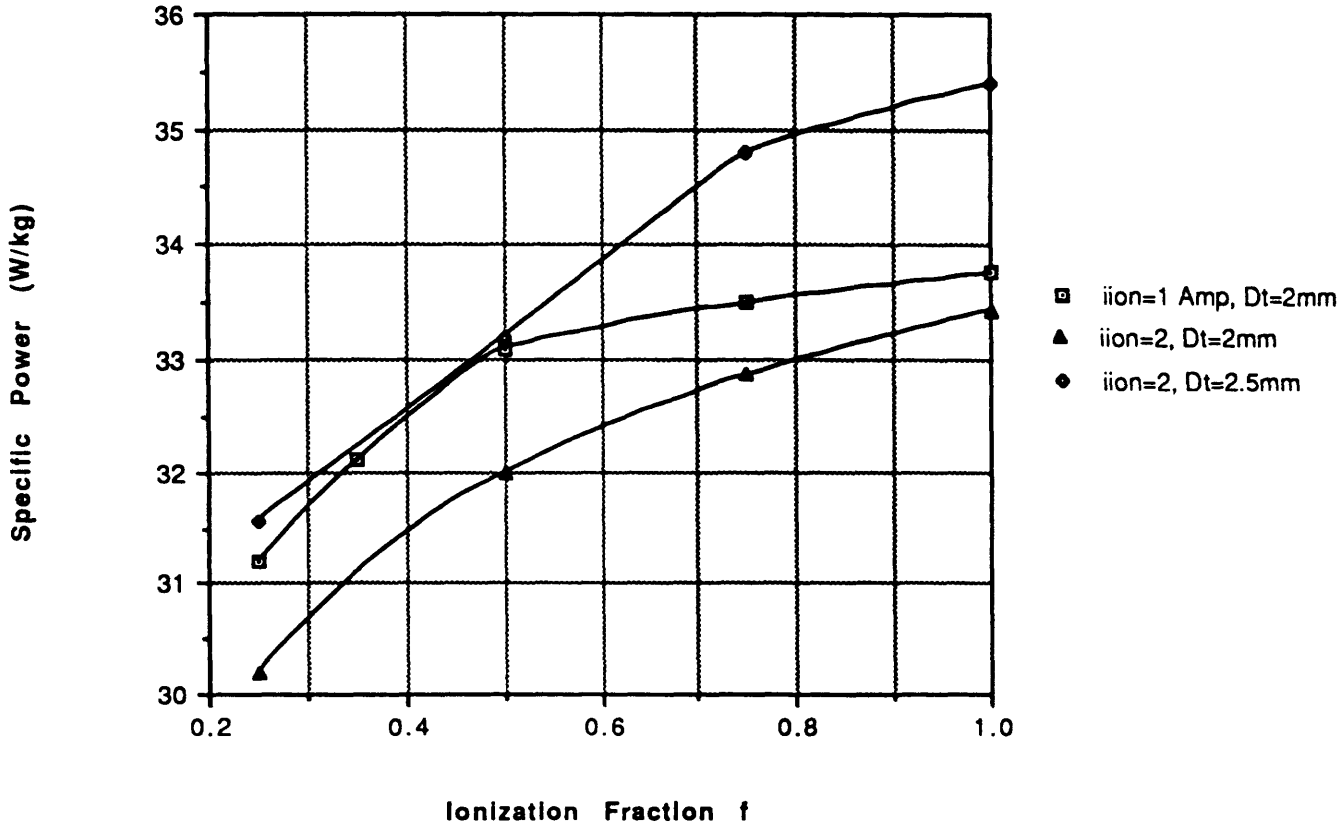

Fig. 23a <Maximum> Power vs. Tether Diameter (Contactor)

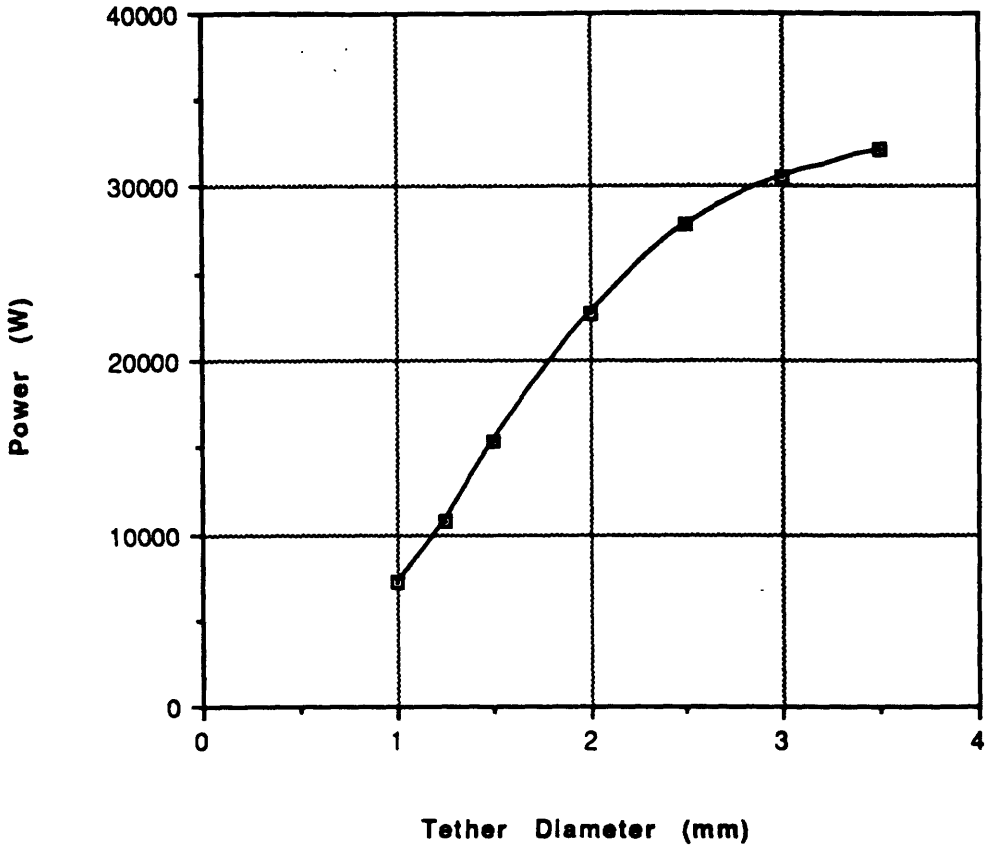

Fig. 23b Specific Power vs. Tether Diameter (Contactor)

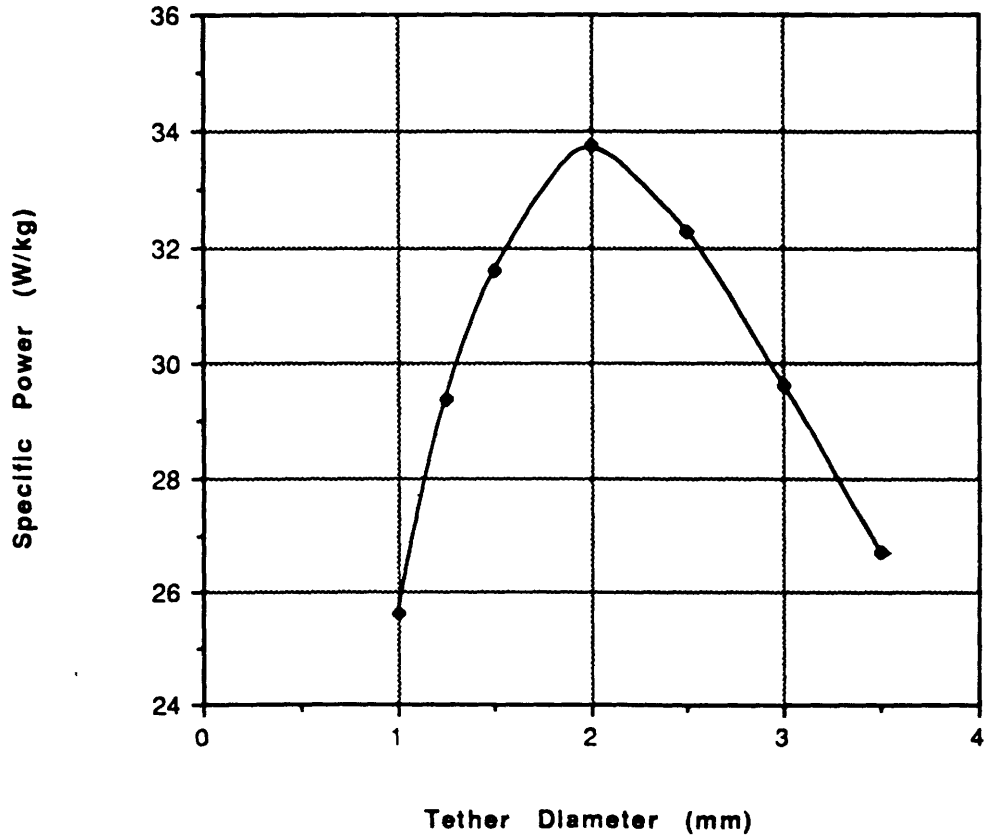

Fig. 24a <Maximum> Power vs. Mol. Wt. of Contactor Gas

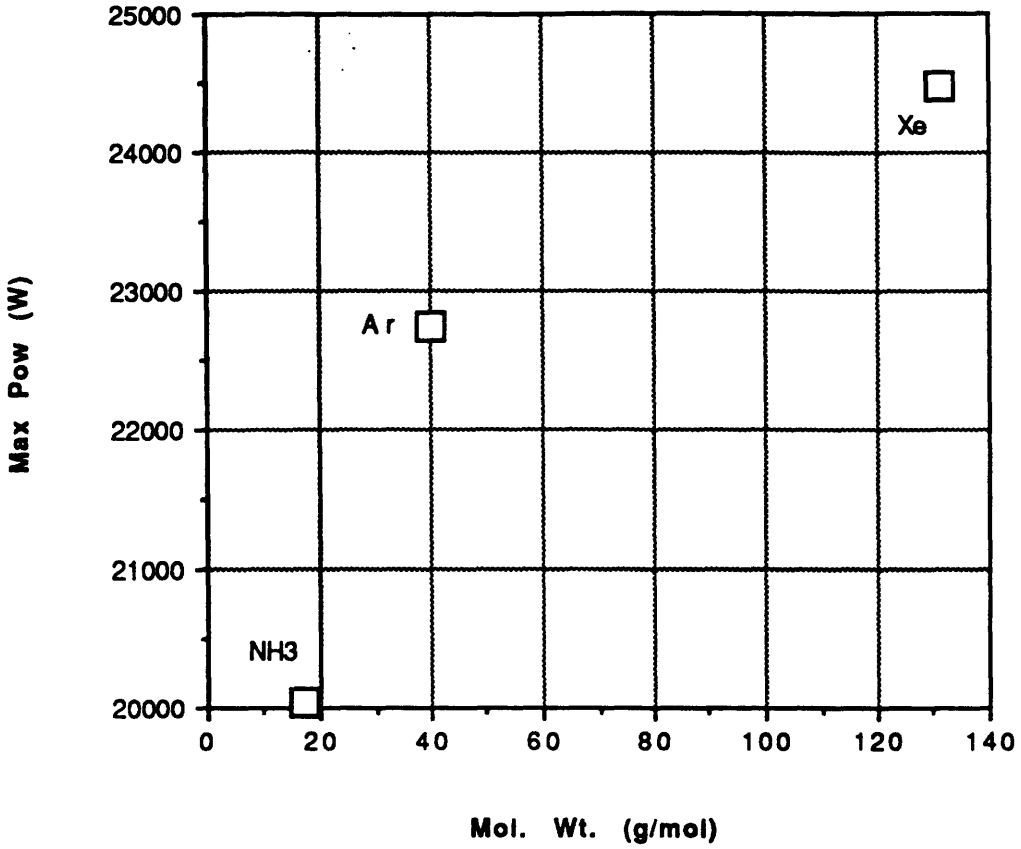

Fig. 24b Specific Power vs. Mol. Wt. of Contactor Gas

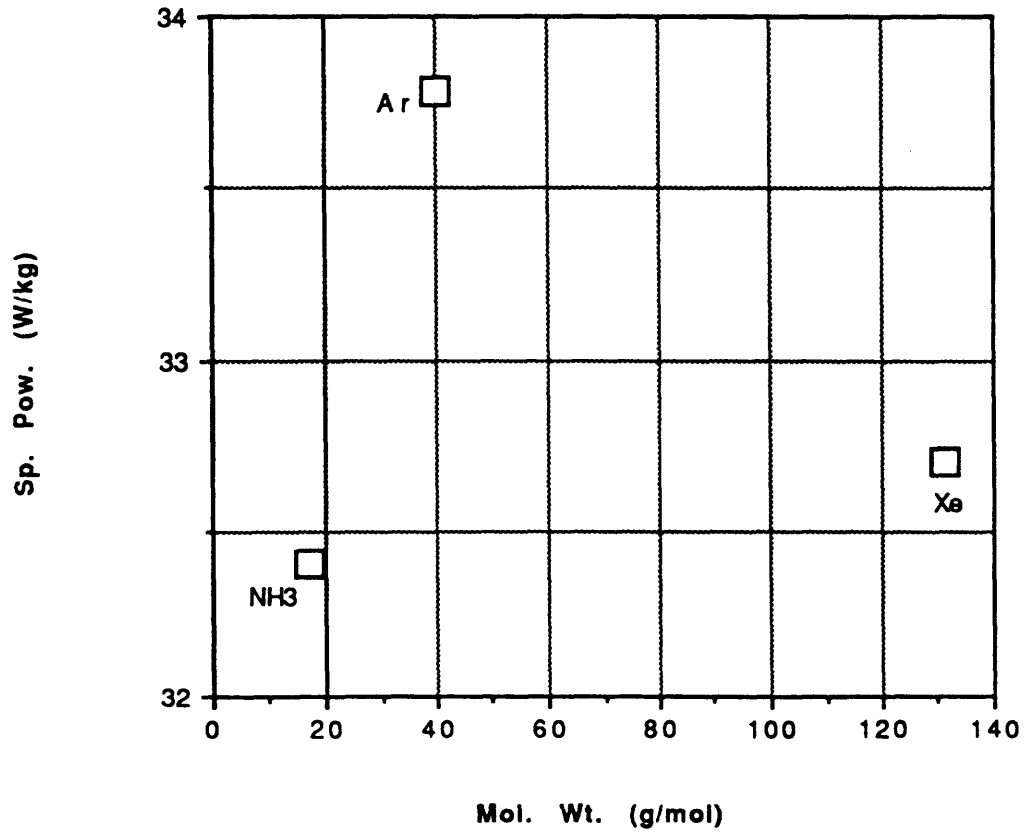

Fig. 25 <Maximum> Power vs. Gas Emission Velocity

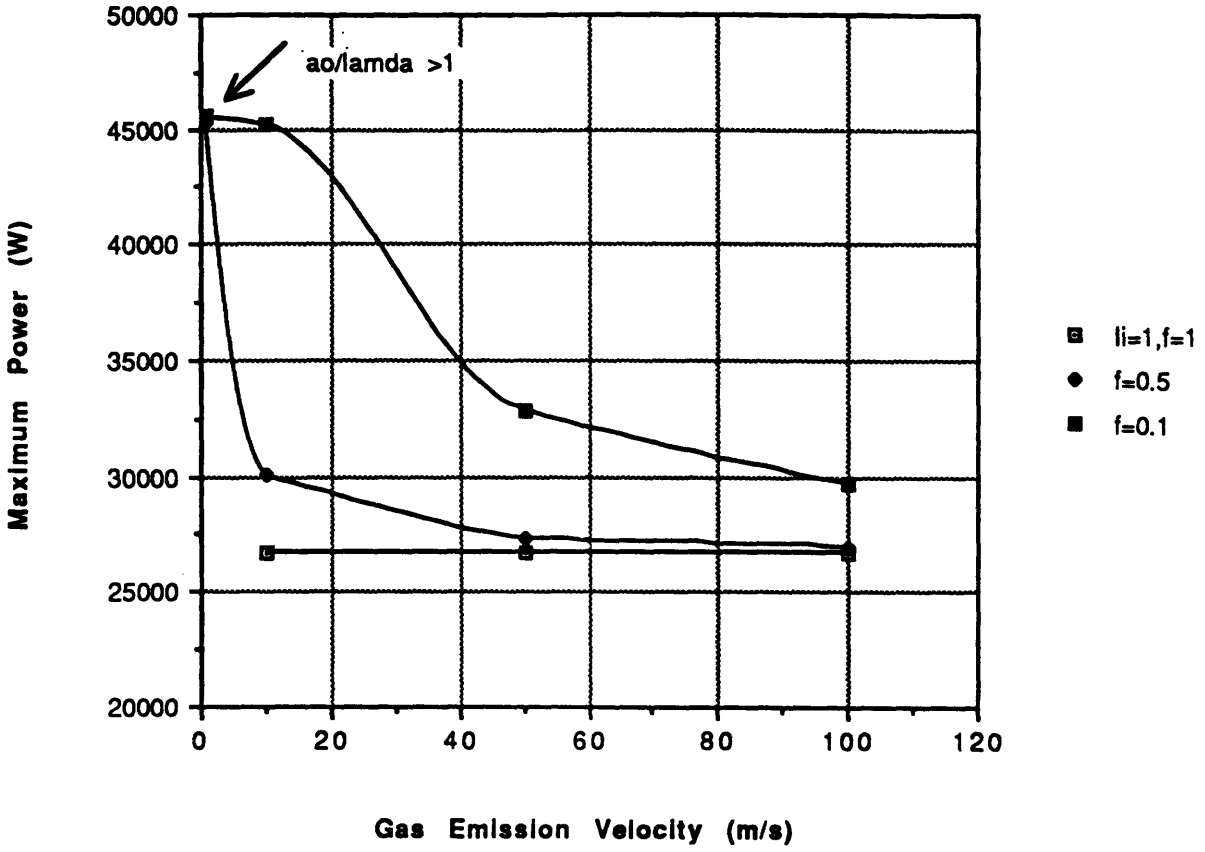

Fig. 26a <Maximum> Power vs. Operating Altitude

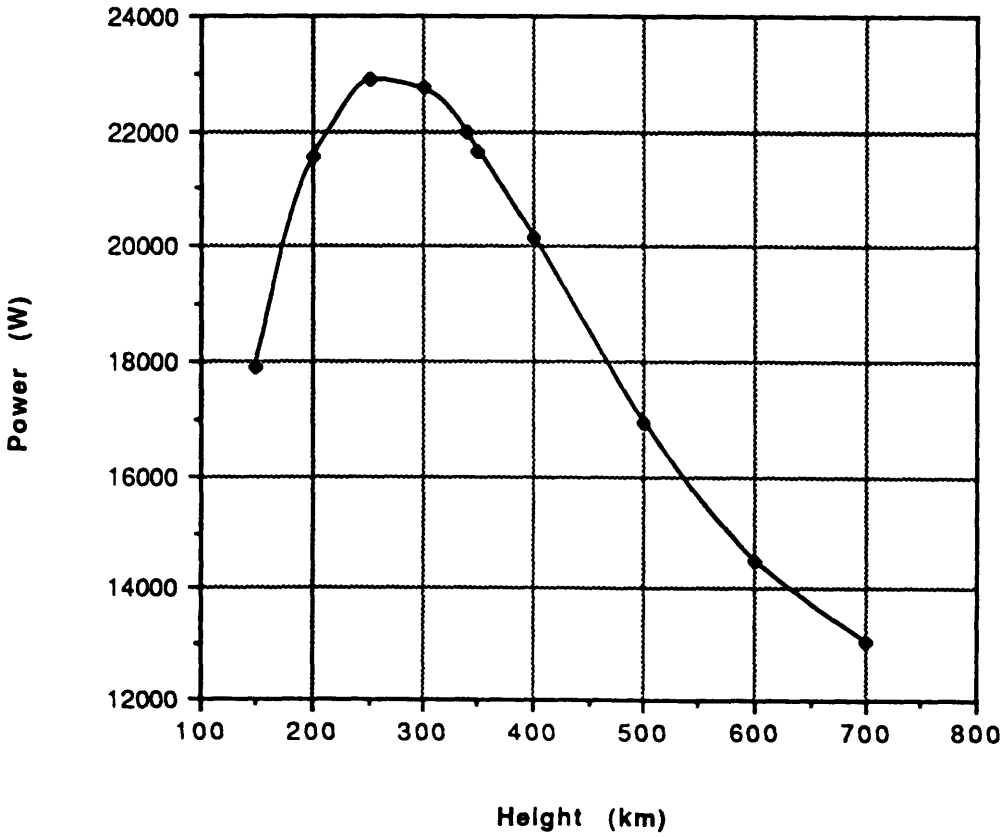

Fig. 26b Specific Power vs. Operating Altitude

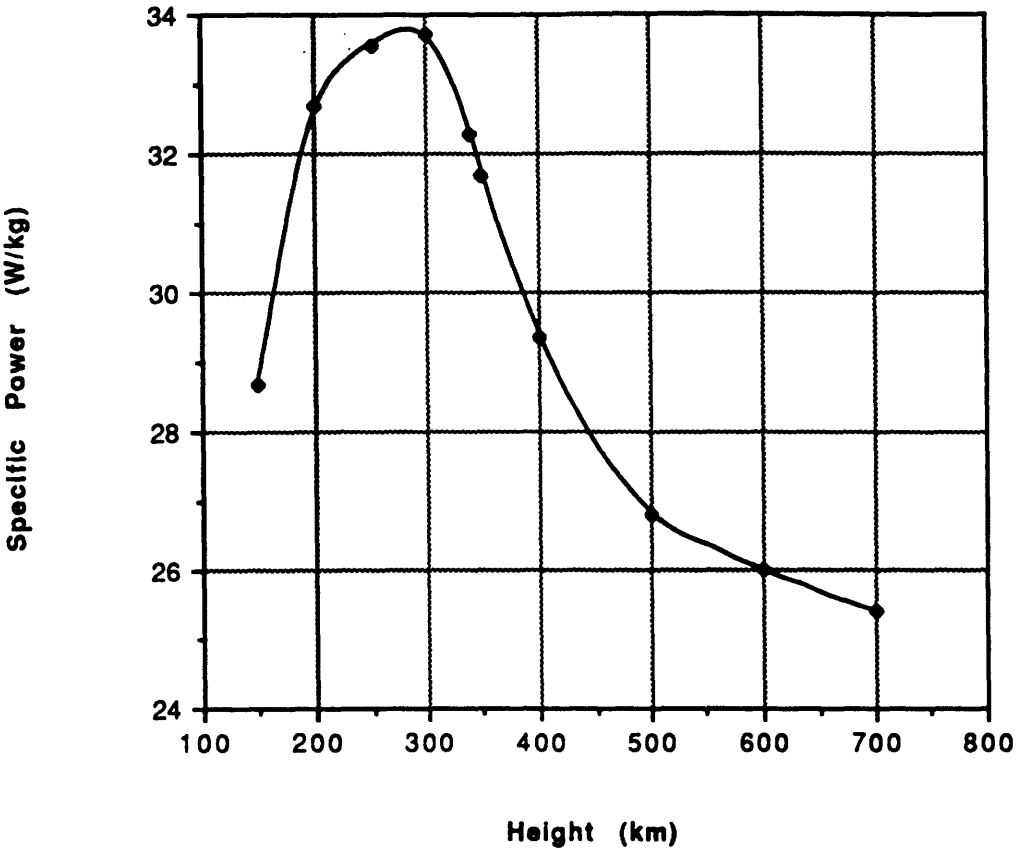

Fig. 27a Variation of <Max.> Power with Sunspot Number and Month

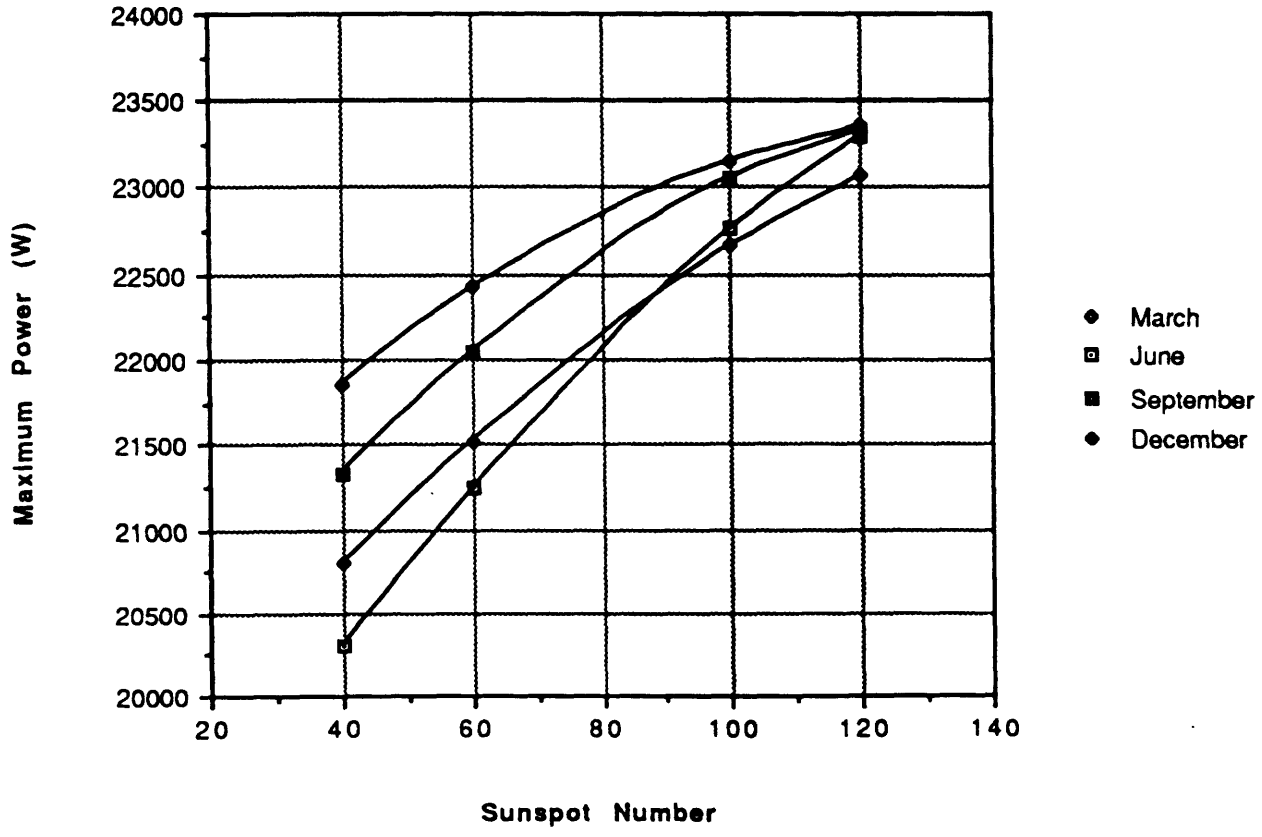

Fig. 27b Variation of Specific Power with Sunspot Number and Month

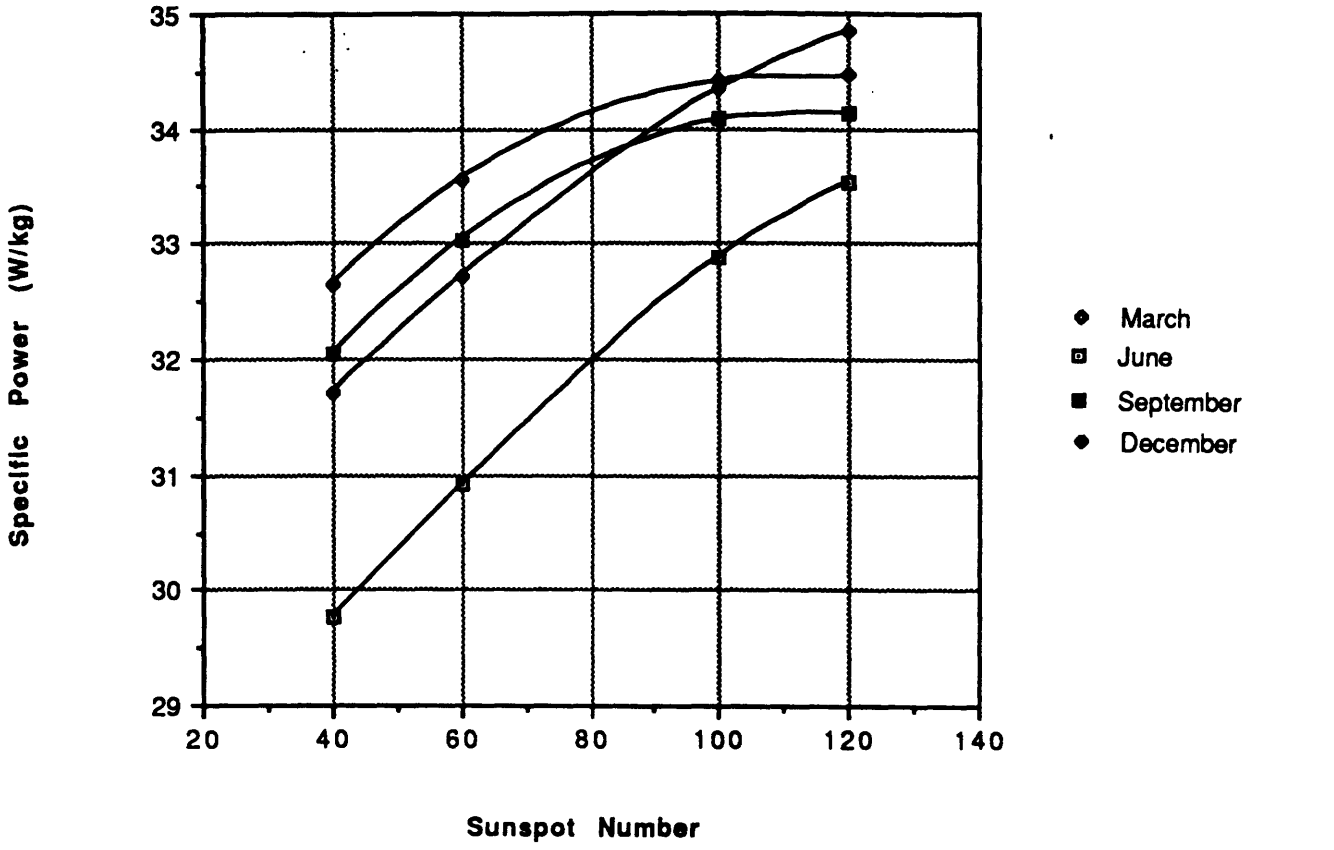

Fig. 28a Comparison of <Maximum> Power

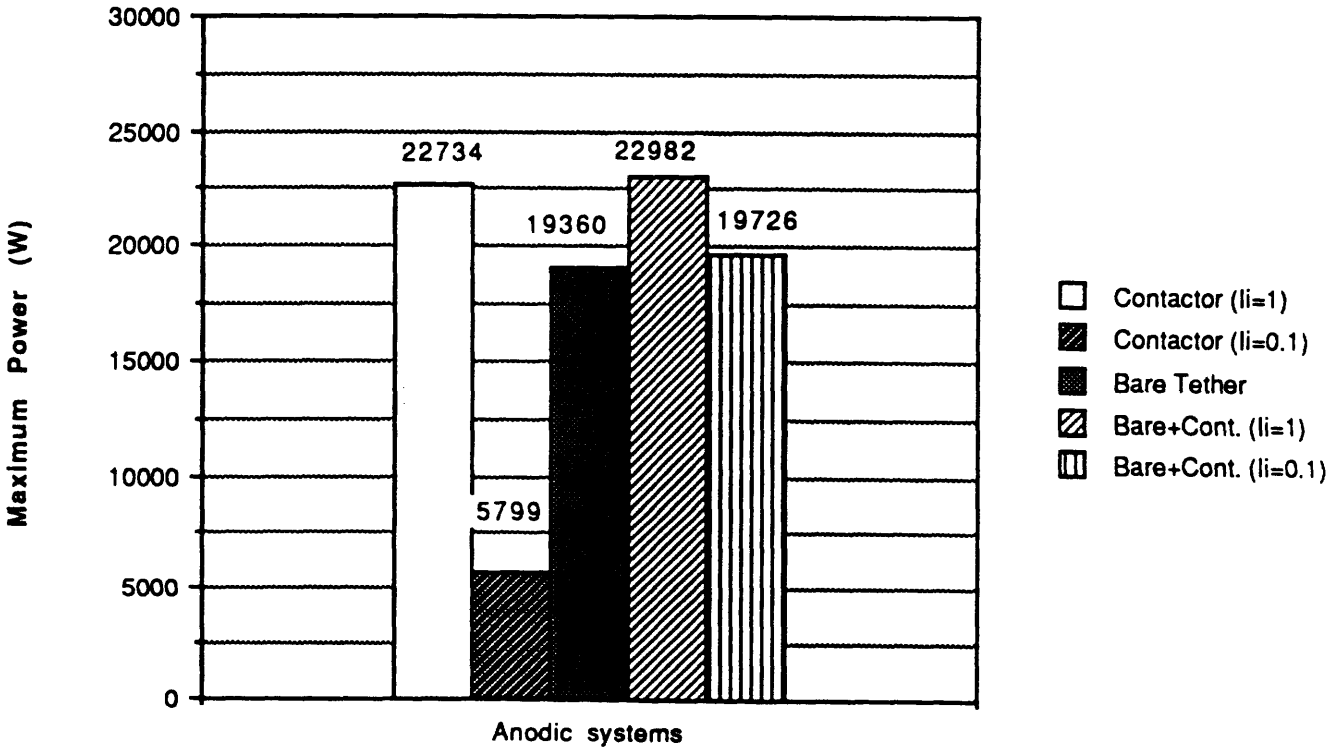

Fig. 28b Comparison of Specific Power

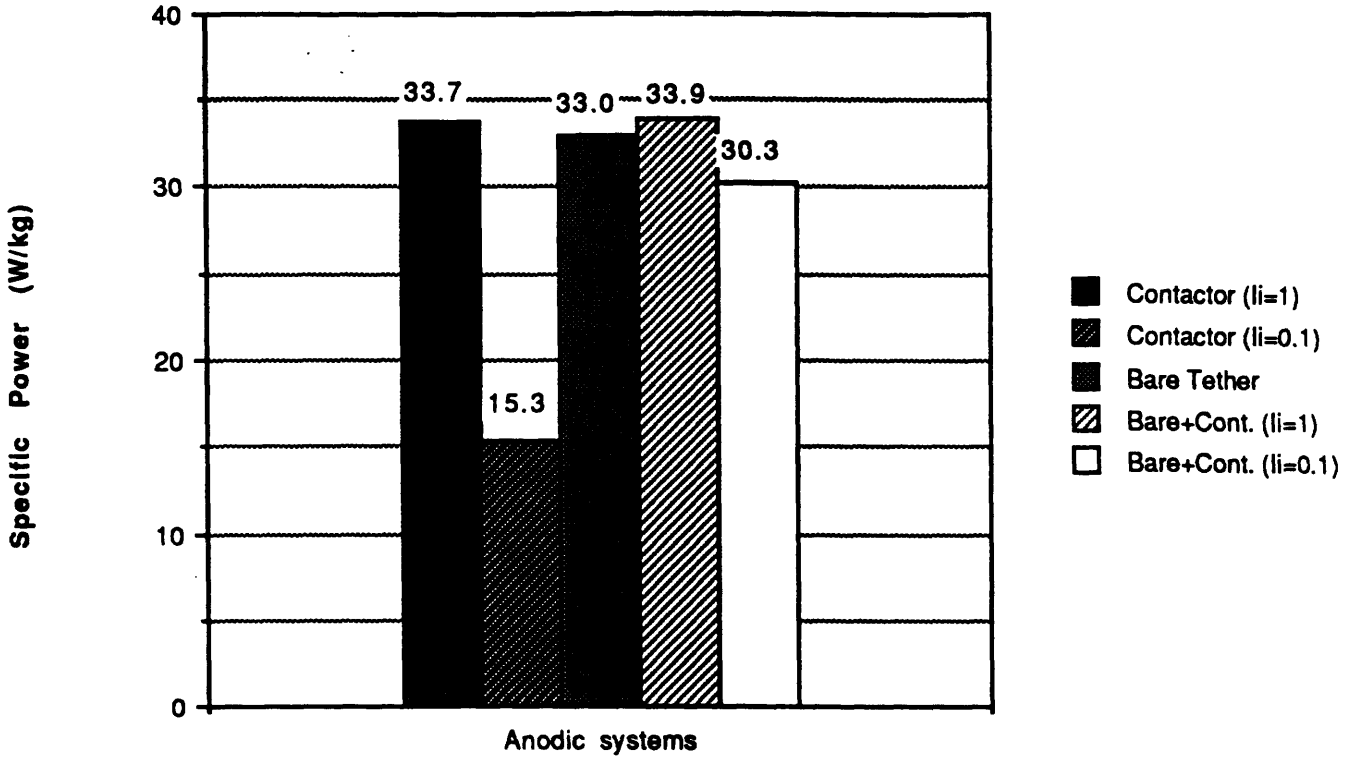

Fig. 28c Comparison of Efficiency

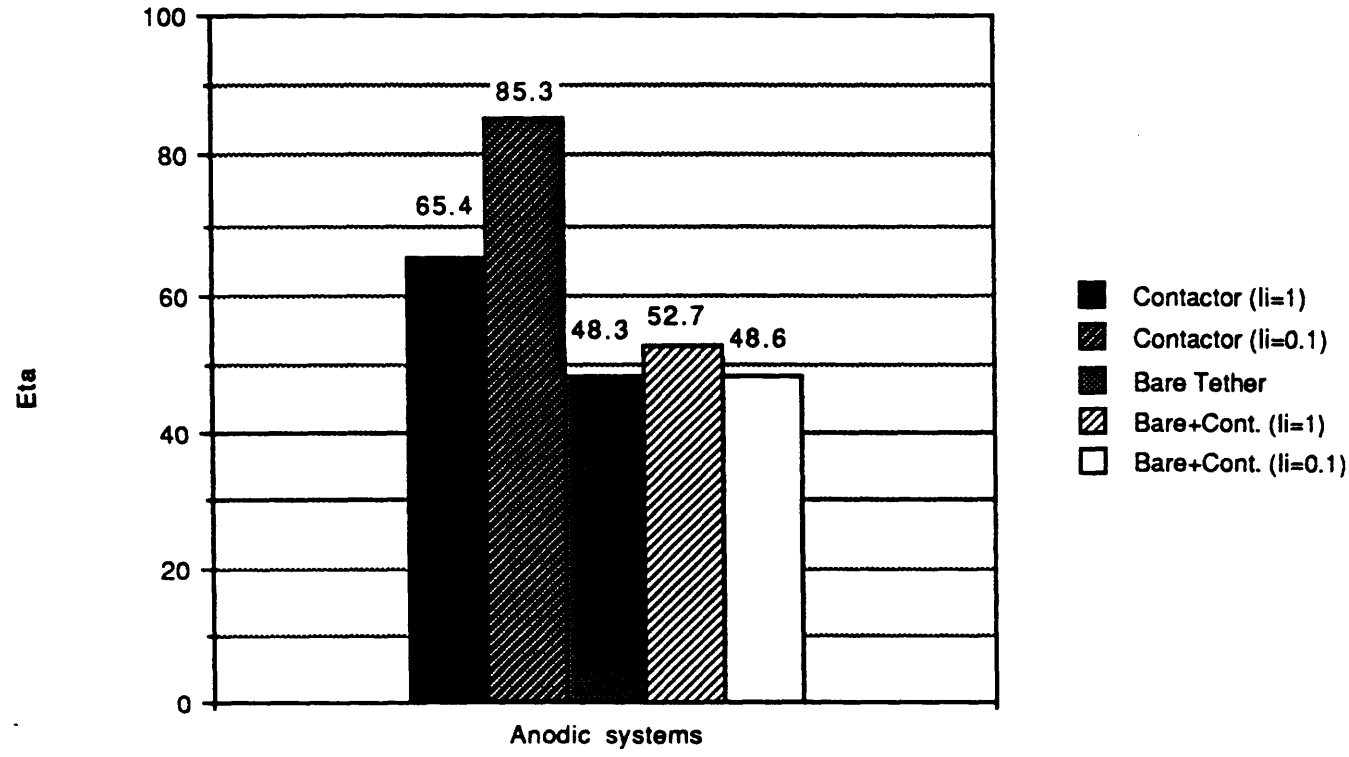

Fig. 28d Comparison of Mass Breakdowns (Maximum Power)

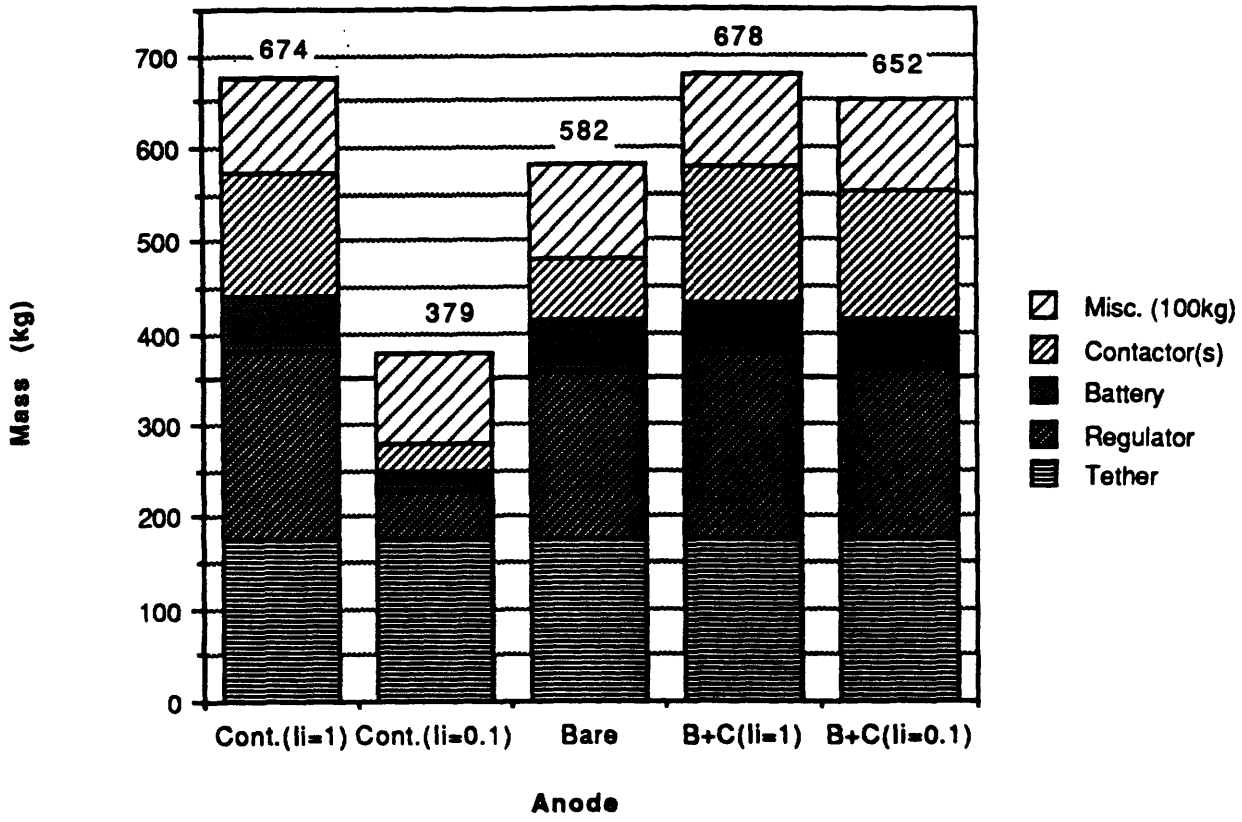

Fig. 28e Drag Makeup Fuel Consumption Per Day (Maximum Power)

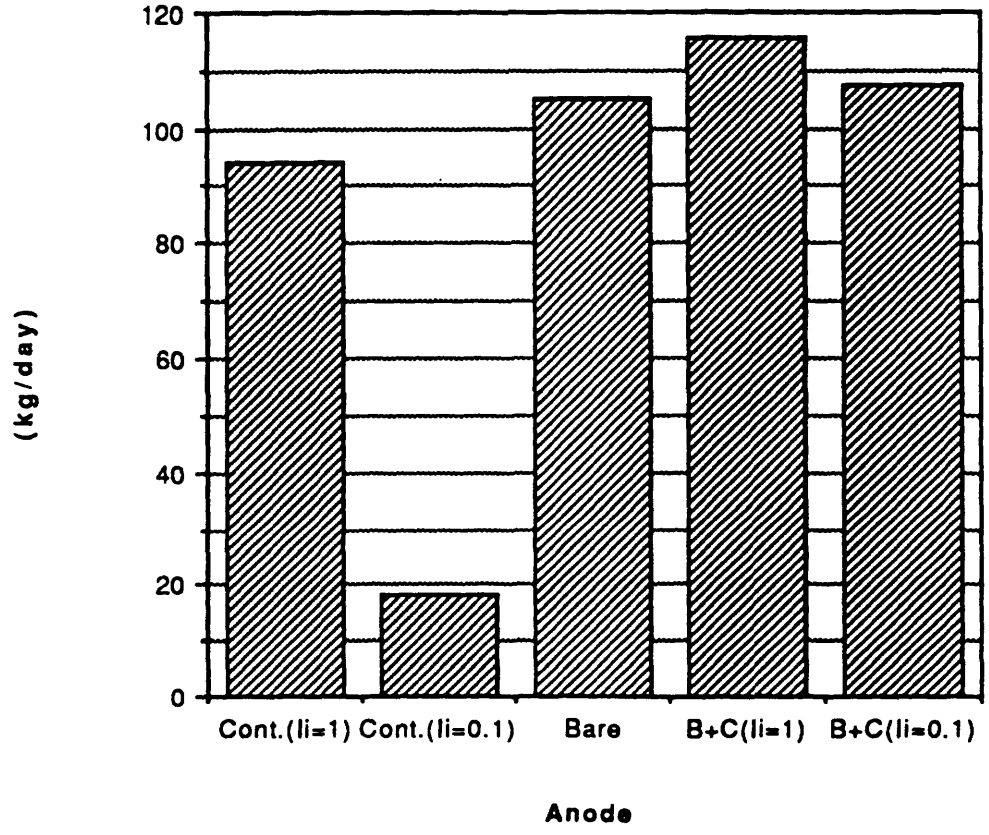

Fig. 28f Contactor Maximum Power Delivered

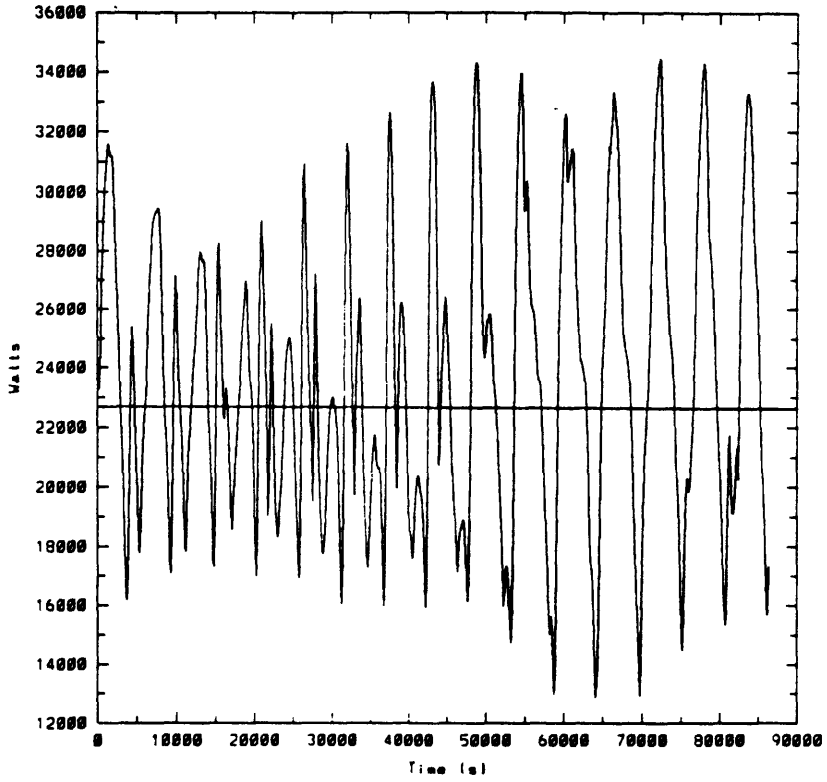

Fig. 28g Bare Tether Maximum Power Delivered

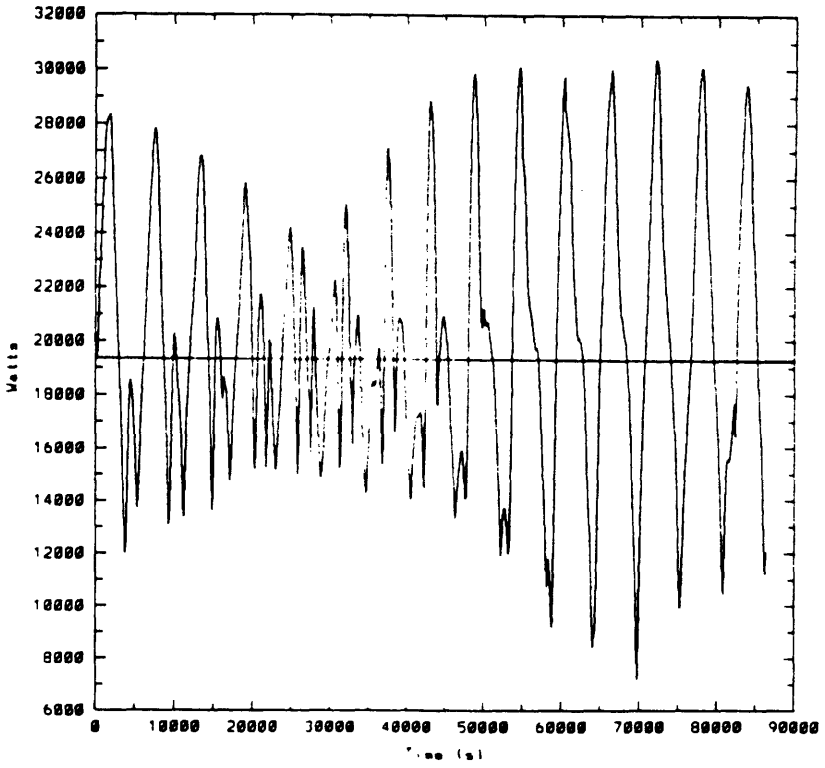

Fig. 28h Bare+Contactor Maximum Power Delivered

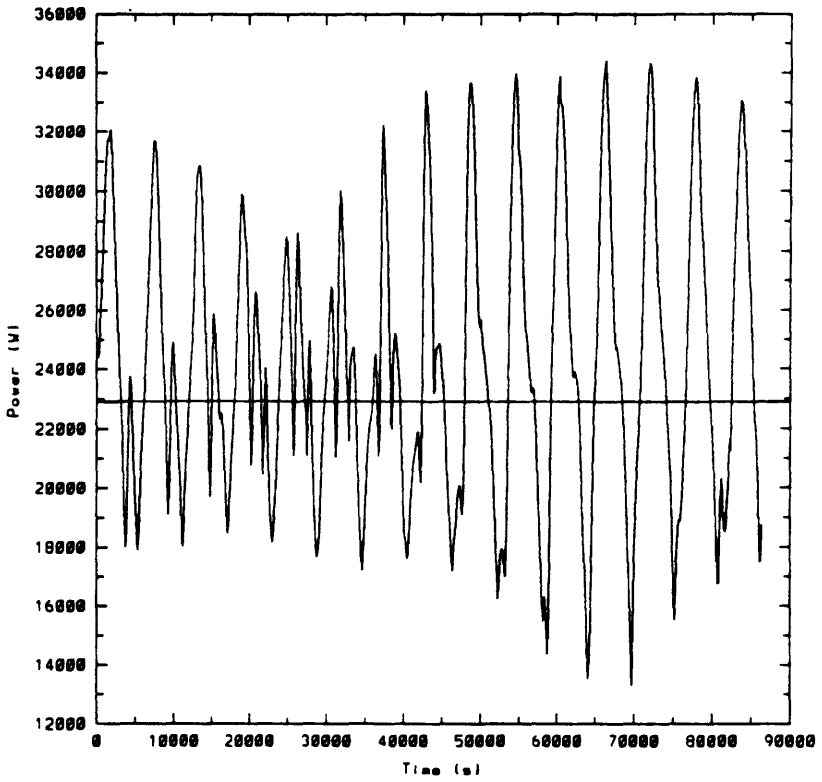

Fig. 28i Contactor Current (Maximum Power)

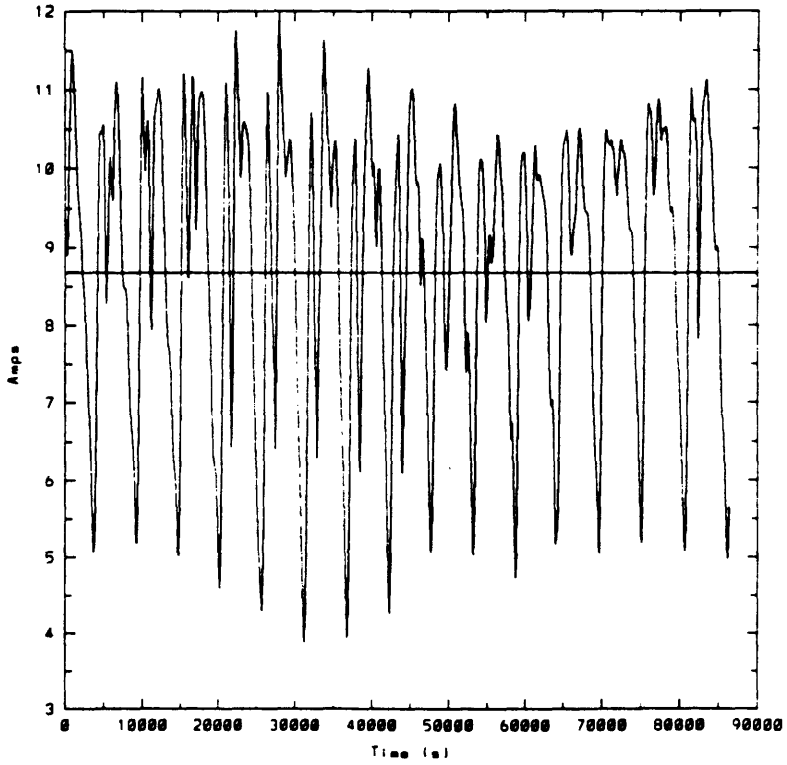

Fig. 28j Bare Tether Current (Maximum Power)

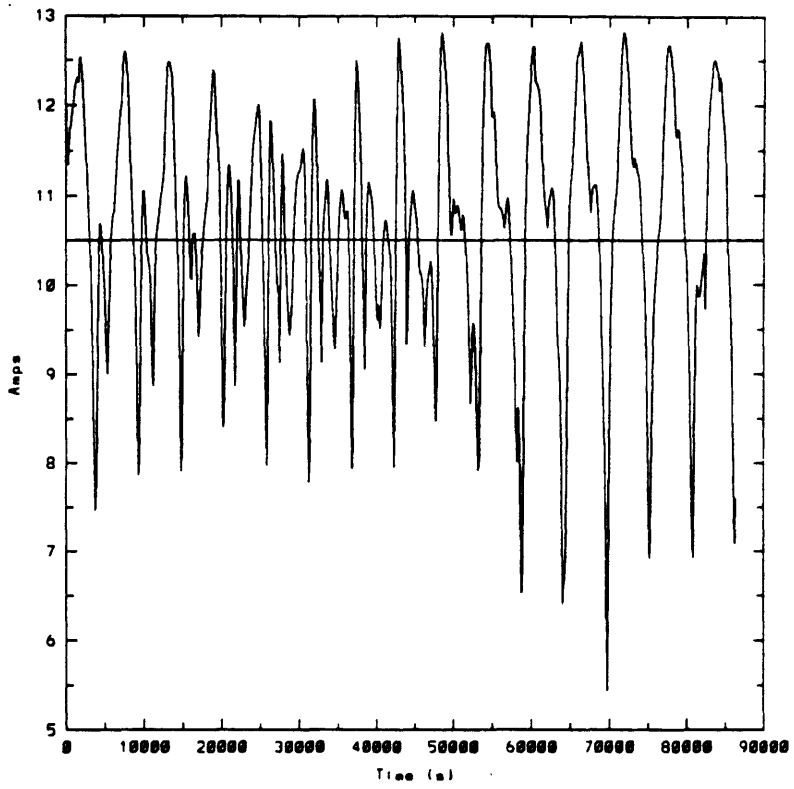

Fig. 28k Bare+Contactor Current (Maximum Power)

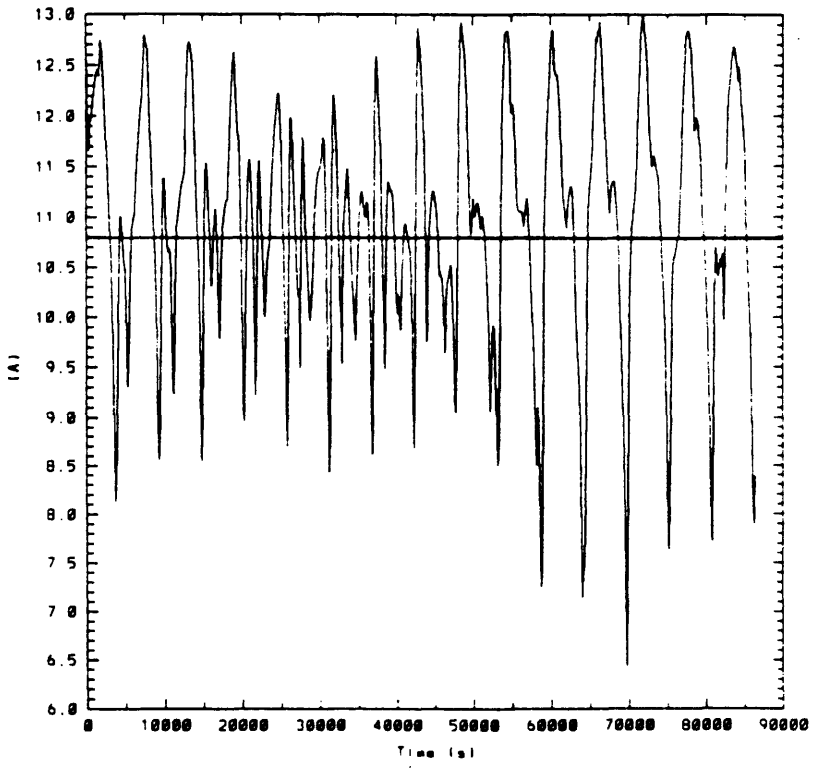

Fig. 28l Bare+Contactor Bare Current (Maximum Power)

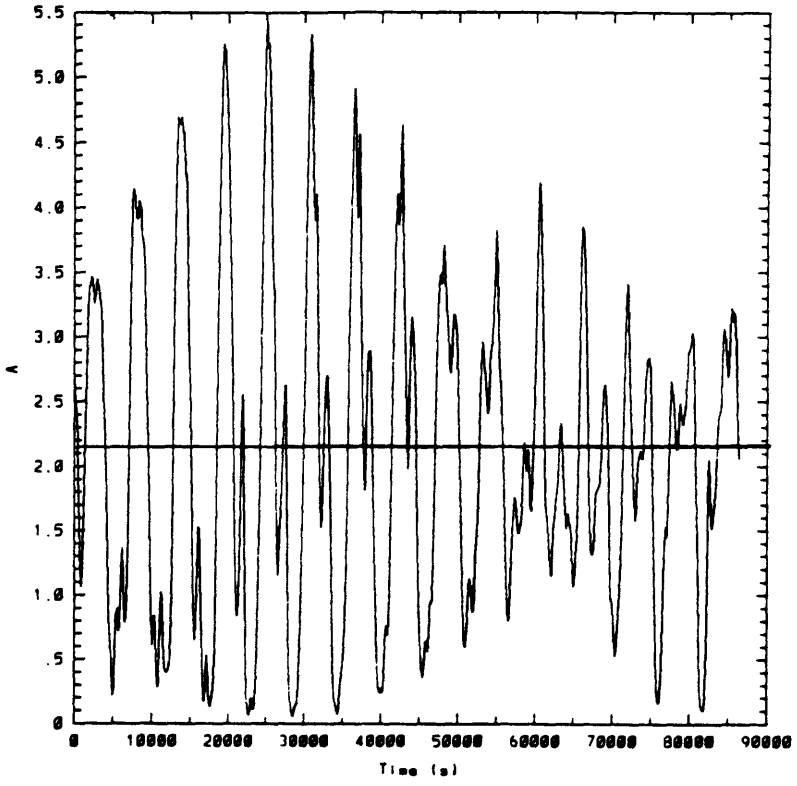

Fig. 28m Bare Tether Collecting Length (Maximum Power)

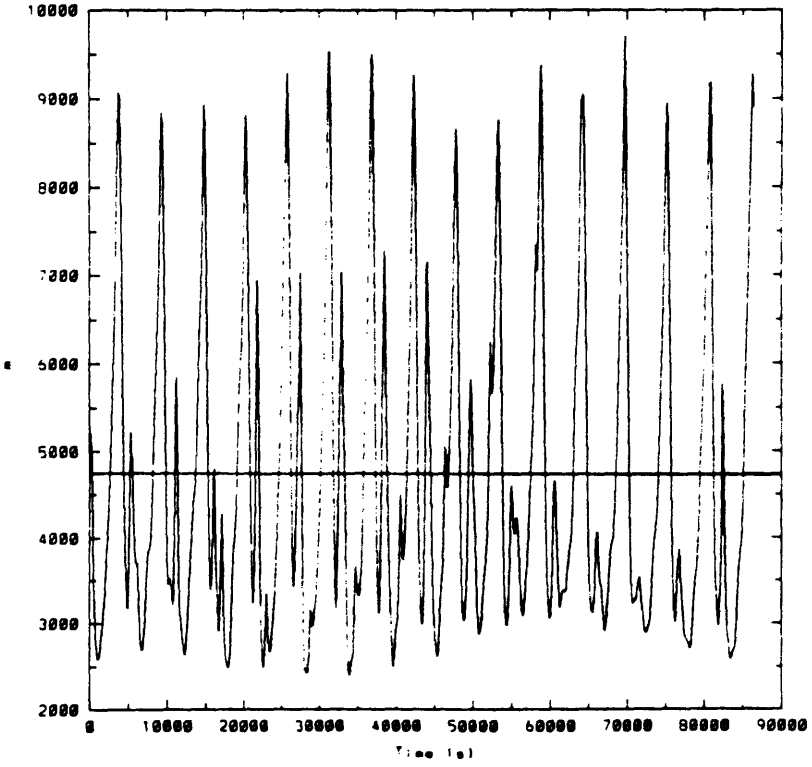

Fig. 28n Bare+Contactor Collecting Length (Maximum Power)

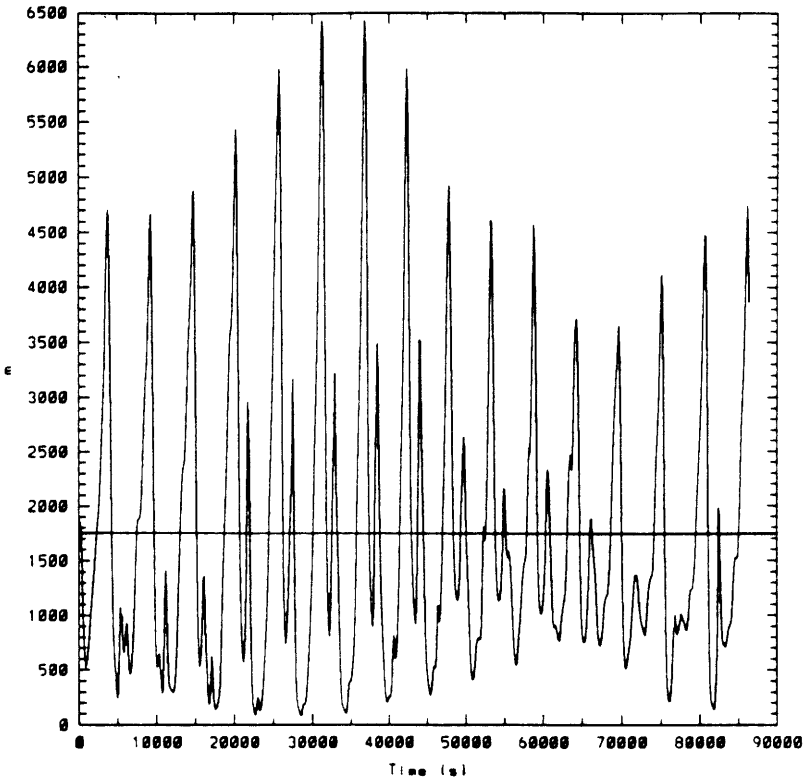

Fig. 28o Contactor Efficiency (Maximum Power)

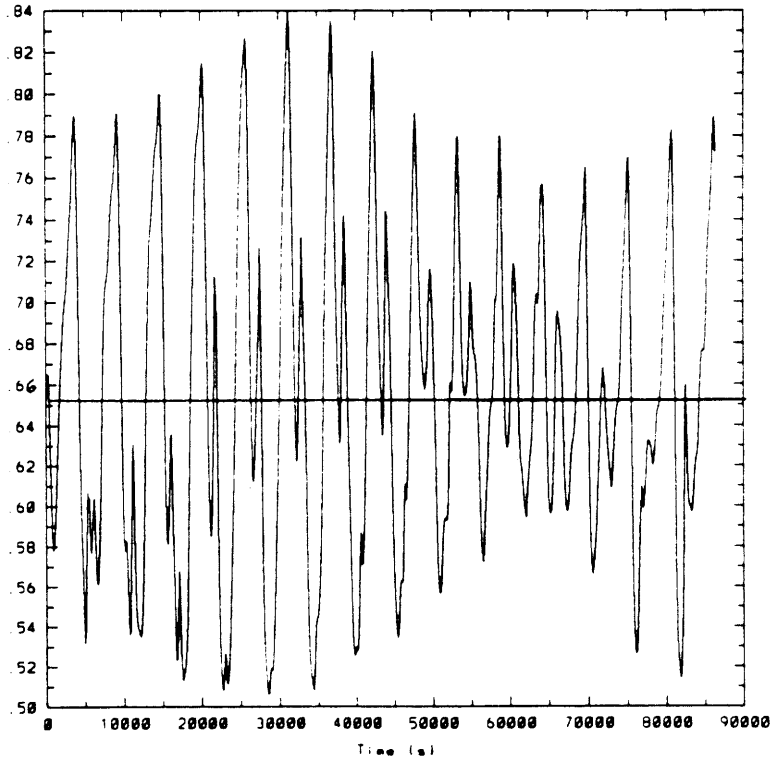

Fig. 28p Bare Tether Efficiency (Maximum Power)

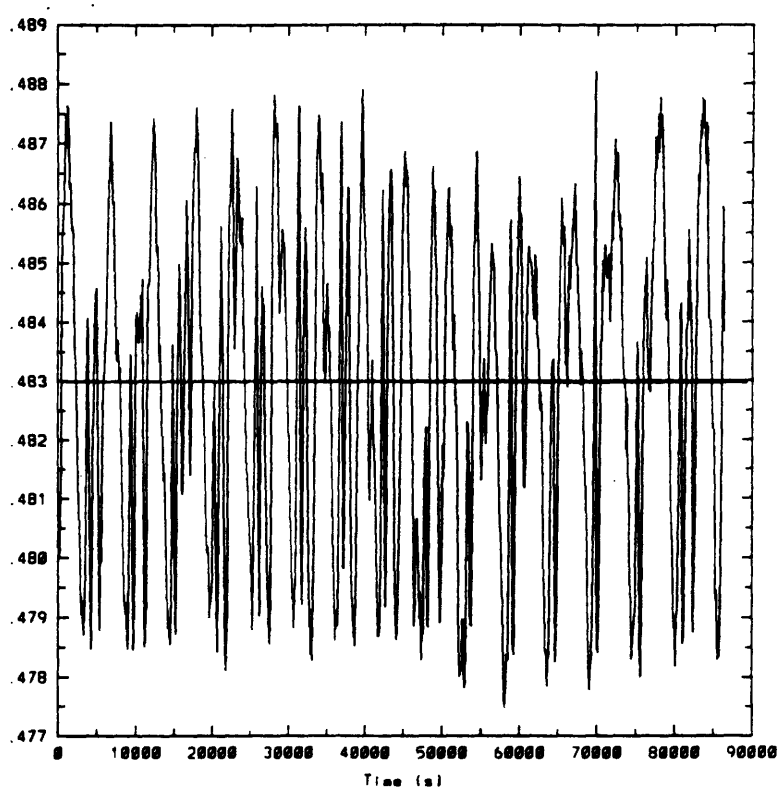

Fig. 28q Bare+Contactor Efficiency (Maximum Power)

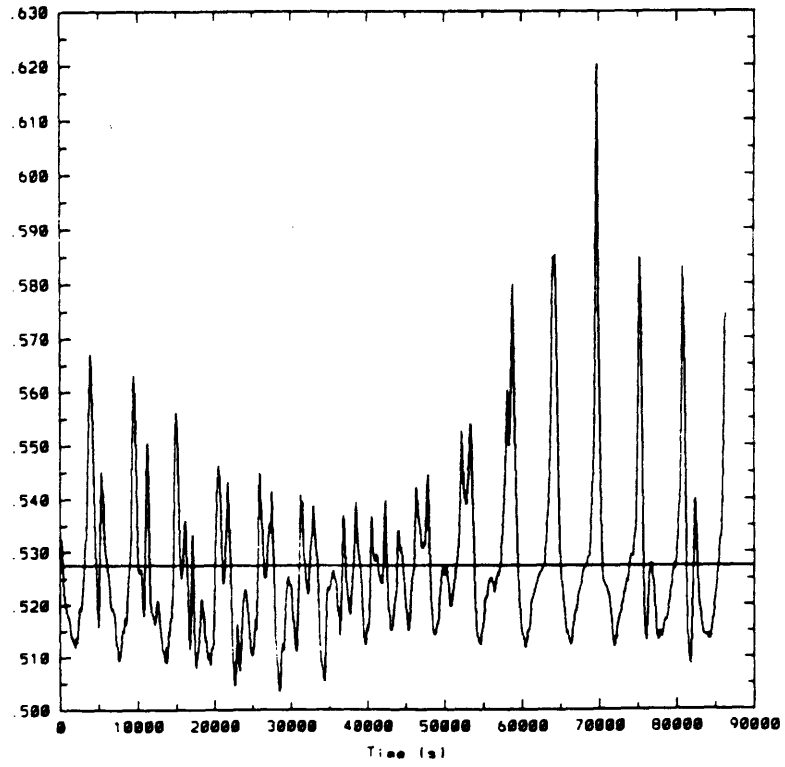

Fig. 28r Anodic Contactor Voltage (Maximum Power)

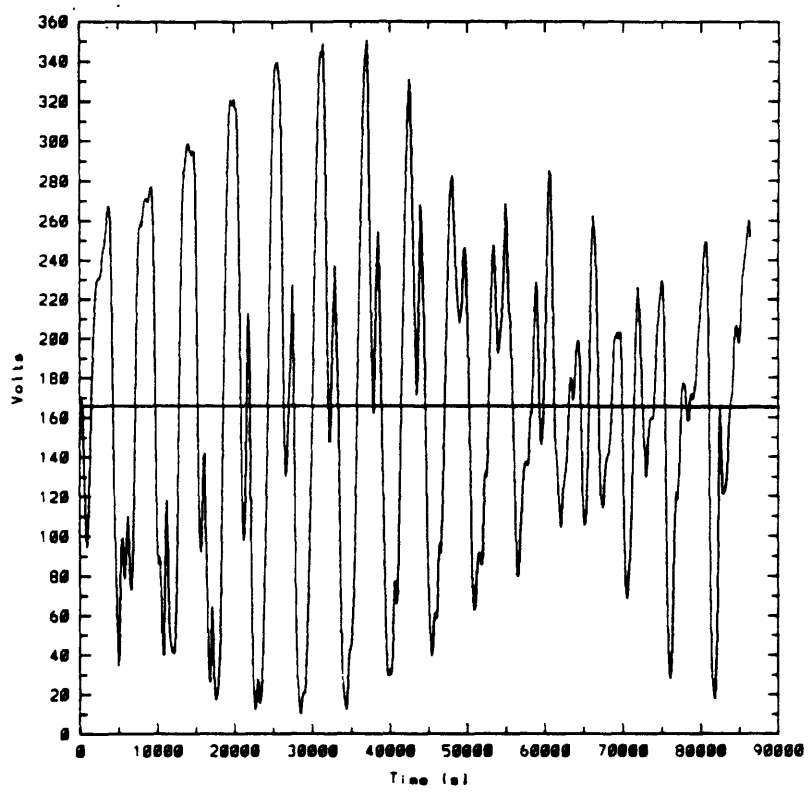

Fig. 28s Bare Anode Voltage (Maximum Power)

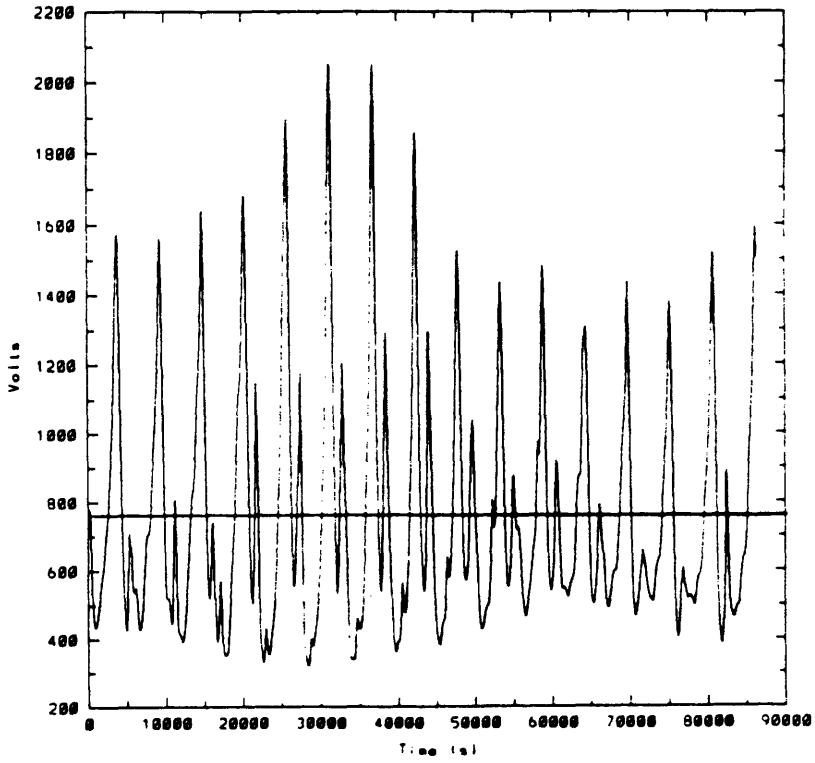

Fig. 28t Bare+Contactor Anodic Voltage (Maximum Power)

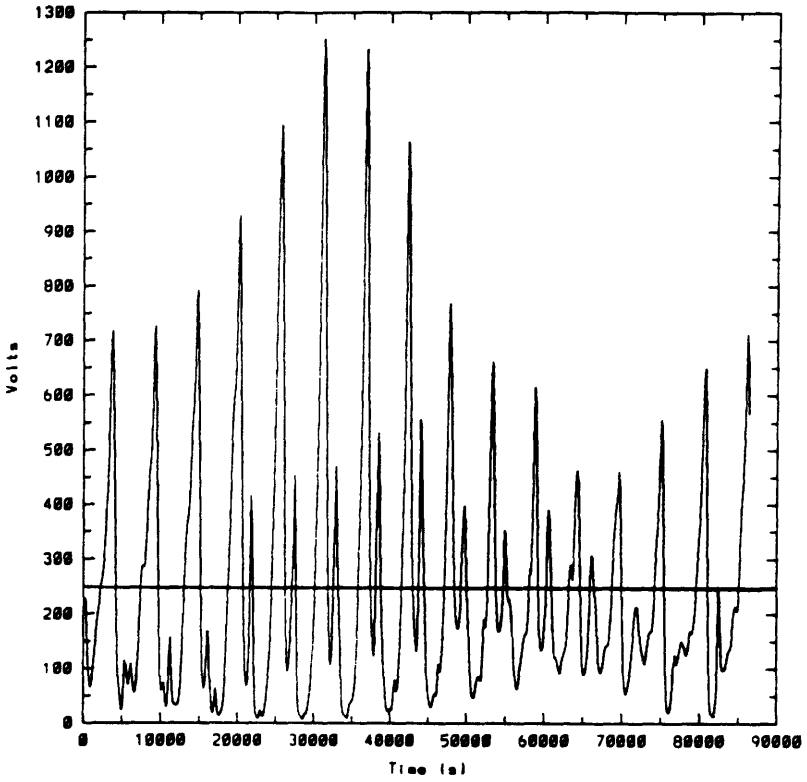

Fig. 28u Contactor Cloud Radius (Maximum Power)

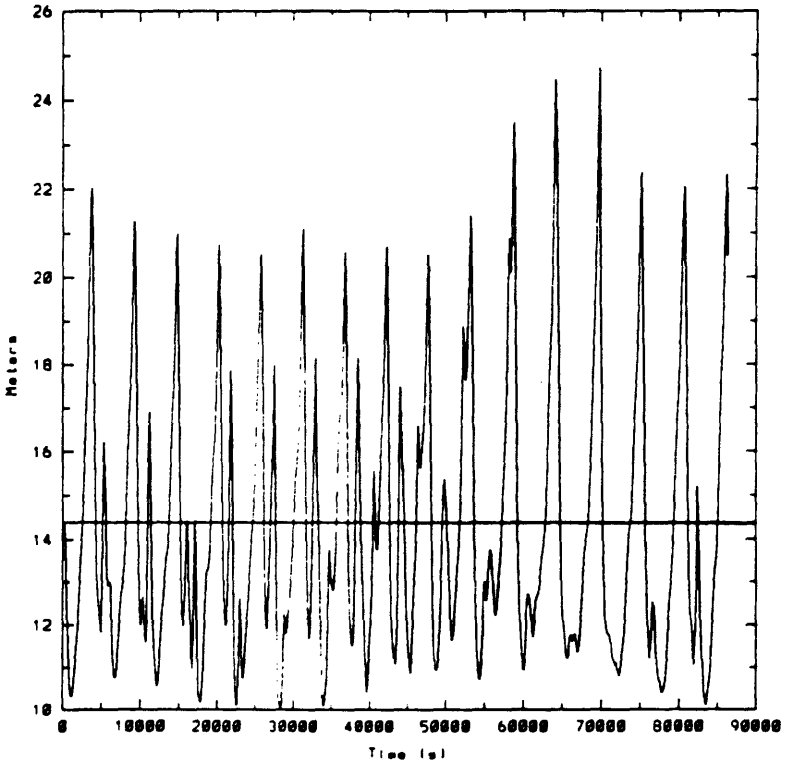

Fig. 29a Comparison of Power Delivered (UL=20kW, LL=19.5kW)

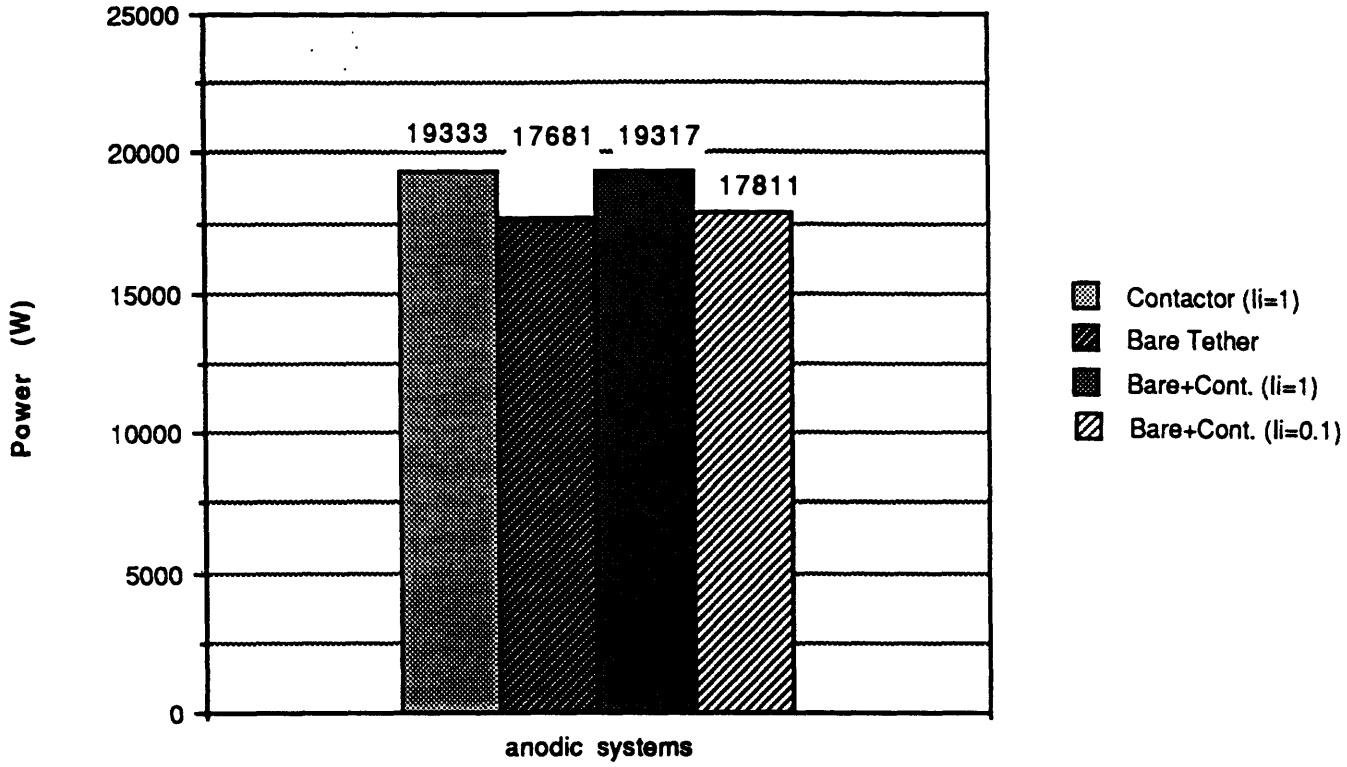

Fig. 29b Comparison of Specific Power (UL=20kW, LL=19.5kW)

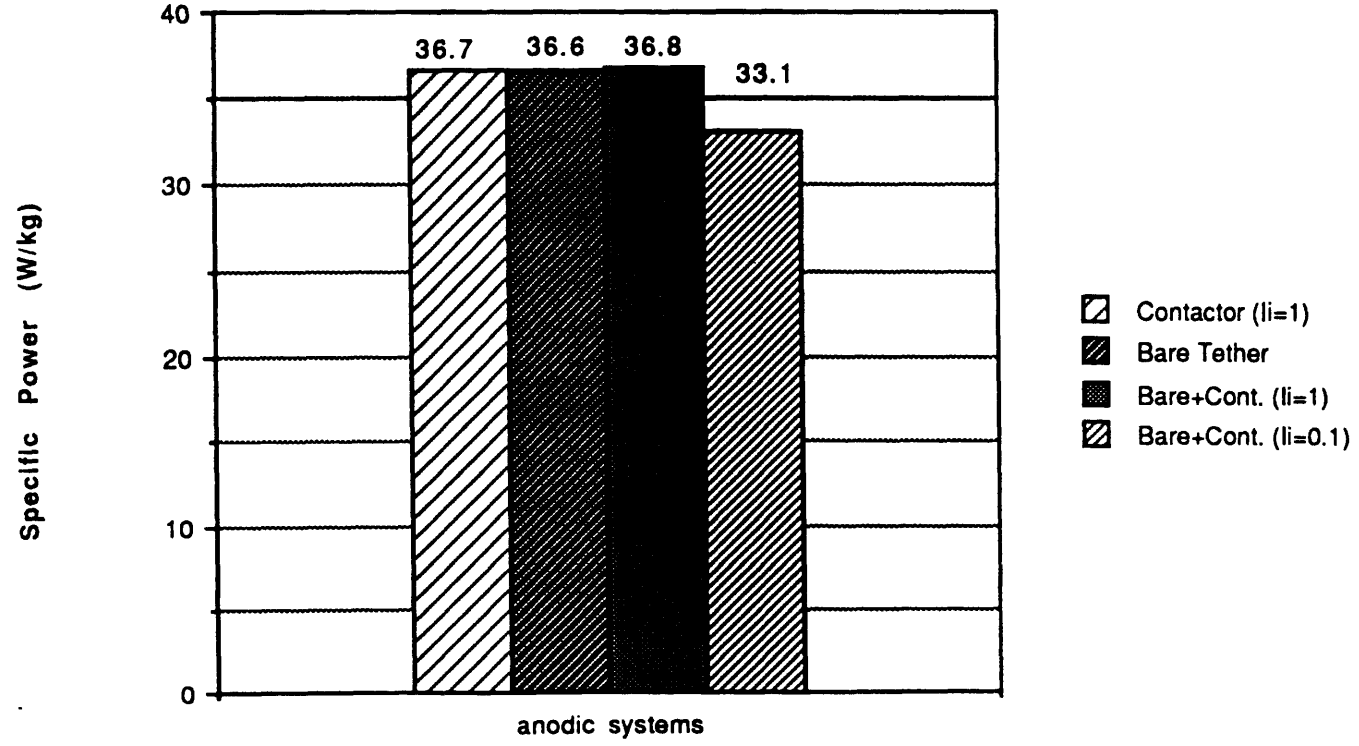

Fig. 29c Comparison of Efficiency (UL=20kW, LL=19.5kW)

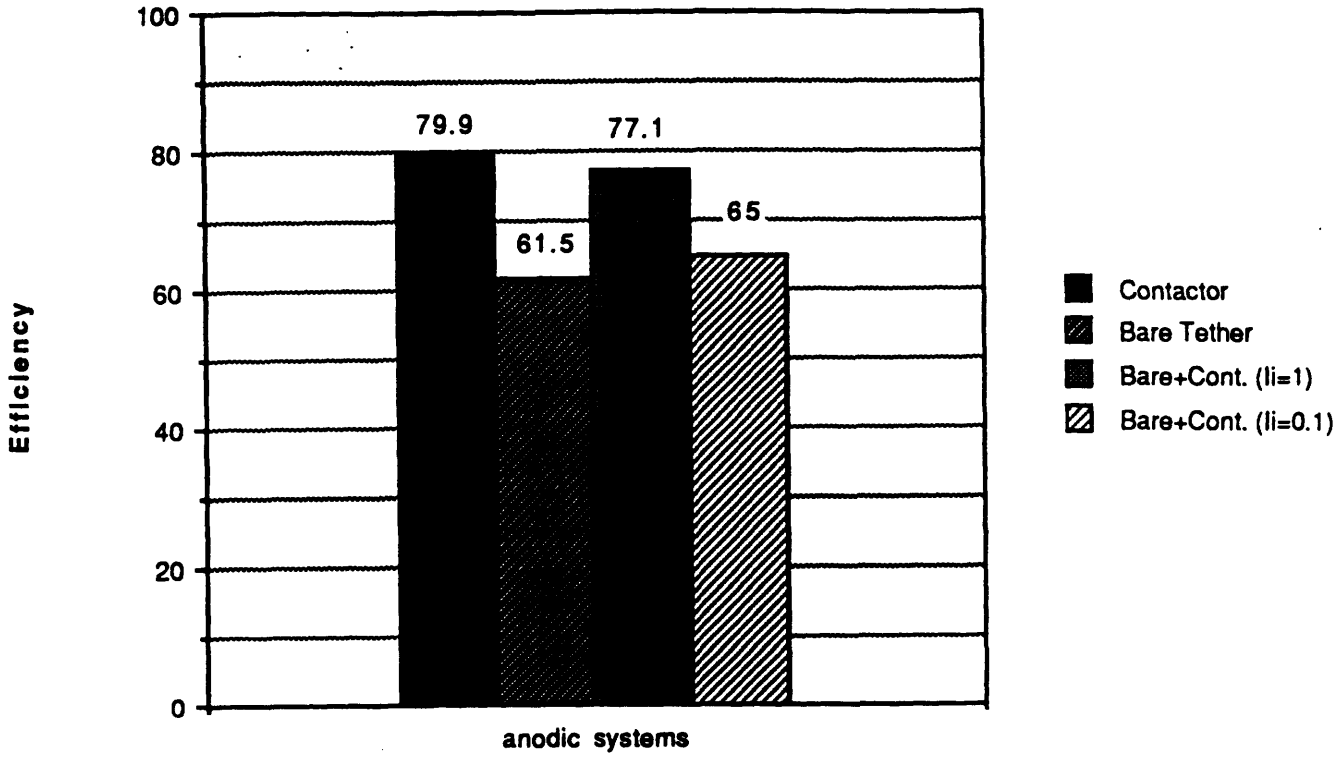

Fig. 29d Comparison of Mass Breakdowns (UL=20kW, LL=19.5kW)

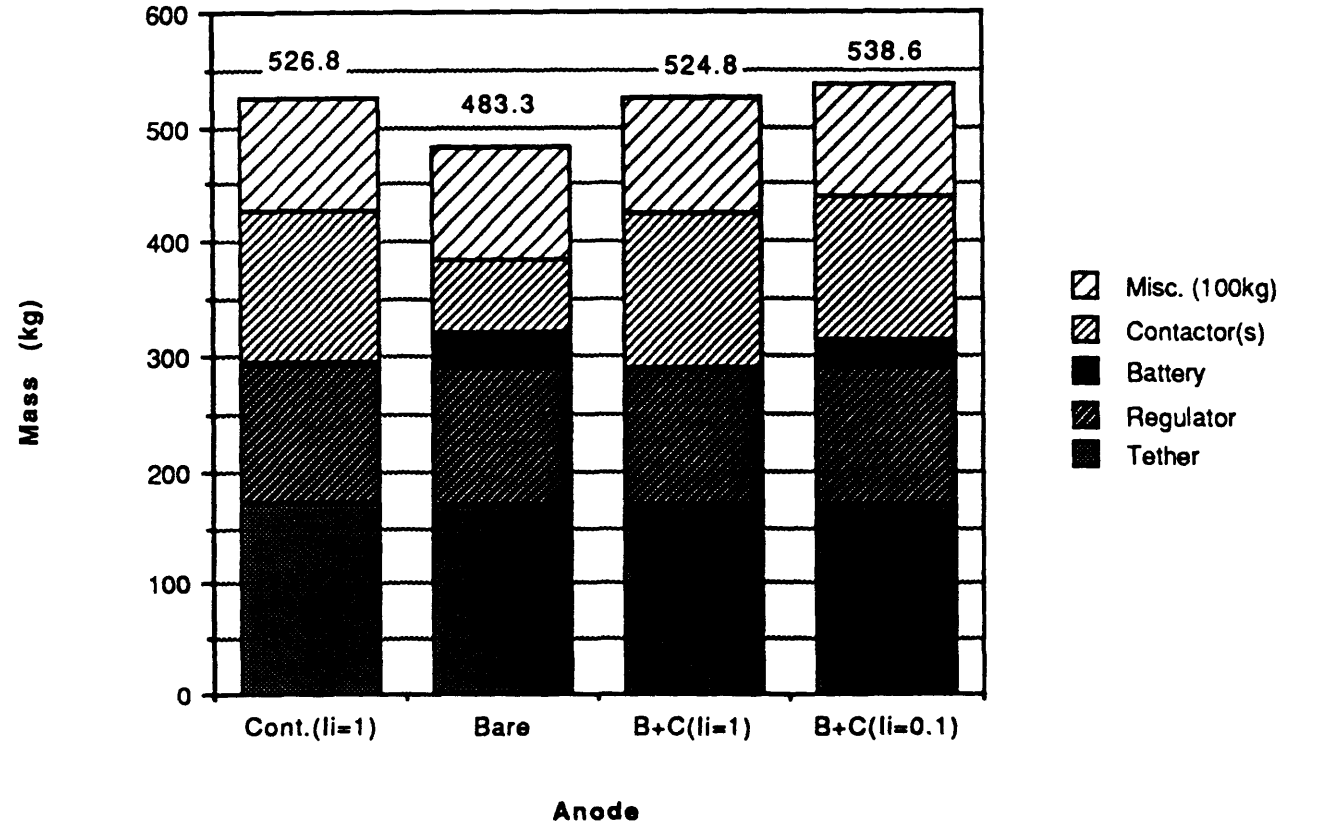

Fig. 29e Drag Makeup Fuel Consumption Per Day (UL=20kW, LL=19.5kW)

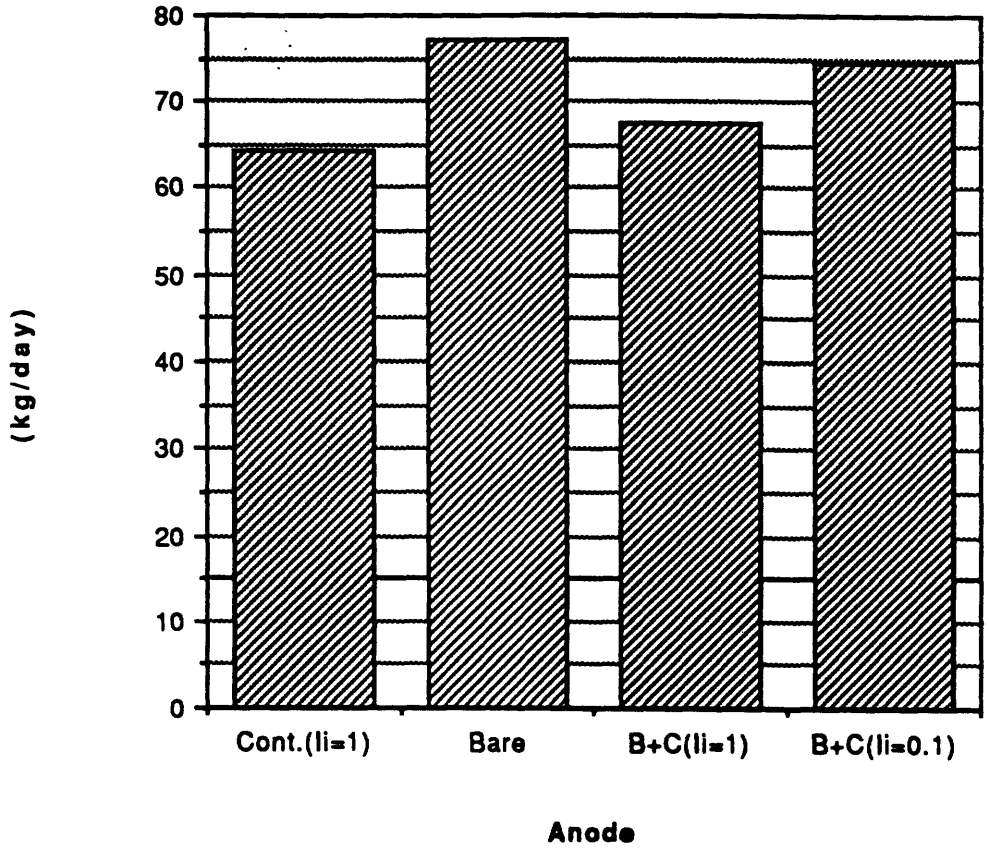

Fig. 29f Contactor Controlled Power (UL=20 kW, LL=19.5 kW)

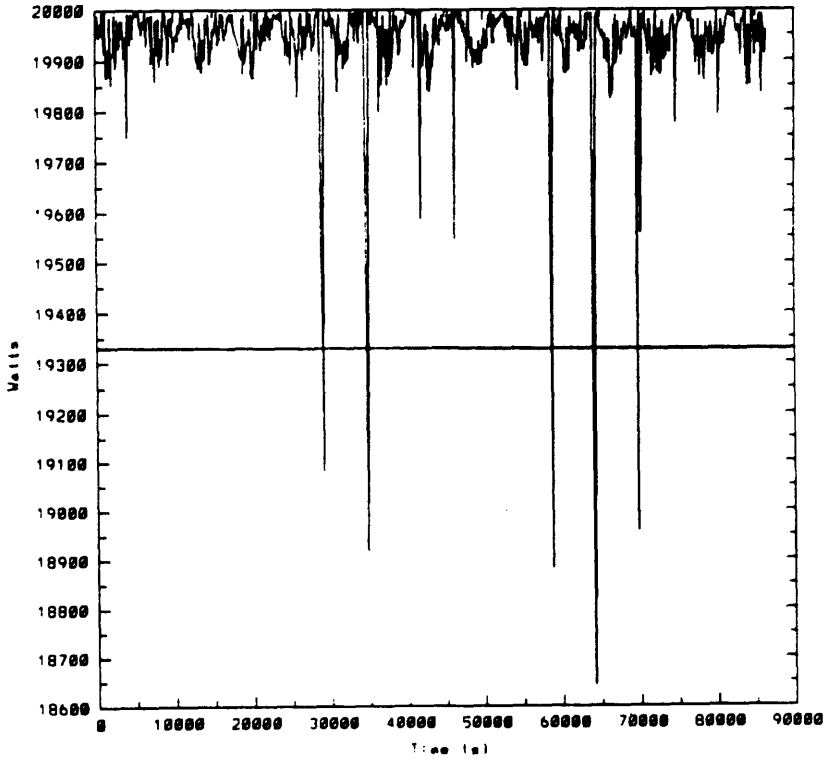

Fig. 29g Bare Tether Controlled Power (UL=20 kW, LL=19.5 kW)

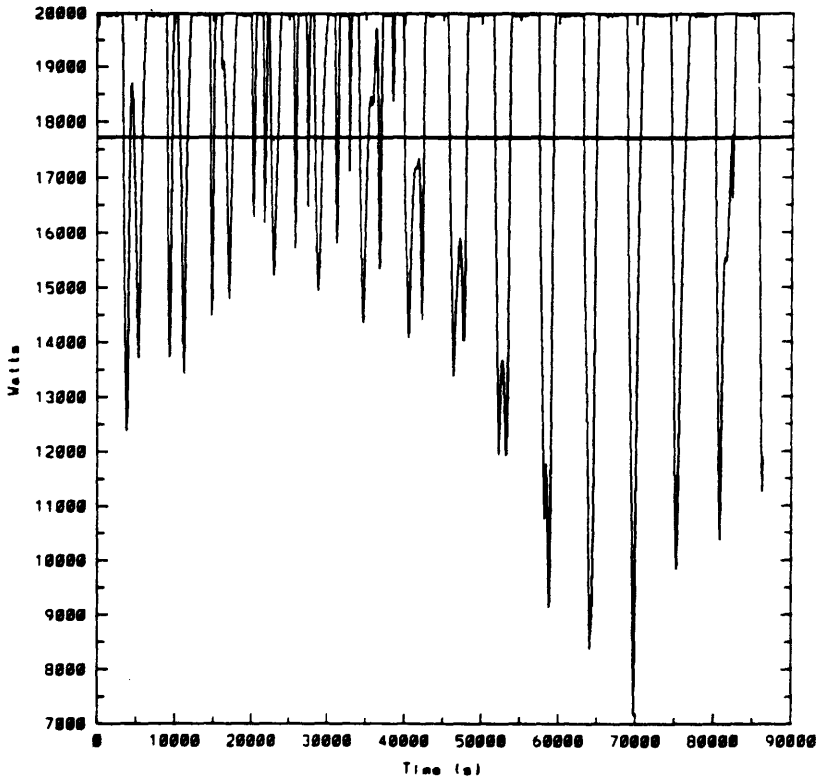

Fig. 29h Bare+Contactor Controlled Power (UL=20 kW, LL=19.5 kW)

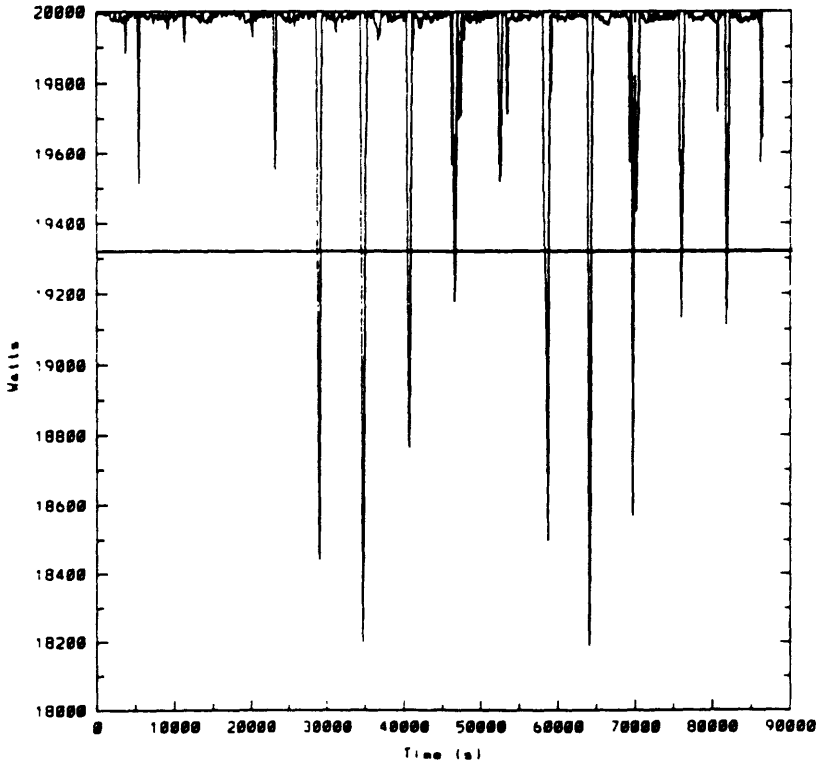

Fig. 29i Contactor Current (Controlled)

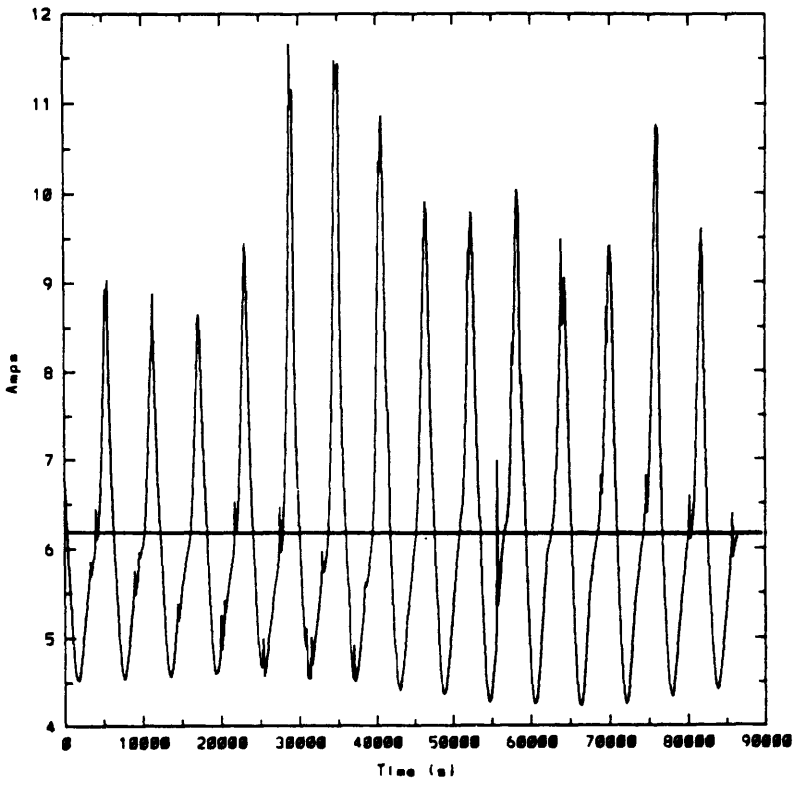

Fig. 29j Bare Tether Current (Controlled)

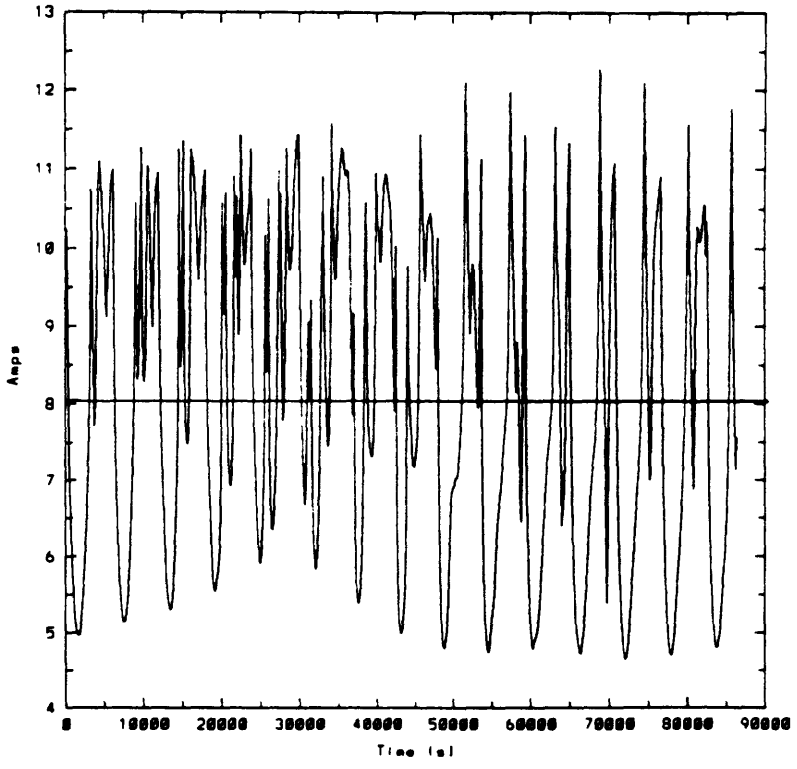

Fig. 29k Bare+Contactor Current (Controlled)

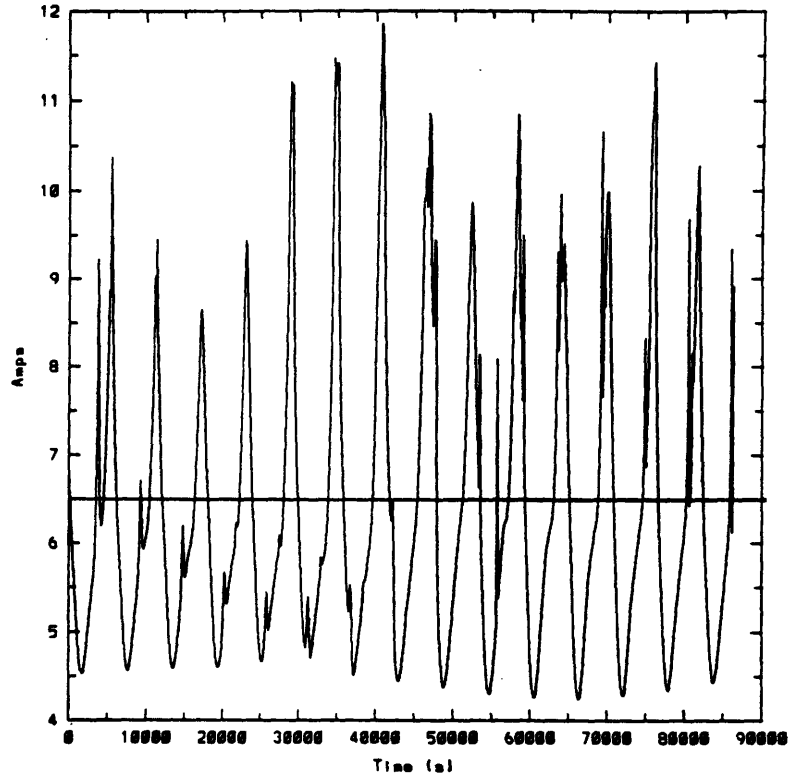

Fig. 29l Bare Tether Collecting Length (Controlled)

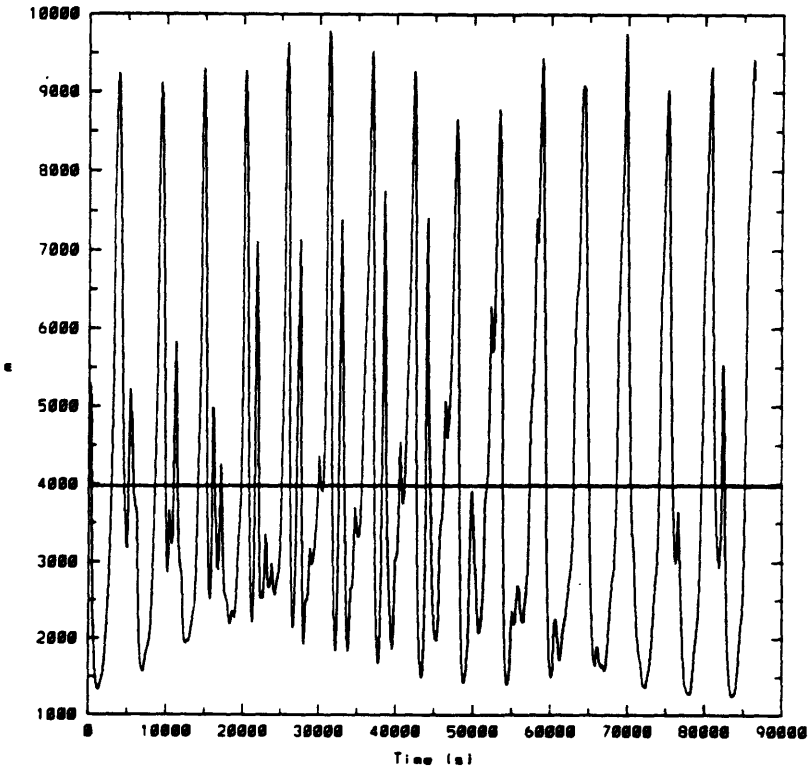

Fig. 29m Bare+Contactor Collecting Length (Controlled)

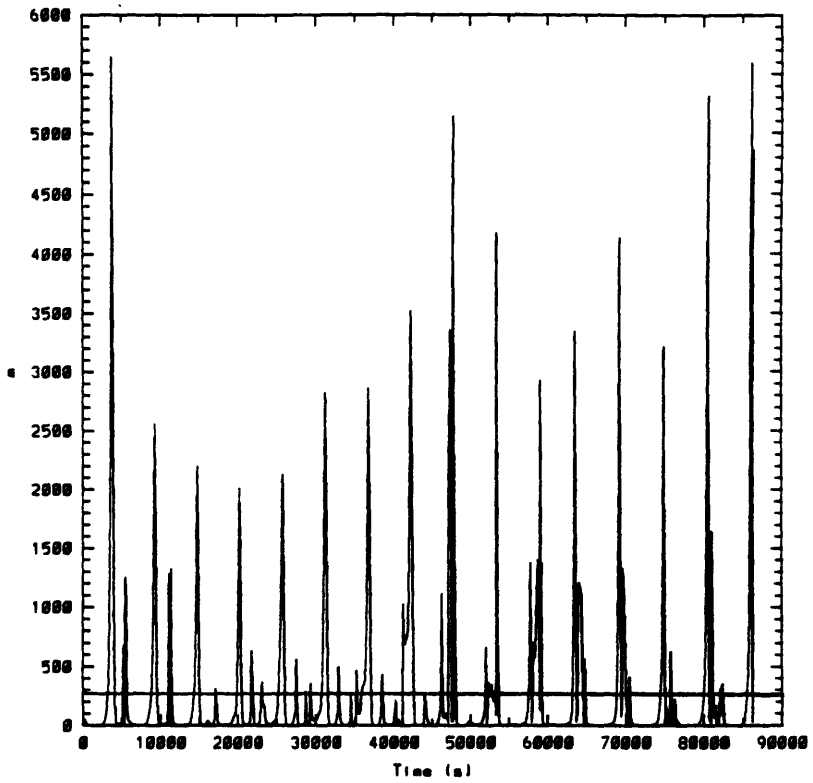

Fig. 29n Contactor Efficiency (Controlled)

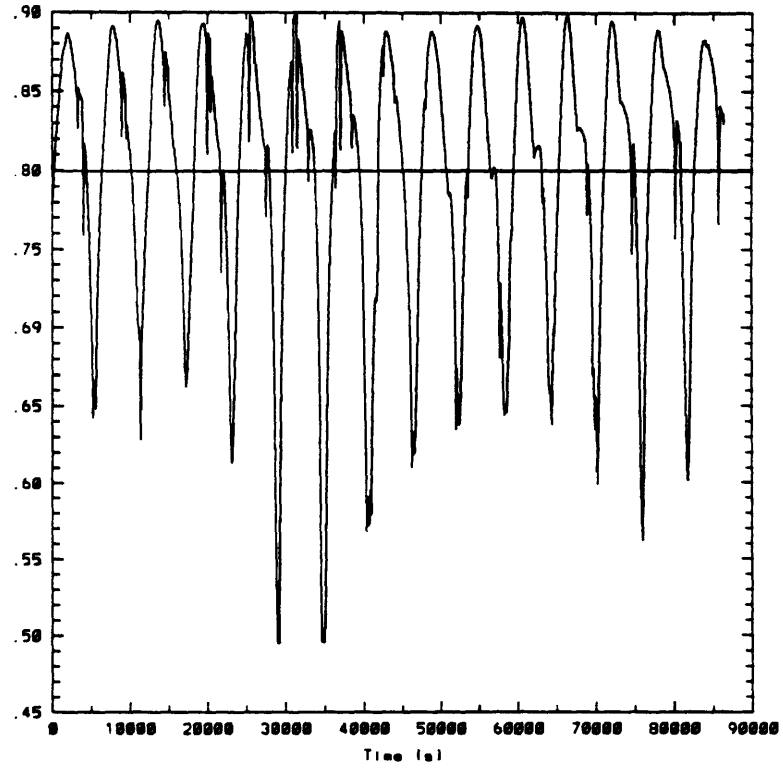

Fig. 29o Bare Tether Efficiency (Controlled)

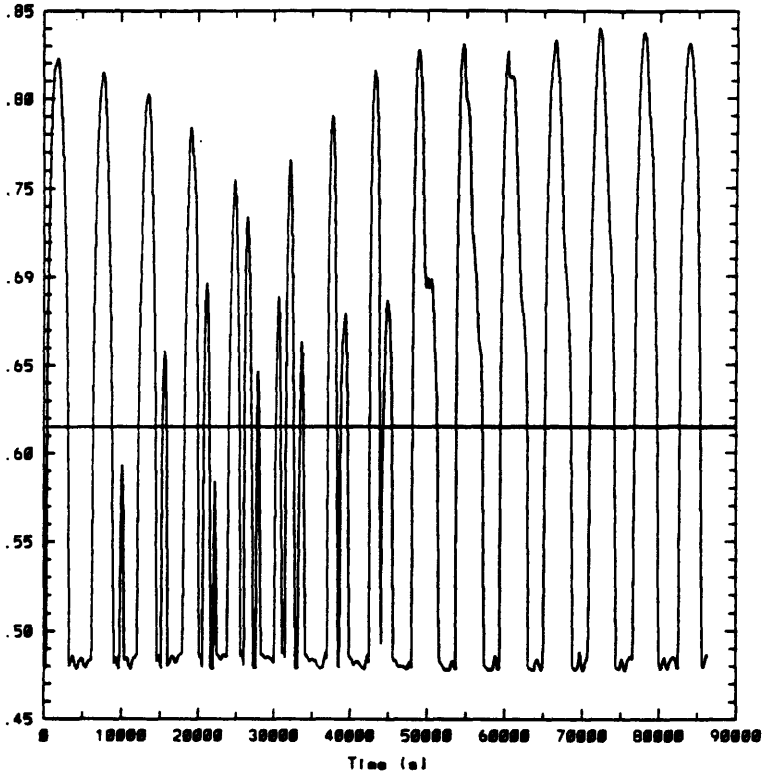

Fig. 29p Bare+Contactor Efficiency (Controlled)

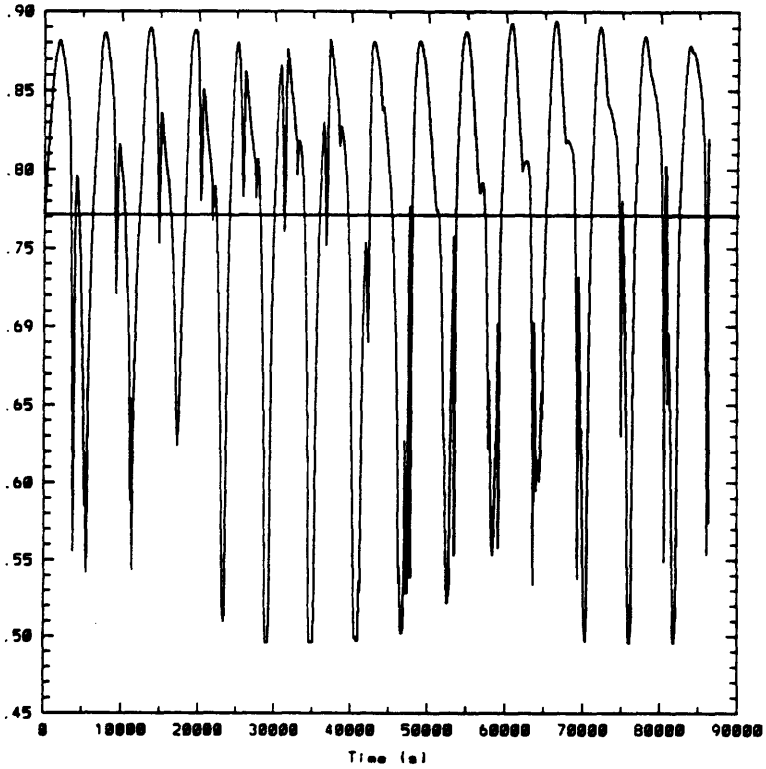

Fig. 29q Contactor Cloud Radius (Controlled)

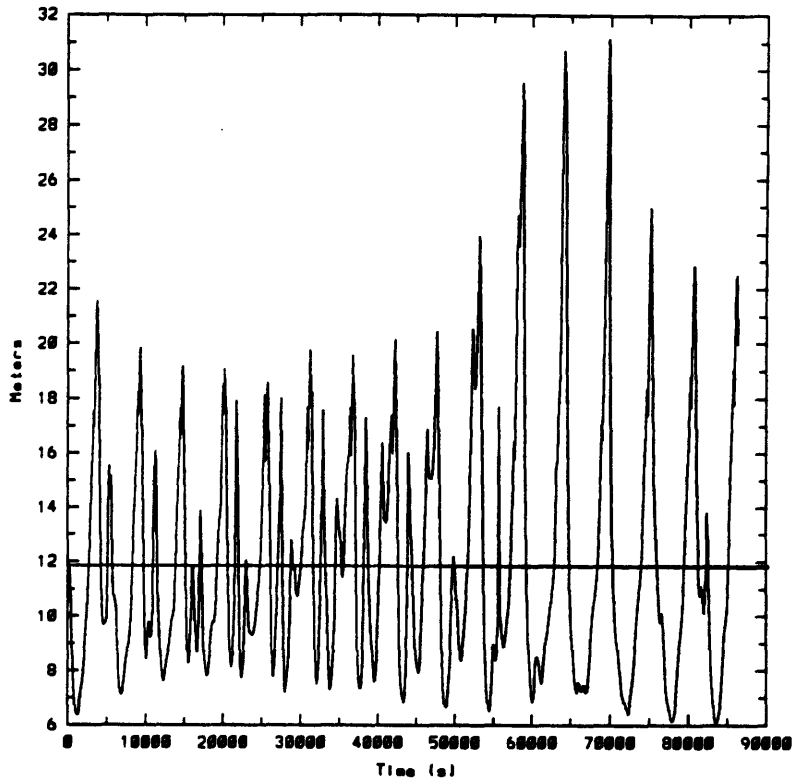

Fig. 30a Tether Deflection (To Scale)
(l=10, Mt=175(2mm), Me=100,500)

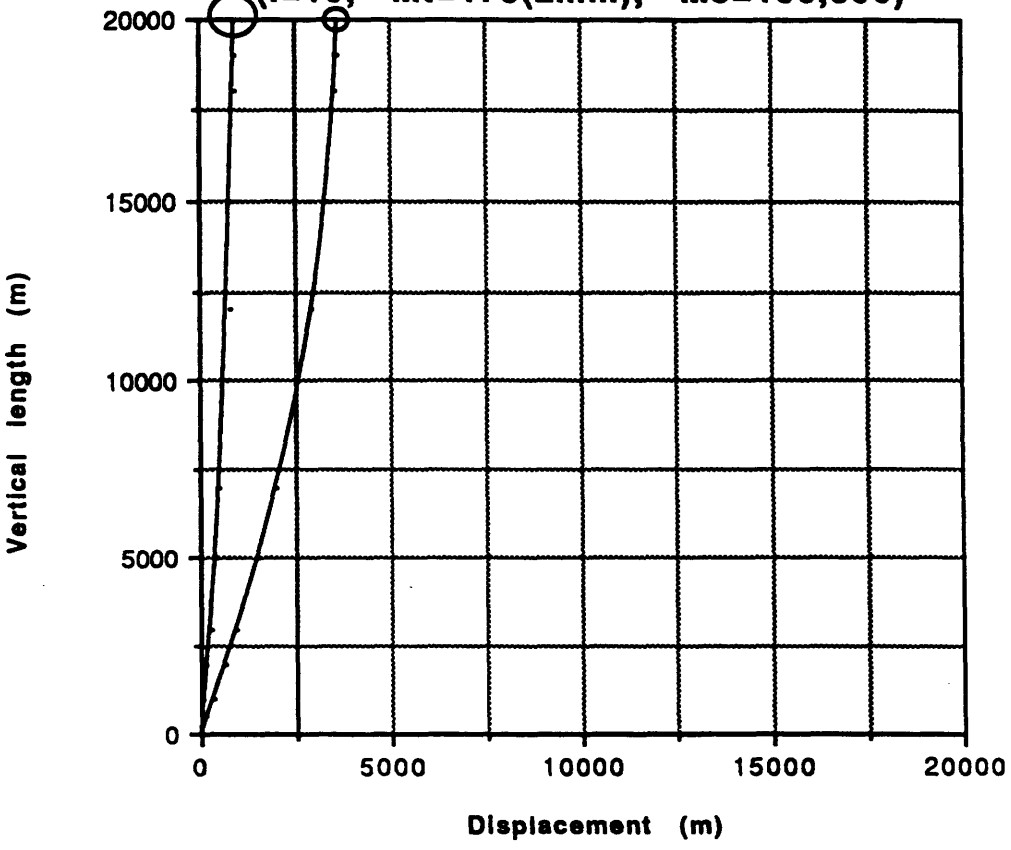

Fig. 30b Endtip Deflection vs. Endmass (I=10A, L=20km, 2mm tether)

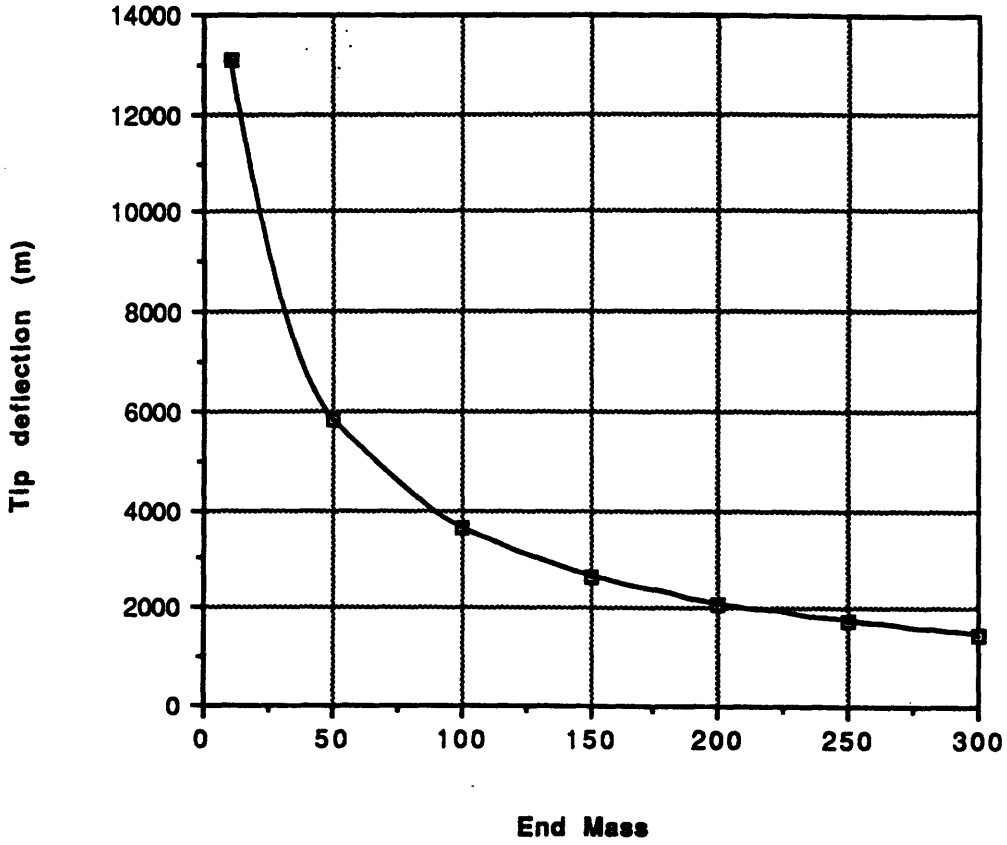

Fig. 30c Base Deflection Angle vs. Endmass (I=10A, L=20km, 2mm tether)

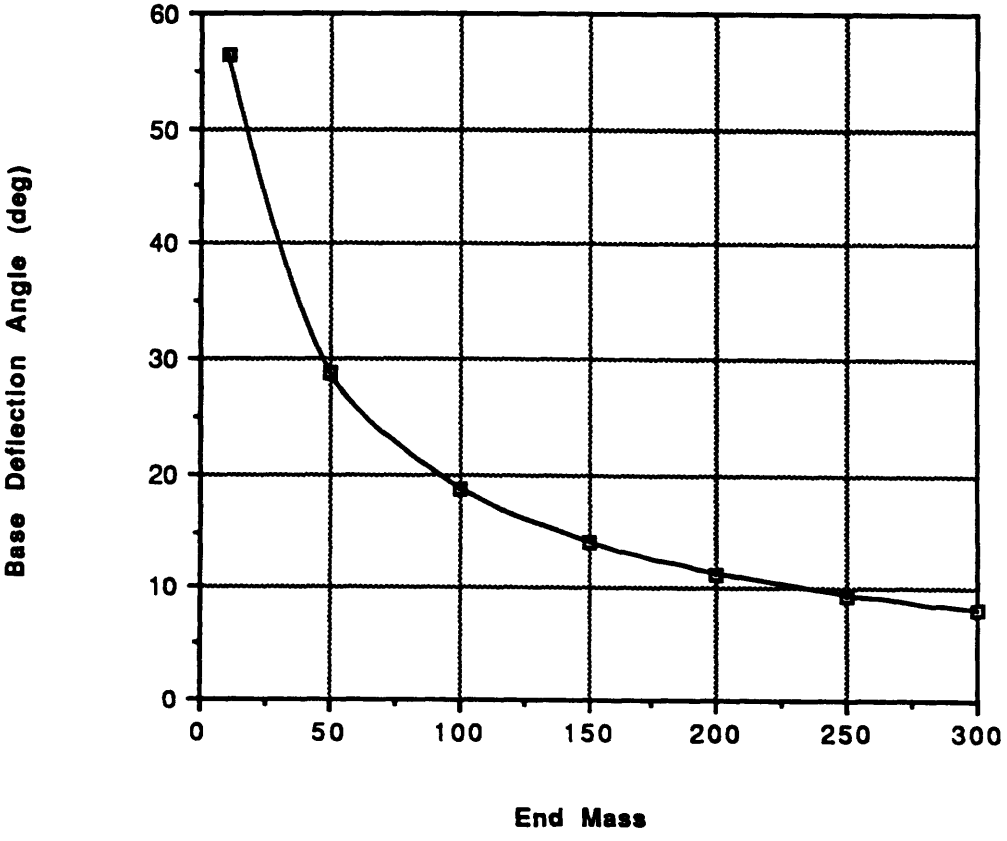

Fig. 30d Entip Deflection vs. Current (L=20km, Me=100kg, 2mm tether)

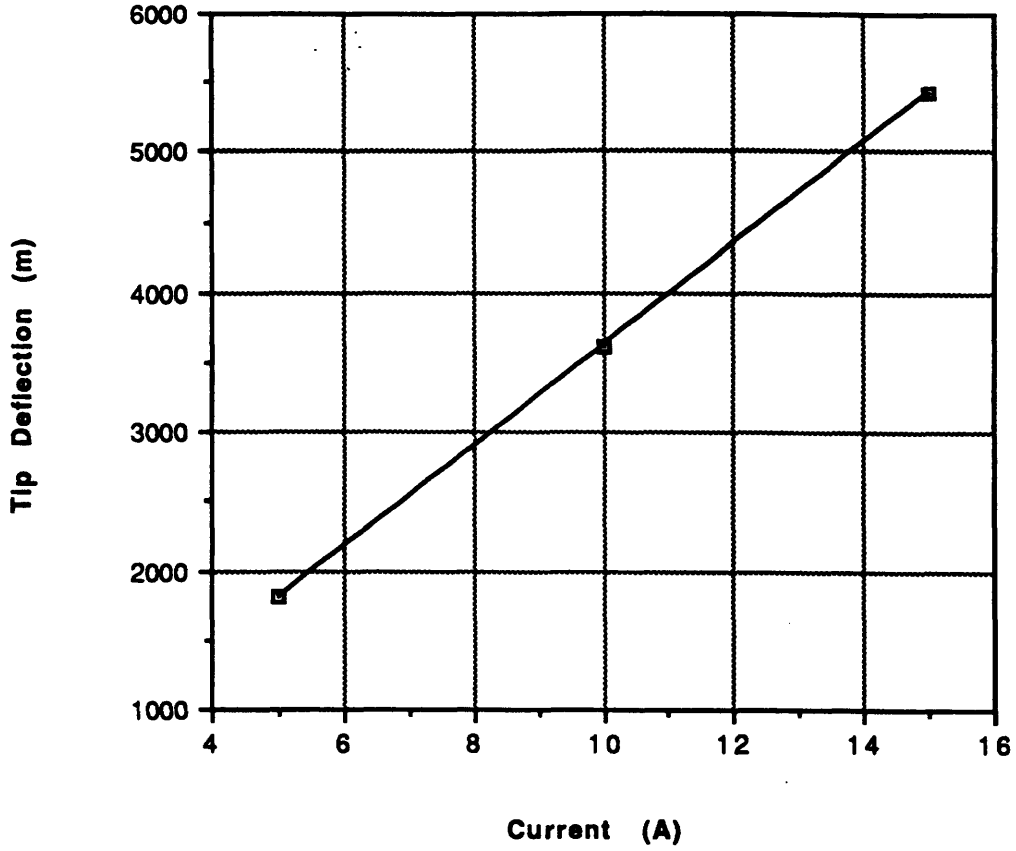

Fig. 30e Base Deflection Angle vs. Current (L=20km, Me=100kg, 2mm tether)

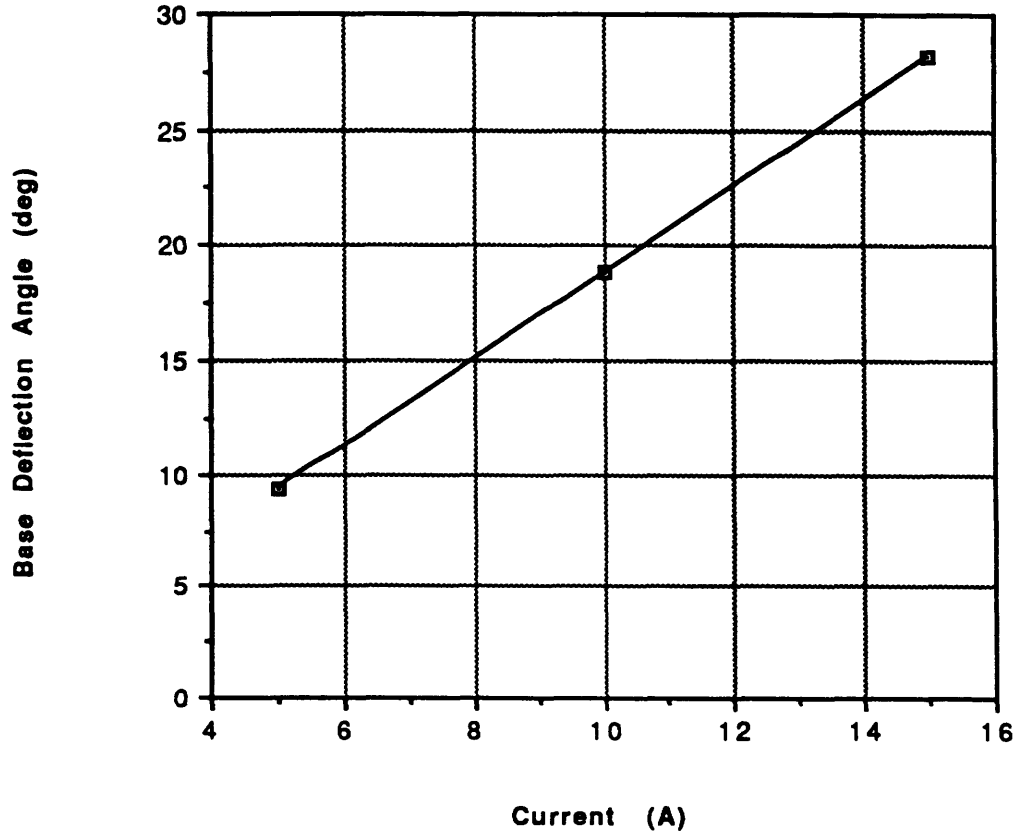

Fig. 30f Entip Deflection and Base Deflection Angle for (Full/Partially) Bare Tether (L=20km, I=10A, Me=100kg, 2mm tether)

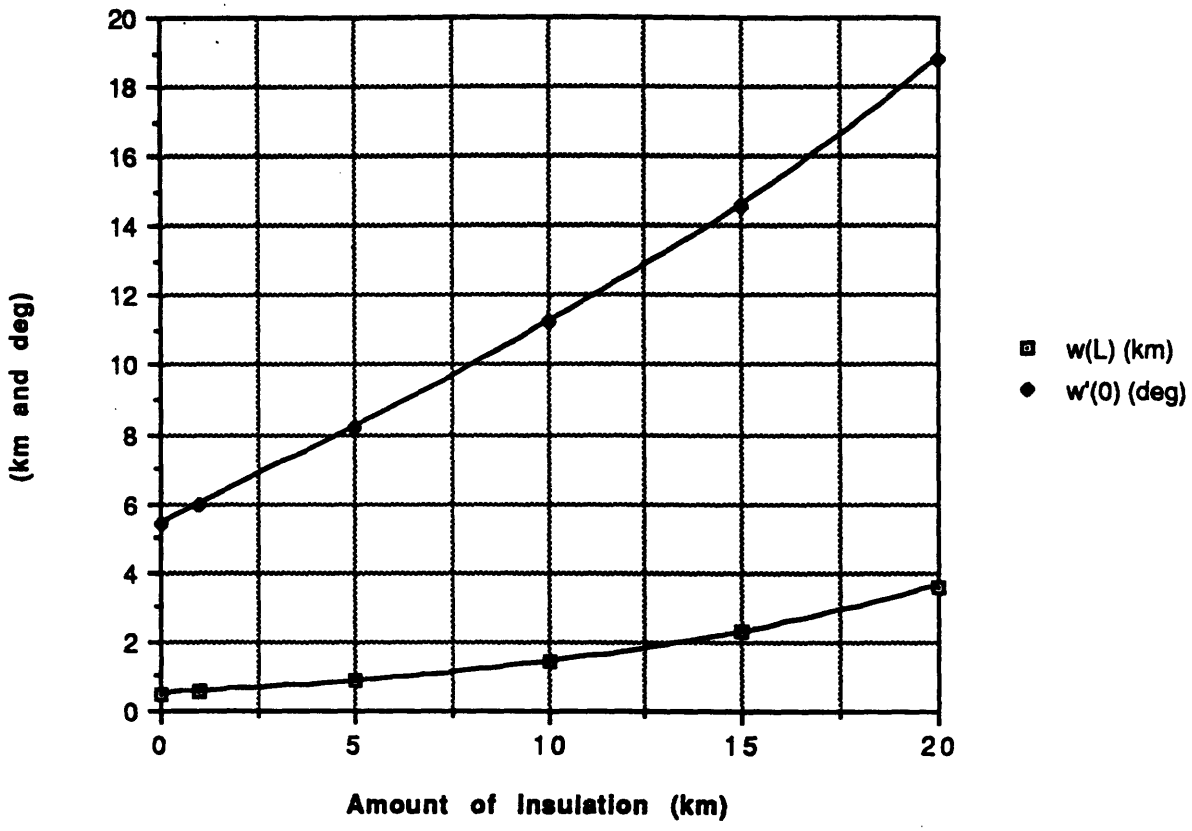

Fig. 31a Tether Heat Flux (0° Declination Angle)

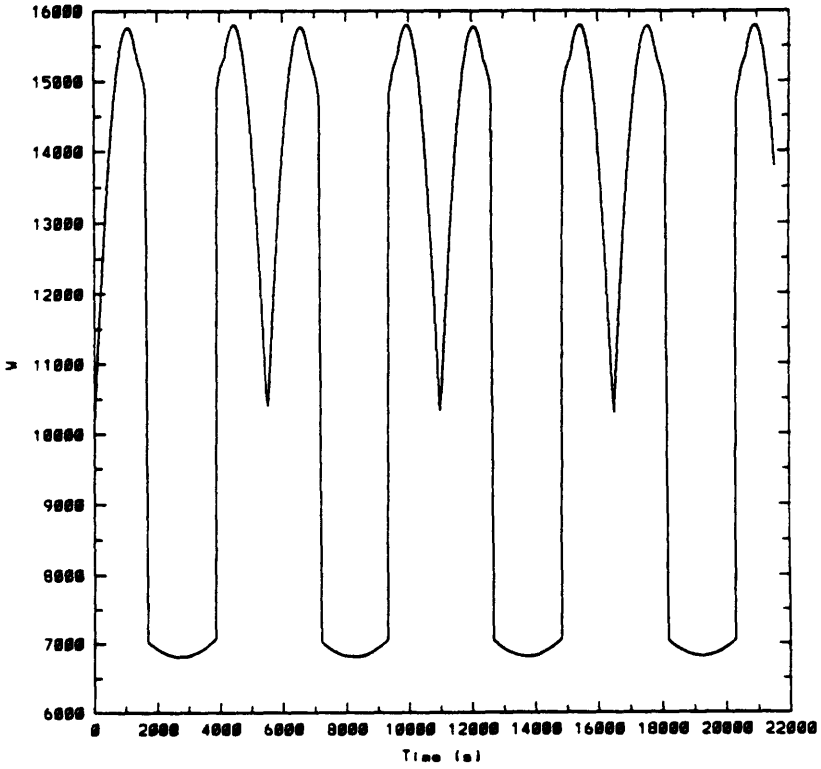

Fig. 31b Tether Heat Flux (23.5° Declination Angle)

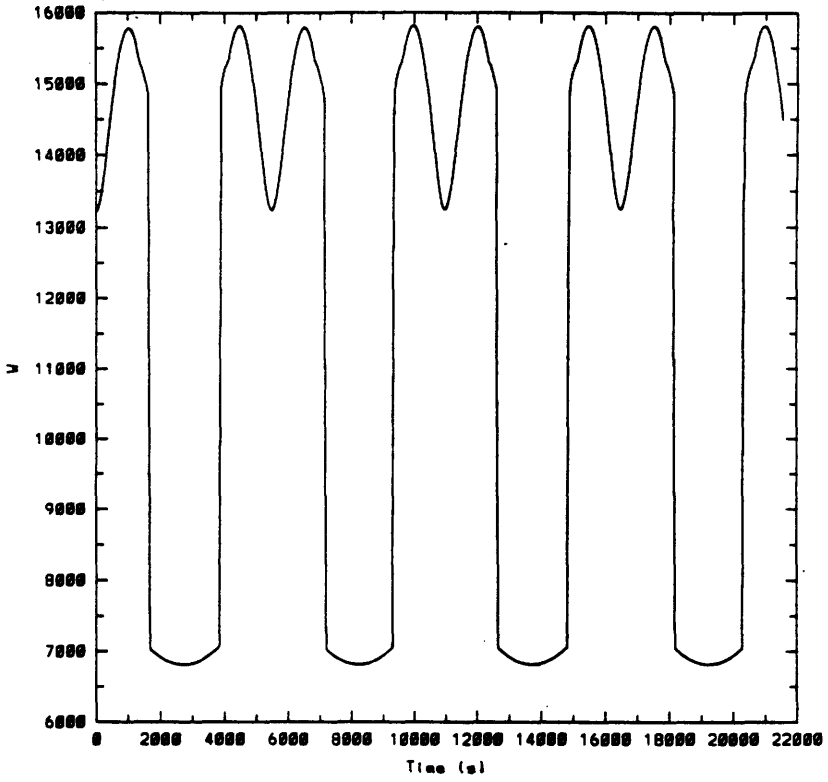

Fig. 31c Tether Temperature, No Ohmic Heating

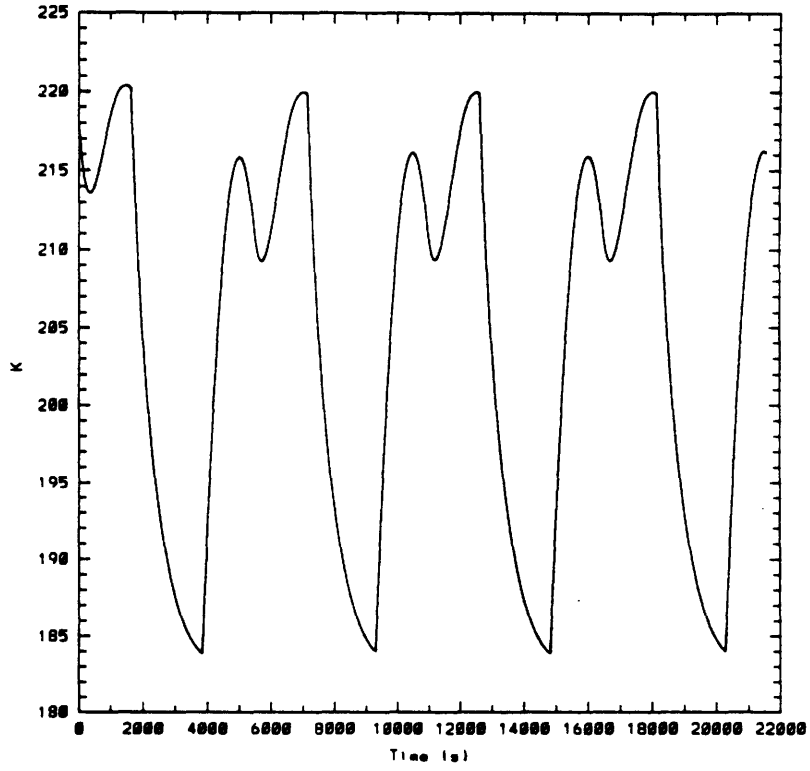

Fig. 31d Tether Temperture, Maximum Power

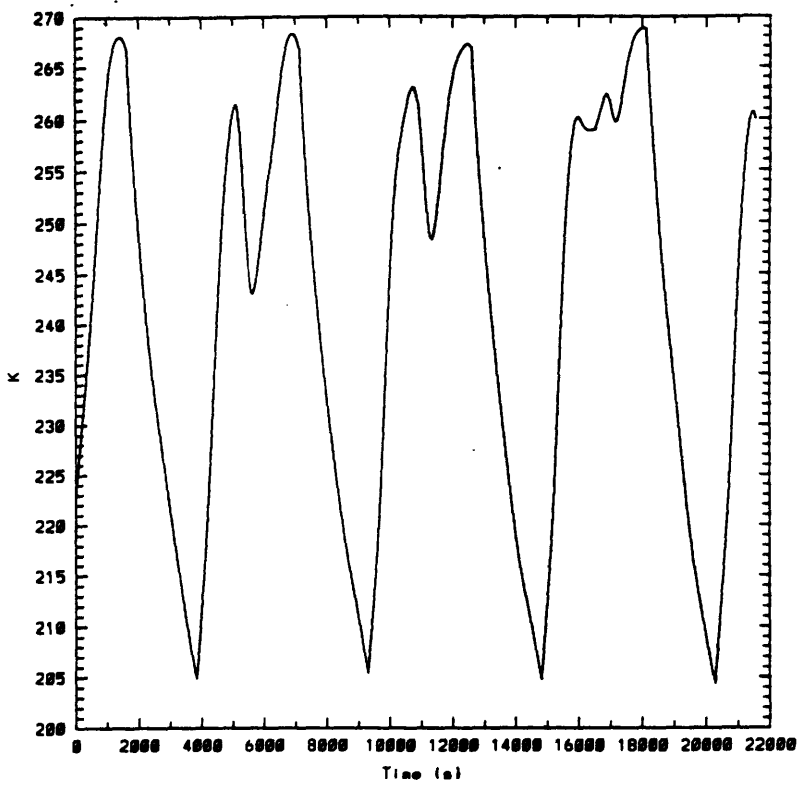

Fig. 31e Tether Temperature (UL=20 kW, LL=19.5 kW)

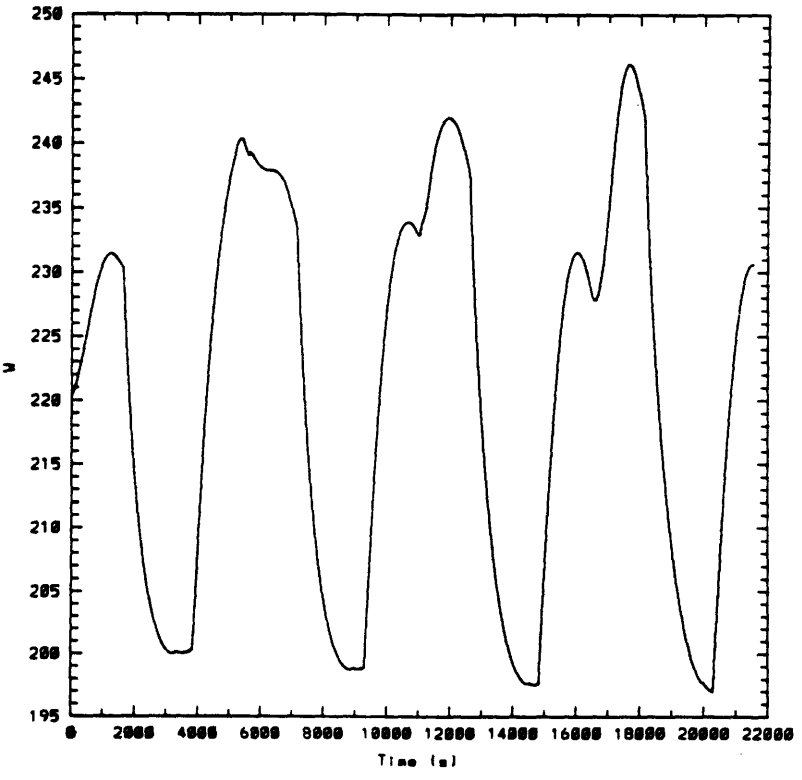

Fig. 31f Tether Resistance Variations

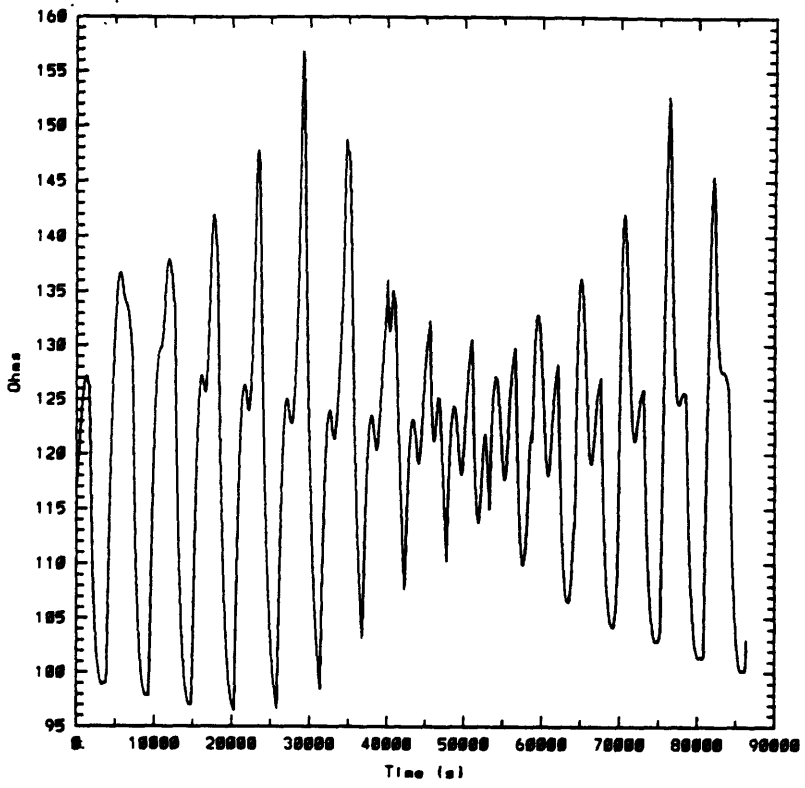

Fig. 31g Tether Length Variations

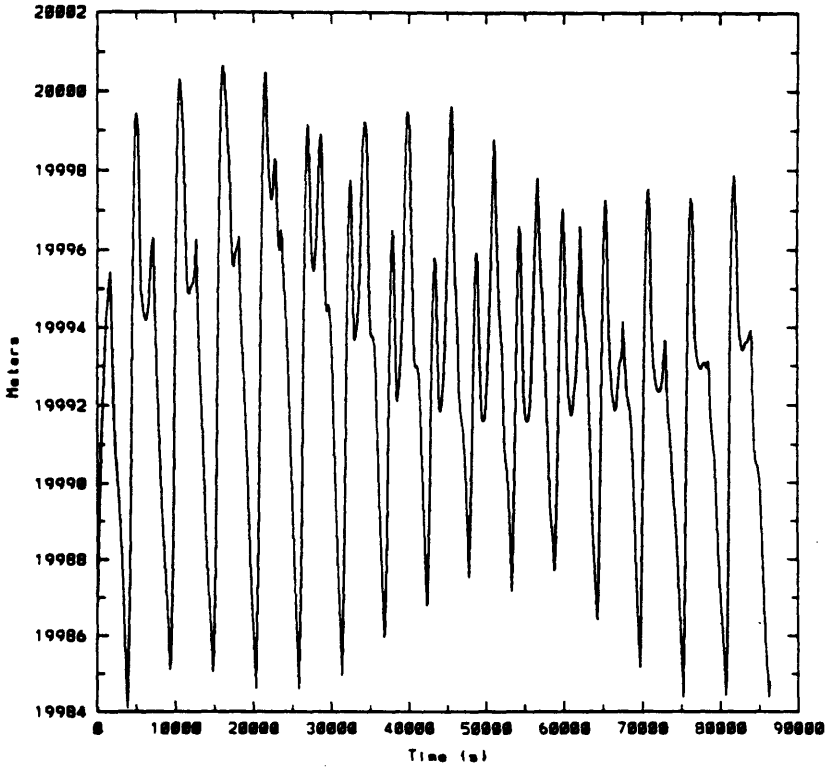

Fig. 32a Total Heat Energy to Tether vs. Diameter (showing maximum and minimum values)

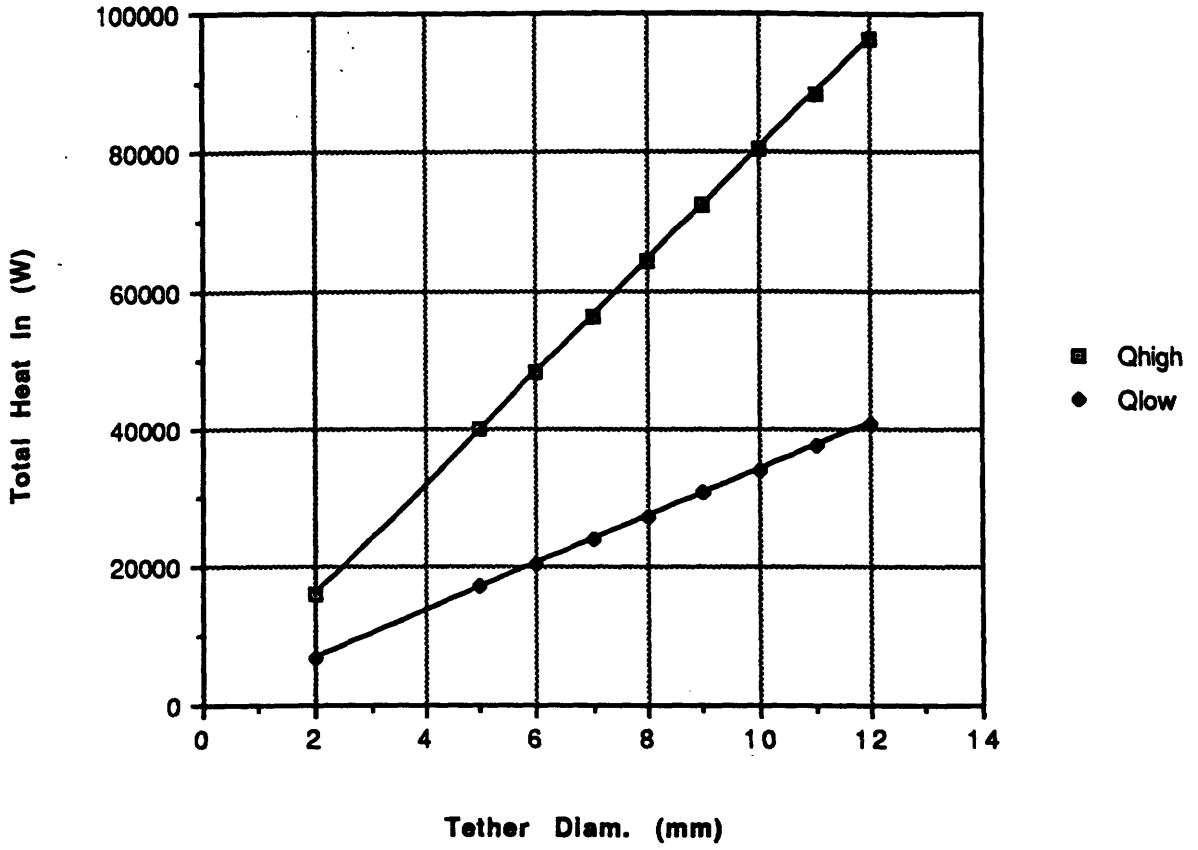

Fig. 32b Pressure Drop Across Tether (20km)

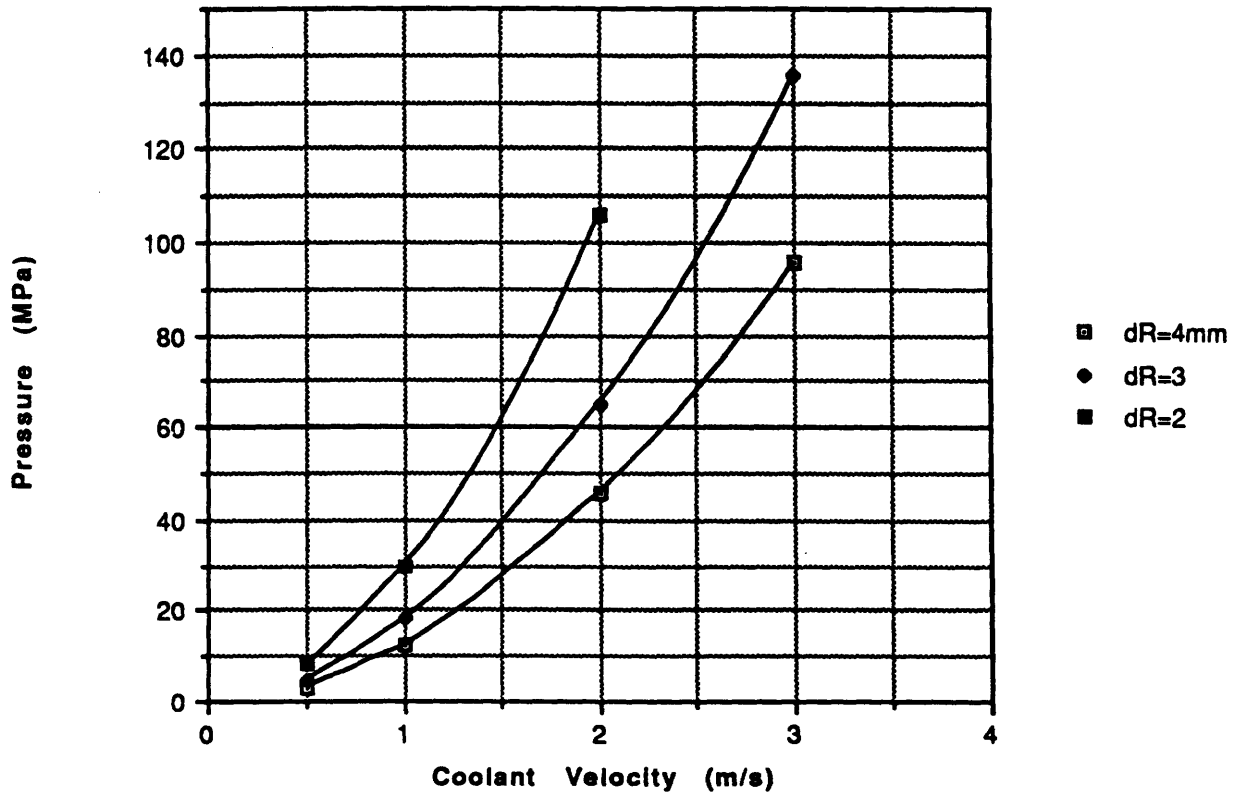

Fig. 32c Coolant Pump Power

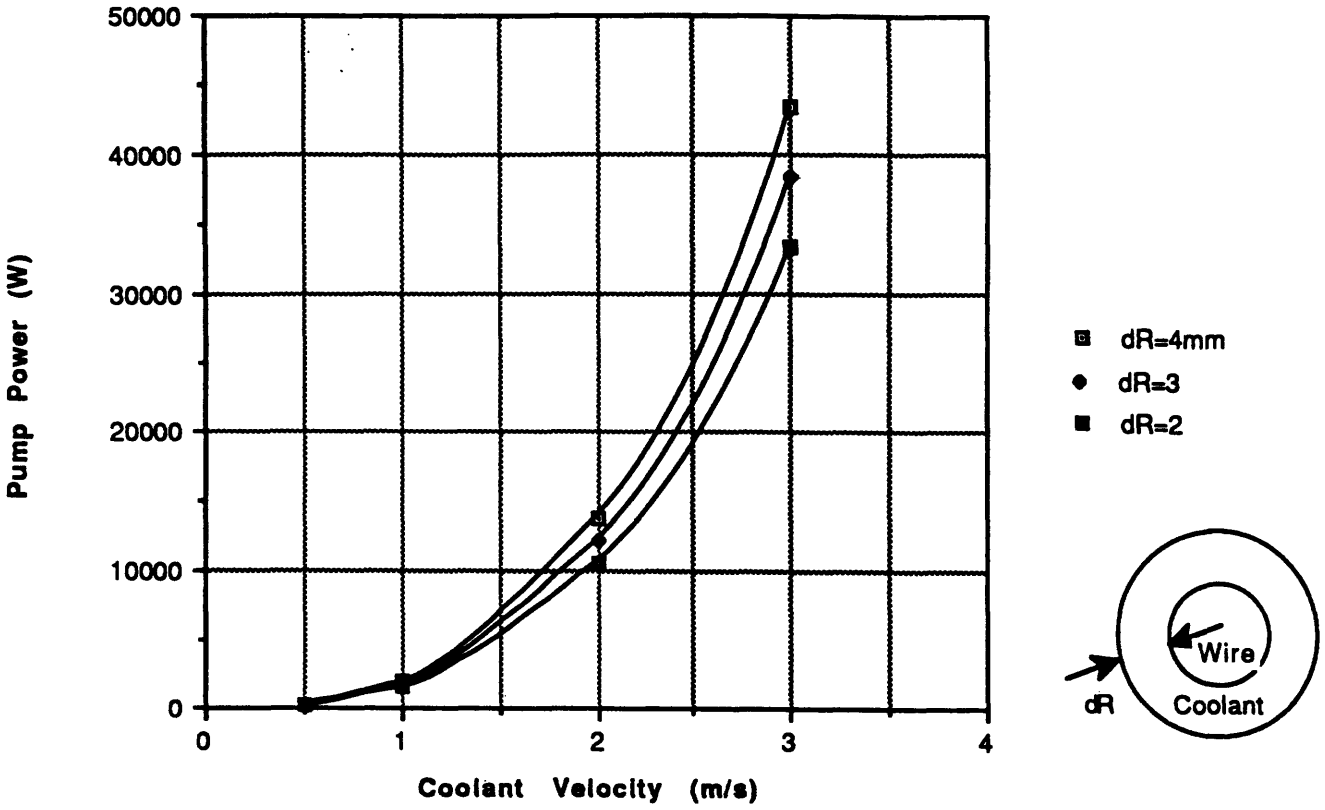

Fig. 32d Daily Coolant Mass Flow Rate

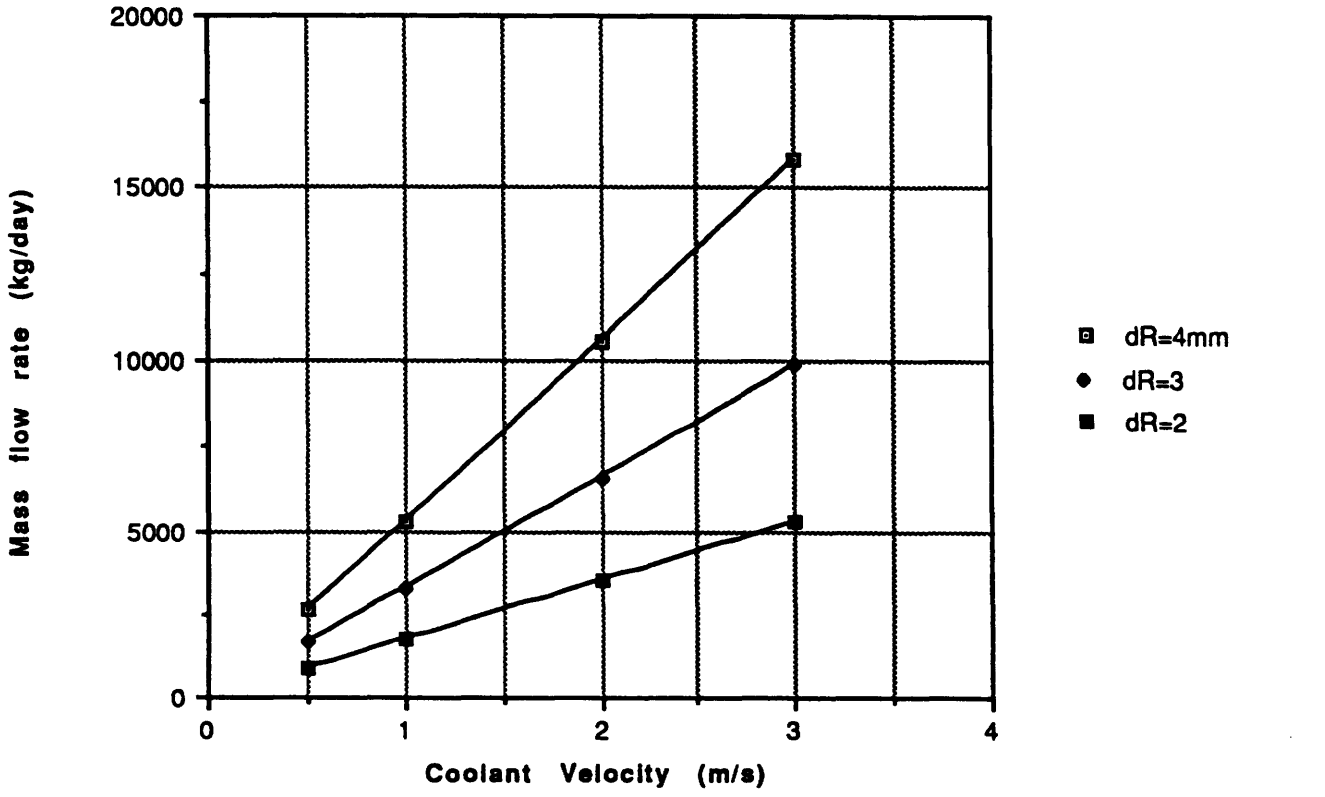

Fig. 32e Final Temperature in Cooling Tube vs. Velocity (for Ti = 50K)

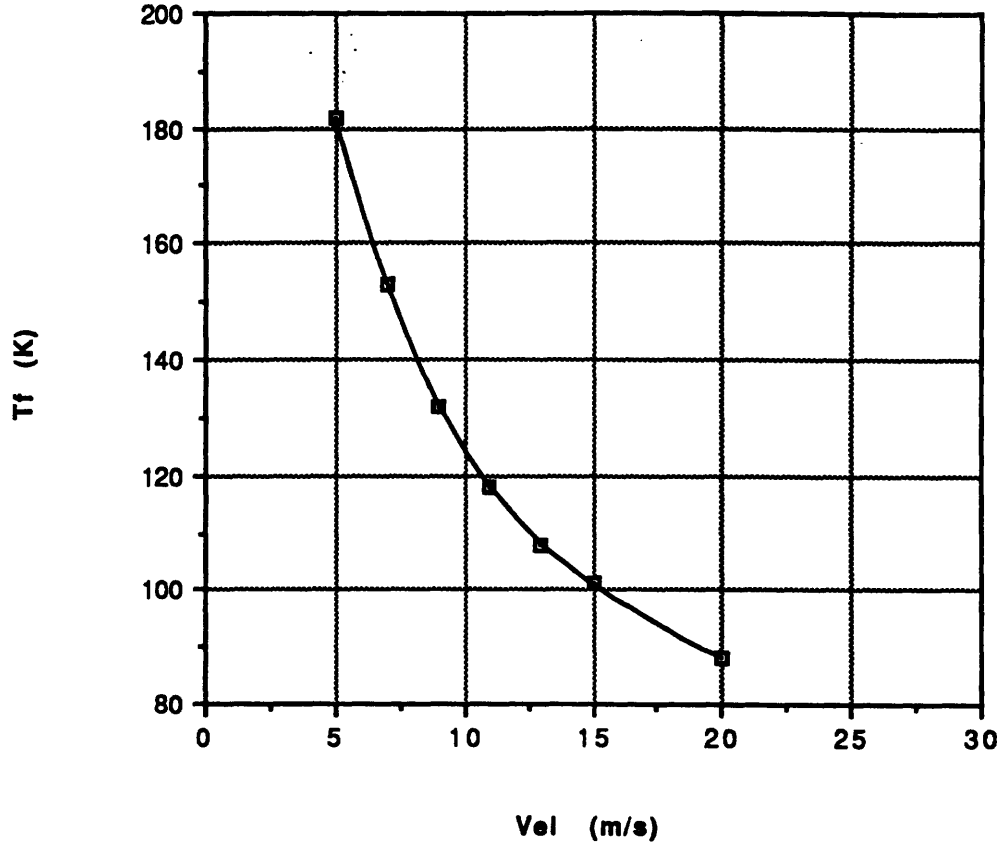

Fig. 32f Maximum Power, Superconducting Tether

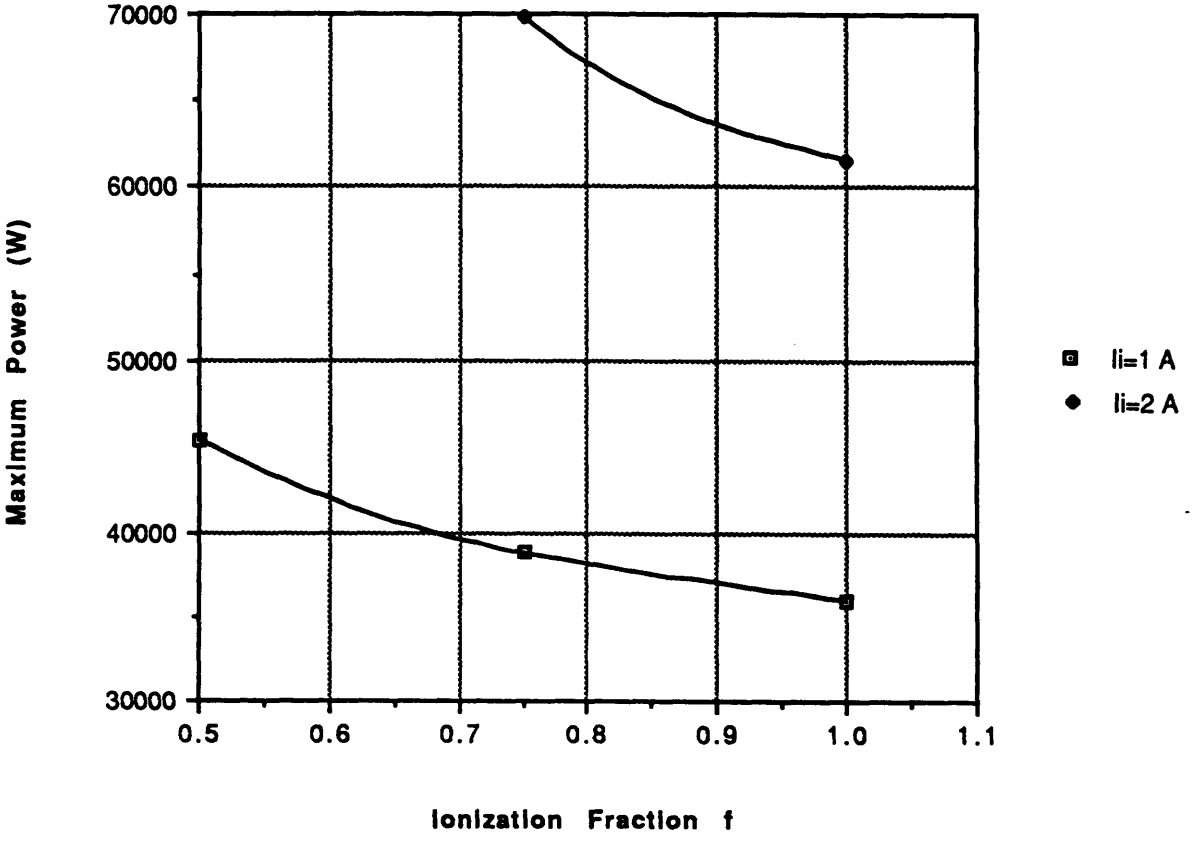

Fig. 32g Specific Power, Superconducing Tether

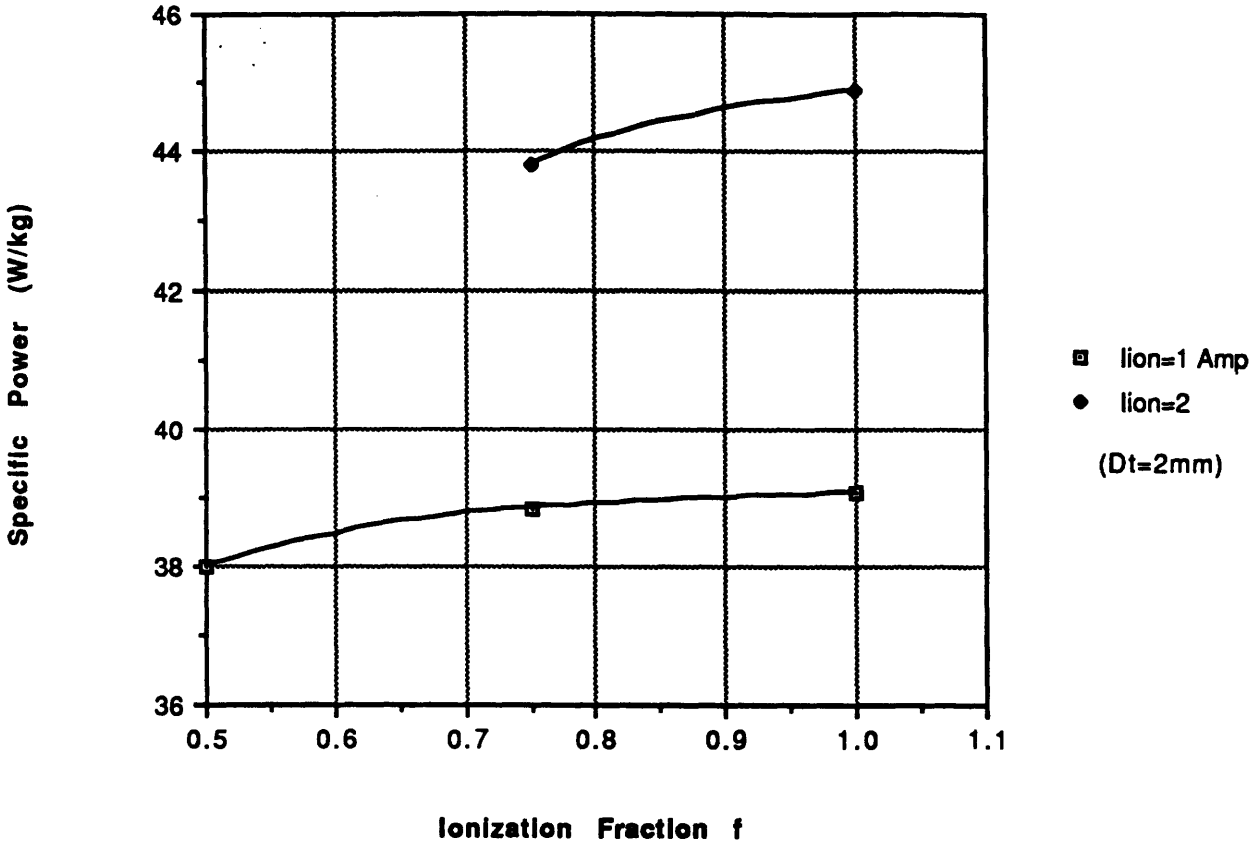

Fig. 33a Electrodynamic Drag (Contactor Maximum Power)

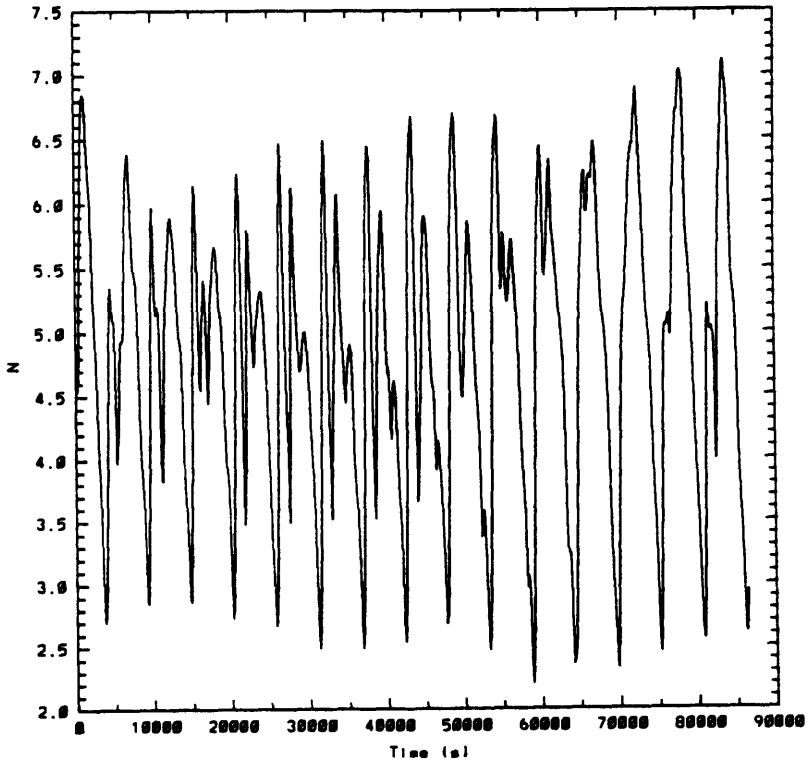

Fig. 33b Semimajor Axis (Contactor Maximum Power)

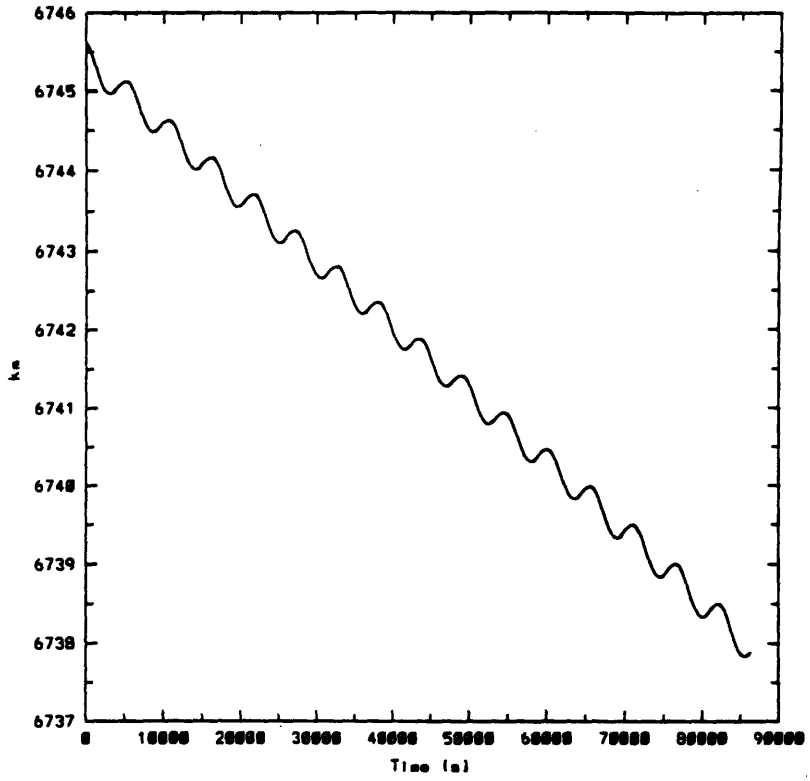

Fig. 33c Semimajor Axis (Thrusting Constant Power, 20 kW)

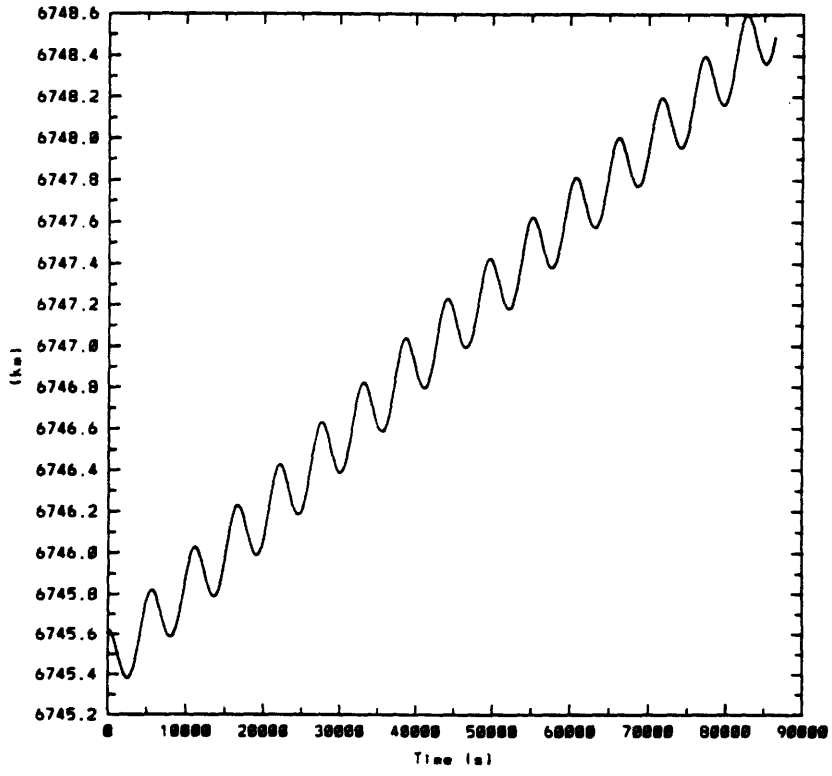

Fig. 33d Longitude of Nodes Variations

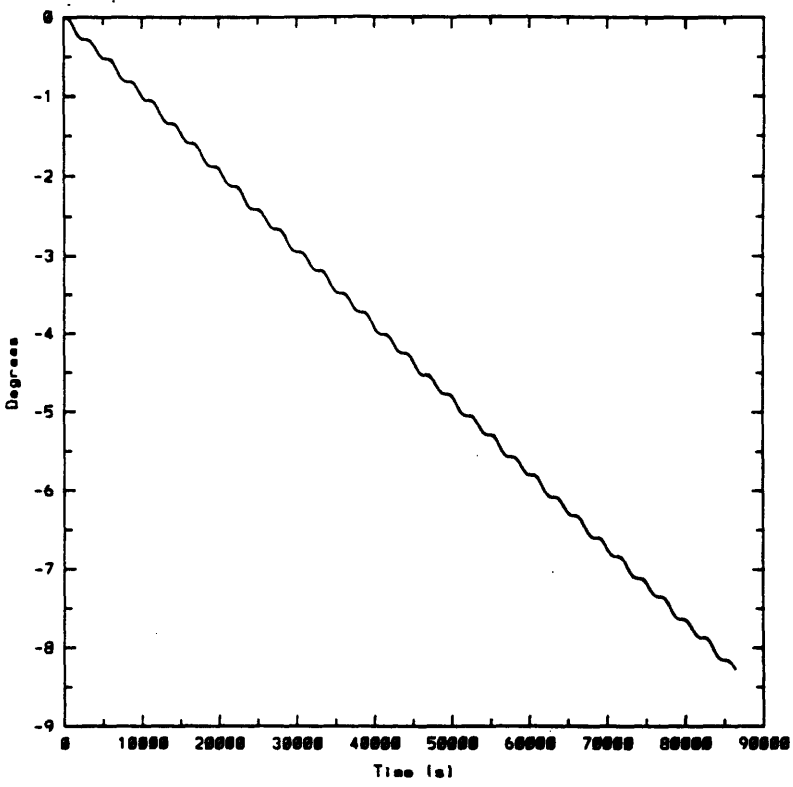

Fig. 33e Argument of Perigee Variations

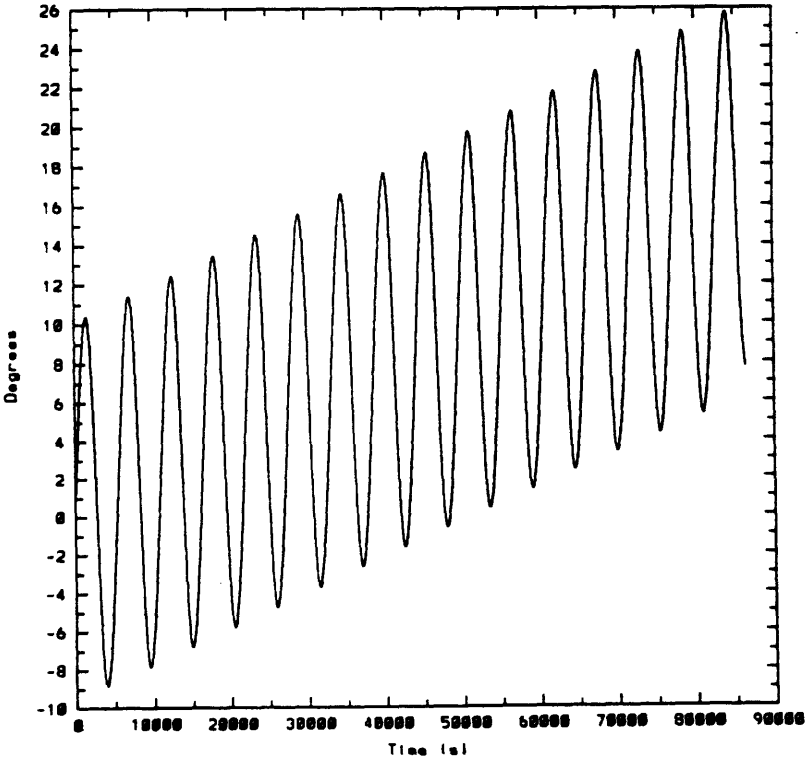

Fig. 33f Eccentricity Variations (Power Generation)

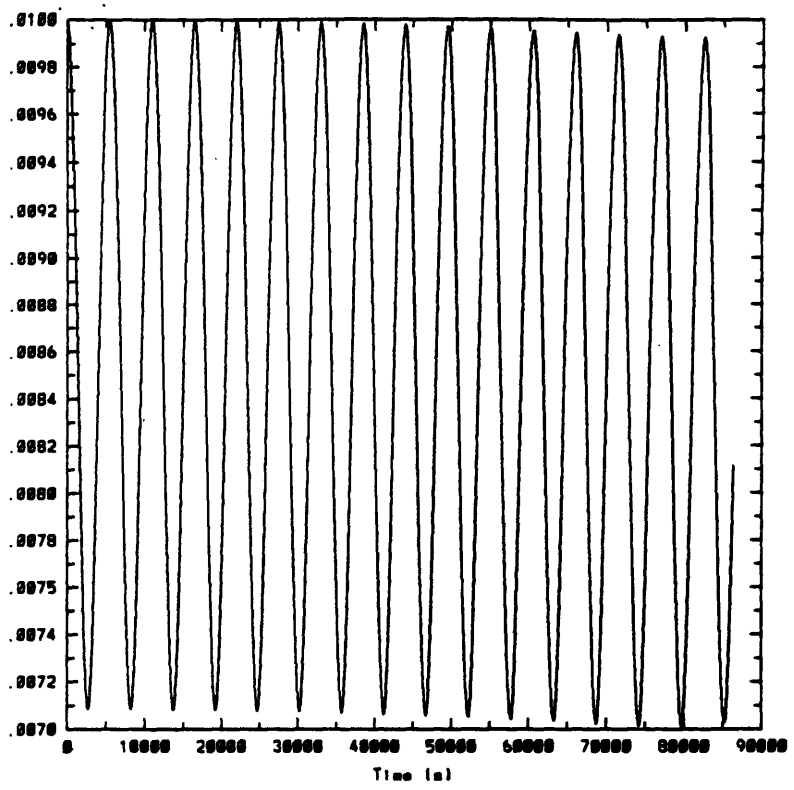

Fig. 33g Eccentricity Variations (Mixed Mode)

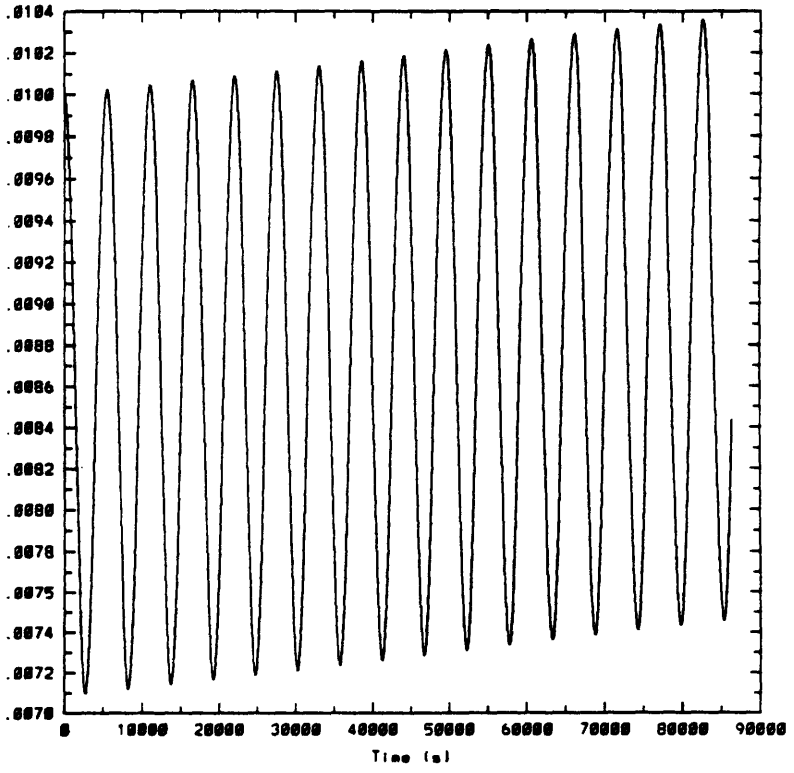

Fig. 33h Inclination Variations

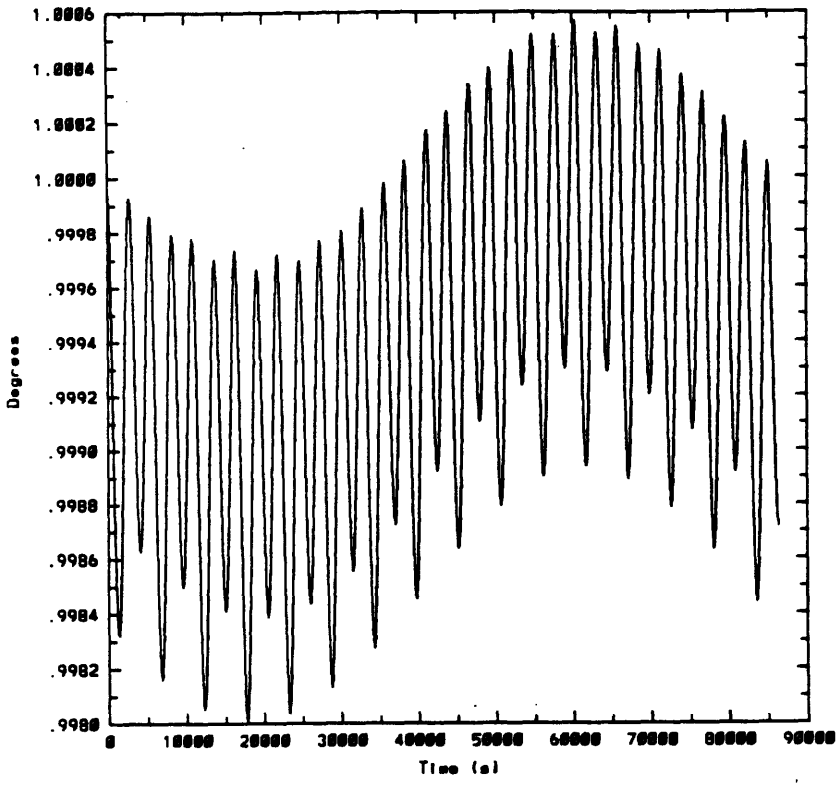

Fig. 34a Average Thrust for Constant Current Thruster (Contactor, 2mm tether)

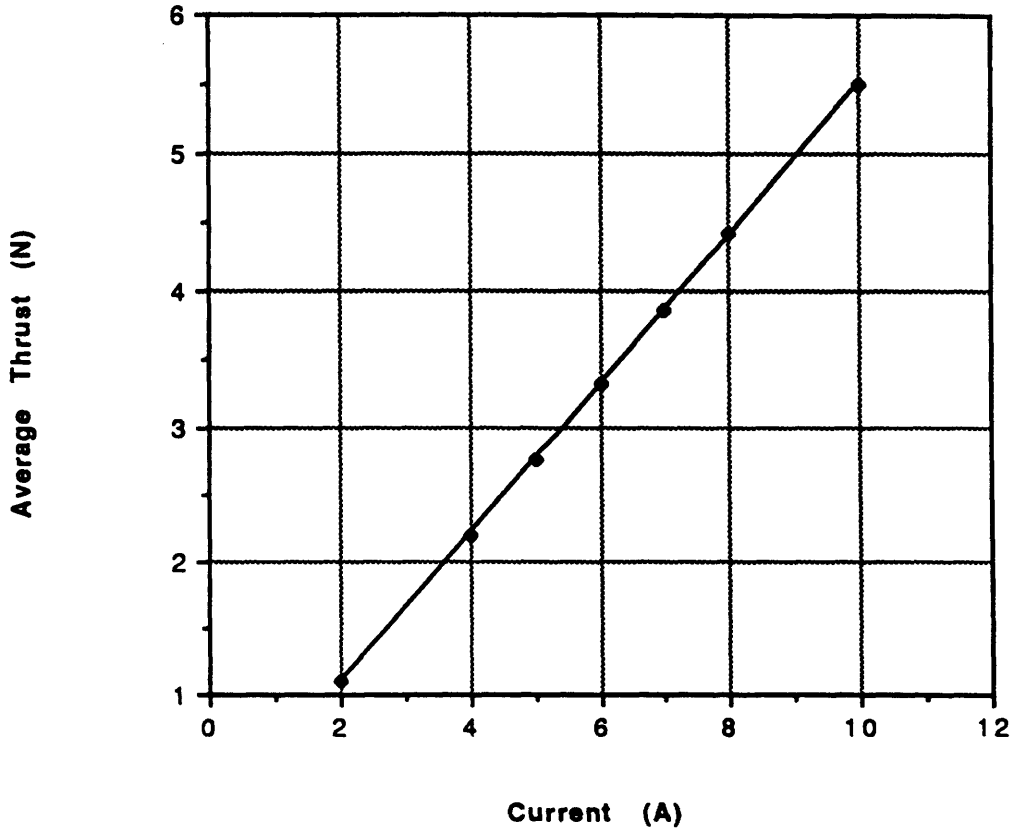

Fig. 34b Mass/<Thrust> for Constant Current Thruster (Contactor, 2mm tether)

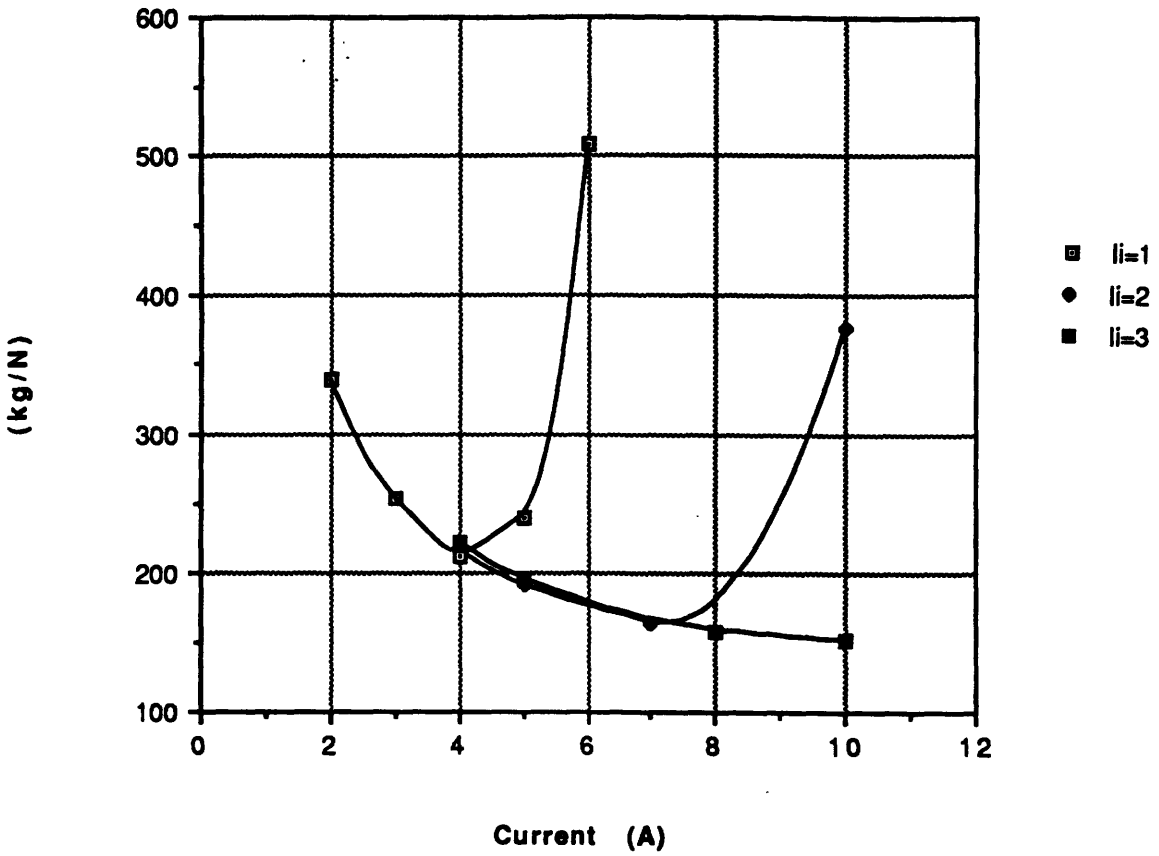

Fig. 34c <Power>/<Thrust> for Const. Current Thruster (Contactor, 2mm tether)

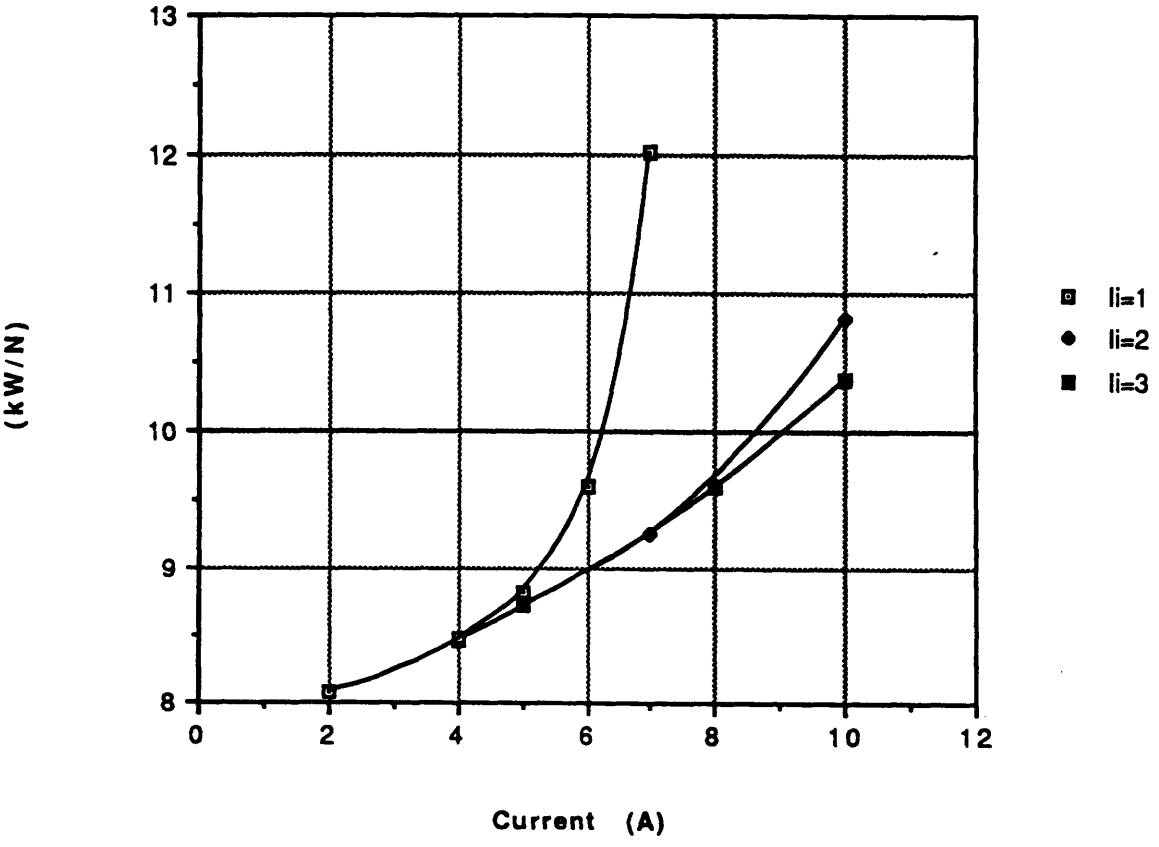

Fig. 34d <Efficiency> of Constant Current Thruster (Contactor, 2mm tether)

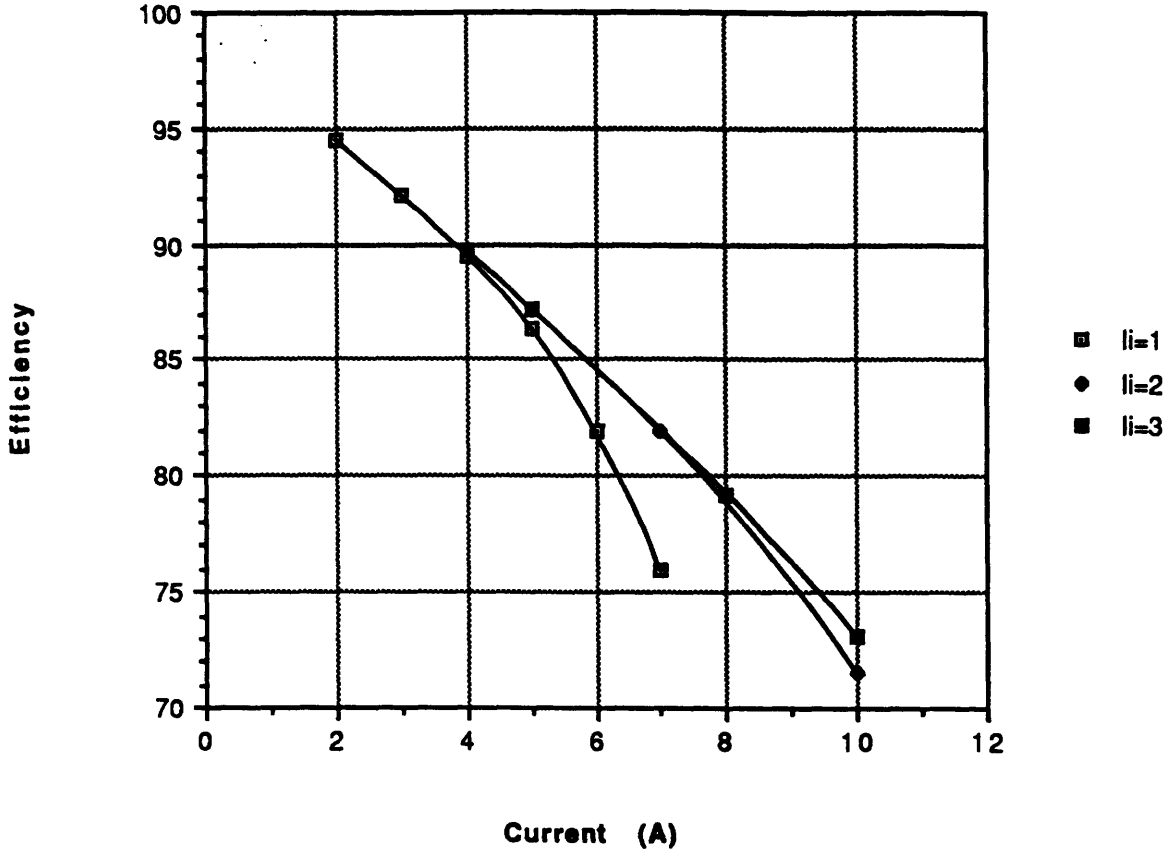

Fig. 34e Supply Voltage for CCT (I=4 A)

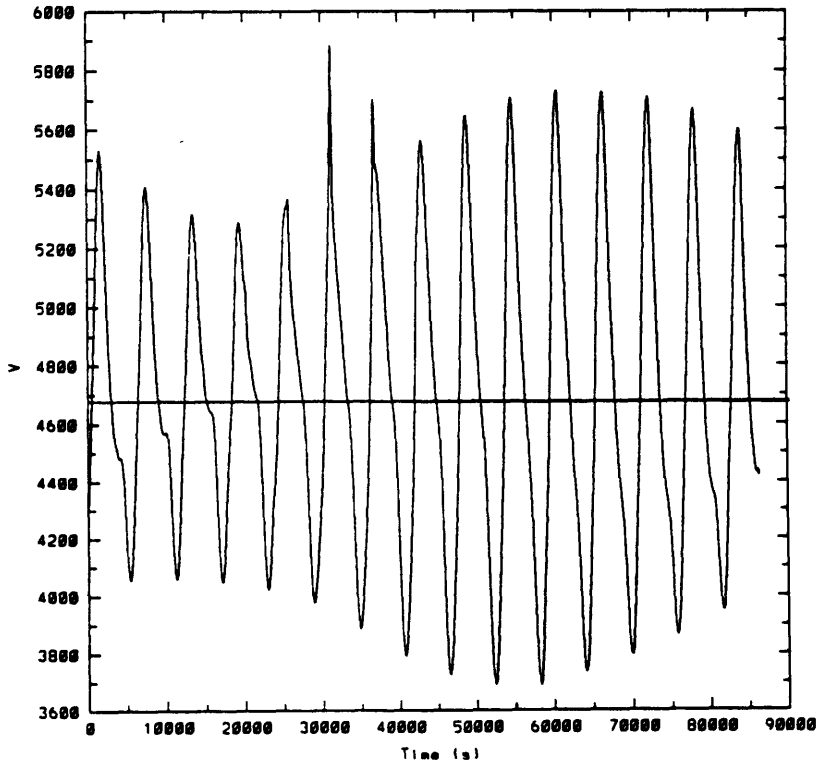

Fig. 34f Supply Power for CCT (I=4 A)

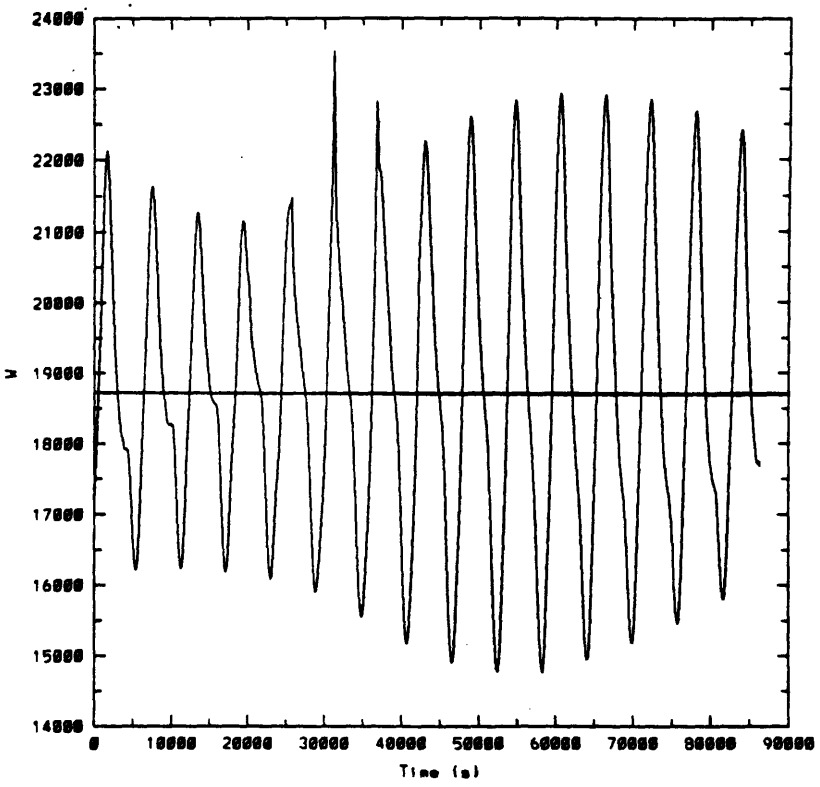

Fig. 34g Thrust for CCT (I=4 A)

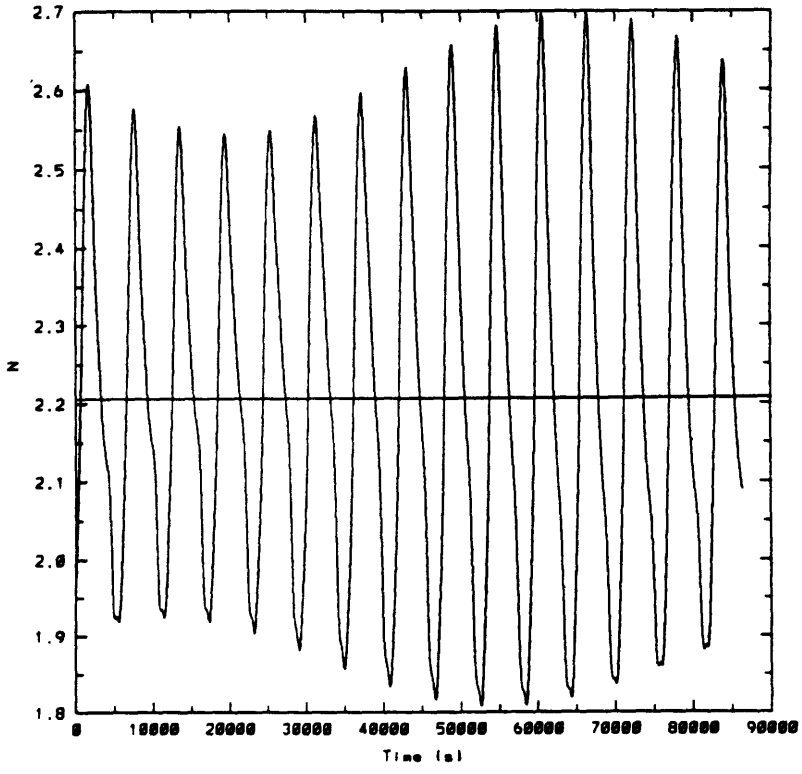

Fig. 35a Average Thrust for Constant Voltage Thruster (Contactor, 2mm tether)

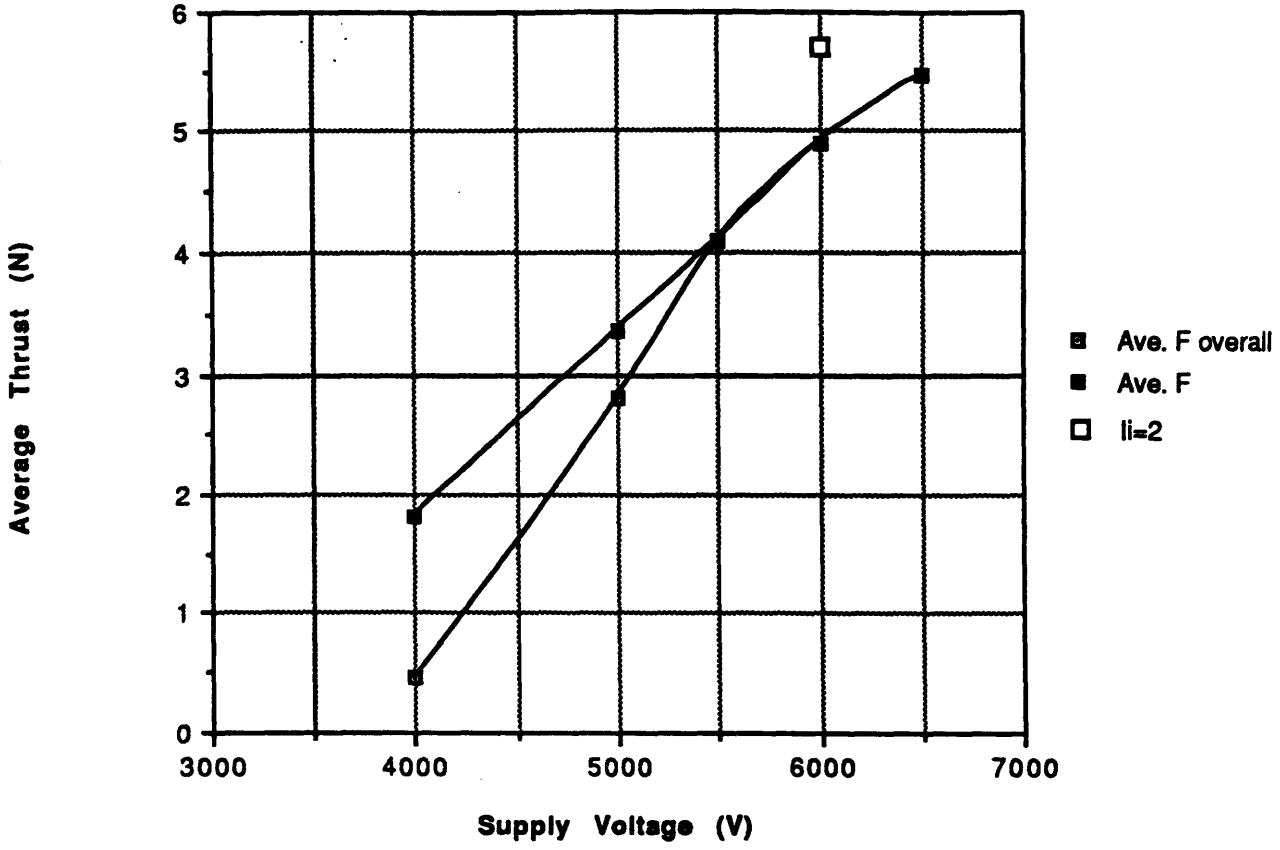

Fig. 35b Mass/<Thrust> for Constant Voltage Thruster (Contactor, 2mm tether)

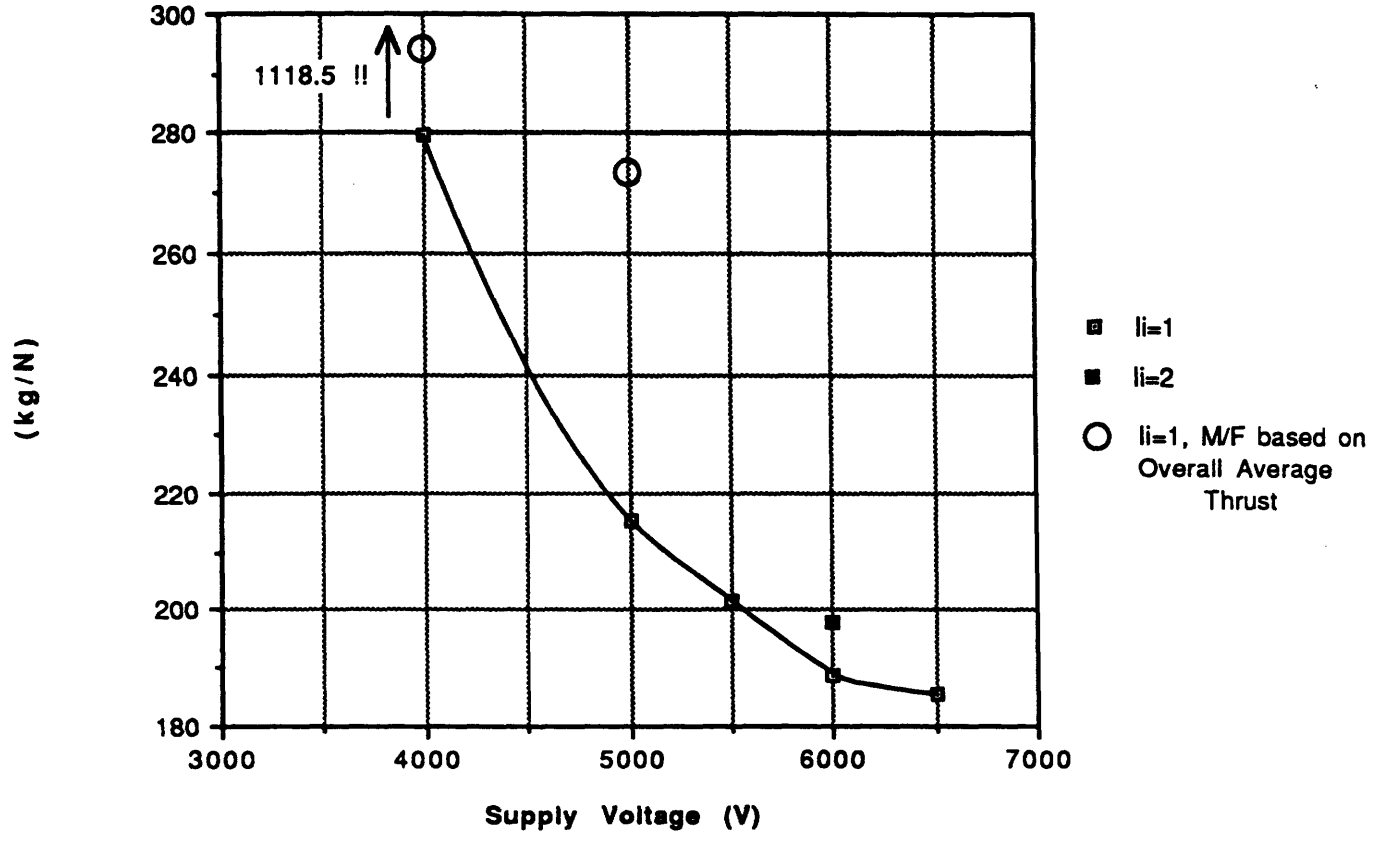

Fig. 35c <Power>/<Thrust> for Const. Voltage Thruster
(Contactor, 2mm tether)

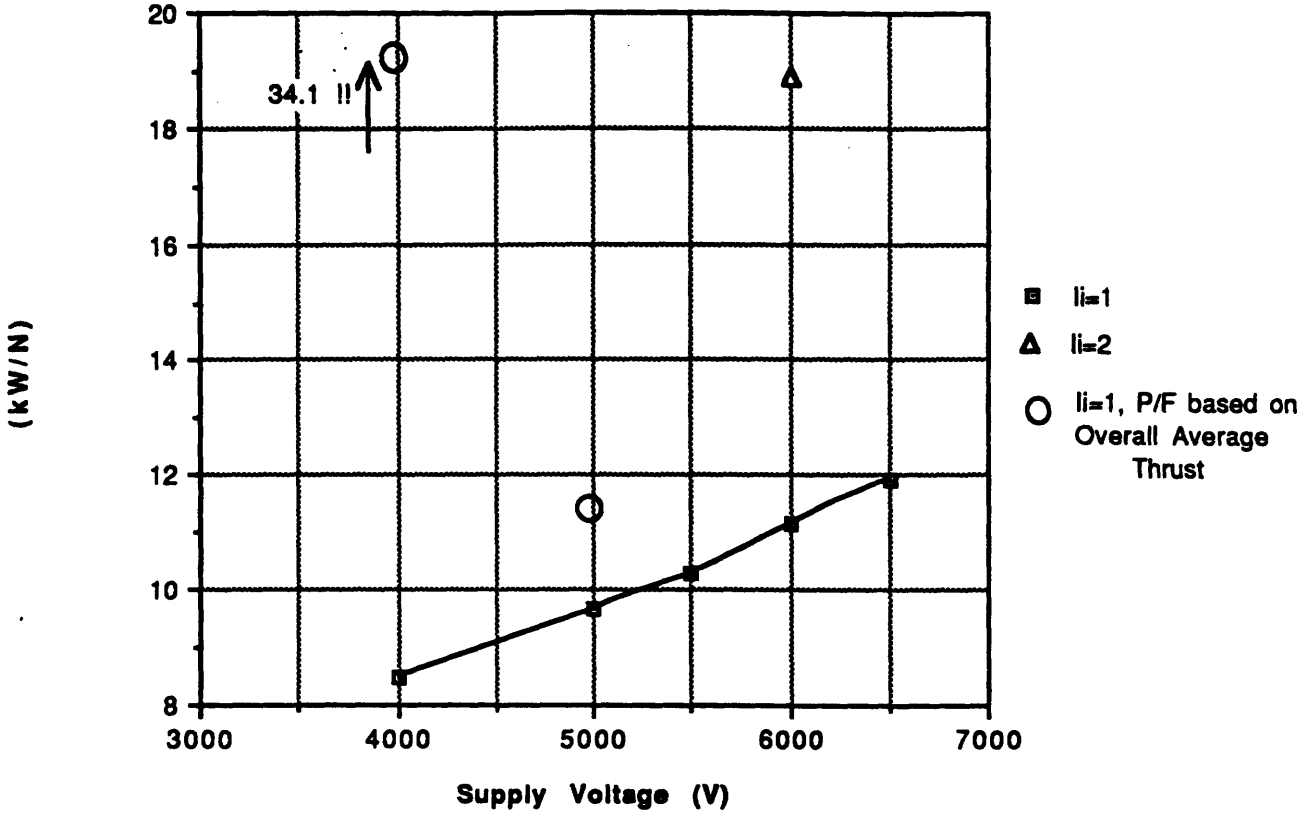

Fig. 35d <Efficiency> of Constant Voltage Thruster
(Contactor, 2mm tether)

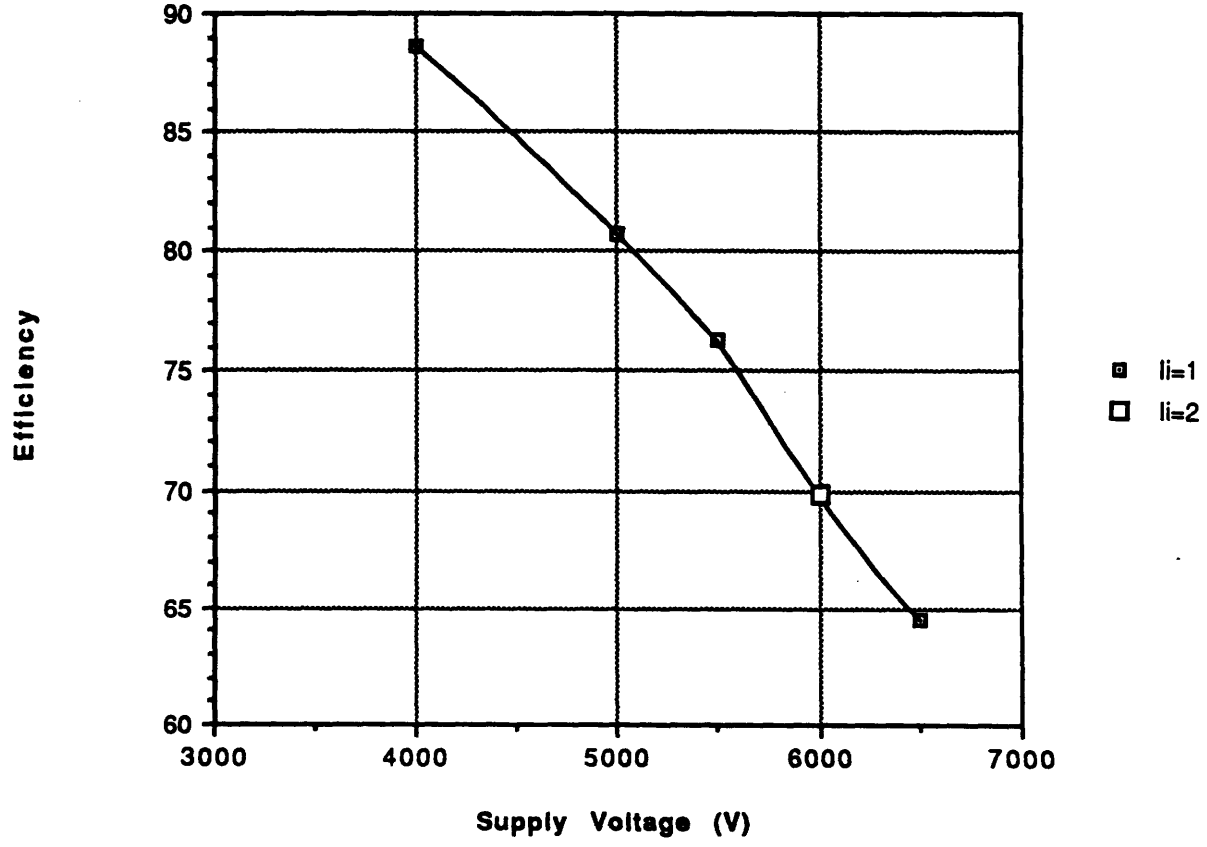

Fig. 35e Supply Power for CVT (V=5000)

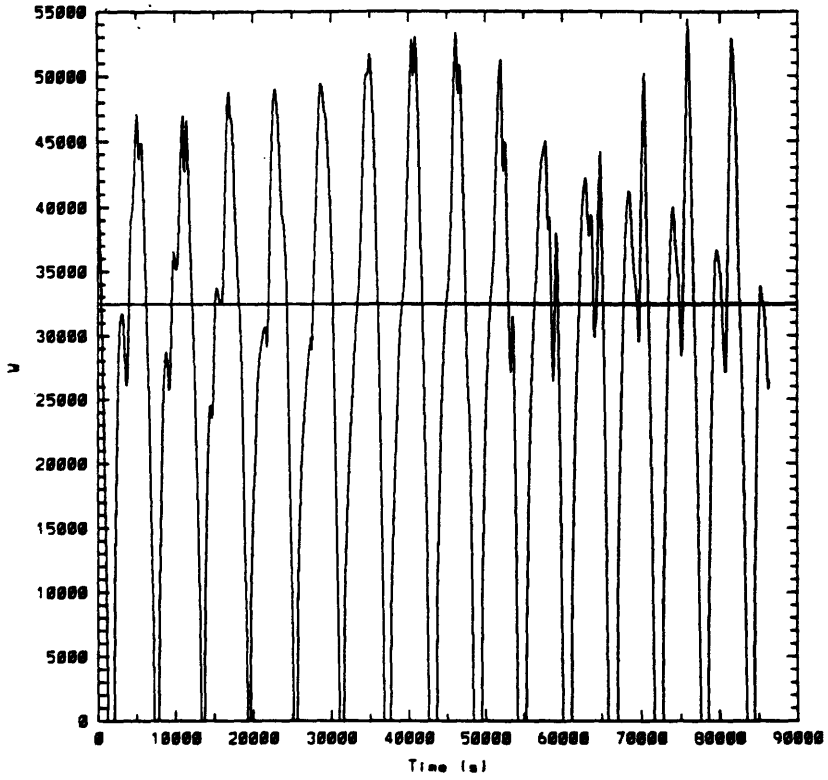

Fig. 35f Current for CVT (V=5000)

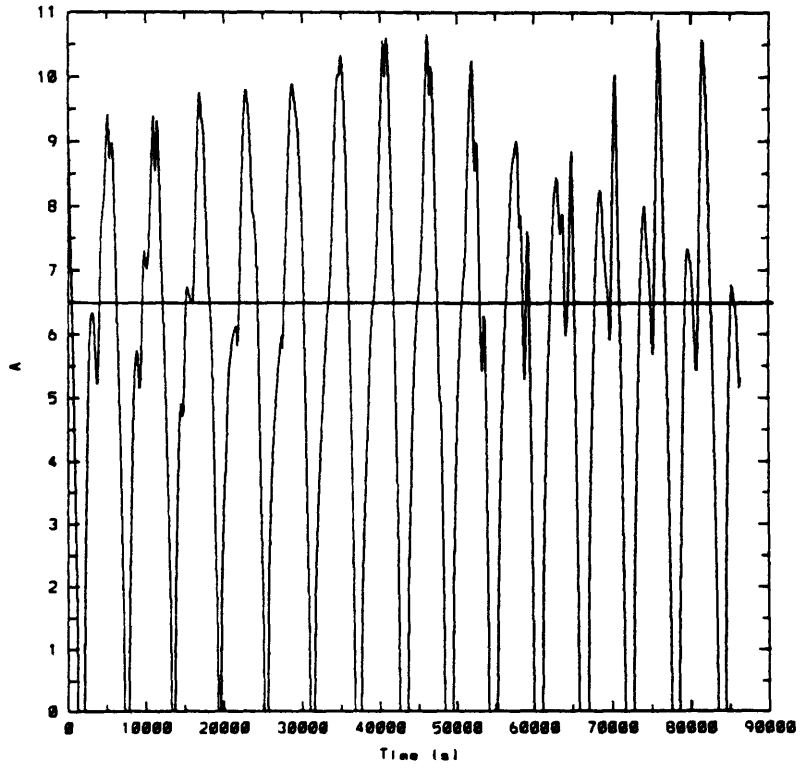

Fig. 35g Thrust for CVT (V=5000)

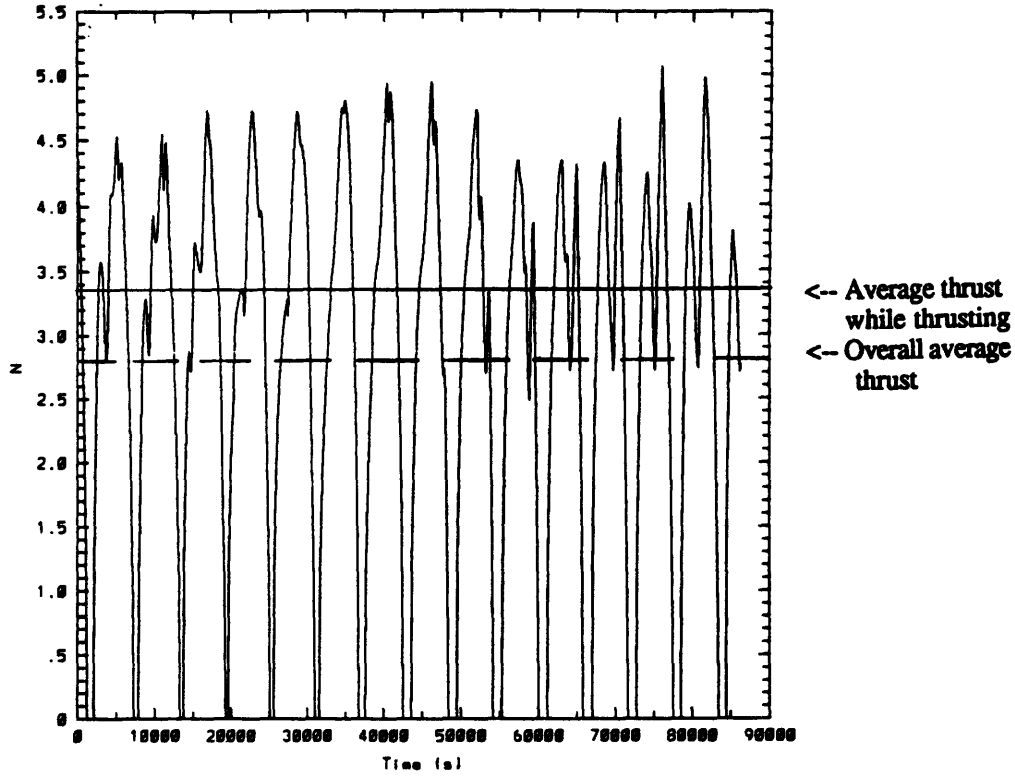

Fig. 36a Average Thrust for Constant Power Thruster (Contactor, 2mm tether)

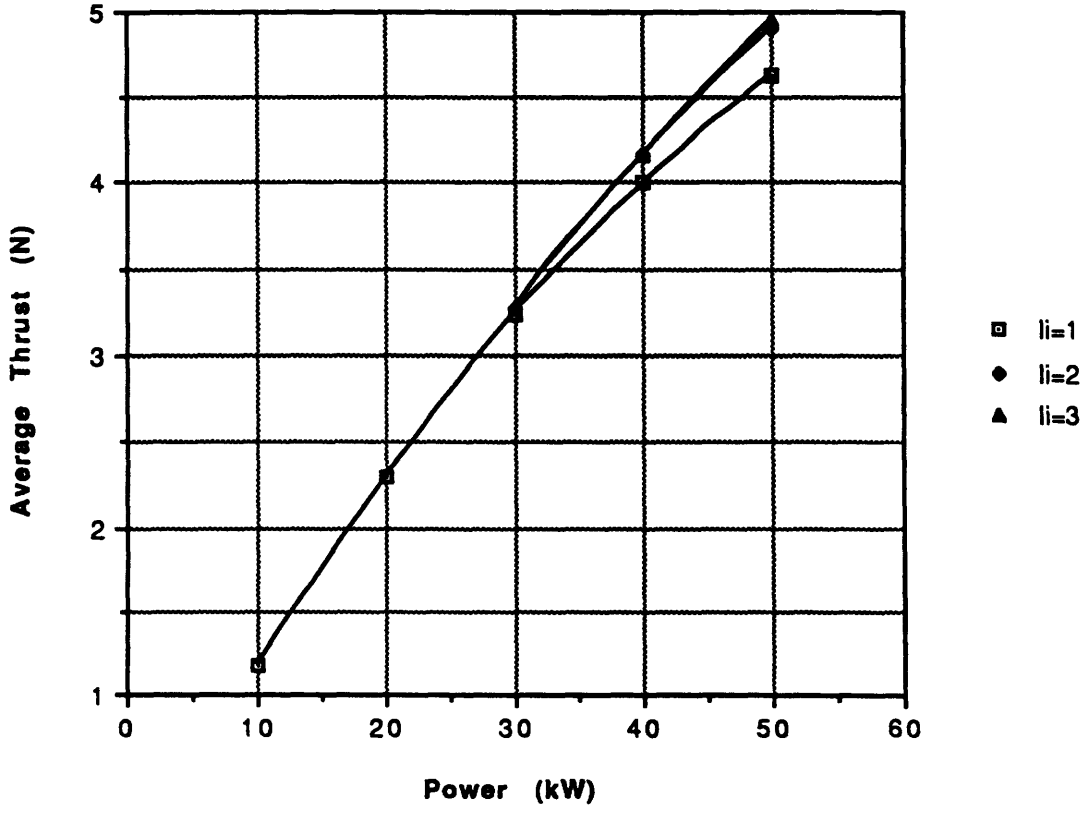

Fig. 36b Mass/<Thrust> for Constant Power Thruster (Contactor, 2mm tether)

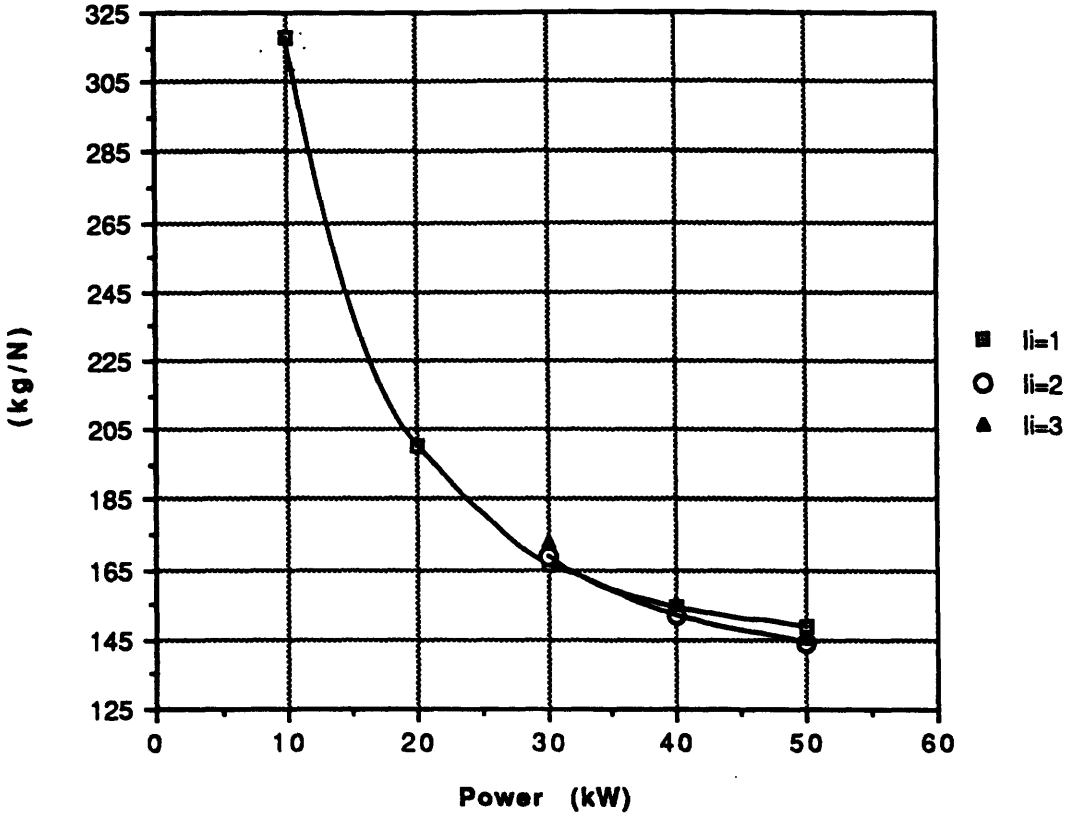

Fig. 36c <Power>/<Thrust> for Const. Power Thruster (Contactor, 2mm tether)

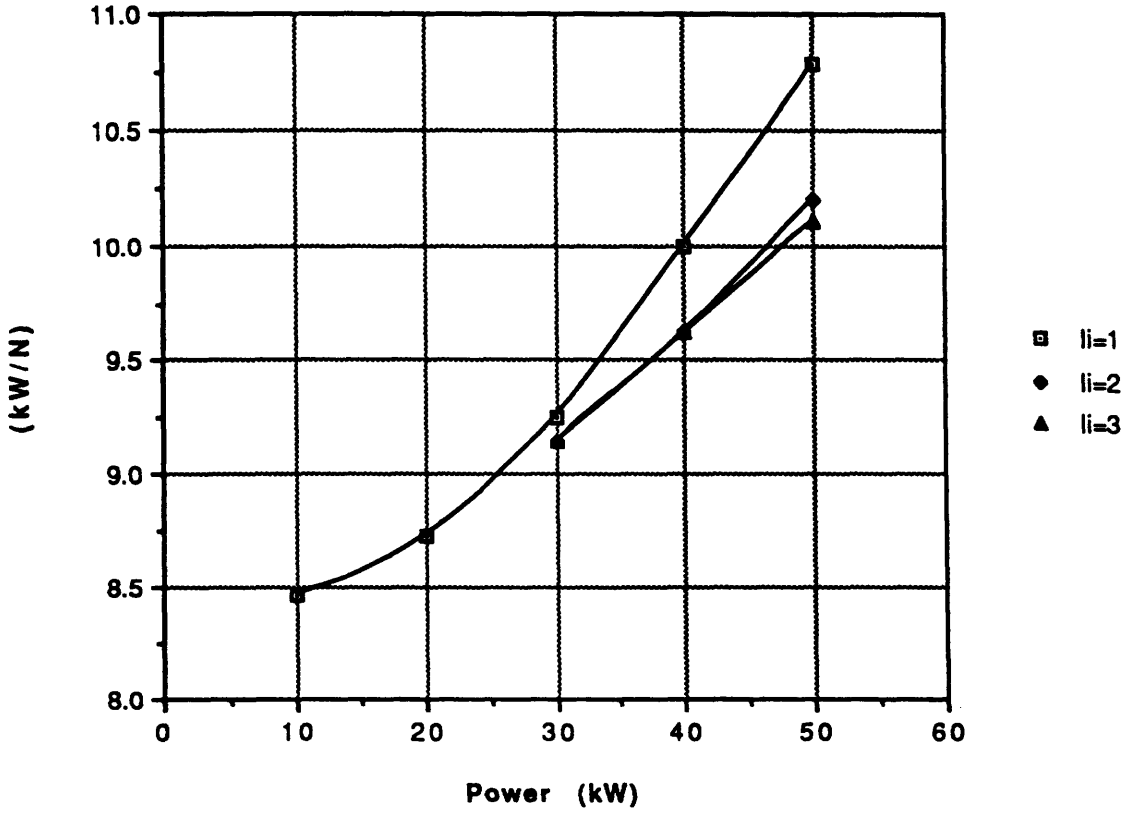

Fig. 36d <Efficiency> of Constant Power Thruster (Contactor, 2mm tether)

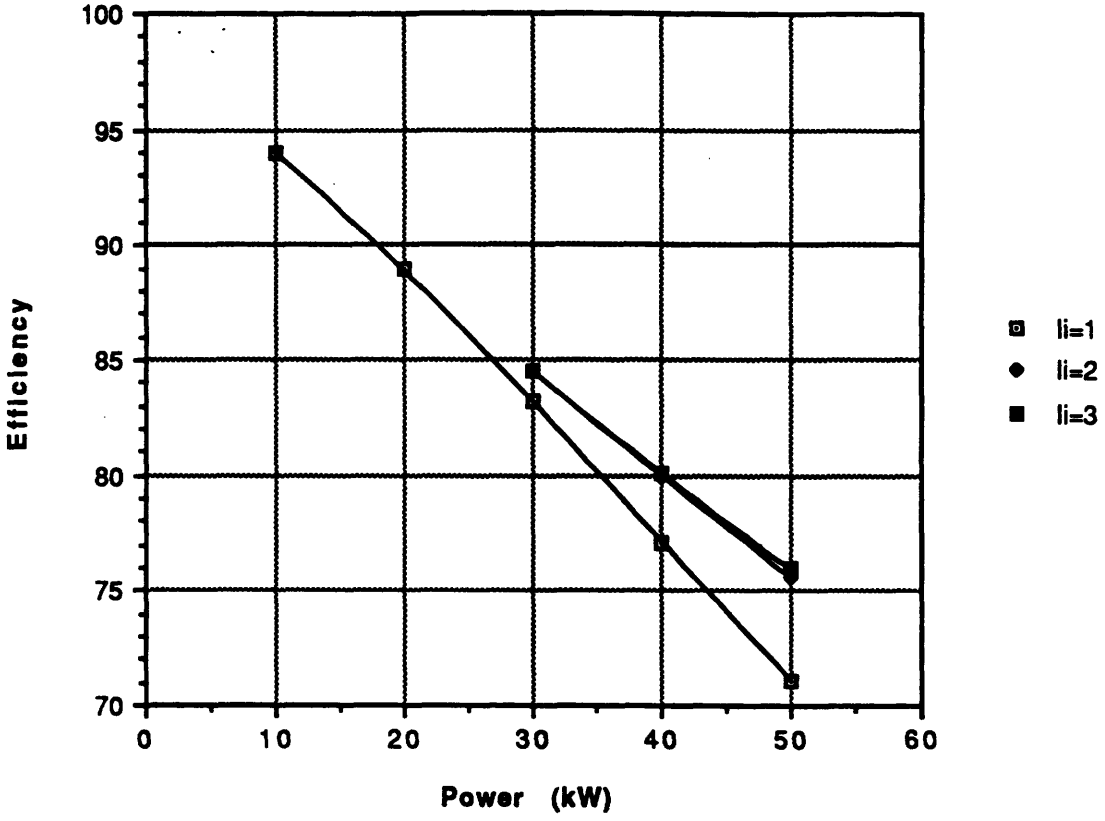

Fig. 36e Supply Voltage for CPT (P=20 kW)

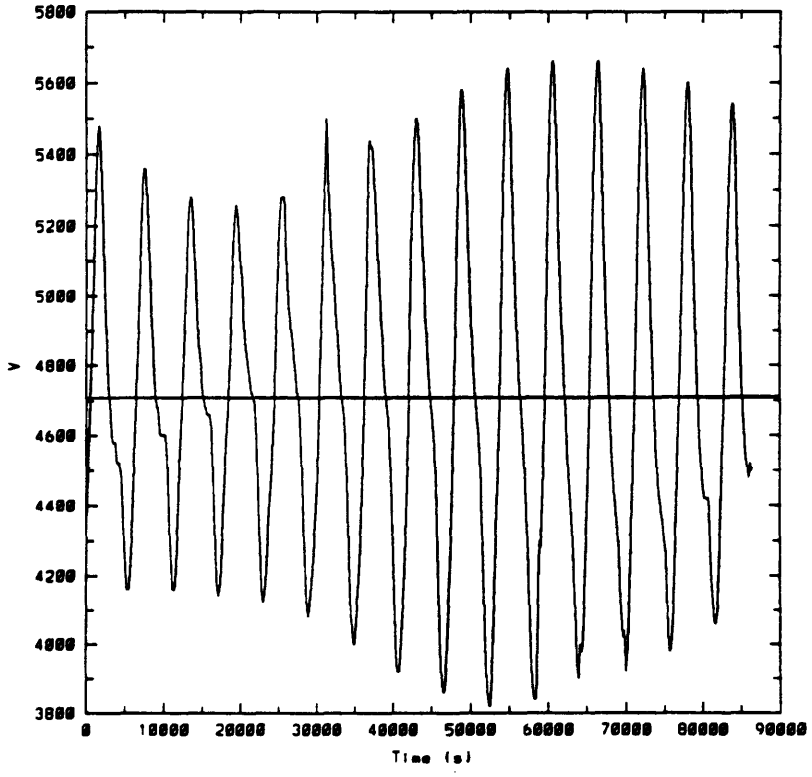

Fig. 36f Current for CPT (P=20 kW)

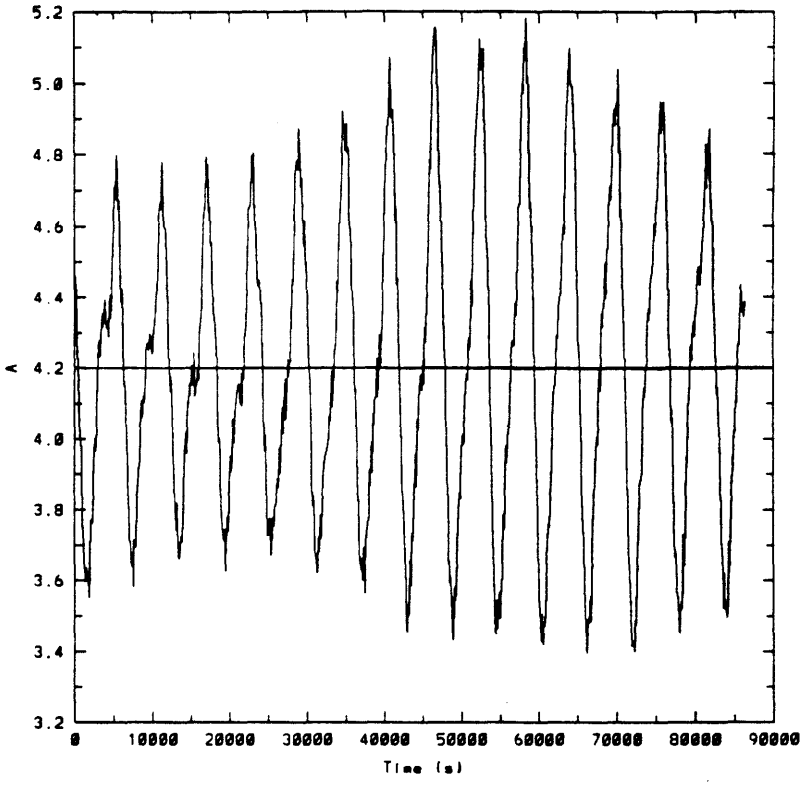

Fig. 36g Thrust for CPT (P=20 kW)

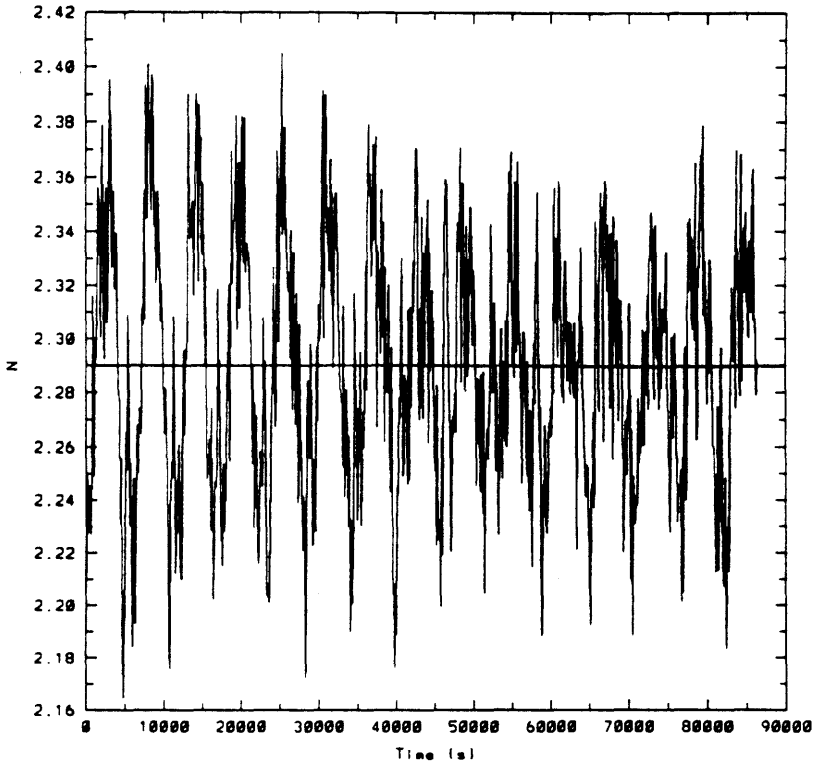

Fig. 37a Mass/<Thrust> for Const. Thrust Thruster
(Contactor, 2mm tether)

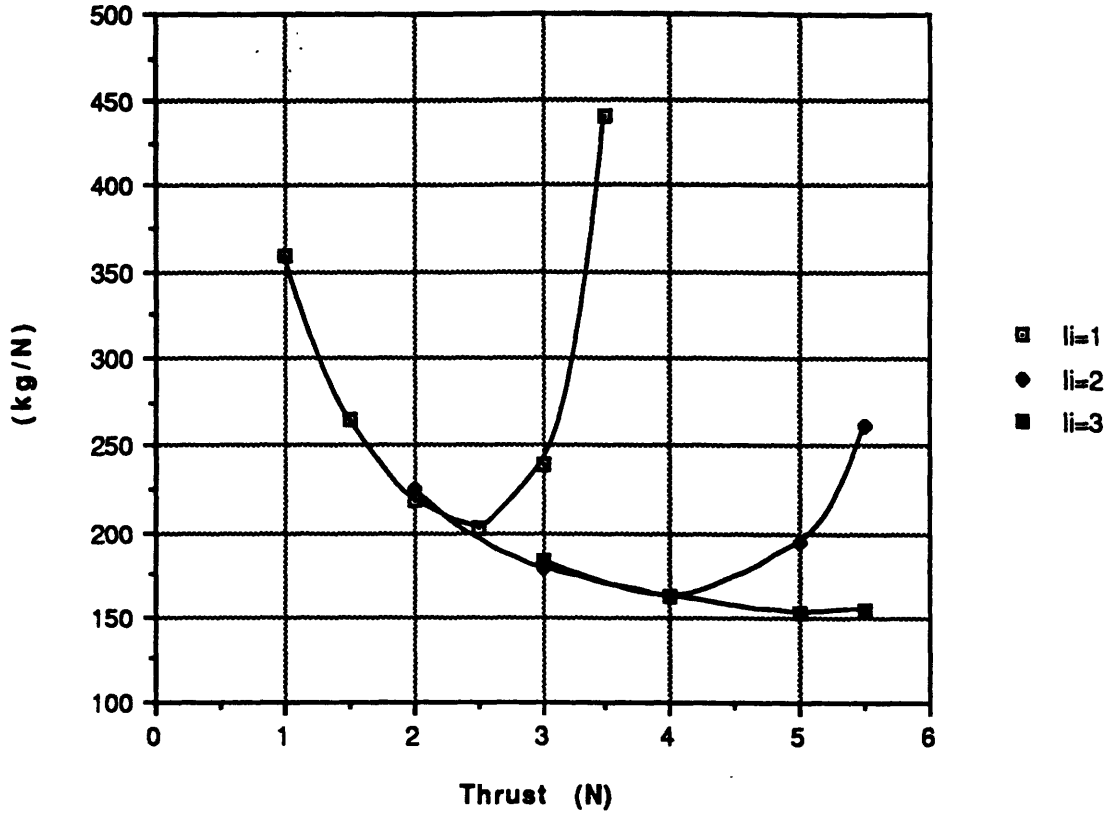

Fig. 37b <Power>/<Thrust> for Const. Thrust Thruster
(Contactor, 2mm tether)

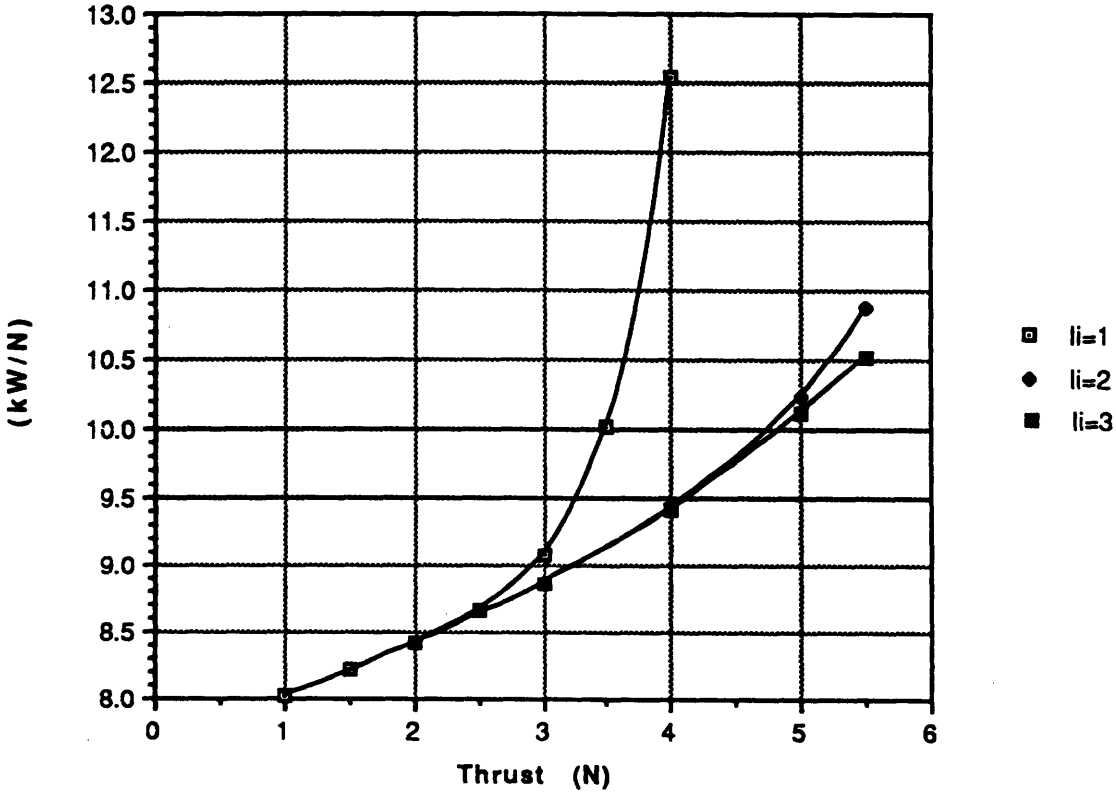

Fig. 37c <Efficiency> of Constant Thrust Thruster (Contactor, 2mm tether)

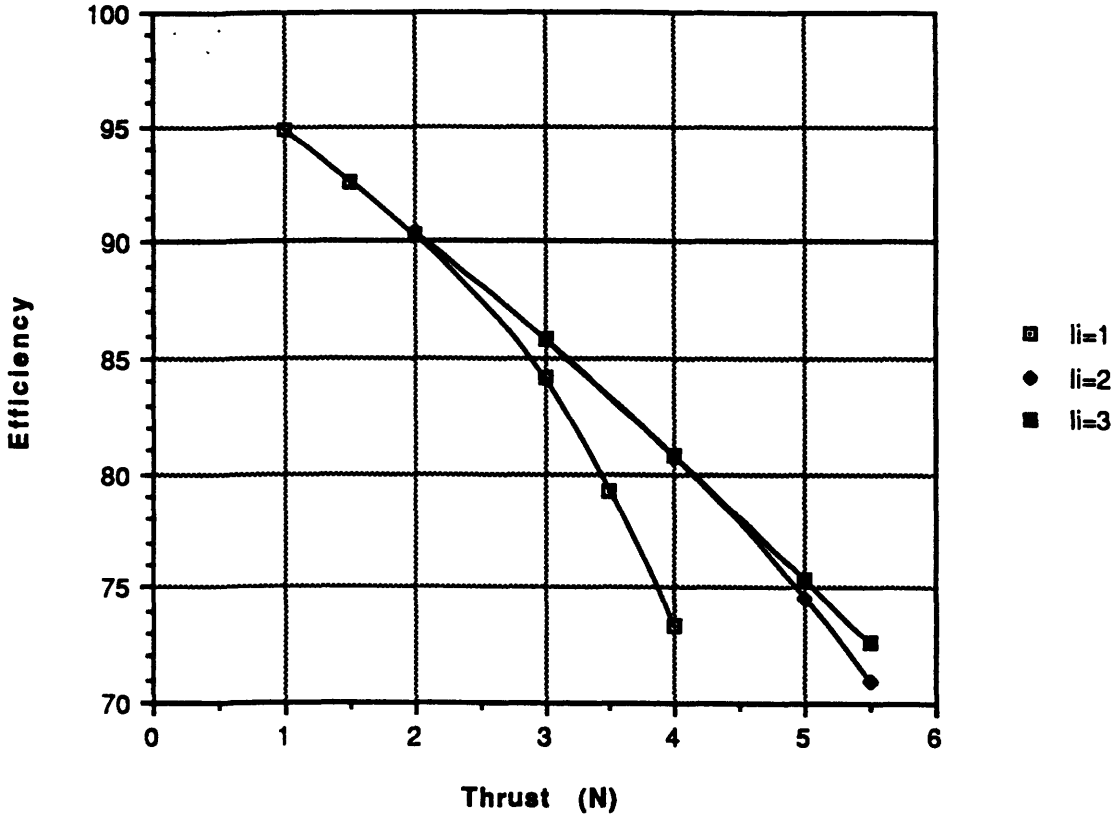

Fig. 37d Supply Voltage for CTT (F=2 N)

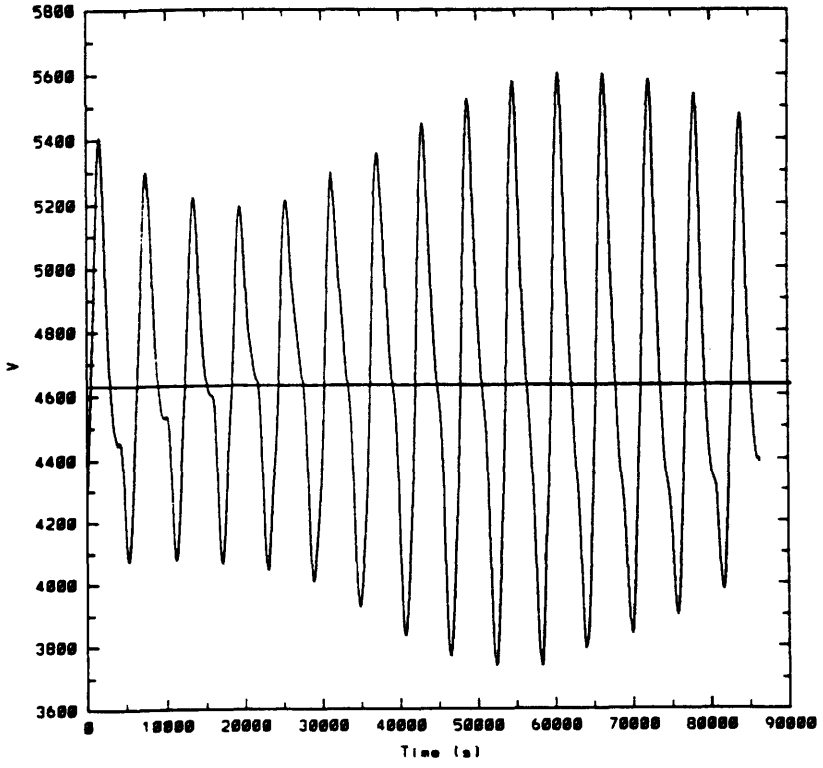

Fig. 37e Supply Power for CTT (F=2 N)

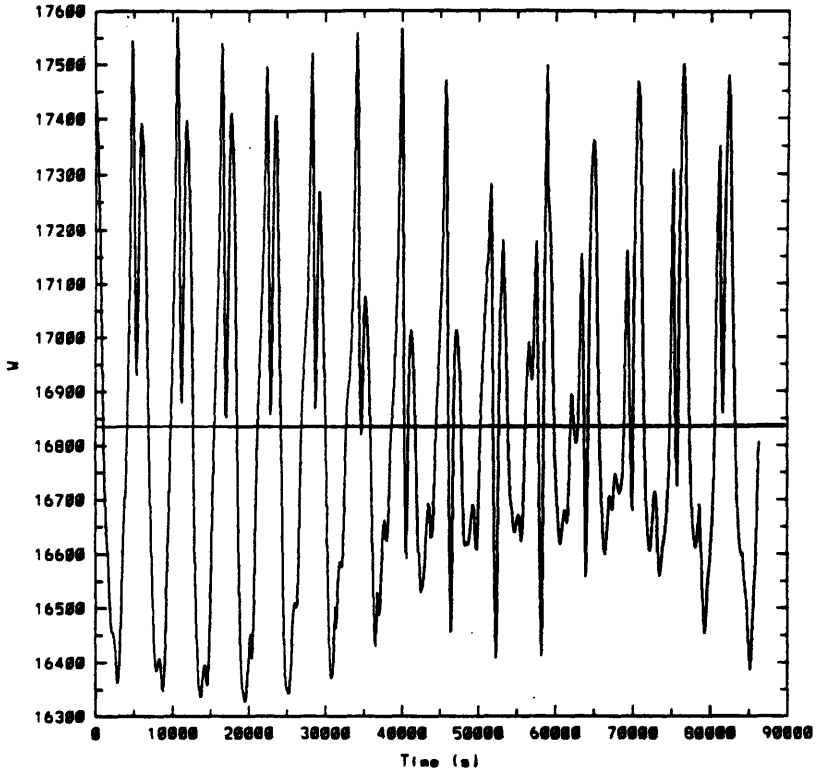

Fig. 37f Current for CTT (F=2 N)

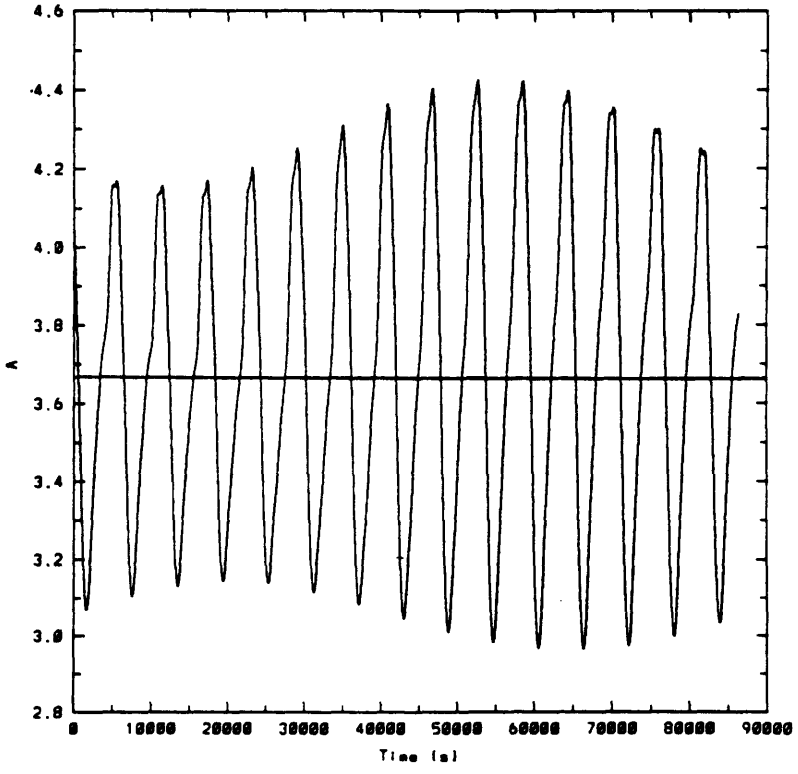

Fig. 38 Mass Comparison of Thrusters with 4 N <Thrust> (Contactor, 2mm tether)

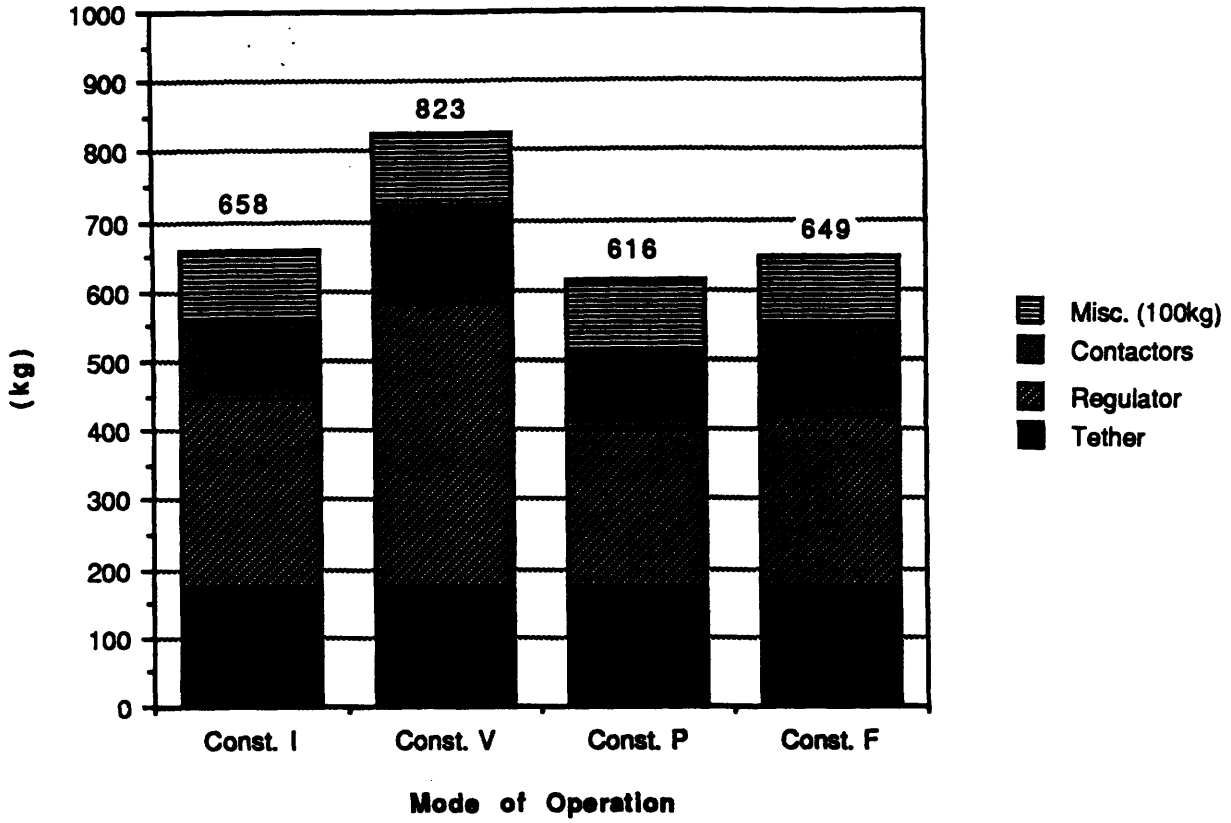

Fig. 39a Thrust and Efficiency of Bare Thruster with varying Insulated Length

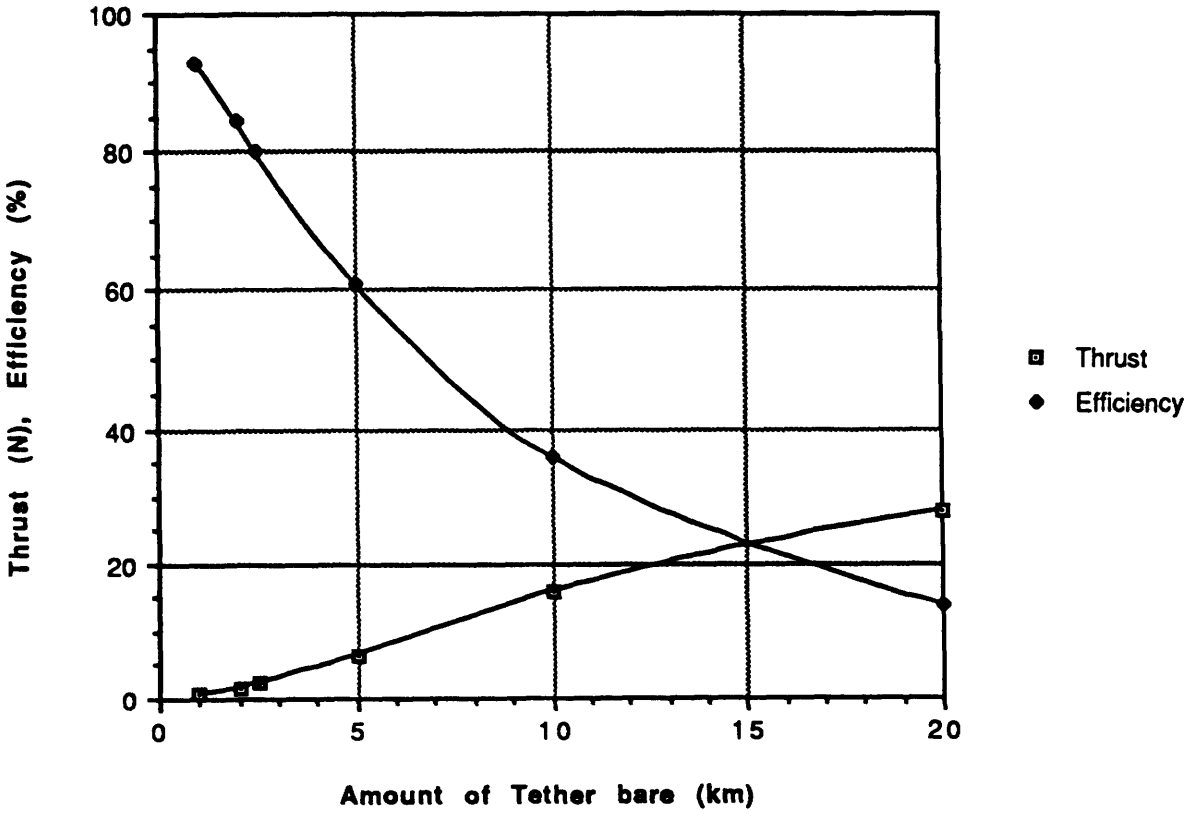

Fig. 39b Current and Power Required for Bare Thruster

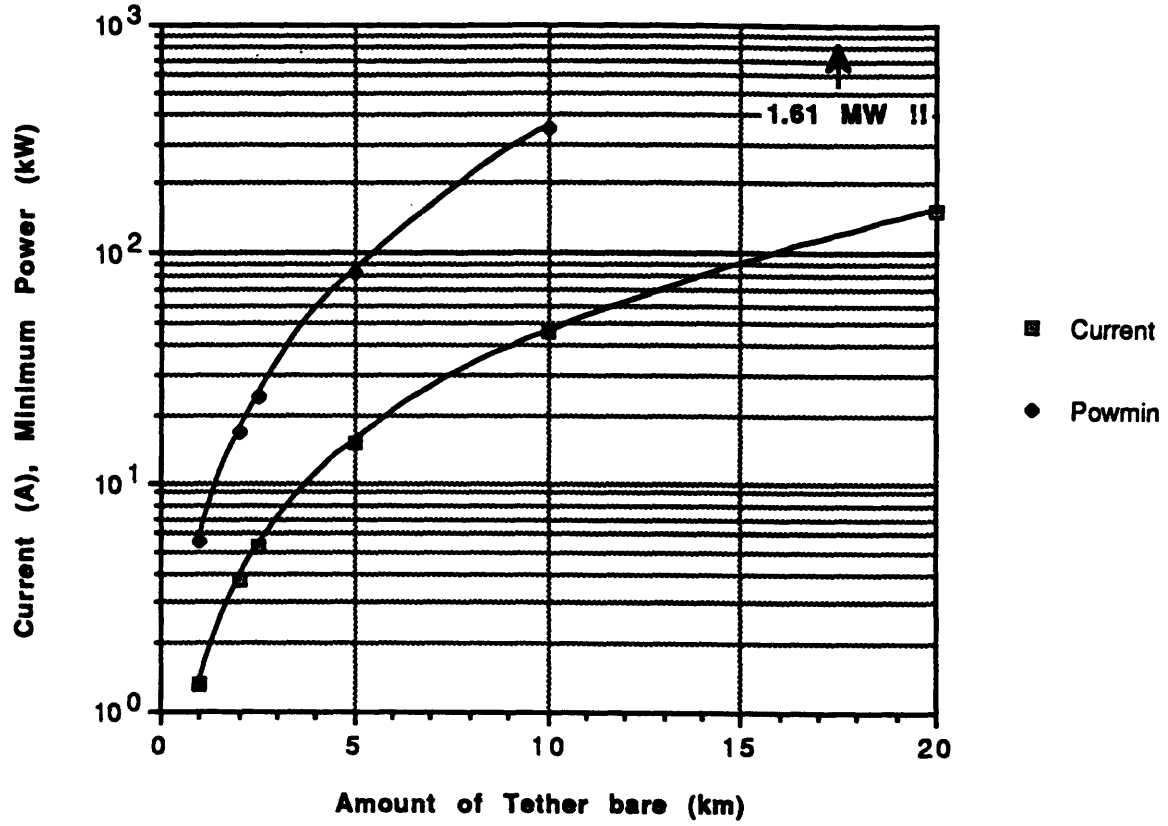

Fig. 39c
Average, Maximum, and Minimum Thrust of Partly Bare Thruster
(L=20km, 2mm tether)

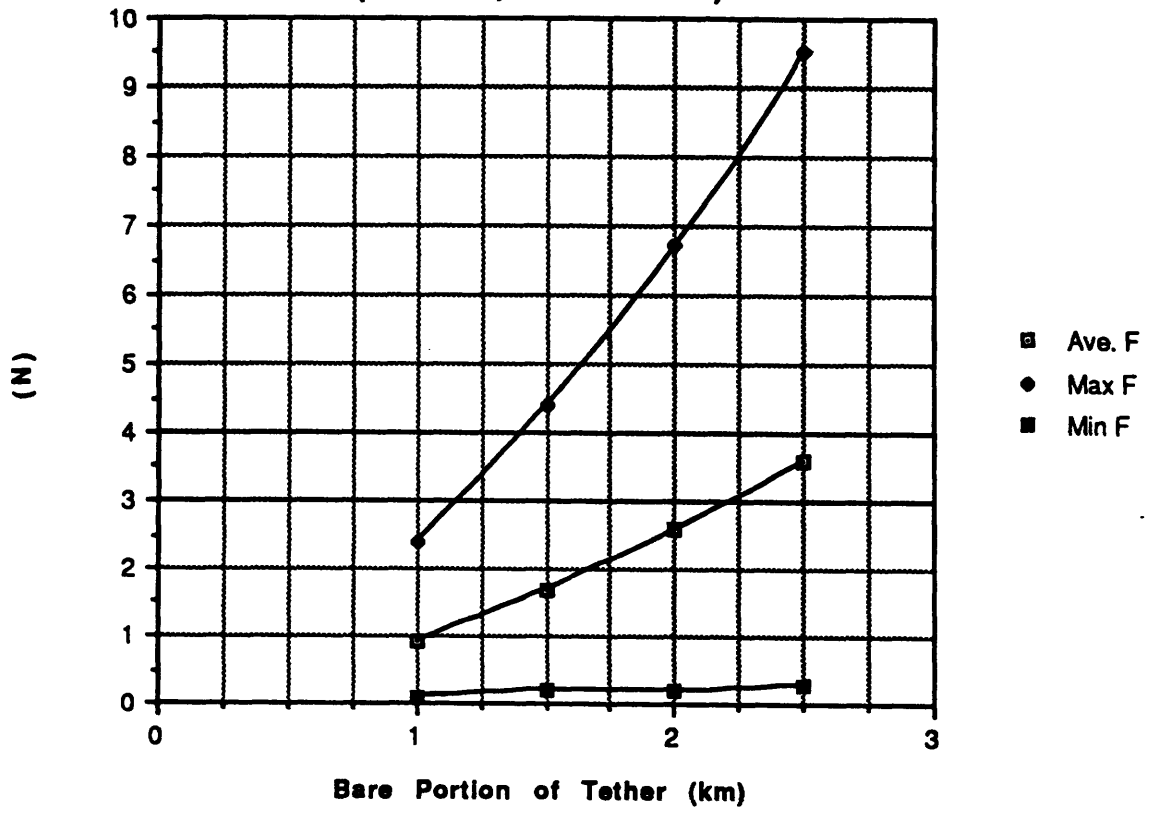

Fig. 39d
Av., Max., and Min. Thrust of Partly Bare Thruster
(L=15km, 2mm tether)

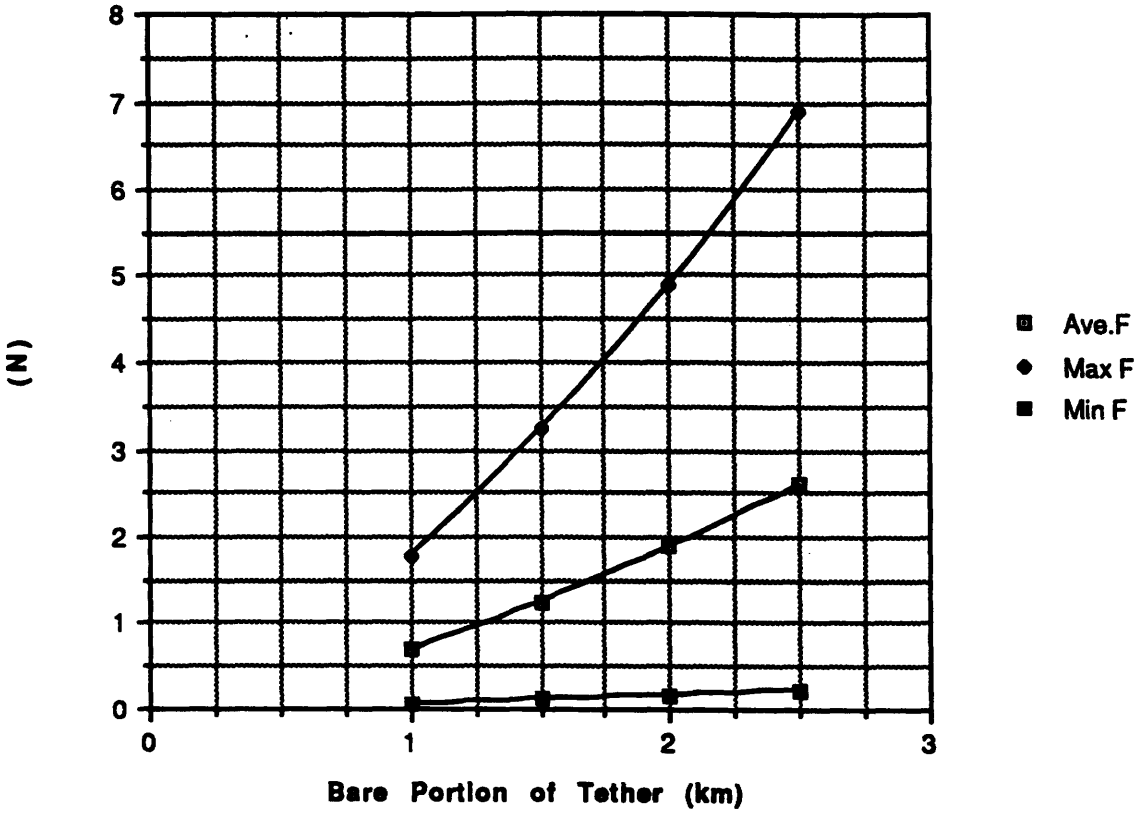

Fig. 39e
Av., Max., and Min. Thrust of Partially Bare Thruster
(Controlled with Fmax=4N, L=20km, 2mm tether)

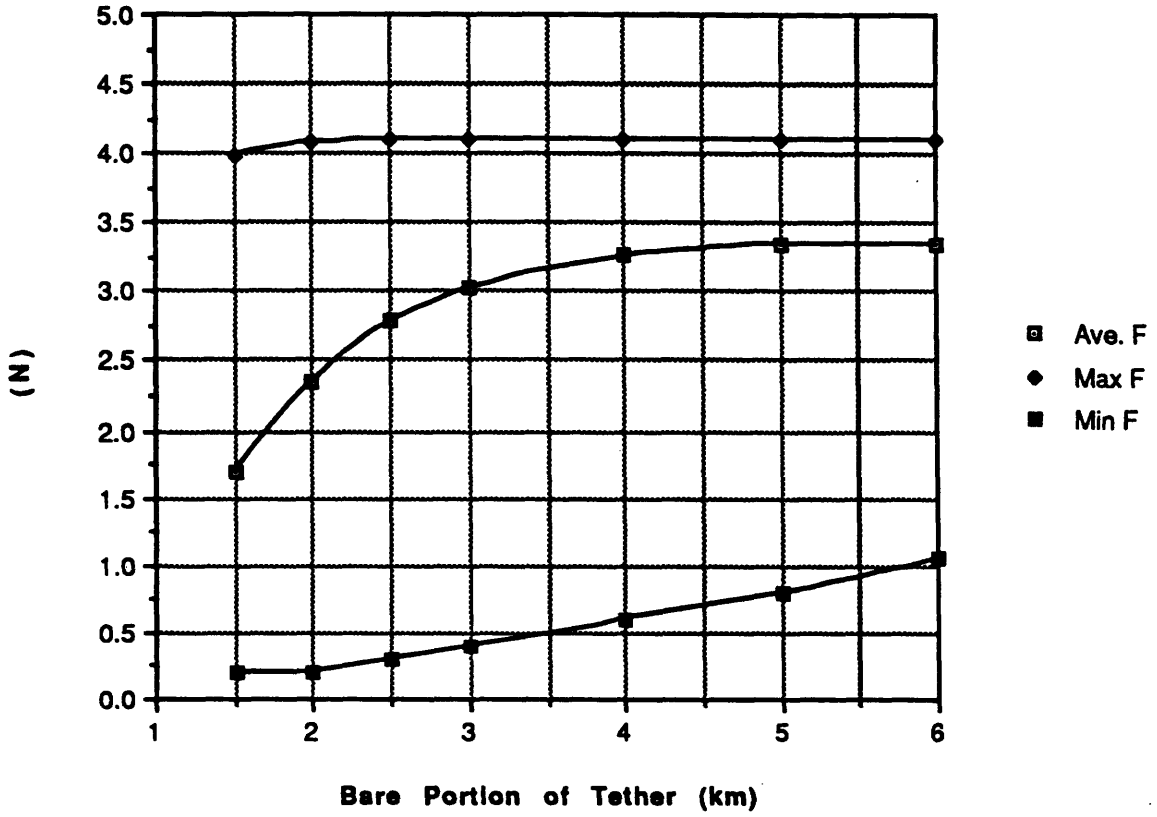

Fig. 39f Av., Max, and Min. Thrust of Partially Bare Thruster (Controlled with Fmax=3N, L=15km, 2mm tether)

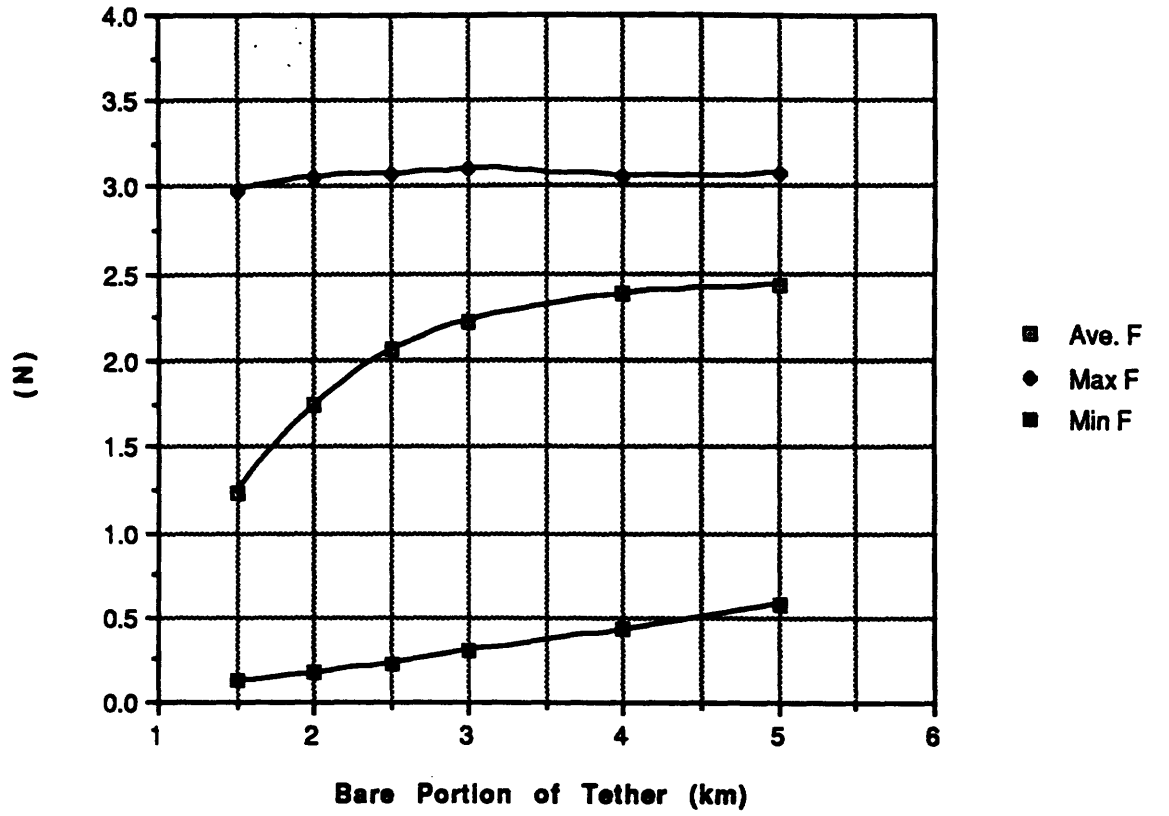

Fig. 39g Mass/<Thrust> for Partly Bare Thruster (2mm tether)

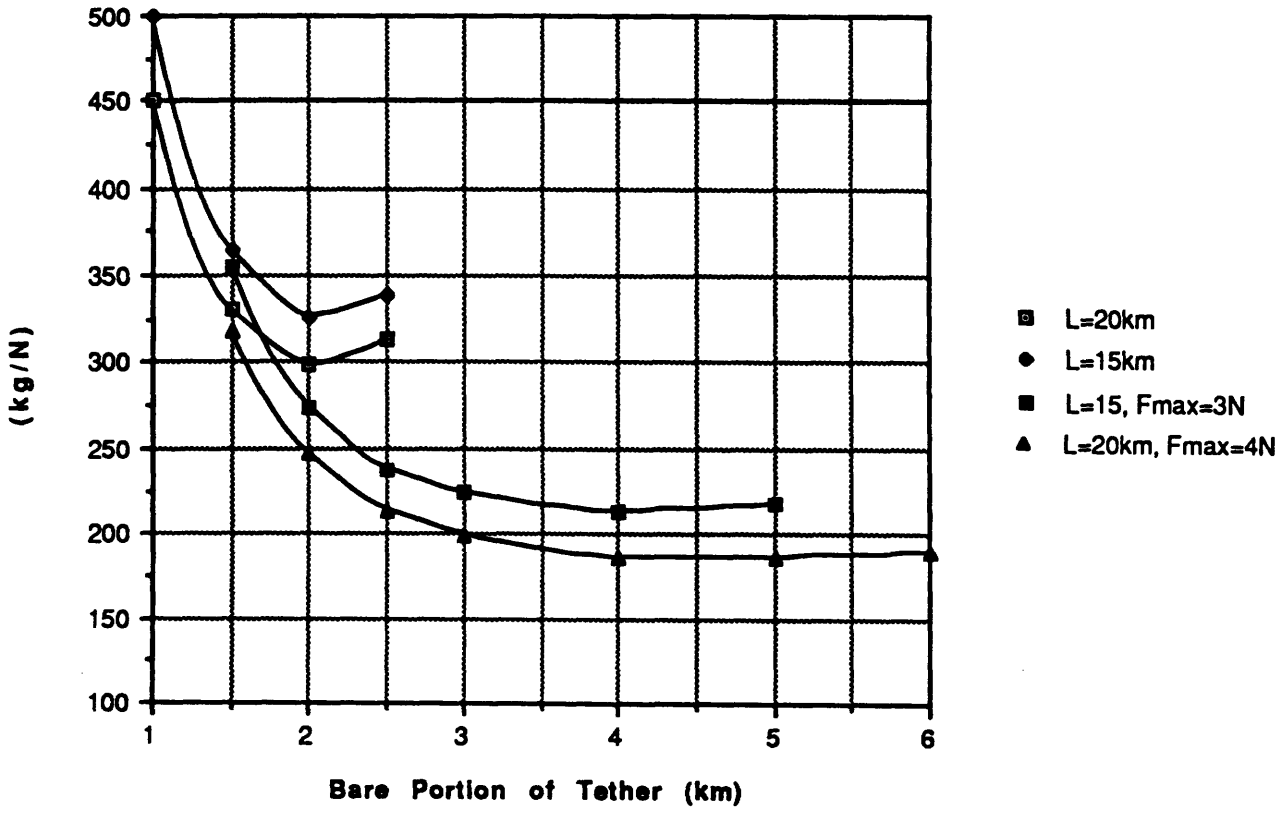

Fig. 39h <Power>/<Thrust> for Partly Bare Thruster (2mm tether)

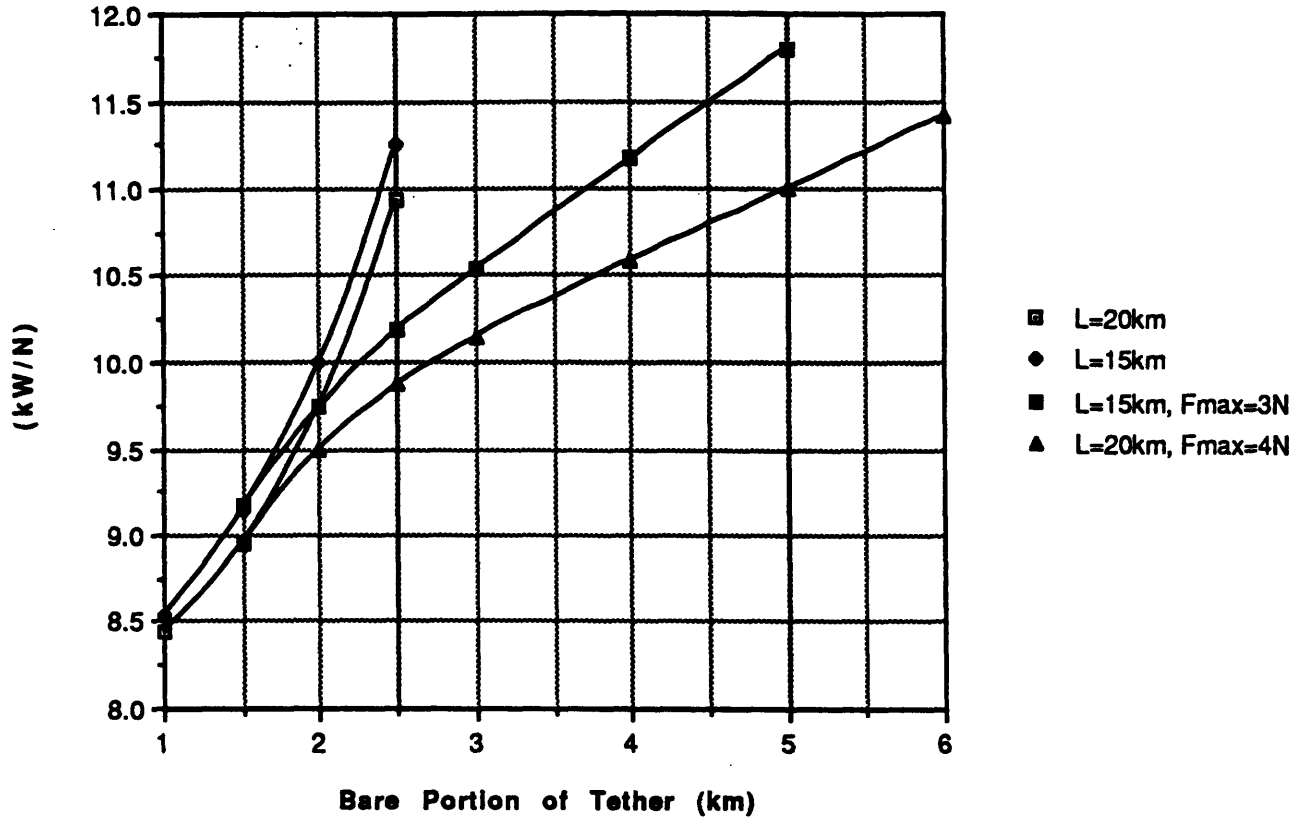

Fig. 39i Bare Thrusting <Efficiency> (2mm tether)

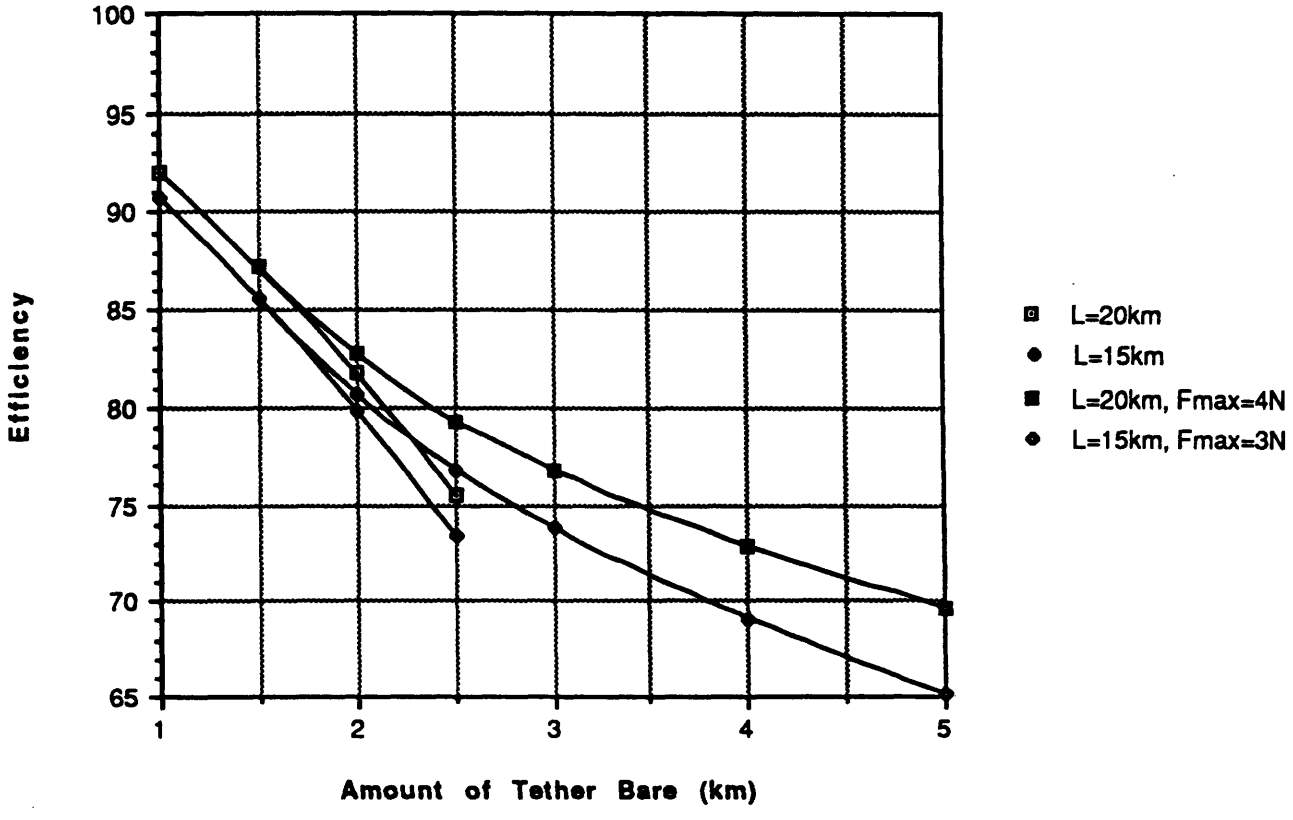

Fig. 39j Supply Power for Bare Thruster (L=20 km, Lb=2 km)

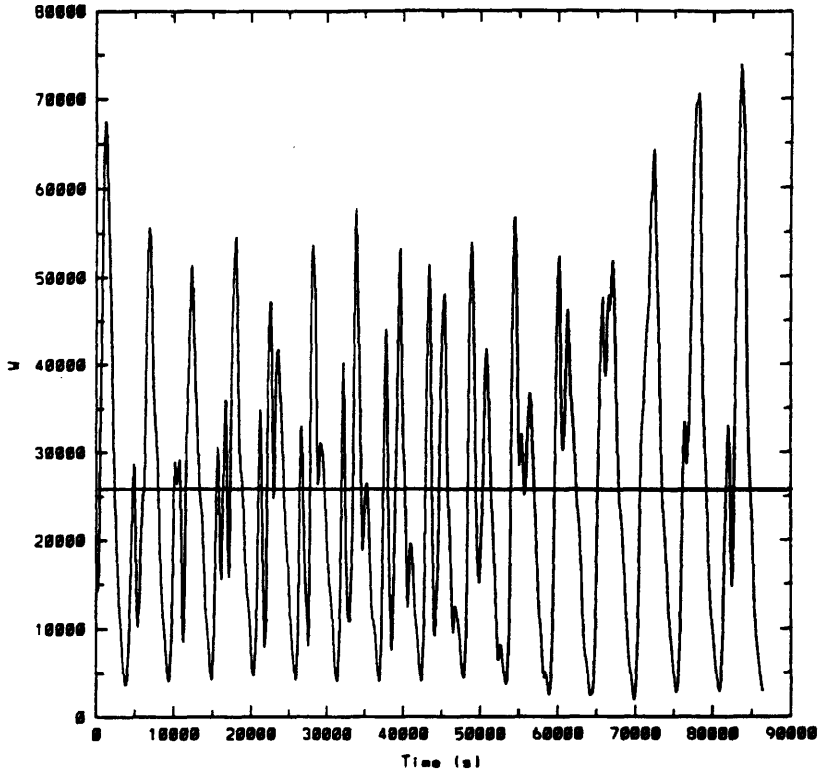

Fig. 39k Supply Voltage for Bare Thruster (L=20 km, Lb=2 km)

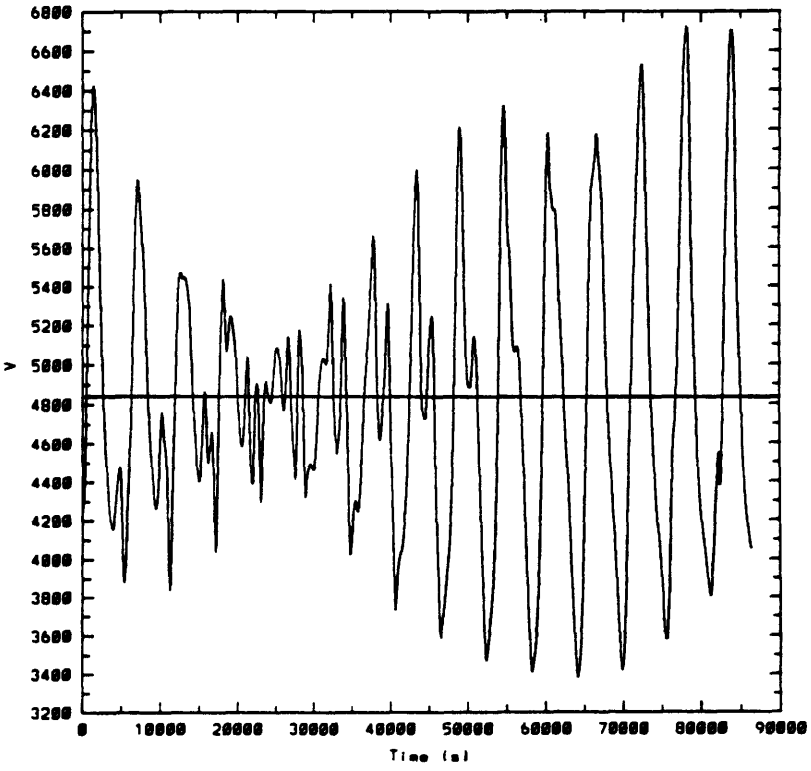

Fig. 39l Current for Bare Thruster (L=20 km, Lb=2 km)

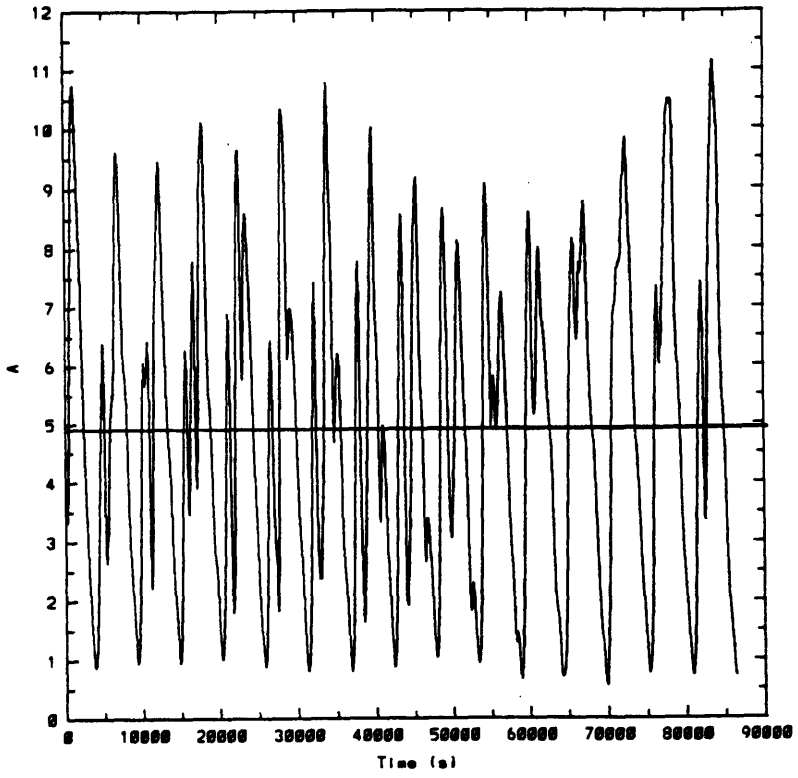

Fig. 39m Thrust for Bare Thruster (L=20 km, Lb=2 km)

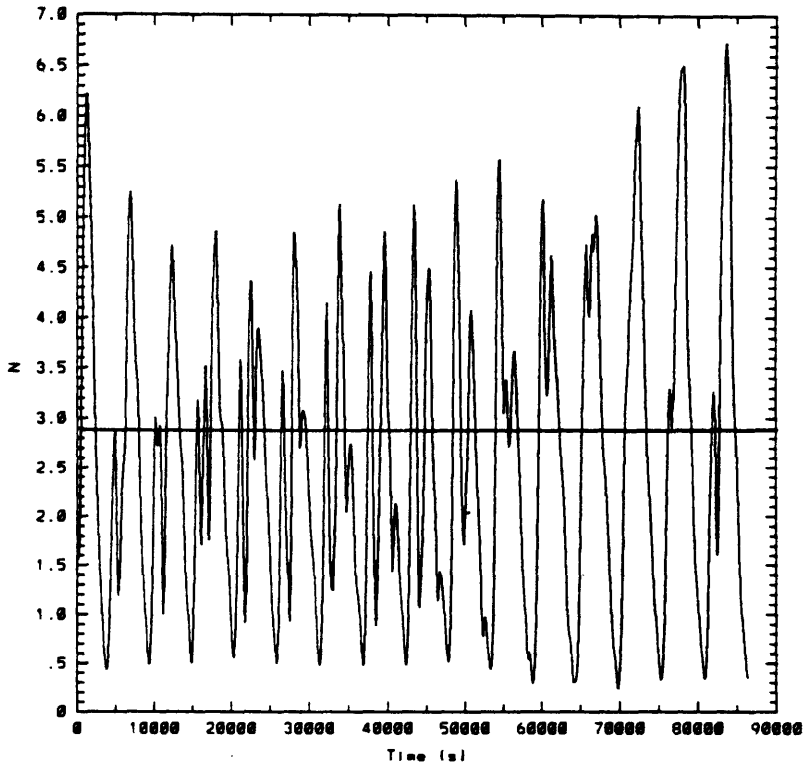

Fig. 39n Supply Power for Controlled Bare Thruster
(L=20 km, Lb=2 km, Fmax=4 N)

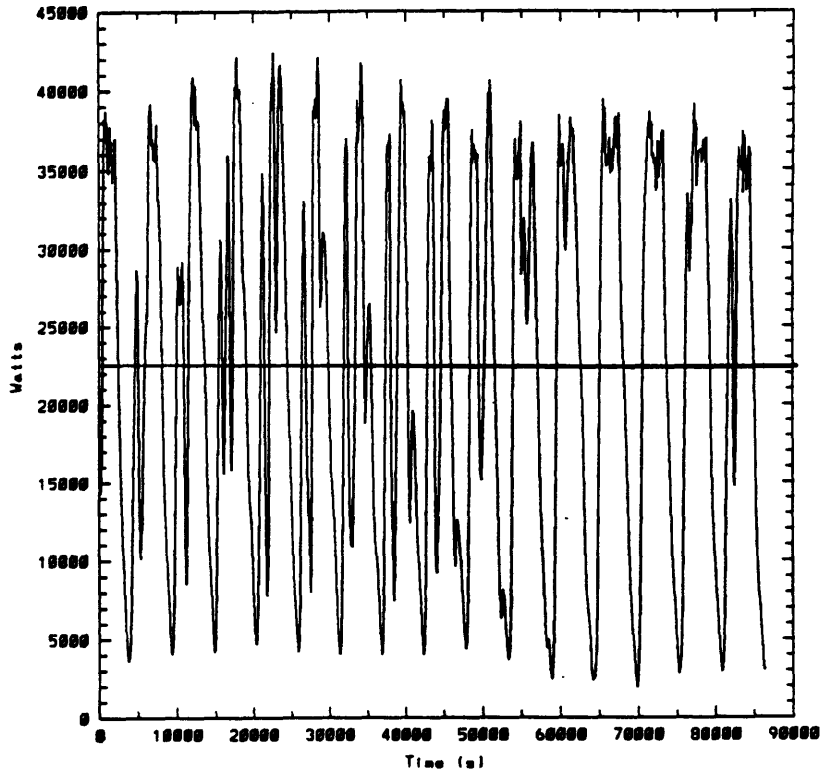

Fig. 39o Mass Comparison of Partly Bare Thrusters (L=15 and 20km, 2mm tether)

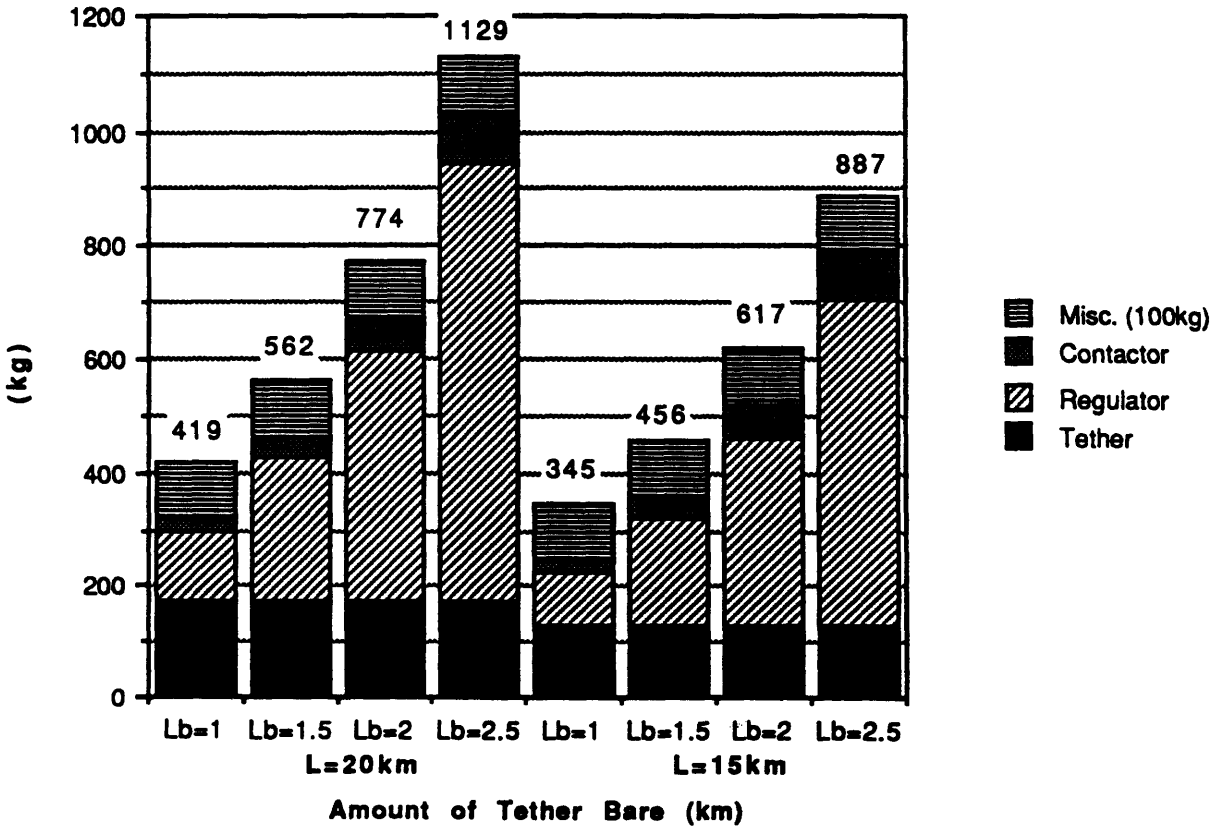

Fig. 39p Mass Comparison of Controlled Bare Thrusters (Fmax=4N, L=20km, 2mm tether)

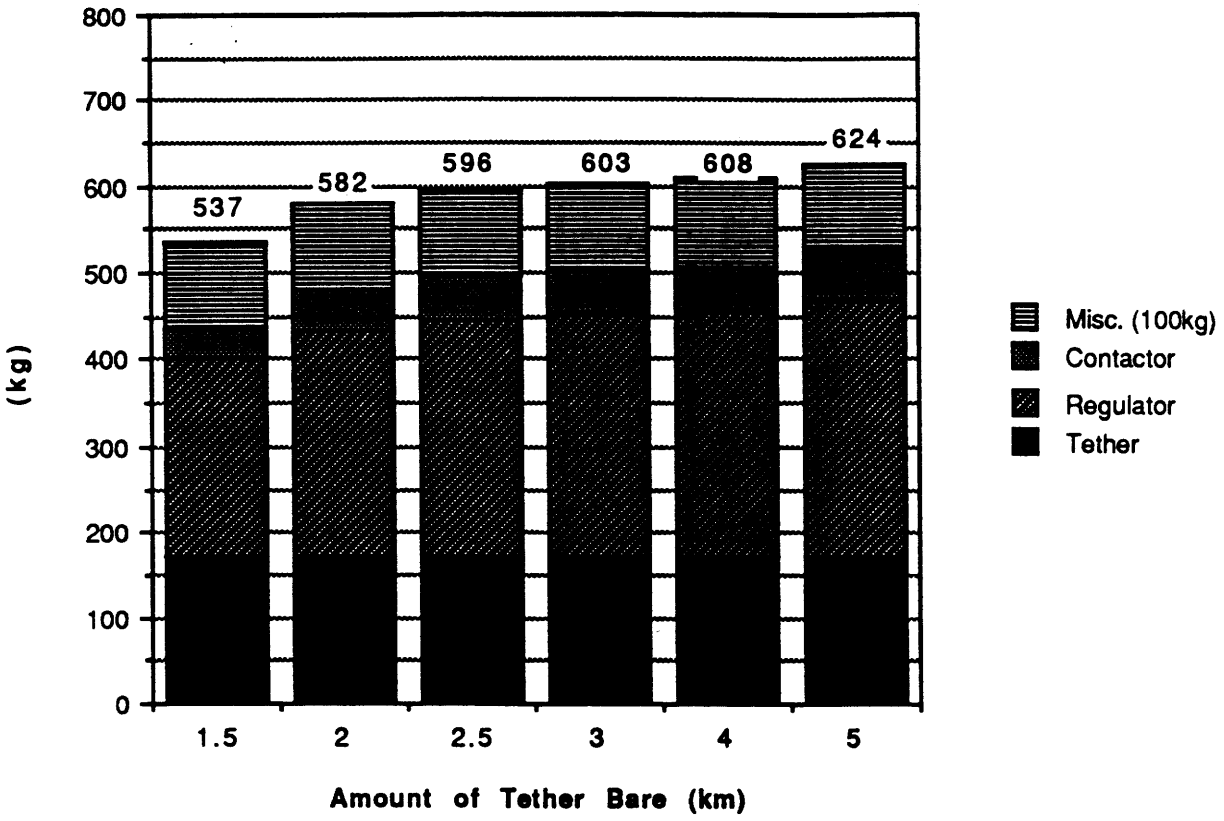

Fig. 40a Radiation Impedance for D=6 m End Contactor

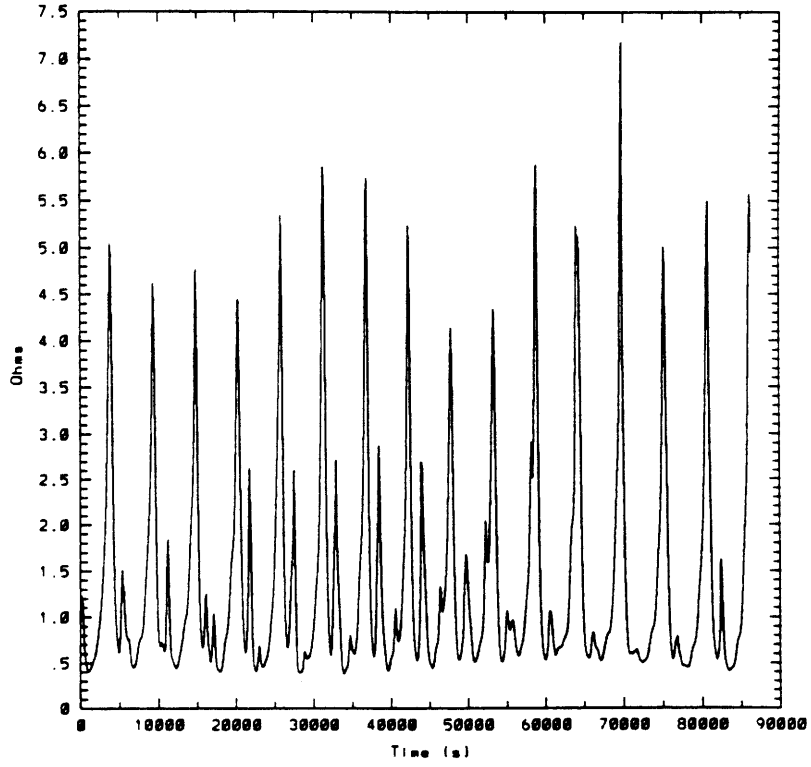

Fig. 40b Radiation Impedance for D=1 m End Contactor

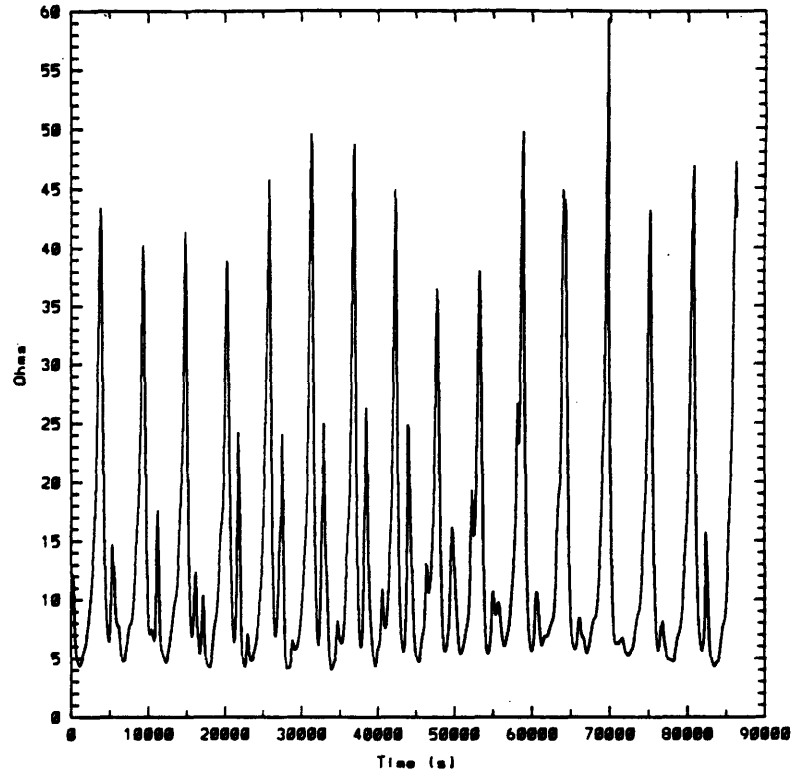

Fig. 40c Radiation Impedance for D=0.5 m End Contactor

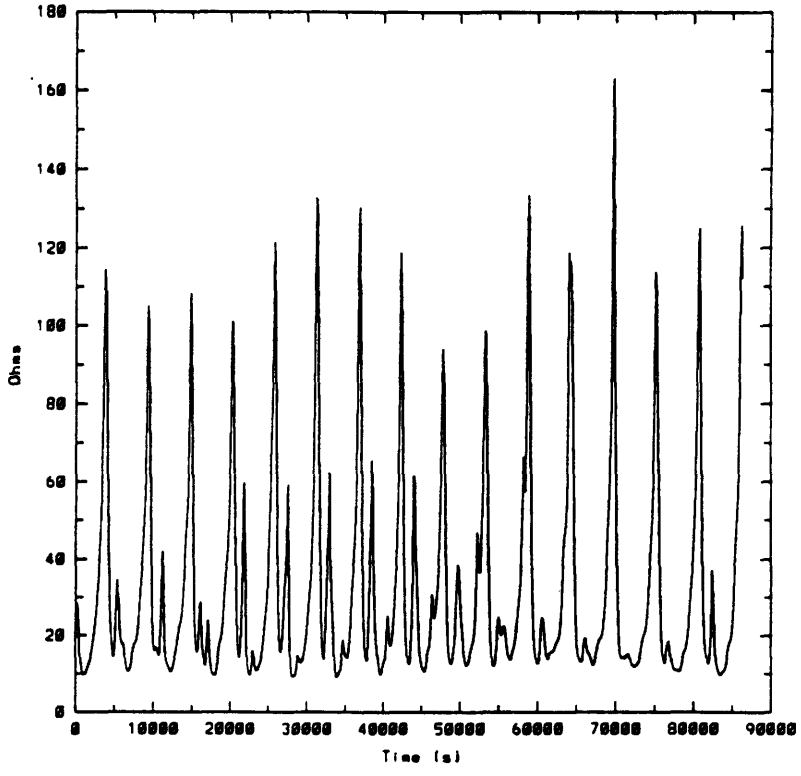

Fig. 40d Effect of Variable Ionospheric Impedance (Maximum Power, Contactor)

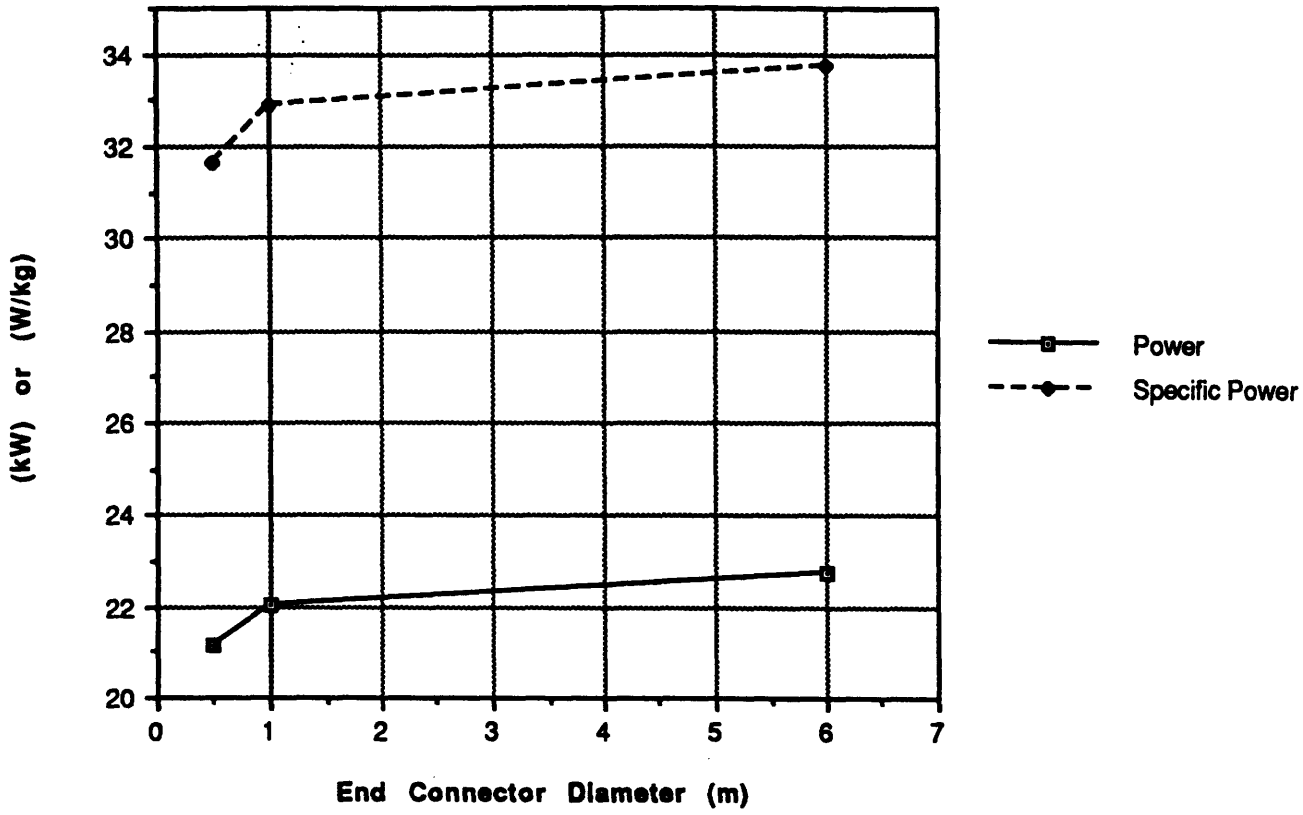

Fig. 40e Effect of Constant Ionospheric Impedance (Maximum Power, Contactor)

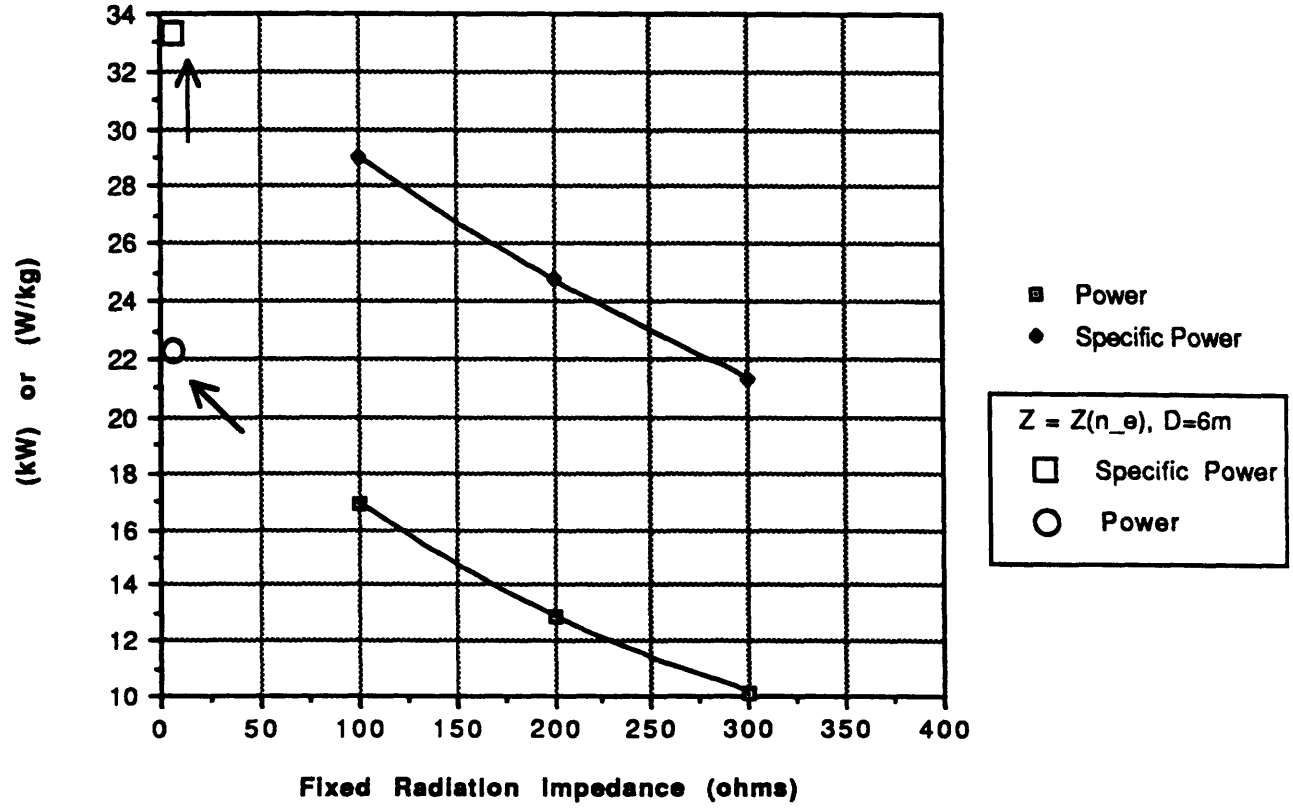

Fig. 41a Hollow Bare Tether <Maximum Power>

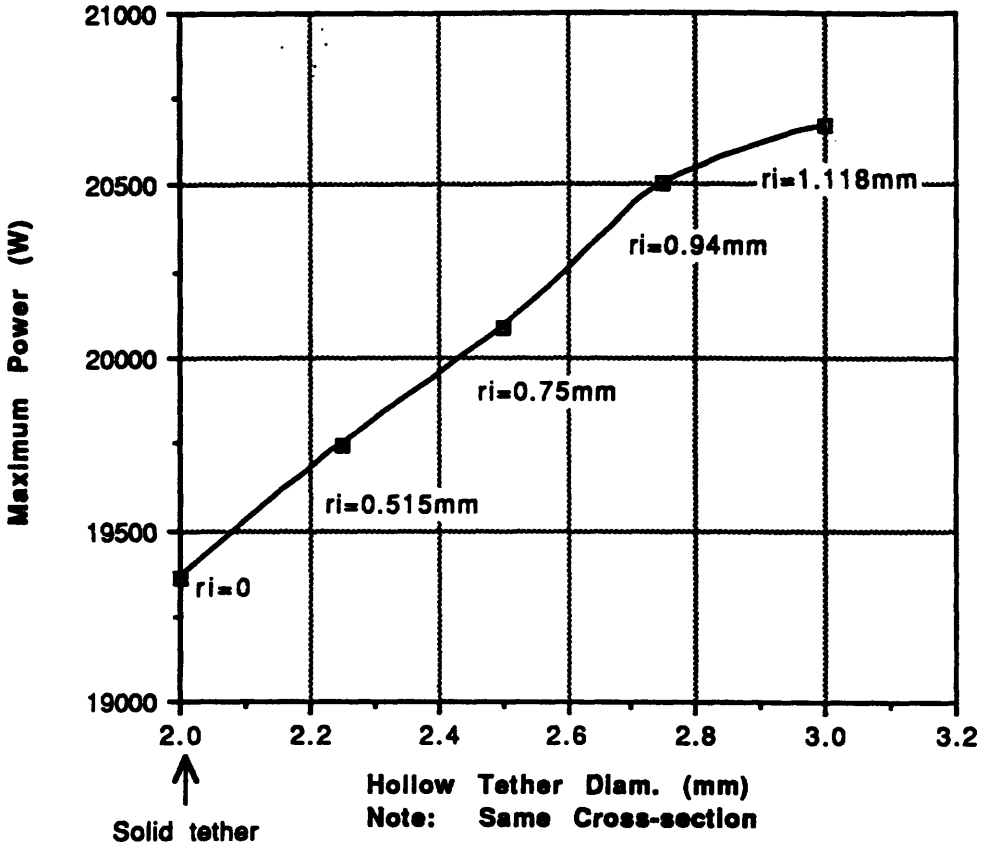

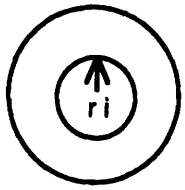

Fig. 41b Hollow Bare Tether Specific Power

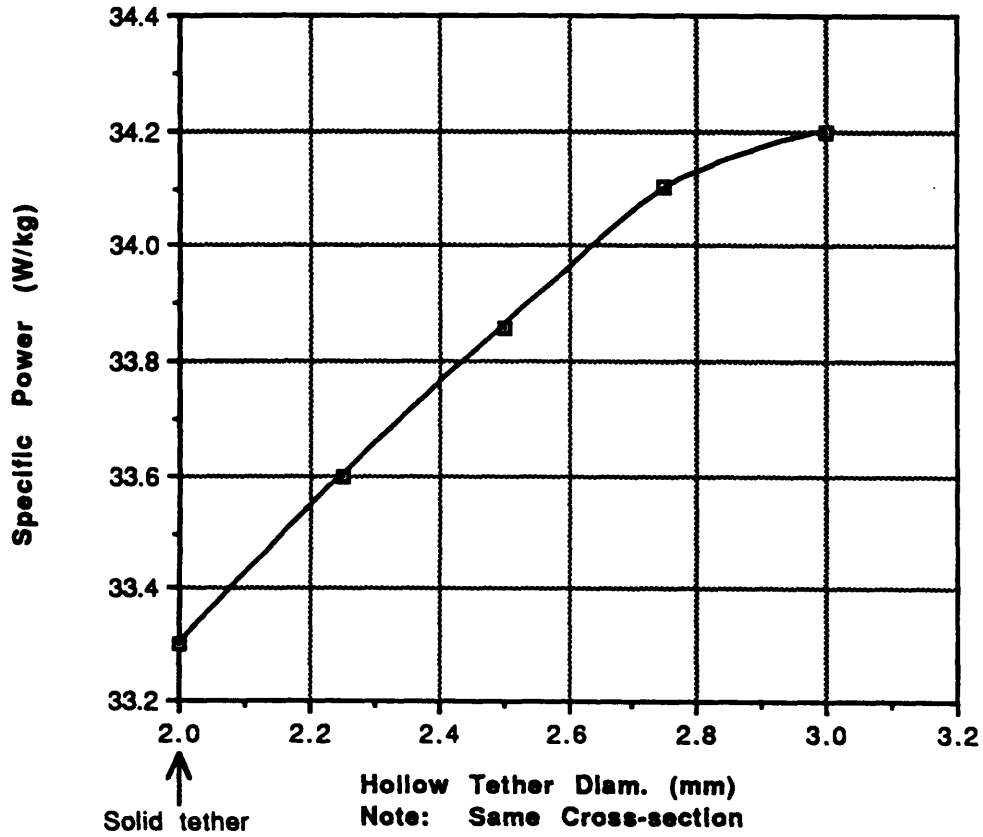

Fig. 42a
<Power> vs. Radius of Inside Hollow for Contactor Tether

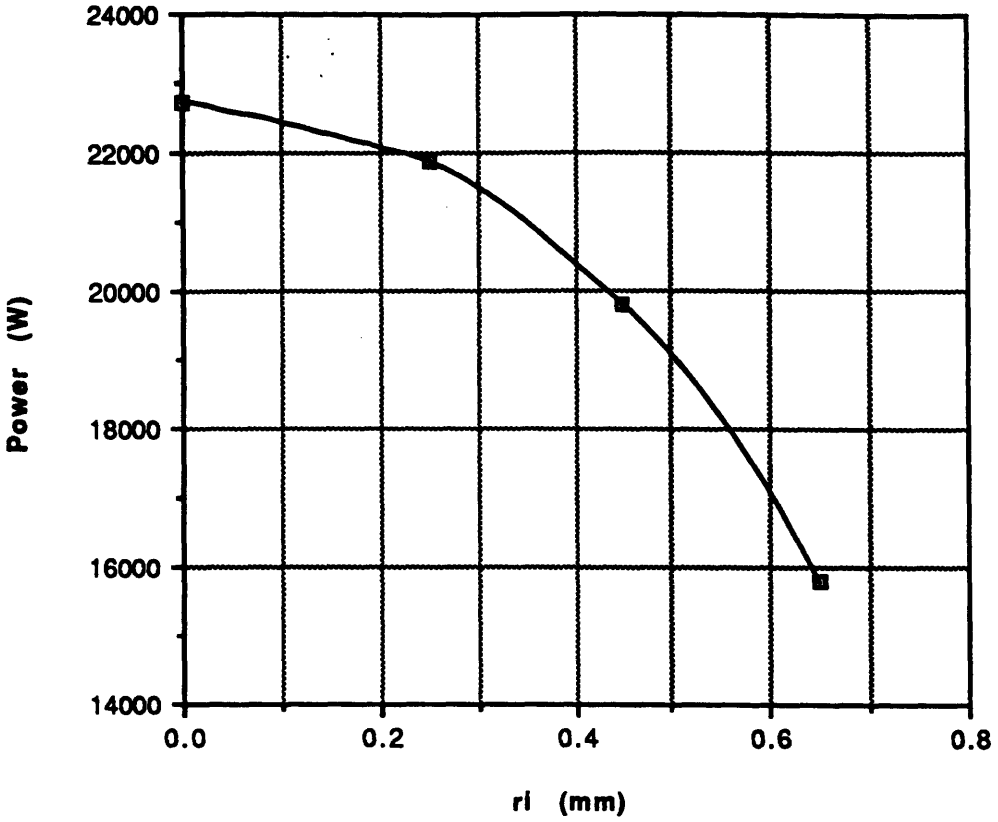

Fig. 42b Specific Power vs. Radius of Inside Hollow of Contactor Tether

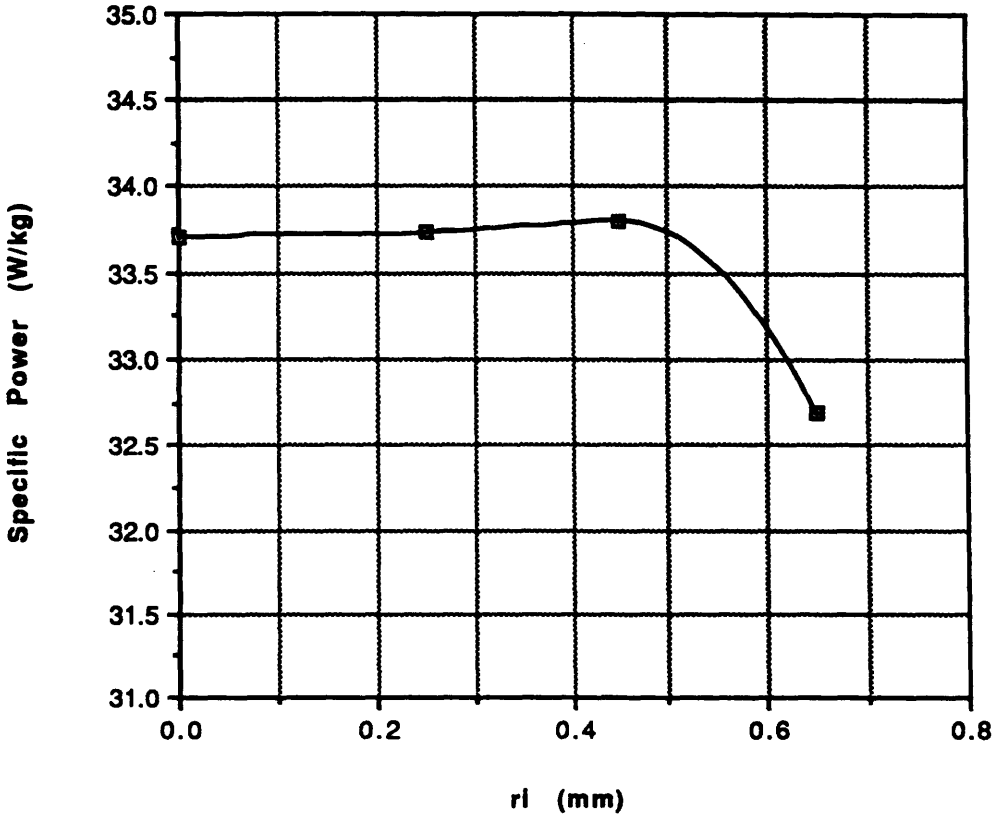

Fig. 43a <Maximum Power> of Multiple Tethers

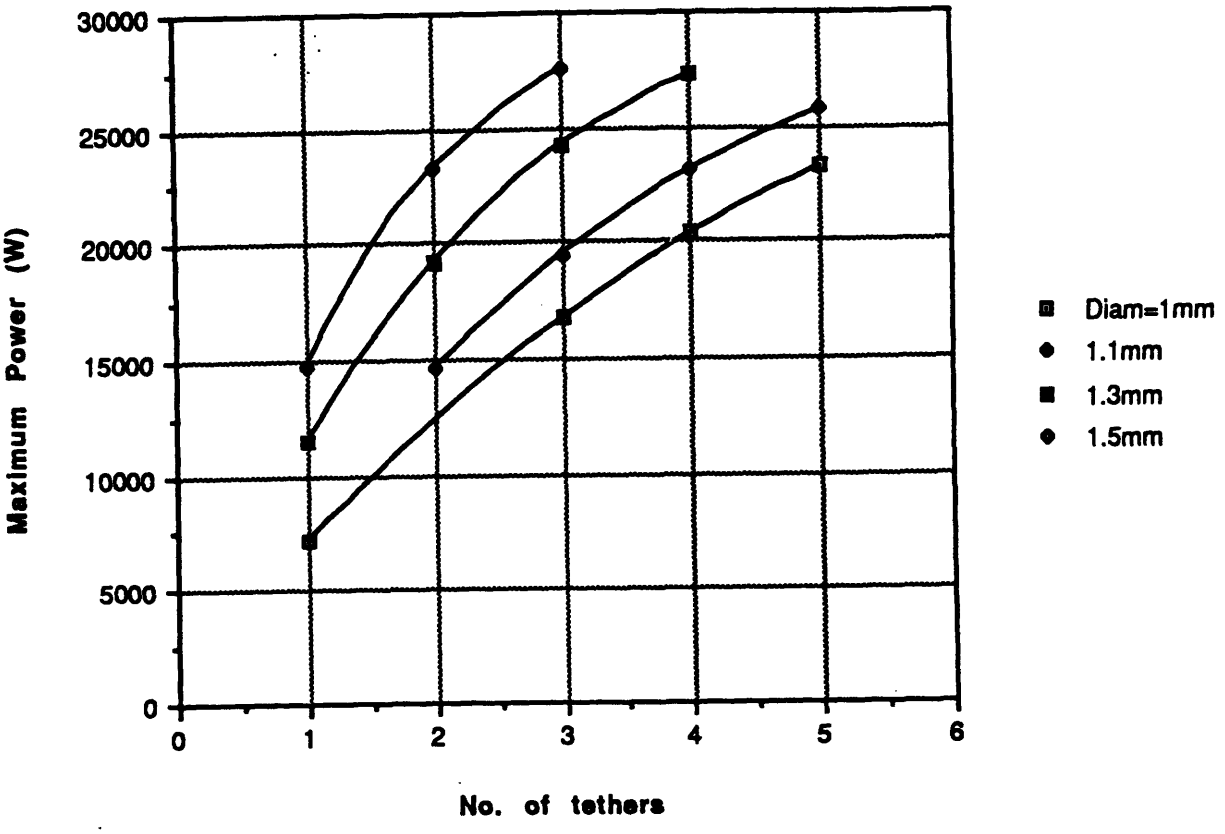

Fig. 43b Specific Powers of Multiple Tethers

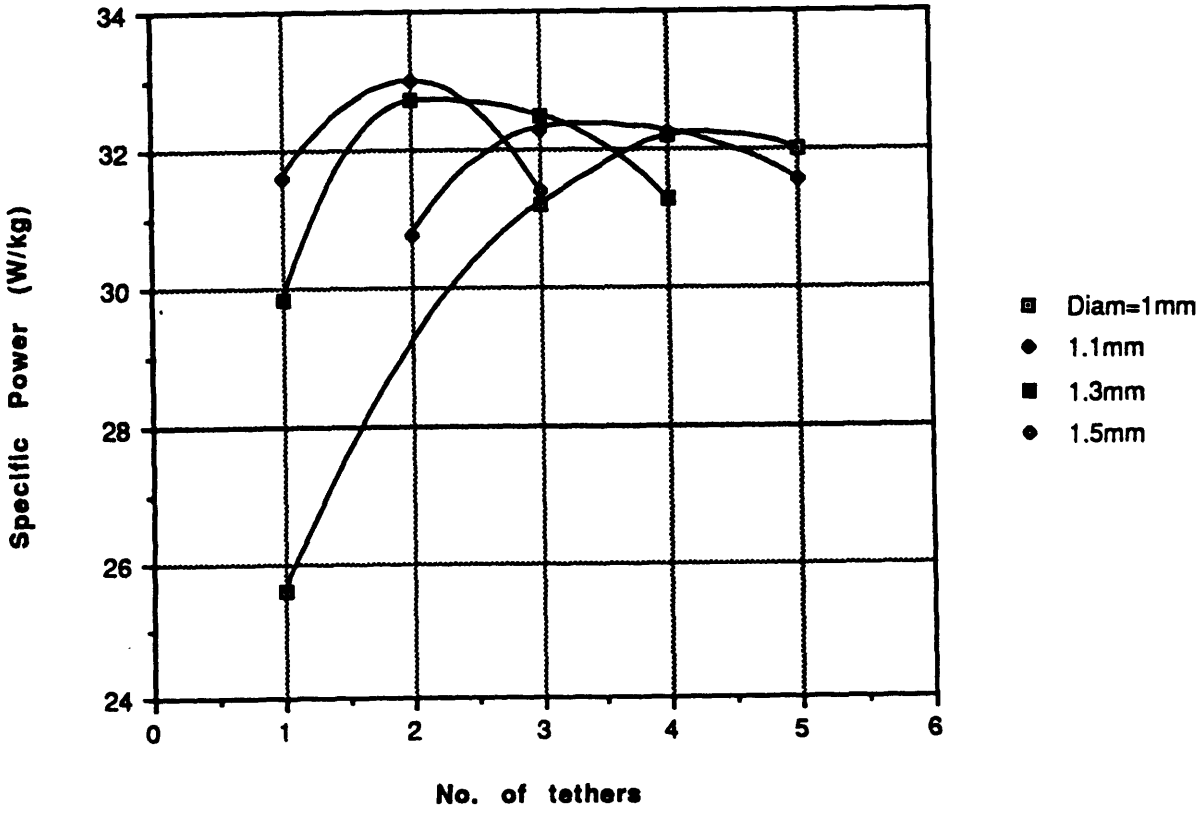

Fig. 44a <Maximum Power> vs. Tether Length

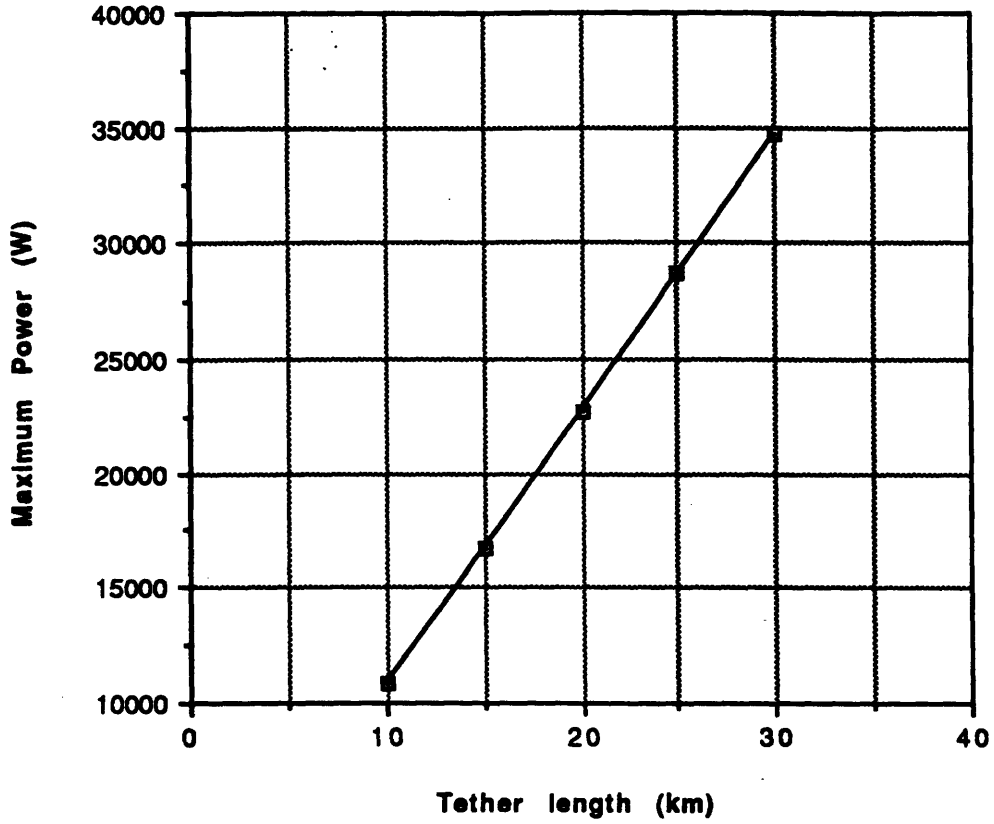

Fig. 44b Specific Power vs. Tether Length

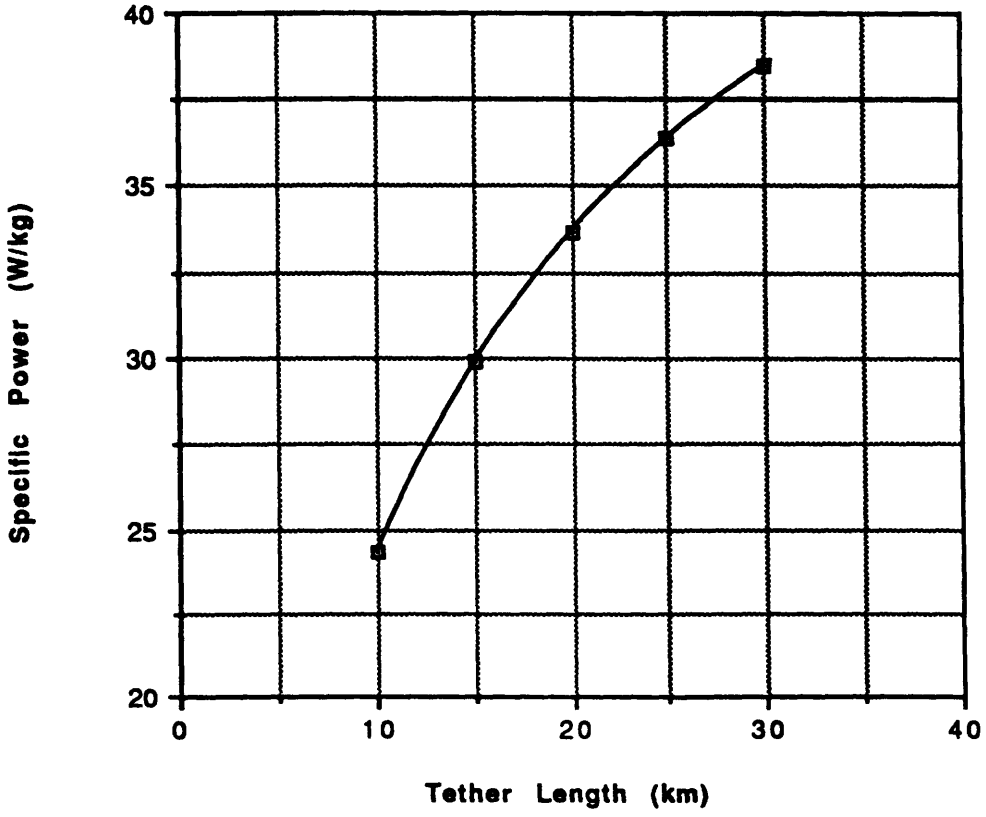

Table 1 Breakeven Points for Maximum Power and Controlled Tethers

Maximum Power:			
	Power (kW)	$\dot{m}_R$ (kg/day)	Breakeven Pt. (days)
Contactor $I_i = 1$	22.7	94.0	5.3
Contactor $I_i = 0.1$	5.8	18.2	10.0
Bare	19.36	105.0	7.0
B+C $I_i = 1$	23.0	115.8	6.3
B+C $I_i = 0.1$	19.7	107.6	7.8
Controlled UL=20 kW LL=19.5 kW :			
	Power (kW)	$\dot{m}_R$ (kg/day)	Breakeven Pt. (days)
Contactor $I_i = 1$	19.34	64.3	4.3
Bare	17.7	77.2	5.1
B+C $I_i = 1$	19.32	67.4	4.4
B+C $I_i = 0.1$	17.81	74.5	5.5

Table 2 Contactor Thruster Performance

	Const. I	Const. V	Const. P	Const. F
Thrust (max/min) [N]	4.89/3.27	5.85/1.27	4.26/3.71	4/4
Power (max/min) [kW]	45.1/29.89	68.28/10.32	37.9/37.9	40.95/35.12

Table 3a Bare Thrusters (Uncontrolled)

Power (max/min) [kW]	Lb = 1	Lb = 1.5	Lb = 2	Lb = 2.5
L = 20 km	21.04/0.65	42.05/1.69	73.92/1.85	129.04/2.61
L = 15 km	15.81/0.49	31.63/0.91	55.11/1.39	95.85/1.96

Table 3b Bare Thrusters (Controlled, L=20 km)

Power [kW]	Lb=1.5	Lb=2	Lb=2.5	Lb=3	Lb=4	Lb=5
(Max/Min)	38.06/1.21	43.63/1.85	45.69/2.61	46.63/3.45	47.18/5.36	49.34/7.68

References

[1] Ahedo E., Martinez-Sanchez M., and Sanmartin J. Current Collection by an Active Spherical Electrode in an Unmagnetized Plasma. Unpublished manuscript, to be submitted to the *Physics of Fluids* (B), 1990.

[2] Arnold, D. Tether Tutorial. In *Second International Conference on Tethers in Space*, Conference Proceedings, 1987.

[3] Barnett A. and Olbert S. Radiation and Waves by a Conducting Body moving through a Magnetized Plasma. *J. Geophys. Res.*, 91, 10:117-135, 1986.

[4] Barron, R. *Cryogenic Systems*. Oxford University Press NY, 1985.

[5] Battin, R. *An Introduction to the Mathematics and Methods of Astrodynamics*. AIAA Education Series, 1987.

[6] Bayles G., Lauer J., Buzzelli E., and Jackovitz J. Silver-Iron Batteries for Submersible Applications. Westinghouse R&D Paper 89-1M2-ELCHC-P3, 1989.

[7] Block L. A Double Layer Review. *Astrophysics and Space Science*, 55:59-83, 1978.

[8] Carroll J. Guidebook for Analysis of Tether Applications. In *Tethers in Space Handbook*, 2nd ed. NASA, 1985.

[9] Dobrowolny M. and Iess L. The Interaction of a Hollow Cathode with the Ionosphere. *Physics of Fluids* (B), Vol.1, No.9:1880-9, Sept. 1989.

[10] *Earth Albedo & Emitted Radiation*. NASA Space Vehicle Design Criteria, SP-8067, July 1971.

[11] Forester T., Ed. *The Materials Revolution*. The MIT Press, Cambridge, MA 1988.

[12] Gabriel S., Jones R., and Garrett H. Alfven Propulsion at Jupiter. In *Second International Conference on Tethers in Space*, Conference Proceedings, 1987.

[13] Gerver M., Hastings D.E., and Oberhardt M. Theory of Plasma Contactors in Ground-based Experiments and Low Earth Orbit. *J. of Spacecraft and Rockets*, 27:391-402, 1990.

[14] Greene M., Wheelock D., and Baginski M. Electrodynamics of the Getaway Tether Experiment. *J. of Spacecraft and Rockets*, 26:452-459, 1989.

[15] Griffith P. Professor of Mechanical Engineering, MIT. Private Communication.

[16] Grossi M. and Arnold D. Engineering Study of the Electrodynamic Tether as a Space borne Generator of Electric Power. NASA Contract NAS-8-35497 Final Report, 1984.

[17] Grossi, M. Tether History and Historiography. In *Second International Conference on Tethers in Space*, Conference Proceedings, 1987.

[18] Hastings D.E. Theory of Plasma Contactors used in the Ionosphere. *J. of Spacecraft and Rockets*, 24:250-256, 1987.

[19] Hastings D.E. and Gatsonis N. Plasma Contactors for use with Electrodynamic Tethers for Power Generation. *Acta Astronautica*, Vol.17, No.8:827-836, 1988.

[20] Jursa, A., Ed., *Handbook of Geophysics and the Space Environment*. Air Force Geophysical Laboratory, 1985.

[21] Kaufmann III, W. *Universe*. W.H. Freeman and Co. NY, 1985.

[22] Keating G., Shorthill R., Masursky H., and Elson L., Eds. *Planetary Studies*. Pergamon Press, 1987.

[23] Kerslake W. and Domitz S. Neutralization Test on the SERT II Spacecraft. NASA Technical Memorandum 79271 (and AIAA Paper 79-2064). Presented at the Fourteenth International Conference on Electric Propulsion, Princeton, New Jersey, 1979.

[24] Kerslake W. and Ignaczak L. SERT II 1980 Extended Flight Thruster Experiments. AIAA Paper 81-0665. Presented at the AIAA/JSASS/DGLR Fifteenth International Electric Propulsion Conference, Las Vegas, Nevada, 1981.

[25] Kessler D., Reynolds R., and Anz-Meador P. Orbital Debris Environment for Spacecraft Designed to Operate in Low Earth Orbit. NASA Technical Memorandum 100 471, 1989.

[26] Kreith, F. *Radiation Heat Transfer*. International Textbook Co. Scranton, Penn. 1962

[27] Laue, J. Status of Tethered Satellite System (TSS) Development. In *Second International Conference on Tethers in Space*, Conference Proceedings, 1987.

[28] Lockheed Missiles & Space Co. SAFE Final Report. NASA Contract NAS-8-31352 Final Report, 1986.

[29] Martinez-Sanchez M. and Hastings D.E. A Systems Study of a 100kW Tether. *J. of Astronautical Sciences*, 35:75-96, 1987.

[30] Martinez-Sanchez M., Rivas D., Prall J., Hastings D.E., and Estes R. A Systems Study of a 100 kW Electrodynamic Tether. NASA Contract NAS-3-24669 Final Report, 1988.

[31] Nagle D. Martin-Marietta Laboratories. Private Communication.

[32] Parks D. and Katz I. Theory of Plasma Contactors for Electrodynamic Tethered Satellite Systems. *J. of Spacecraft and Rockets*, 24:245-249, 1987.

[33] Prall J. Thermal and Dynamical Effects on Electrodynamic Space Tethers. MIT Aero/Astro S.M. Thesis, 1987.

[34] Rivas D. A Systems Study of an Electrodynamic Tether. MIT Aero/Astro S.M. Thesis, 1987.

[35] Sanmartin J., Martinez-Sanchez M., and Ahedo E. Bare Wire Anodes for Electrodynamic Tethers. Unpublished manuscript, to be submitted to the *AIAA Journal*, 1990.

[36] Serway R. *Physics for Scientists and Engineers, with Modern Physics*. Saunders College Pub. Philadelphia, 1990.

[37] Urrutia J. and Stenzel R. Modeling of Induced Currents form Electrodynamic Tethers in a Laboratory Plasma. *Geophys. Res. Letters*, 17, 10:1589-1592, 1990

[38] Wang J. and Hastings D.E. The Radiation Impedance of an Electrodynamic Tether with End Connectors. *Geophys. Res. Letters*, 14:519-522, 1987.

[39] Wei R. and Wilbur P. Space charge limited Current Flow in a Spherical Double Sheath. *J. of Applied Physics*, 60:2280-2284, 1986.